

UNIVERSITY OF OKLAHOMA

GRADUATE COLLEGE

A STUDY ON THE INFLUENCE OF SELECTED GEOGRID INDEX PROPERTIES
ON THEIR IN-AGGREGATE PERFORMANCE

A DISSERTATION

SUBMITTED TO THE GRADUATE FACULTY

in partial fulfillment of the requirements for the

Degree of

DOCTOR OF PHILOSOPHY

By

TAHSINA MAHMOOD

Norman, Oklahoma

2013

A STUDY ON THE INFLUENCE OF SELECTED GEOGRID INDEX PROPERTIES
ON THEIR IN-AGGREGATE PERFORMANCE

A DISSERTATION APPROVED FOR THE
SCHOOL OF CIVIL ENGINEERING AND ENVIRONMENTAL SCIENCE

BY

Dr. Kianoosh Hatami, Chair

Dr. Musharraf Zaman

Dr. Gerald A. Miller

Dr. Kanthasamy Muraleetharan

Dr. Kurt Gramoll

© Copyright by TAHSINA MAHMOOD 2013
All Rights Reserved.

Dedication

To my parents

Flt. Lt. Mir Mahmoodul Hoque

Sultana Reza (Snigdha)

&

To my one and only adorable younger brother

Mir Mujahid Bin Mahmood

Acknowledgements

First of all, I would like to express my sincere thanks and appreciation to my advisor, Dr. Kianoosh Hatami for his patience and strong guidance all through my doctoral study. Without Dr. Hatami's expert advice, kind support and friendly encouragement, this dissertation would not have been accomplished. I am very blessed and honored to be his first doctoral student. He set an example of a very good mentor. His gentle behavior and kind way of communication always amazed me. I will try hard to follow his advice throughout my life.

I also wish to express my deep appreciation to Dr. Musharraf Zaman for his constant encouragement, thoughtful discussion, and constructive suggestions. I am very thankful that he served on my Doctoral Committee. He has always been a source of inspiration and motivation for me.

I would like to say thanks to Dr. Gerald A. Miller, Dr. Kanthasamy Muraleetharan and Dr. Kurt Gramoll for serving on my Doctoral Committee. I am truly grateful for their time and valuable comments. They were always very supportive and available to help me whenever I needed. I would also like to thank Dr. Amy B. Cerato, who served on my committee during the initial stage of my PhD program.

I am also very grateful to the CEES staff at the University of Oklahoma (OU), especially to Susan R. Williams, Brenda G. Clouse, Audre L. Carter, Molly Smith and Karen Horne at the COE (College Of Engineering) Dean's Office.

I would also like to acknowledge the invaluable assistance from Mr. Michael Schmitz at the OU Fears Laboratory, Dr. Christopher Ramseyer and that of the following undergraduate research assistants: Jesse Berdis, Max Newton, Derek Reid, Kyle Olson, Evan Burns, Brandi Dittrich, Carlos Chang, Thai Dinh, Alex Haluska, Grayson Niemeyer, Carl Walkup, Chris Barclay, Juan Pereira, Mariam Edwar, Nicholas Iburguen, Adam Burke and Owen Watley in setting up and carrying out the tests described in this dissertation. The help from Dr. Sesh Commury and the generous loan of the field compactor equipment by the Haskell Lemon Construction Co. is also acknowledged. The Oklahoma Department of transportation (ODOT) and the Oklahoma Transportation Center (OkTC) are greatly acknowledged for providing the financial support for this study.

I would like to thank my colleagues Rouzbeh Ghabchi, Juan M. Pereira Villarroel, Callie M. French, Fabien Pariot, Nur Hossain, Hasan Kazmee, Dr. Dharamveer Singh, Dr. Botao Lin, Dr. Zahid Hossain, Lina M. Garcia Tellez, Jaime E. Granados Rueda, Danial Esmaili, Atefeh Fathi, Hessam Yazdani and Arash Hassanikhah for their help, friendly advice and support.

I am grateful for the love and care that I got from my extra-ordinary awesome friends: Syed Maruful Huq, Yasmin Zahir, Dr. Md. Atiquzzaman, Ahsanur Rahman, Dulchi Fatema, Mourushi Muhoo, Ashfia Salemin Treena, Dr. Soumitra Nandi, Dr. Monayem Hossain Mazumder, Fariz Ibn Afzal, Tania Munmun, Debaroti Ghosh, Salman Ahmed, Fauzia Ahmed and Kaji Md. Hasibur R. Fuad.

Finally, my deep thanks go to my parents for their love and support they gave to me from my birth. I also would like to acknowledge my one and only brother, my adorable younger brother, Mir Mujahid Bin Mahmood, whom I could not see through the four years of my doctoral study.

Table of Contents

List of Tables	xii
List of Figures.....	xv
Abstract.....	xxxi
CHAPTER ONE.....	1
INTRODUCTION	1
1.1. Background.....	1
1.2. Problem Statement and Research Need.....	3
1.3. Objectives	4
CHAPTER TWO.....	7
LITERATURE REVIEW.....	7
2.1. Laboratory and Numerical Simulation Studies	7
2.2. Design Methods for Reinforced Aggregate Base Layers	14
2.2.1. The Cover Based Design Method.....	15
2.2.2. Modified Steward et al. (1977) Method	15
2.2.3. AASHTO PP 46-01 (2001) Method.....	16
2.2.4. Empirical Design Method of Giroud and Han (2004a)	20
2.2.5. Mechanistic-Empirical Pavement Design Guide Method	23

CHAPTER THREE	25
SURVEY AND CLASSIFICATION OF GEOGRID PRODUCTS	25
3. 1. Survey of Geogrid Products	25
3.2. DOT Agencies Data	31
CHAPTER FOUR	34
DETERMINATION OF JUNCTION STRENGTH PROPERTIES	34
4.1. Fabrication of Junction Strength Testing Clamps	34
4.2. Junction Strength Test Results	37
CHAPTER FIVE	53
DETERMINATION OF RIB STRENGTH PROPERTIES	53
5.1. Fabrication of Rib Strength Testing Clamps for EGG	53
5.2. Fabrication of Rib Strength Testing Clamps for NEGG	61
5.3. Rib Strength Test Results	62
CHAPTER SIX	78
LABORATORY TESTING OF SAND AND AGGREGATES	78
6.1. Gradation Analysis	78
6.2. Durability Analysis.....	80
6.3. Small-Scale Direct Shear Tests (DST) on Sand	81
6.3.1. Material Properties and Test Setup.....	81
6.3.2. Direct Shear Test Results	83

6.4. Large Scale Direct Shear Tests (DST) on Sand and Aggregate	86
6.4.1. Preparation of the Soil Samples	86
6.4.2. Shear Test Results	90
CHAPTER SEVEN	96
INSTALLATION DAMAGE TESTING OF GEOGRIDS	96
7.1. General	96
7.2. Summary of the Installation Damage Test Procedure	96
7.3. Size of the Test Bed Area.....	99
7.4. Geogrid Sampling and Specimen Preparation.....	100
7.5. Compaction Equipment	106
7.6. Steel Plates.....	109
7.7. Measuring Density of Compacted Aggregate	110
7.8. Site Preparation	111
7.9. Key Steps in the Field.....	114
7.10. Geogrid Samples after Exhumation.....	122
7.11. Obtaining Representative Test Specimens from Exhumed Samples ..	127
7.12. Junction Strength Tests on Damaged Geogrid Specimens.....	131
7.13. Rib Strength Tests on Damaged Geogrid Specimens.....	132
7.14. Installation Damage Reduction Factors.....	136

CHAPTER EIGHT	138
INFLUENCE OF IN-ISOLATION PROPERTIES OF GEOGRIDS ON THEIR PULLOUT PERFORMANCE	138
8.1. General	138
8.2. Fabrication of a New Pullout Box	138
8.3. Pullout Test Setup and Procedure.....	139
8.4. Pullout Test Results and Analysis	153
8.5. Determination of the Peak Pullout Resistance	167
8.6. Relationship between Peak P_r and Overburden Pressure	168
8.7. Correlations between Peak P_r and Geogrid Strength Properties	170
CHAPTER NINE	181
RESPONSE OF GEOGRID-REINFORCED AGGREGATE-SUBSTRATE SPECIMENS TO SIMULATED WHEEL LOAD.....	181
9.1. Static Plate Load Tests	181
9.2. Cyclic Plate Load Tests	186
9.2.1. Preparation of New Test Setup for Cyclic Plate load Tests	186
9.2.2. Strain Gauge Attachment Technique.....	188
9.2.3. Cyclic Plate Load Test Setup	202
9.2.4. Preliminary Plate Load Tests and Results	215
9.2.5. Final Cyclic Plate Load Tests and Results	219

9. 3. TBR Correlation Equations for the Plate Load Test Models	250
9.3.1. Development of TBR Equations	250
9.3.2. Verification of TBR Correlation Equations	253
9.3.3. The Final TBR Model Based on Rib Strength Properties	270
CHAPTER TEN	273
CONCLUSIONS AND RECOMMENDATIONS	273
10.1. Conclusions	273
10.2. Recommendations	277
REFERENCES	279
APPENDIX	285
DATABASE OF GEOGRID PROPERTIES SURVEYED IN THIS STUDY	285

List of Tables

Table 1.1. Geogrids properties of interest in this study.....	4
Table 2.1. FEM studies for geosynthetic-reinforced flexible pavement design (After Zornberg and Gupta 2010)	13
Table 2.2. List of geogrid properties examined for base reinforcement applications in the current and related previous studies	14
Table 3.1. List of candidate geogrids with either aperture size or 5%-strain tensile strength comparable to those of ODOT Type-1 and Type-2 geogrids.....	28
Table 3.2. General information on geogrid products tested in this study.....	30
Table 3.3. State DOTs providing geogrid specifications for base reinforcement	32
Table 4.1. Summary of junction strength test results in MD.....	51
Table 4.2. Summary of junction strength test results in XD	52
Table 5.1. Summary of rib tensile strength values at 2% strain in MD	72
Table 5.2. Summary of rib tensile strength values at 2% strain in XD	73
Table 5.3. Summary of rib tensile strength values at 5% strain in MD	74
Table 5.4. Summary of rib tensile strength values at 5% strain in XD	75
Table 5.5. Summary of ultimate rib tensile strength values in MD	76
Table 5.6. Summary of ultimate rib tensile strength values in XD	77
Table 6.1. LA abrasion test results for ODOT Type-A aggregate	81

Table 7.1. Compactor Specifications.....	107
Table 7.2. Specifications of steel plates used in the installation damage test bed.....	110
Table 7.3. Summary of installation damage tests on geogrids in ODOT Type-A aggregate.....	122
Table 7.4. Installation damage factors of the geogrids tested in this study.....	137
Table 8.1. Summary of pullout tests on geogrids in this study	152
Table 8.2. Statistical data for the results shown in Figure 8.57	170
Table 9.1. Summary of static plate load tests.....	184
Table 9.2. Regression coefficients for EGG products using Model #1	251
Table 9.3. Regression coefficients for EGG products using Model #2.....	251
Table 9.4. Regression coefficients for NEGG products using Model #1	252
Table 9.5. Regression Coefficients for NEGG products using Model#2.....	252
Table 9.6. R ² -values for EGG regression equations using Model #1.....	253
Table 9.7. R ² -values for EGG regression equations using Model #2.....	253
Table 9.8. R ² -values for NEGG regression equations using Model #1.....	254
Table 9.9. R ² -values for NEGG regression equations using Model #2.....	254
Table 9.10. Summary of test types, geogrid properties and TRB values reported in selected previous studies	255
Table 9.11. Properties of geogrids used in the study by Abu-Farsakh and Chen (2011)	263
Table 9.12. Properties of geosynthetics used in the study by Cuelho and Perkins (2009)	264
Table 9.13. Summary of test section properties and comparative rutting performance in the study by Cuelho and Perkins (2009).....	265

Table 9.14. Structure parameters of test slabs (Chehab et al. 2007)	267
Table 9.15. Properties of geosynthetics used in the study by Tingle and Jersey (2005)	269

List of Figures

Figure 3.1. Distribution of MD strength at 2% rib strain of uniaxial and biaxial geogrids surveyed in this study	26
Figure 3.2. Distribution of MD strength at 2% rib strain of bi-axial geogrids available on the market	27
Figure 3.3. Procedure used to select geogrid products for testing in this study	29
Figure 3.4. (a) EB2 geogrid, (b) Polyester ties which are used to stitched together the two layers of the geogrid	31
Figure 3.5. Classification of the geogrid products used in the study	33
Figure 4.1. Clamp and example test specimen used in junction tests (junctions in the specimen shown are one inch apart from each other)	35
Figure 4.2. Tensile testing frame for testing rib and junction strength of geogrid specimens	35
Figure 4.3. Specimen failure as captured on the data acquisition system screen	36
Figure 4.4. Different failure modes observed in junction testing of extruded geogrids: (a) Brittle failure (b) Ductile failure	36
Figure 4.5. EGG1 geogrid junction strength specimens after the test (a) MD, (b) XD..	37
Figure 4.6. EGG2 (single layer) geogrid junction strength specimens after the test: (a) in MD and (b) in XD	37
Figure 4.7. EGG3 geogrid junction strength specimens: (a) before the test, (b) after failure (MD), (c) after failure (XD)	38
Figure 4.8. EGG4 geogrid junction strength specimens: (a) before the test, (b) after failure (MD), (c) after failure (XD)	39
Figure 4.9. WGG1 geogrid junction strength specimens in XD: (a) before failure, (b) after failure	39
Figure 4.10. WGG2 geogrid junction strength specimens: (a) before the test, (b) after failure (MD), (c) after failure (XD)	40

Figure 4.11. WGG3 geogrid junction strength specimens (a) before the test, (b) after failure (MD), (c) after failure (XD).....	40
Figure 4.12. KGG1 geogrid junction strength specimens: (a) before the test, (b) after failure (MD), (c) after failure (XD).....	41
Figure 4.13. EGG4 specimen in junction strength test: (a) before test, (b) after failure	42
Figure 4.14. Junction strength test results for EGG1 test specimens (a) MD, (b) XD...	43
Figure 4.15. Junction strength test results for EGG2-single layer test specimens (a) MD, (b) XD.....	44
Figure 4.16. Junction strength test results for EGG3 test specimens (a) MD ribs (30° from MD), (b) XD	45
Figure 4.17. Junction strength test results for EGG4 test specimens (a) MD ribs (30° from MD), (b) XD	46
Figure 4.18. Junction strength test results for WGG1 test specimens (a) MD, (b) XD .	47
Figure 4.19. Junction strength test results for WGG2 test specimens (a) MD, (b) XD	48
Figure 4.20. Junction strength test results for WGG3 test specimens (a) MD, (b) XD	49
Figure 4.21. Junction strength test results for KGG1 test specimens (a) MD, (b) XD ..	50
Figure 5.1. Rib strength test clamp for extruded geogrids and accessories	54
Figure 5.2. (a) Sandpapers mounted on test clamps (b) alignment of test specimen and spacer pieces on clamps.....	55
Figure 5.3. (a) Geogrid specimen secured in the clamps, (b) test setup mounted on the tension frame, (c) view from digital camera, ready to record the specimen deformation.....	56
Figure 5.4. (a) and (b) Two- and five-aperture-size-long specimens which failed at their junctions in rib strength tests, (c) specimen failed in cross-machine direction	59
Figure 5.5. Geogrid specimens for rib strength tests (a) EGG3, (b) EGG4	60
Figure 5.6. EGG3 geogrid sample for rib strength tests (a) before test, (b) after failure	60

Figure 5.7. EGG4 geogrid sample for rib strength tests (a) before test, (b) after failure	61
Figure 5.8. Clamping system fabricated to test non-extruded geogrids	62
Figure 5.9. Rib strength testing of non-extruded geogrid in progress.....	62
Figure 5.10. Tensile strength test results for EGG1 geogrid specimens (a) MD, (b) XD	63
Figure 5.11. Tensile strength test results for EGG2 (single layer) geogrid specimens (a) MD, (b) XD	64
Figure 5.12. Tensile strength test results for EGG3 geogrid specimens (a) MD (30 □ from MD), (b) XD	65
Figure 5.13. Tensile strength test results for EGG4 geogrid specimens (a) MD (30 □ from MD), (b) XD	66
Figure 5.14. Tensile strength test results for WGG1 geogrid specimens (a) MD, (b) XD	67
Figure 5.15. Tensile strength test results for WGG2 geogrid specimens (a) MD, (b) XD	68
Figure 5.16. Tensile strength test results for WGG3 geogrid specimens (a) MD, (b) XD	69
Figure 5.17. Tensile strength test results for KGG1 geogrid specimens (a) MD, (b) XD	70
Figure 6.1. Sieve analysis equipment at the OU Broce Laboratory	78
Figure 6.2. Gradation curves for the ODOT Type-A aggregates used in this study	79
Figure 6.3. Los Angeles (LA) abrasion tests	80
Figure 6.4. Dover sand in the test cell of the small-scale DST machine.....	82
Figure 6.5. Final setup of the test cell the DST machine	83
Figure 6.6. Small-scale test results on the subgrade sand at 138 kPa overburden pressure ($\gamma = 16.25 \text{ kN/m}^3$)	84

Figure 6.7. Small-scale test results on the subgrade sand at 276 kPa overburden pressure ($\gamma = 16.25 \text{ kN/m}^3$)	84
Figure 6.8. Small-scale test results on the subgrade sand at 414 kPa overburden pressure ($\gamma = 16.25 \text{ kN/m}^3$)	85
Figure 6.9. Mohr-Coulomb failure envelope for the sand (small-scale DST).....	85
Figure 6.10. Assembly of the large-scale shear box: (a) the lower half, (b) the spacer, (c) the upper half	86
Figure 6.11. Setting up the large-scale DST machine to test sand specimens	87
Figure 6.12. (a) Placing of first layer of aggregate in the shear box, (b) Compaction of first layer of aggregate with a mallet, (c) Second layer of aggregate after compaction, (d) Third (i.e. final) layer of aggregate after compaction	87
Figure 6.13. The top cap with stud	88
Figure 6.14. (a) Front panel of the DST machine (b) Positioning of the vertical load cell on the test cell.....	89
Figure 6.15. Large-scale direct shear test setup	89
Figure 6.16. Large-scale test results on the subgrade sand at 138 kPa overburden pressure ($\gamma = 16.25 \text{ kN/m}^3$).....	90
Figure 6.17. Large-scale test results on the subgrade sand at 276 kPa overburden pressure ($\gamma = 16.25 \text{ kN/m}^3$).....	91
Figure 6.18. Large-scale test results on the subgrade sand at 414 kPa overburden pressure ($\gamma = 16.25 \text{ kN/m}^3$).....	91
Figure 6.19. Mohr-Coulomb failure envelope for the sand (large-scale DST)	92
Figure 6.20. Mohr-Coulomb failure envelopes of the sand at different scale DST	92
Figure 6.21. Large-scale test results on ODOT Type-A aggregate at 103 kPa overburden pressure ($\gamma = 20.41 \text{ kN/m}^3$).....	93
Figure 6.22. Large-scale test results on ODOT Type-A aggregate at 138 kPa overburden pressure ($\gamma = 20.41 \text{ kN/m}^3$).....	94
Figure 6.23. Large-scale test results on ODOT Type-A aggregate at 172 kPa overburden pressure ($\gamma = 20.41 \text{ kN/m}^3$).....	94

Figure 6.24. Mohr-Coulomb failure envelope for the ODOT Type-A aggregate (large-scale DST)	95
Figure 7.1. Schematic diagrams of the test bed for installation damage tests: (a) Plan view (Note: Solid triangles indicate the locations where the thickness of the aggregate layer was measured), (b) Elevation view (indicating the thicknesses of aggregate layers)	100
Figure 7.2. Geogrid sample preparation	101
Figure 7.3. Preparing EGG4 geogrid specimen for installation damage tests.....	101
Figure 7.4. EGG1 geogrid specimen prepared for installation damage tests	102
Figure 7.5. EGG2 geogrid specimen (single layer) prepared for installation damage tests	102
Figure 7.6. EGG3 geogrid specimen prepared for installation damage tests	103
Figure 7.7. EGG4 geogrid specimen prepared for installation damage tests	103
Figure 7.8. WGG1 geogrid specimen prepared for installation damage tests.....	104
Figure 7.9. WGG2 geogrid specimen prepared for installation damage tests.....	104
Figure 7.10. WGG3 geogrid specimen prepared for installation damage tests.....	105
Figure 7.11. KGG1 geogrid specimen prepared for installation damage tests.....	105
Figure 7.12. Compaction equipment (Source: http://www.volvo.com)	107
Figure 7.13. The forklift used in this study to lift the steel plates	108
Figure 7.14. The front-loader tractor used in this study	108
Figure 7.15. Steel plates with lifting chains	109
Figure 7. 16. Moving of the steel plates from the lab to the test site	110
Figure 7.17. Test site for the installation damage tests of geogrids outside the Fears Laboratory	112
Figure 7.18. Marking the boundaries of the test site	112

Figure 7.19. Clearing the test area from existing vegetation.....	113
Figure 7.20. Concrete beams placed on both sides of the test section with soil support on the outside.....	113
Figure 7.21. Four steel plates were placed in the test bed to facilitate the exhumation process of geogrids after they were covered by compacted aggregate.....	114
Figure 7.22. Aggregate was taken from a nearby stockpile using a front-loader tractor	115
Figure 7.23. Spreading ODOT Type-A aggregate in the test bed	115
Figure 7.24. First layer of aggregate in the test bed before compaction	116
Figure 7.25. Compacting the first layer of aggregate with a vibratory roller compactor	116
Figure 7.26. Measuring the in-situ density of aggregates (a) Model HM-310 Volu vessel Rubber Balloon densometer, (b) The densometer in use on the test bed ...	117
Figure 7.27. Four extruded geogrids placed on the first layer of compacted aggregate	118
Figure 7.28. Spreading the second layer of aggregate in the test bed	118
Figure 7.29. Compaction of the second layer of aggregate with the vibratory roller compactor	119
Figure 7.30. The top (second) layer of aggregate in the test bed after compaction	119
Figure 7.31. Forklift connected to the lifting chains	120
Figure 7.32. Tilting of steel plates from underneath the compacted aggregate	121
Figure 7.33. Tilting of steel plates and removing of aggregates to facilitate exhumation process	121
Figure 7.34. EGG1 geogrid specimen after exhumation.....	123
Figure 7.35. EGG2 geogrid specimen (single layer) after exhumation.....	123
Figure 7.36. EGG3 geogrid specimen after exhumation.....	124
Figure 7.37. EGG4 geogrid specimen after exhumation.....	124
Figure 7.38. WGG1 geogrid specimen after exhumation.....	125

Figure 7.39. WGG2 geogrid specimen after exhumation.....	125
Figure 7.40. WGG3 geogrid specimen after exhumation.....	126
Figure 7.41. KGG1 geogrid specimen after exhumation	126
Figure 7.42. EGG1 geogrid sample with marked damaged area.....	127
Figure 7.43. EGG2 geogrid sample (single layer) with marked damaged area.....	128
Figure 7.44. EGG3 geogrid sample with marked damaged area.....	128
Figure 7.45. EGG4 geogrid sample with marked damaged area.....	129
Figure 7.46. KGG1 geogrid sample with marked damaged area	129
Figure 7.47. Layout of specimens obtained from each geogrid sample	130
Figure 7.48. Damaged EGG1 geogrid junction strength test specimens before the test: (a) MD specimens, (b) XD specimens	131
Figure 7.49. Damaged EGG2 (single layer) geogrid rib strength test specimens before the test: (a) MD specimens, (b) XD specimens	132
Figure 7.50. Damaged EGG2 (single layer) geogrid rib strength test specimens after the test: (a) MD specimens, (b) XD specimens.....	133
Figure 7.51. Damaged KGG1 geogrid rib strength test specimens before the test: (a) MD specimens, (b) XD specimens	133
Figure 7.52. Damaged KGG1 geogrid rib strength test specimens after the test: (a) MD specimens, (b) XD specimens	134
Figure 7.53. Rib strength testing of an extruded [EGG2 (single layer)] geogrid product: (a) before the test, (b) after the test.....	135
Figure 7.54. Rib strength testing of a non-extruded (WGG3) geogrid product: (a) before the test, (b) after the test	135
Figure 8.1. Newly fabricated pullout test box at the OU Fears laboratory	139
Figure 8.2. Pullout test box before placing the aggregate	141

Figure 8.3. Compacted aggregate in the pullout box (the 203 mm-wide lower steel sleeve can be seen in the foreground).....	141
Figure 8.4. Drilling of the geogrid junctions to connect the extensometers.....	142
Figure 8.5. Connecting wires to geogrid specimen	142
Figure 8.6. Tell-tale wires connected to wire potentiometers	143
Figure 8.7. Top surface of the aggregate	143
Figure 8.8. A separator geotextile was placed on the top of the aggregate	144
Figure 8.9. An earth pressure cell was placed on a 25 mm sand layer on top of the aggregate.....	144
Figure 8.10. Air bag was used (if necessary) to generate additional overburden pressure on the geogrid-aggregate interface	145
Figure 8.11. Closing of the pullout test box before the test	145
Figure 8.12. Geogrid was connected to the roller clamp.....	146
Figure 8.13. Geogrid attachment to the roller clamp.....	146
Figure 8.14. Completed pullout test setup before the test	147
Figure 8.15. A pullout test in progress	147
Figure 8.16. EGG1 geogrid (a) before pullout test, (b) after pullout test.....	148
Figure 8.17. EGG2 (single layer) geogrid (a) before pullout test, (b) after pullout test.....	149
Figure 8.18. EGG3 geogrid (a) before pullout test, (b) after pullout test.....	149
Figure 8.19. EGG4 geogrid (a) before pullout test, (b) after pullout test.....	150
Figure 8.20. WGG1 geogrid (a) before pullout test, (b) after pullout test	150
Figure 8.21. WGG2 geogrid (a) before pullout test, (b) after pullout tes.....	151
Figure 8.22. WGG3 geogrid (a) before pullout test, (b) after pullout test	151
Figure 8.23. KGG1 geogrid (a) before pullout test, (b) after pullout test	151

Figure 8.24. Pullout response results of EGG1 geogrid in ODOT Type-A aggregate subjected to 3.30 kPa overburden pressure (WP: Wire-line Potentiometers)	153
Figure 8.25. Pullout response results of EGG1 geogrid in ODOT Type-A aggregate subjected to 7.07 kPa overburden pressure	154
Figure 8.26. Pullout response results of EGG1 geogrid in ODOT Type-A aggregate subjected to 11.65 kPa overburden pressure	154
Figure 8.27. Pullout response results of EGG1 geogrid in ODOT Type-A aggregate subjected to 3.3 kPa overburden pressure (0.6 m embedment length)	155
Figure 8.28. Pullout response results of EGG2 (single layer) geogrid in ODOT Type-A aggregate subjected to 4.95 kPa overburden pressure	155
Figure 8.29. Pullout response results of EGG2 (single layer) geogrid in ODOT Type-A aggregate subjected to 6.6 kPa overburden pressure	156
Figure 8.30. Pullout response results of EGG3 geogrid in ODOT Type-A aggregate subjected to 3.3 kPa overburden pressure	156
Figure 8.31. Pullout response results of EGG3 geogrid in ODOT Type-A aggregate subjected to 3.3 kPa overburden pressure (0.6 m embedded length)	157
Figure 8.32. Pullout response results of EGG3 geogrid in ODOT Type-A aggregate subjected to 4.95 kPa overburden pressure (0.6 m embedment length)	158
Figure 8.33. Pullout response results of EGG3 geogrid in ODOT Type-A aggregate subjected to 6.6 kPa overburden pressure (0.6 m embedment length)	158
Figure 8.34. Pullout response results of EGG4 geogrid in ODOT Type-A aggregate subjected to 3.3 kPa overburden pressure	159
Figure 8.35. Pullout response results of EGG4 geogrid in ODOT Type-A aggregate subjected to 4.95 kPa overburden pressure	159
Figure 8.36. Pullout response results of EGG4 geogrid in ODOT Type-A aggregate subjected to 6.6 kPa overburden pressure	160
Figure 8.37. Pullout response results of WGG1 geogrid in ODOT Type-A aggregate subjected to 3.3 kPa overburden pressure	160
Figure 8.38. Pullout response results of WGG1 geogrid in ODOT Type-A aggregate subjected to 6.60 kPa overburden pressure	161

Figure 8.39. Pullout response results of WGG1 geogrid in ODOT Type-A aggregate subjected to 11.61 kPa overburden pressure	161
Figure 8.40. Pullout response results of WGG1 geogrid in ODOT Type-A aggregate subjected to 3.3 kPa overburden pressure (0.6 m embedment length).....	162
Figure 8.41. Pullout response results of WGG2 geogrid in ODOT Type-A aggregate subjected to 3.30 kPa overburden pressure	162
Figure 8.42. Pullout response results of WGG2 geogrid in ODOT Type-A aggregate subjected to 4.95 kPa overburden pressure	163
Figure 8.43. Pullout response results of WGG2 geogrid in ODOT Type-A aggregate subjected to 6.60 kPa overburden pressure	163
Figure 8.44. Pullout response results of WGG2 geogrid in ODOT Type-A aggregate subjected to 11.5 kPa overburden pressure	164
Figure 8.45. Pullout response results of WGG3 geogrid in ODOT Type-A aggregate subjected to 3.30 kPa overburden pressure	164
Figure 8.46. Pullout response results of WGG3 geogrid in ODOT Type-A aggregate subjected to 6.6 kPa overburden pressure	165
Figure 8.47. Pullout response results of WGG3 geogrid in ODOT Type-A aggregate subjected to 11.96 kPa overburden pressure	165
Figure 8.48. Pullout response results of KGG1 geogrid in ODOT Type-A aggregate subjected to 3.3 kPa overburden pressure	166
Figure 8.49. Pullout response results of KGG1 geogrid in ODOT Type-A aggregate subjected to 6.6 kPa overburden pressure	166
Figure 8.50. Pullout response results of KGG1 geogrid in ODOT Type-A aggregate subjected to 11.5 kPa overburden pressure	167
Figure 8.51. Peak pullout resistance of geogrids tested in this study as a function of overburden pressure.....	169
Figure 8.52. Correlations between pullout force and rib tensile strengths in MD at (a) 2% strain, (b) 5% stain and (c) Ultimate rib strengths and (d) Ultimate junction strengths of geogrids examined in this study (EGG: represented by solid markers, NEGG: represented by hollow markers)	173
Figure 8.53. Correlation between pullout force and rib tensile strengths in XD at (a) 2% strain, (b) 5% stain and (c) Ultimate rib strengths and (d) Ultimate junction	

strengths of geogrids examined in this study (EGG: represented by solid markers, NEGG: represented by hollow markers)	174
Figure 8.54. Correlation between pullout force and rib tensile strengths in MD at (a) 2% strain, (b) 5% stain and (c) Ultimate rib strengths and (d) Ultimate junction strengths of NEGG geogrids	176
Figure 8.55. Correlation between pullout force and rib tensile strengths in XD at (a) 2% strain, (b) 5% stain and (c) Ultimate rib strength and (d) Ultimate junction strengths of NEGG geogrids	177
Figure 8.56. Correlation between pullout force and rib tensile strengths in MD at (a) 2% strain, (b) 5% stain and (c) Ultimate rib strengths and (d) Ultimate junction strengths of EGG geogrids	179
Figure 8.57. Correlation between pullout force and rib tensile strengths in XD at (a) 2% strain, (b) 5% stain and (c) Ultimate rib strengths and (d) Ultimate junction strengths of EGG geogrids	180
Figure 9.1. Preparation of the geogrid and geotextile specimen for a static plate load test	182
Figure 9.2. Static plate load test setup.....	183
Figure 9.3. Test box used for the static plate load tests.....	183
Figure 9.4. Load-settlement responses of aggregate-sand substrate models.....	185
Figure 9.5. The new Data Acquisition System used in the cyclic plate load tests	186
Figure 9.6. Redesigned and retrofitted steel loading frame at the Fears Laboratory ...	187
Figure 9.7. The newly fabricated large steel test box for cyclic plate load tests.....	187
Figure 9.8. Cyclic loading tests on reinforced base-substrate models using the new controller system	188
Figure 9.9. Cleaning the surface of geogrid with industrial tissue or cloth.....	190
Figure 9.10. Abrasive paper was used to roughen the surface of the extruded geogrid	191
Figure 9.11. A brush was used to remove dust due to abrasion	191
Figure 9.12. Adhesive, primer and sealant used in this study	192

Figure 9.13. Application of adhesive material to the geogrid	192
Figure 9.14. Application of adhesive material to the back of the strain gauge base	193
Figure 9.15. Gauges were held in place with the Scotch tape while the adhesive was cured	193
Figure 9.16. Pressure was applied to the gauge to cure.....	194
Figure 9.17. The tape was peeled off carefully from the strain gauge	194
Figure 9.18. The gauge surface was covered with coating material	195
Figure 9.19. Wire tie was used to hold the strain gauge wire in position	195
Figure 9.20. Geogrid with strain gauges attached	196
Figure 9.21. Flexible rubber tube was used to cover strain gauges.....	196
Figure 9.22. Silioccon rubber sealant was applied on the strain gauge	197
Figure 9.23. Geogrid sample left for 24 hours in order for the adhesive and sealant materials to dry out.....	197
Figure 9.24. Geogrid specimen used in a cyclic plate load tests before instrumentation: (a) EGG1, (b) WGG1, (c) KGG1	199
Figure 9.25. Geotextile placed below the subgrade layer in the test box.....	200
Figure 9.26. Pressure was applied to the gauges to cure their adhesive layer.....	201
Figure 9.27. Example geogrid specimens instrumented with strain gauges: (a) EGG1, (b) WGG3	202
Figure 9.28. Schematic elevation view of the test box and the instrumentation layout in the final cyclic plate load tests.....	203
Figure 9.29. The redesigned and retrofitted steel loading frame with the actuator, which is connected to the hydraulic pump and the controller system.....	206
Figure 9.30. Styrofoam panels placed at the bottom and against the walls of the test box	206
Figure 9.31. Cyclic plate load test box after placing the geotextile separator on Styrofoam panels on the bottom of the test box	207

Figure 9.32. Measuring the in-situ density of sand by Model HM-310 Volu vessel rubber balloon densometer.....	207
Figure 9.33. Marked locations of extensometer readings to measure deformation profile at the bottom of the aggregate layer due to cyclic loading.....	208
Figure 9.34. Attachment of brass wires to geotextile separator to measure its settlement	208
Figure 9.35. 25 mm-thick aggregate layer placed on the top of the geotextile separator	209
Figure 9.36. Placing geogrid reinforcement on the 25 mm-thick aggregate layer	209
Figure 9.37. Careful placement of aggregate on the geogrid layer	210
Figure 9.38. Compacted aggregate layer placed on the geogrid reinforcement	210
Figure 9.39. Brass wires connected to the wire potentiometers to measure the base layer deformation.....	211
Figure 9.40. A telltale plate (50 mm × 50 mm) attached with brass wire to measure the surface deflection of the aggregate layer.....	212
Figure 9.41. Setup of the telltale plates on the top of the aggregate layer	212
Figure 9.42. Vertical telltale plate to measure the aggregate deformation near the circular loading plate	213
Figure 9.43. Connecting strain gauges to the DAS (Data Acquisition System).....	213
Figure 9.44. Eight strain gauges connected to the DAS	214
Figure 9.45. Monitoring data in the Data Acquisition System while the cyclic plate load test is in progress	214
Figure 9.46. The position of the circular loading plate at the end of a test	215
Figure 9.47. Load-settlement response of the aggregate-sand model subjected to a static (incremental static loading) plate load test in the large test box	216
Figure 9.48. Load-settlement response of the preliminary periodic plate load tests with EGG1 geogrid.....	217
Figure 9.49. Load-settlement response of the preliminary periodic plate load tests with WGG3 geogrid	218

Figure 9.50. CBR test result of the subgrade sand with a dry unit weight of 16.22 kN/m ³	219
Figure 9.51. Plate load-settlement response of the aggregate-substrate model with EGG1 geogrid (1000 load cycles)	220
Figure 9.52. Plate load-settlement response of the aggregate-substrate model with EGG2-single layer geogrid (1000 load cycles)	221
Figure 9.53. Plate load-settlement response of the aggregate-substrate model with EGG3 geogrid (1000 load cycles)	222
Figure 9.54. Plate load-settlement response of the aggregate-substrate model with EGG4 geogrid (1000 load cycles)	223
Figure 9.55. Plate load-settlement response of the aggregate-substrate model with WGG1 geogrid (1000 load cycles).....	224
Figure 9.56. Plate load-settlement response of the aggregate-substrate model with WGG2 geogrid (1000 load cycles).....	225
Figure 9.57. Plate load-settlement response of the aggregate-substrate model with WGG3 geogrid (1000 load cycles).....	226
Figure 9.58. Plate load-settlement response of the aggregate-substrate model with KGG1 geogrid (1000 load cycles).....	227
Figure 9.59. Plate load-settlement response of the aggregate-substrate model without any geogrid (1000 load cycles).....	228
Figure 9.60. EGG1 geogrid specimen after the cyclic plate load test	229
Figure 9.61. EGG2 geogrid specimen after the cyclic plate load test	229
Figure 9.62. EGG3 geogrid specimen after the cyclic plate load test	230
Figure 9.63. EGG4 geogrid specimen after the cyclic plate load test	230
Figure 9.64. WGG1 geogrid specimen after the cyclic plate load test.....	231
Figure 9.65. WGG2 geogrid specimen after the cyclic plate load test.....	231
Figure 9.66. WGG3 geogrid specimen after the cyclic plate load test.....	232
Figure 9.67. KGG1 geogrid specimen after the cyclic plate load test.....	232

Figure 9.68. Comparison of (a) Maximum plate settlement under cyclic loading, (b) SRF values among among test cases examined	234
Figure 9.69. Comparison of (a) Number of cycles to reach 25 mm of settlement under cyclic loading, (b) Traffic Benefit Ratios (TBR) among test cases examined	235
Figure 9.70. Comparison of top surface deflections in different cases at the end of 1000 cycles	236
Figure 9.71. Comparison of subgrade deflection profiles in different test cases at the end of 1000 cycles.....	237
Figure 9.72. Strain distributions in the EGG1 geogrid.....	239
Figure 9.73. Strain distributions in the WGG2 geogrid	239
Figure 9.74. Strain distributions in the WGG3 geogrid	240
Figure 9.75. Strain distributions in the KGG1 geogrid	240
Figure 9.76. Correlation between SRF from cyclic plate load tests and rib strength values (a) at 2% strain in MD, (b) in XD, (c) at 5% strain in MD, (d) in XD, (e) ultimate rib strength in MD, (f) in XD.....	244
Figure 9.77. Correlation between SRF and ultimate junction strength in (a) MD, (b) XD	245
Figure 9.78. Correlation between (a) TBR and rib strengths at 2% strain in MD, (b) in XD, (c) TBR and rib strengths at 5% strain in MD, (d) in XD, (e) TBR and ultimate rib strengths in MD, (f) in XD.....	248
Figure 9.79. Correlation between TBR and ultimate junction strength (a) in MD, (b) in XD	249
Figure 9.80. Predicted TBR values using Equation 9.3.5 , vs. measured TBR values in the current and previous studies	256
Figure 9.81. Predicted TBR values using Equation 9.3.6 vs. measured TBR values in the current and previous studies	256
Figure 9.82. Predicted TBR values using Equation 9.3.7 vs. measured TBR values in the current and previous studies	257
Figure 9.83. Predicted TBR values using Equation 9.3.8 vs. measured TBR values in the current and previous studies	257

Figure 9.84. Predicted TBR values using Equation 9.3.9 vs. measured TBR values in the current and previous studies	258
Figure 9.85. Predicted TBR values using Equation 9.3.10 vs. measured TBR values in the current and previous studies	258
Figure 9.86. Predicted TBR values using Equation 9.3.11 vs. measured TBR values in the current and previous studies	259
Figure 9.87. Predicted TBR values using Equation 9.3.14 vs. measured TBR values in the current and previous studies	259
Figure 9.88. Predicted TBR values using Equation 9.3.16 vs. measured TBR values in the current and previous studies	260
Figure 9.89. Predicted TBR values using Equation 9.3.18 X_3 vs. measured TBR values in the current and previous studies	260
Figure 9.90. Laboratory test box, hydraulic actuator and reaction system in the study by Abu-Farsakh and Chen (2011)	262
Figure 9.91. Rutting accumulation for locations where maximum rut occurred in case of APT I (Chehab et al. 2007).....	266
Figure 9.92. Rutting accumulation for locations where maximum rut occurred in APT II test series (Chehab et al. 2007).....	268
Figure 9.93. Laboratory pavement test items: (a) plan and (b) profile layout (Tingle and Jersey 2005).....	270

Abstract

Geogrids are polymer-based products which are commonly used to reinforce soil walls, steep slopes and roadway bases. Inclusion of geogrids as aggregate base reinforcement, with proper installation, has been shown to result in increased stiffness and service life of flexible pavements. It also results in reduced distress and deformations, improved performance and hence, reduced repair and maintenance costs of pavements. The relationship between the in-isolation and in-aggregate properties of a geogrid depends on several factors including the geogrid and aggregate properties, their frictional and interlocking interaction mechanisms and the overburden pressure.

However, the influence of individual index properties of geogrids on their in-aggregate performance is still not well understood and requires further study. Currently, there is a lack of: 1) a universally accepted design methodology that would incorporate in-isolation material properties of geogrids for base aggregate reinforcement and subgrade stabilization applications, and 2) agreement as to which geogrid properties are most relevant to their in-aggregate performance. This is particularly important as new geogrids and manufacturing processes are introduced in the market on a continuous basis.

Realizing the need for further research in this area, the influence of selected index properties of geogrids on their in-aggregate performance is examined in this study. A series of in-isolation and large-scale in-aggregate (i.e. pullout, installation damage and cyclic plate load) tests was carried out on selected geogrid products in

ODOT Type-A aggregate, which is a dense-graded aggregate commonly used in Oklahoma Department of Transportation (ODOT) projects. The in-isolation properties studied included the geogrids low-strain (i.e. 2% and 5% strain) and ultimate rib strength, and their junction strength in both machine (MD) and cross-machine (XD) directions. The geogrids investigated in the study were classified in two basic categories of extruded (EGG) and non-extruded (NEGG) geogrids. The latter category primarily included the woven and knitted geogrid products.

Results of the study indicated that for both categories of extruded (EGG) and non-extruded (NEGG) geogrids examined, greater rib and junction strength properties overall resulted in greater pullout resistance. Geogrids junction strength and low-strain rib strength showed a reasonably strong correlation with their pullout performance regardless of the geogrid category examined. The rib strength at 2% strain showed a stronger correlation than the 5%-strain strength with the geogrid pullout performance. However, ultimate rib strength of geogrid showed convincing correlations with their pullout performance only when they were examined in separate categories with respect to their manufacturing technique (i.e. when the EGG and NEGG geogrids were examined as separate categories). The installation damage test results revealed that reduction factors for rib strength values at 2% strain were significant. Partial reduction factors for installation damage for the EGG products were generally found to be larger than those for the NEGG products. Cyclic plate load test results indicated that the Strength Reduction Factor (SRF) and Traffic Benefit Ratio (TBR) values of the test models were proportional to the rib strengths of the geogrid reinforcement. However,

the SRF and TBR values in either of the EGG or NEGG geogrid categories did not show a convincing dependence on their ultimate junction strength. A set of equations were developed to calculate a predicted TBR value for the reinforced aggregate-subgrade models with EGG and NEGG products as separate categories. The findings of this study are beneficial in relating the in-isolation properties of geogrids to their in-aggregate performance.

CHAPTER ONE

INTRODUCTION

1.1. Background

Roadway maintenance is a costly and challenging problem worldwide. In order to improve the service life and performance of pavements and reduce maintenance costs, factors leading to pavement distress, excessive deformation (rutting) or failure of pavement structures need to be addressed in the design stage and during construction. Use of geosynthetic reinforcement (geogrid) for aggregate base reinforcement, with proper installation, has been shown to result in increased service life, improved performance and substantial reduction in repair and maintenance costs of pavements (e.g., Perkins 1999, Leng and Gabr 2002, Perkins et al. 2004, Giroud and Han 2004, Gabr et al. 2006, Aran 2006, Holtz et al. 2008, Kwon and Tutumluer 2009). The improved performance of the pavement due to geosynthetic reinforcement has been attributed to three leading mechanisms: (1) lateral restraint, (2) increased bearing capacity, and (3) the tensioned membrane effect (Giroud and Noiray 1981, Giroud and Bonaparte 1985, Perkins and Ismeik 1997, and, Holtz et al. 1998). Geogrids also offer improved interface shear resistance with soils and aggregates due to interlocking without impeding the drainage condition of pavements.

Adequate mechanical properties (e.g. rib and junction strength) are essential for biaxial geogrids in order to transfer and distribute the traffic load in their longitudinal and transverse ribs effectively and thereby provide adequate confining effects on the aggregates in base reinforcement and subgrade stabilization applications. It has been shown that strains in geogrids placed in the aggregate base course can reach or exceed 2% during construction (Christopher et al. 2008). It could be expected that these strains are at least partly locked in when the roadway is fully constructed. However, greater strains (e.g. as high as 5% or more) could be expected in the geogrid reinforcement during construction or when a flexible pavement is subjected to truck load. Therefore, investigation of geogrid properties should be done not only with respect to their ultimate rib strength but also with respect to their low-strain strength.

Correlations between index properties of geogrids and their in-aggregate performance have been the subject of a few past studies (e.g., Perkins 1999, Perkins et al. 2004, Giroud and Han 2004, Gabr et al. 2006, Chehab et al. 2007, Christopher et al. 2008, Tang et al. 2008, Perkins et al. 2009, Kwon and Tutumluer 2009, Tingle and Jersy 2009, Hatami et al. 2011b). These studies involved laboratory tests and/or large-scale field tests on geogrid-reinforced pavements to examine the interaction between the geogrids and their surrounding (i.e. base and subgrade) materials. Results of these studies indicated that geogrid reinforcement reduces pavement deformation and distress and hence results in a more durable and economical pavement in the long run.

1.2. Problem Statement and Research Need

The previously cited studies cited earlier (and those surveyed in more detail in Chapter 2) have revealed the significance of geogrid mechanical properties on their in-aggregate performance. However, the influence of individual index properties of geogrids on their in-aggregate performance is still not well understood and requires further study. Currently, there is a lack of:

1) A universally accepted design methodology that would incorporate in-isolation material properties of geogrids for base aggregate reinforcement and subgrade stabilization applications. Currently available design methods for base reinforcement are often proprietary and product-specific.

2) Agreement as to which geogrid properties are most relevant to their in-aggregate performance in order to develop consistent materials specifications for departments of transportation and similar agencies in charge of construction and maintenance of roads and highways. This is particularly important as new geogrids and manufacturing processes are introduced in the market on a continuous basis. Alzamora and Anderson (2012) highlighted challenges that different state DOTs and research institutions face in establishing a direct connection between index properties of geogrids and their field performance.

The above discussion highlights the need for reliable analysis and design methodologies that would relate geogrid index properties to the predicted field performance of reinforced flexible pavements. This will help make such design methods

more generic, reliable and cost effective by encompassing a larger selection of available products as compared to the limited products and/or index properties that are currently specified by departments of transportation.

1.3. Objectives

The primary objective of this study was to investigate the influence of selected in-isolation properties of geogrids on their in-aggregate performance. The focus of the study was on the rib and junction strength properties of geogrids relative to their pullout, cyclic plate load and installation damage tests. More specifically, the ultimate junction strength, ultimate rib strength and small-strain rib strength values (i.e. those at 2% strain and 5% strain) were investigated in machine (MD) and cross-machine (XD) directions. The geogrids investigated in the study were classified in two basic categories of extruded (EGG) and non-extruded (NEGG) geogrids. The latter category primarily included the woven (WGG) and knitted (KGG) geogrid products. Geogrid properties of interest in this study are listed in **Table 1.1**.

Table 1.1. Geogrids properties of interest in this study

Mechanical Properties (MD and XD)	Manufacturing Technique
Ultimate Rib Strength	Extruded vs. Non-extruded
Rib Strength at 2% Elongation	
Rib Strength at 5% Elongation	
Ultimate Junction Strength	

The research program included the following specific tasks:

1. Survey and classify geogrid specifications for aggregate base reinforcement based on the currently available geogrid products and guidelines by departments of transportation (DOT) in the United States. The results of this survey were used to determine a range of geogrid strength properties for their classification.

2. Determine the index properties of geogrids (e.g., ultimate junction strength, rib strength at 2% strain and 5% strain and ultimate rib strength in both MD and XD) in order to quantify their influence on the geogrids in-aggregate performance in subsequent tests.

3. Carry out a series of pullout tests at different overburden pressures and comparing the laboratory pullout test results of different geogrids. This part of the study included the determination of:

- Geogrid pullout performance
- Relationship between the geogrid pullout capacity and overburden pressure
- Correlation between the geogrid pullout capacity and its in-isolation properties

4. Study the survivability of geogrids as a function of their index properties when subjected to higher strain levels during compaction. Laboratory-scale field installation damage tests were carried out on both extruded and non-extruded geogrids to investigate their survivability during construction. This part of the study included:

- Evaluating installation damage factors for geogrids ultimate rib and junction strength
- Determining installation damage factors for geogrid ribs at different strain levels

5. Investigate the influences of in-solation properties of geogrids on their in-aggregate performance when subjected to vertical load simulating tire pressure. A series of large-scale plate load tests (i.e. static and cyclic loading tests) was carried out on unreinforced and reinforced aggregate base models for this purpose. This part of the study included:

- Developing strain gauge attachment techniques for extruded and non-extruded geogrid products
- Determining the Traffic Benefit Ratio (TBR) and Strength Reduction Factor (SRF) values for selected geogrid products to evaluate the plate settlement response of reinforced specimens under cyclic loading
- Comparing top surface deflection profiles and subgrade deflection profiles of different reinforced specimens
- Investigating strain distributions in geogrid ribs due to cyclic loading
- Examining the influence of index properties of geogrids on the measured TBR and SRF values

CHAPTER TWO

LITERATURE REVIEW

2.1. Laboratory and Numerical Simulation Studies

Geosynthetics have been used to reinforce the base layer of pavement systems. Several studies have been performed to better understand the behavior of reinforced base pavements using laboratory tests and numerical simulations. An overview of previous and ongoing research on aggregate base reinforcement applications of geosynthetics is given in this section.

Yoder and Witczak (1975) stated that design of flexible pavements is generally focused on two critical locations within the pavement structure: (1) the horizontal tensile strain at the bottom of the asphalt layer, which should be minimized in order to prevent fatigue cracking, and (2) the vertical stress on the top of the subgrade, which should be minimized in order to reduce permanent deformations. The allowable vertical stress on the subgrade is governed by the shear strength of the subgrade. The granular base in flexible pavements should be thick enough so that the compressive vertical stress in the subgrade is decreased below the allowable stress level.

Jewell et al. (1984) studied soil-geogrid interaction mechanisms through large shear box tests. Seven granular soils reinforced with a biaxial geogrid with an aperture

width of 17.3 mm were tested. The peak shear forces measured for soils with different gradations indicated that aggregate particle size and gradation as compared to the grid aperture influenced the size of the rupture zone (the area on geogrids where rupture occurred).

The benefits of geogrids in unpaved low-volume roads were shown in several laboratory and full-scale experiments (e.g., Hass et al. 1988, Webster 1993, Collin et al. 1996, Fannin and Sigurdsson 1996, Knapton and Austin 1996, Gabr et al. 2001 Leng and Gabr 2002). These experiments served as a basis for the development of empirical design methods (NCHRP 2004, AASHTO 2009) for geogrid-reinforced roads.

Giroud and Han (2004a) developed a procedure for the design of geosynthetic reinforced unpaved roads, which considers stress distribution at depth, base course resilient modulus, and degradation of material stiffness with repeated loading. This approach is discussed later in this section.

Perkins et al. (2004) developed numerical models and test methods to determine input parameters for the geogrid reinforcement and its interaction with the aggregate and subgrade materials. The purpose of their project was to develop design methods for geosynthetic reinforced flexible pavements that are compatible with the methods developed in NCHRP Project 1-37A (NCHRP Project 1-37A, NCHRP 2004). Perkins et al. (2004) proposed material models for the reinforcement and shear interaction models for the reinforcement-aggregate and reinforcement-subgrade interfaces. They also proposed tests methods to determine the parameters needed for their material and

interface models. These testing methods included: (1) Tension tests for evaluating non-linear direction dependent elastic constants for the reinforcement and (2) Cyclic pullout tests for evaluating a stress dependent interface shear resilient modulus.

Perkins et al. (2004) used the NCHRP 1-37A Design Guide model for unbound aggregates as a basis to develop a damage model to determine permanent deformations of unbound aggregate within a zone influenced by the reinforcement. However, the damage model parameters were adjusted as a function of reinforcement ratios. Reinforcement ratios were defined as the ratio of any given performance parameter (i.e., permanent surface deformation of unbound aggregate, lateral stresses in the aggregate) for a reinforced aggregate layer to that of an otherwise identical unreinforced aggregate. These reinforcement ratios were applied to the unreinforced performance parameters to determine the corresponding values for a reinforced layer for a given set of aggregate and reinforcement properties. They performed large-scale cyclic triaxial tests on reinforced aggregate specimens to determine the extent of reinforced zone and the corresponding reinforcement ratios. Perkins et al. (2004) carried out wide-width tensile tests according to ASTM D4595 with a cyclic loading protocol on three geosynthetic reinforcement products. They examined the influences of the geogrids elastic tensile modulus, equivalent isotropic modulus and Poisson's ratio on the elastic response of their reinforced pavement models. They also carried out cyclic pullout tests on selected geogrids in an aggregate used for asphalt concrete which showed that the interface shear modulus was dependent on the magnitudes of normal and shear stress at the interface.

Chehab et al. (2007) studied the effects of aperture size, tensile strength at 2% strain, ultimate tensile strength, junction strength and flexural rigidity of geogrids on rutting performance of small-scale roadway models. They performed Accelerated Pavement Tests (APT) in a 2.2 m-wide by 3.7 m-long test pit. The pit was originally 4.3 m deep but was backfilled with a Type-2A aggregate base conforming to the PennDOT specifications. The densely-compacted aggregate layer served as a bedrock-like support. The top 400 mm was considered as the pavement section. A silty-sandy soil typical of central Pennsylvania was used as the subgrade and Type-2A aggregate according to PennDOT specifications was used as the base layer in their model. An asphalt slab was constructed on the top of the base layer. Chehab et al. (2007) proposed a series of correlations between the geogrid index properties and the rutting performance of their reinforced models. They concluded that for a geogrid to develop significant pullout capacity it needs to have adequate ultimate junction strength. Chehab et al. (2007) stated that there was a good correlation between the combined geogrid tensile strength and junction strength properties and the results of their direct shear and pullout tests. They concluded that the wide width tensile strength and junction strength were the most significant properties of geogrids influencing their in-aggregate performance.

Christopher et al. (2008) suggested that rib and junction strength at 2% strain is a suitable serviceability design value for geogrids in base reinforcement applications. They concluded that junction strength at 2% strain should therefore be used as an appropriate value to achieve a consistent design.

Tang et al. (2008) carried out direct shear and pullout tests to examine the influences of the aperture size, wide-width tensile strength and junction strength of four geogrid products on their in-aggregate performance. They found that junction and tensile strength properties of geogrids at small strains showed strong correlations with their in-aggregate performance. Tang et al. (2008) observed that the geogrids coefficients of interaction from pullout testes increased with their junction strength and rib tensile strength at 2% strain.

Cuelho and Perkins (2009) constructed field test sections to evaluate the performance of several geosynthetics for subgrade stabilization applications. A sandy clay soil was prepared as a weak roadbed material at a CBR value of approximately 1.8 and a 200 mm-thick aggregate layer was compacted over the geosynthetic reinforcement. They examined the effects of the tensile strength at 2% strain, 5% strain and the ultimate tensile strength on the rutting performance of geogrid-reinforced roadway test sections. Cuelho and Perkins (2009) acknowledged that a number of geosynthetic properties may be working together to stabilize a subgrade. However, they attributed a majority of the stabilization benefit to the geosynthetics ability to support loads in a direction transverse to the applied load, i.e. their cross-machine direction. They made a direct comparison between the rib tensile strength in the cross-machine direction at 2% and 5% strain and the number of traffic passes to produce 75 mm and 100 mm of rut depth in their field-scale model. Cuelho and Perkins (2009) concluded that increasing the geogrid 2% strain and (to a lesser extent) 5% strain tensile strength

values in the cross machine direction could reduce the amount of rutting and hence improve the performance of the pavement.

Kwon and Tutumluer (2009) developed a mechanistic model for the analysis of geogrid-reinforced flexible pavements based on the finite element method (FEM). They modeled a stiffer layer near the geogrid reinforcement due to aggregate interlock resulting from compaction-induced residual stresses as the initial condition in their FEM analysis. They conducted dynamic cone penetrometer (DCP) tests on geogrid reinforced base pavement sections in California and observed increased base course strength and stiffness properties. They also simulated several pullout tests using the Discrete Element Method (DEM) which indicated that a stiffened zone within 10 to 15 cm above and below the geogrid retained higher contact forces after unloading following aggregate compaction.

Zornberg and Gupta (2010) summarized research conducted specifically in North America addressing the following objectives: (i) determining the governing mechanisms and relevant properties of geosynthetics that contribute to the enhanced performance of pavement systems, (ii) developing appropriate analytical, laboratory and field methods capable of quantifying the above properties for geosynthetics, and (iii) enabling the prediction of pavement performance depending on the various types of geosynthetics used. Their review paper focused on the reinforcement function of geosynthetics in flexible pavements (**Table 2.1**).

Table 2.1. FEM studies for geosynthetic-reinforced flexible pavement design (After Zornberg and Gupta 2010)

References	Type of analysis	Geosynthetic constitutive model	Geosynthetic element type	Interface element type	Load type	Validation
Burd and Housby (1989)	Plain strain	Isotropic linear-elastic	Membrane	None	Monotonic	None
Barksdale <i>et al.</i> (1989)	Axi-symmetric	Isotropic linear-elastic	Membrane	Linear elastic perfectly plastic	Monotonic	Field results
Burd and Brocklehurst (1990)	Plane strain	Isotropic linear-elastic	Membrane	None	Monotonic	None
Miura <i>et al.</i> (1990)	Axi-symmetric	Isotropic linear-elastic	Truss	Linear elastic joint element	Monotonic	Field results
Dondi (1994)	Three-dimensional	Isotropic linear-elastic	Membrane	Elasto-plastic Mohr-Coulomb	Monotonic	None
Wathugala <i>et al.</i> (1996)	Axi-symmetric	Isotropic linear-elastic	Solid Continuum	None	Single cycle	None
Perkins (2001)	Three-dimensional	Anisotropic elasto-plastic	Membrane	Mohr-Coulomb	Multiple cycles	Lab and test tracks
Kwon <i>et al.</i> (2005)	Axi-symmetric	Isotropic linear-elastic	Membrane	Linear-elastic	Monotonic	Test tracks

Tutumluer et al. (2012) investigated geogrid-aggregate interlock mechanisms using an aggregate imaging-based discrete element method (DEM) approach. They used this approach in an attempt to better quantify the factors affecting the interaction or interlocking mechanisms between geogrids and aggregates. Tutumluer et al. (2012) demonstrates the effectiveness of their aggregate image-aided DEM model through direct shear tests performed on reconstituted clean dolomite aggregate samples with and without geogrid reinforcement.

Based on the survey of above studies, geogrid properties that have been the subject of previous investigations are compared with those which are the focus of the current study in **Table 2.2**.

Table 2.2. List of geogrid properties examined for base reinforcement applications in the current and related previous studies

Mechanical Properties (MD and XD)	Webster (1992)	Giroud and Hann (2004)	Chehab et al. (2007)	Tang et al. (2008)	Christopher et al. (2008)	Cuelho and Perkins (2009)	Tingle and Jersey (2009)	Abu-Farsakh and Chen (2011)	Current Study
Ultimate Rib Strength			√	√		√			√
Rib Strength at 2% Elongation			√	√	√	√			√
Rib Strength at 5% Elongation						√	√		√
Junction Strength	√		√	√	√				√
Tensile Modulus		√							
Aperture Size	√		√	√			√	√	
Flexural Rigidity			√	√					
Aperture Stability Modulus		√				√		√	
Rib Thickness	√								
Rib Cross-Section Shape	√								

2.2. Design Methods for Reinforced Aggregate Base Layers

The design methods for flexible pavements and use of geogrids in base reinforcement applications are discussed in this section.

2.2.1. The Cover Based Design Method

The Cover Based Design Method was developed to design flexible pavement systems after the great depression in the 1930s. This method required the California Bearing Ratio (CBR) as a single input parameter and relied heavily on engineering judgment. This method did not include the effect of geogrids.

After completion of the American Association of State Highway Officials (AASHTO) Road Test in 1960s, a series of design methods were proposed to design flexible pavements as described below.

2.2.2. Modified Steward et al. (1977) Method

Steward et al. (1977) developed an empirical design procedure for geotextile-reinforced unpaved roads using solutions based on a limit equilibrium bearing capacity theory. Tingle and Webster (2003) modified Steward et al.'s design method to include geogrid reinforcement which was subsequently adopted in the Corps of Engineers (COE) method for design of low-volume geotextile- and geogrid-reinforced unpaved roads (USCOE, 2003). Tingle and Webster (2003) suggested a bearing capacity factor of 5.8 for the geogrid-reinforced case and recommended that a geotextile should be used as a separator layer. Tingle and Webster's design method includes the following factors in the design:

- Number of vehicle passes
- Equivalent axle load

- Axle configuration
- Tire pressure
- Subgrade strength
- Rut depth

However, it is bound by the following limitations:

- The aggregate layer must be of high-quality (e.g. its laboratory CBR value based on ASTM D 1883 ≥ 80) and it should be cohesionless (nonplastic)
- Vehicle passes less than 10,000
- Geotextile survivability criteria must be considered
- Subgrade undrained shear strength less than about 90 kPa (2000 psf) (CBR < 3)

2.2.3. AASHTO PP 46-01 (2001) Method

The American Association of State Highway and Transportation Officials (AASHTO) guide for design of pavement structures is one of the most widely used methods for flexible pavement design in North America. AASHTO PP 46-01 (2001) provides guidelines for design of geogrid-reinforced base courses in flexible pavements. The AASHTO method uses empirical equations developed from the AASHO road tests, which were conducted in the late 1950s. The design steps follow a procedure that was initially reported by Berg et al. (2000) and AASHTO (1993).

$$\log W_{18} = Z_R \times S_O + 9.36 \times \log(SN+1) - 0.2 + \frac{\log \frac{\Delta PSI}{2.7}}{0.4 + \frac{1094}{(SN+1)^{5.19}}} + 2.32 \log M_R - 8.07 \quad (2.2.1)$$

where,

W_{18} = Anticipated cumulative 18-kip Equivalent Single-Axle Loads (ESALs)
over the design life of the pavements

Z_R = Standard normal deviate for reliability level

S_O = Overall standard deviation

ΔPSI = Allowable loss in serviceability

M_R = Resilient modulus (stiffness) of the underlying subgrade

SN = Structural number of the pavement

Once the required overall SN has been determined, the individual layer's thickness can be determined by using the following equation:

$$SN = (a \times d)_{hms} + (a \times d \times m)_{base} + (a \times d \times m)_{subbase} \quad (2.2.2)$$

where,

a = coefficient of relative strength

d = thickness in inches of each layer

m = modifier accounting for moisture characteristics of the pavement

SN = Structural number of the pavement

In this method, the improvements to the pavement system provided by geosynthetic reinforcement have been quantified in terms of the Traffic Benefit Ratio (TBR) and the Base Course Reduction (BCR) ratio.

The TBR is defined as the ratio between the number of load cycles on a reinforced section (N_R) to reach a defined failure state (e.g. a given rutting depth) and the number of load cycles on an unreinforced section (N_U) with the same geometry and material constituents that reaches the same defined failure state (Berg et al. 2000). The TBR can be defined as:

$$\text{TBR} = N_R/N_U \quad (2.2.3)$$

Use of the TBR in pavement design leads to an extended pavement life defined by:

$$W_{18} (\text{reinforced}) = \text{TBR} * W_{18} (\text{unreinforced}) \quad (2.2.4)$$

The BCR has been determined from laboratory and field tests. The BCR is defined as the reduction in the base-course thickness due to an addition of geosynthetic reinforcement (T_R) in relation to the thickness of the flexible pavement with the same

materials but without reinforcement (T_U), to reach the defined failure state. The BCR is defined as follows:

$$BCR = \frac{T_R}{T_U} \quad (2.2.5)$$

The BCR is sometimes referred to as the layer coefficient ratio (LCR) and it is used as a modifier which is applied to the SN of the pavement as follows:

$$SN = (a \times d)_{hma} + BCR.(a \times d \times m)_{base} + (a \times d \times m)_{subbase} \quad (2.2.6)$$

The AASHTO design method is empirical in nature and does not directly consider several important factors such as: mechanics of the pavement structure, climatic effects, or changes in traffic loads and material properties over the design life of the pavement. Also, application of this design methodology to geosynthetic-reinforced pavements is not clear. Difference in geosynthetic reinforcement products, materials, geometries, failure criteria and loads used in different test sections are not explained sufficiently. Moreover, this method needs to provide a consistent groundwork for performance comparisons among various geosynthetics available for base reinforcement and subgrade stabilization applications. In addition, it has been difficult to incorporate the BCR and TBR ratios into the design where the objective of the reinforcement is to provide both an increased pavement life and a reduced base course thickness. Although research conducted to date has supported the AASHTO design

method to some extent, long-term information about the projects designed using this method is not found in order to establish confidence limits.

2.2.4. Empirical Design Method of Giroud and Han (2004a)

Giroud and Han (2004a) developed a theoretically based and empirically calibrated design method specifically designed for geogrid-reinforced unpaved roads. This method takes into account the distribution of stresses, strength of base course material, geogrid-aggregate interlock and geogrid in-plane stiffness in addition to conditions considered in earlier methods (e.g., traffic volume, wheel loads, tire pressure, subgrade strength, rut depth and influence of reinforcing geosynthetics). The properties of the base course material are considered in Giroud and Han's design approach which is an improvement over previous methods. In this design method, the base course material is characterized by its CBR (California Bearing Ratio) value using an AASHTO chart that includes a correlation with the resilient modulus for the subbase material (AASHTO 1993).

Giroud and Han (2004a) developed the following design equation for base course thickness through calibration and verification with laboratory and field data:

$$h = \frac{0.868 + (0.661 - 1.006J^2) \left(\frac{r}{h}\right)^{1.5} \log N}{1 + 0.204[R_E - 1]} \left[\sqrt{\frac{\frac{P}{\pi r^2}}{\left(\frac{s}{f_s}\right) \left\{ 1 - 0.9 \exp\left[-\left(\frac{r}{h}\right)^2\right]\right\} N_c f_c CBR_{sg}} - 1} \right] r \quad (2.2.7)$$

where,

$$(0.661-1.006 J^2) > 0$$

h = required base course thickness (m or in)

J = geogrid aperture stability modulus (N.m/° or ft.lbs/°)

N = number of axle passes

P = wheel load (kN or lbs)

r = radius of the equivalent tire contact area (m or in)

R_E = modulus ratio of base course to subgrade soil = $E_{bc}/E_{sg} = 3.28$

$$CBR_{bc}^{0.3}/CBR_{sg} \leq 5$$

E_{bc} = base course resilient modulus (Mpa or psi)

E_{sg} = subgrade soil resilient modulus (Mpa or psi)

CBR_{bc} = CBR of the base course materials (aggregate)

CBR_{sg} = CBR of the subgrade soil

f_s = rut depth factor

s = maximum rut depth (m or in)

N_c = bearing capacity factor

= 3.14 for unreinforced roads

= 5.14 for geotextile reinforced roads

= 5.71 for geogrid reinforced roads

f_c = factor relating subgrade CBR to undrained cohesion, $c_u = 30$ kPa (4.3 psi)

According to FHWA (2008), the validity of the Giroud and Han (2004a) method is limited by the following conditions:

- Rut depth from 50 to 100 mm (2 to 4 in)
- Field subgrade CBR less than 5
- Maximum ratio of base course modulus E_{bc} to subgrade soil modulus E_{sg} of 5
- Maximum number of passes: Based on the current state of practice, the traffic load for unpaved roads is limited to 10,000 ESALs
- The tension membrane effect was not taken into account since it is negligible for rut depths less than 100 mm (4 in)
- The influence of geogrid reinforcement is included through a bearing capacity factor of $N_c = 5.71$ and the aperture stability modulus (J) of geogrid
- The influence of geotextile reinforcement is considered through a bearing capacity factor of $N_c = 5.14$, and the aperture stability modulus (J) equal to zero
- For the unreinforced unpaved roads, the design is valid for bearing capacity factor of $N_c = 3.14$, and the aperture stability modulus (J) equal to zero
- Minimum thickness of 100 mm (4 in) for the base course aggregate

Giroud and Han (2004b) suggested that these limitations may change as additional empirical data become available.

2.2.5. Mechanistic-Empirical Pavement Design Guide Method

The NCHRP Project 1-37A Mechanistic-Empirical Pavement Design Guide (MEPDG) (AASHTO 2008) along with its supporting software (MEPDG, Version 1.1) is a major upgrade of an older AASHTO (1993) design method. Major steps of the mechanistic-empirical (M-E) design method include:

- Selection of the pavement structure (layers, type of materials, thicknesses)
- Characterization of climate, traffic and materials for the specific project location
- Analysis of the pavement structure mechanistic model
- Calculation of critical responses (stresses, strains)
- Evaluation of the accumulated damage and associated distress with reference to preset criteria
- The design may require several iterations considering different pavement structures. Design is completed when for a specific section the levels of distress do not exceed the acceptable design levels.

Inclusion of geosynthetic reinforcement introduces a new set of design parameters to be considered to design flexible pavements efficiently from both mechanical and economical standpoints. Important parameters may include

geosynthetic type, flexural stiffness, tensile modulus and strength, aperture size and placement location within the pavement structure.

NCHRP Mechanistic-Empirical Method (2004): In the recent years, attempts have been made to incorporate the use of geosynthetic reinforcement into AASHTO and M-E design methods. Early design approaches for reinforced flexible pavements modify equations in order to reveal the benefit achieved by adding geosynthetics. A National Cooperative Highway Research Program (NCHRP) study aimed at developing a methodology to incorporate the reinforcing function of geosynthetics in the M-E design approach for pavement structures (NCHRP 2004).

The main parameters used in the M-E method are the mechanistic properties of each pavement layer, including Poisson's ratio (ν) and Resilient Modulus (M_R). Both M_R and the Young's Modulus (E) influence the strain response of the material to applied stresses. The value of E influences the initial deformation of the material, whereas M_R influences the elastic deformation of the material after cyclic loading.

CHAPTER THREE

SURVEY AND CLASSIFICATION OF GEOGRID PRODUCTS

3. 1. Survey of Geogrid Products

As a first step of this study, a survey was carried out on a wide range of commonly available geogrids on the market in order to identify candidate products for ODOT's new geogrid specifications. Candidate geogrids were initially screened from the 2009 issue of the Geosynthetics Specifier's Guide (IFAI 2009) on the basis of their aperture size and rib strength at 5% strain. Tensar BX1100 and BX1200 geogrids which are primarily used in ODOT projects are referred to as the control geogrids in this study. These geogrids are referred to as Type-1 and Type-2 geogrids, respectively in the ODOT specifications manual.

Several geogrid producers and suppliers were contacted for additional information on their products. A database of surveyed geogrids and their selected properties (aperture size, rib strength at 5% strain and ultimate strength) is given in **APPENDIX**. **Figure 3.1** shows a histogram of geogrid products available on the market based on their machine direction (MD) rib strength at 2% strain, which is used in specifications published by several U.S. State DOTs (**Section 3.2**). The rib strength at 2% strain has been recommended as a serviceability criterion in previous studies (e.g.

Christopher et al. 2008). The histogram in **Figure 3.1** was produced based on a survey of 113 geogrids from available sources.

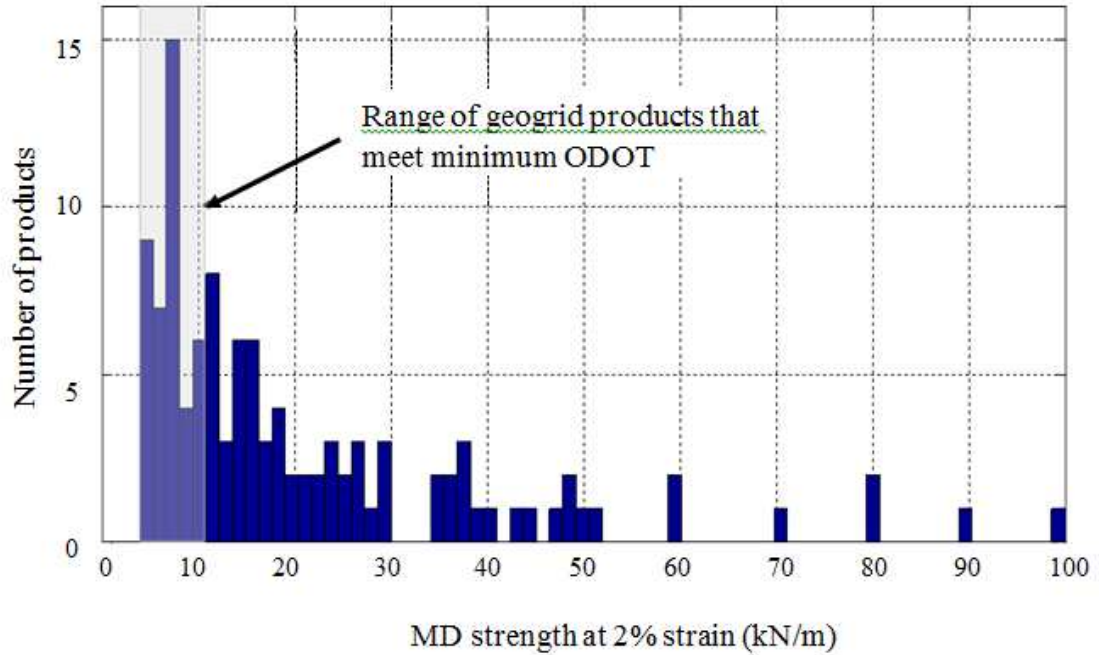


Figure 3.1. Distribution of MD strength at 2% rib strain of **uniaxial and biaxial** geogrids surveyed in this study

Among these 113 geogrids surveyed, 66 geogrids were biaxial. Since this study was focused on biaxial geogrids used for base reinforcement, the distribution of MD rib strength at 2% strain of biaxial geogrids as a subset of what is shown in **Figure 3.1** is shown in **Figure 3.2**.

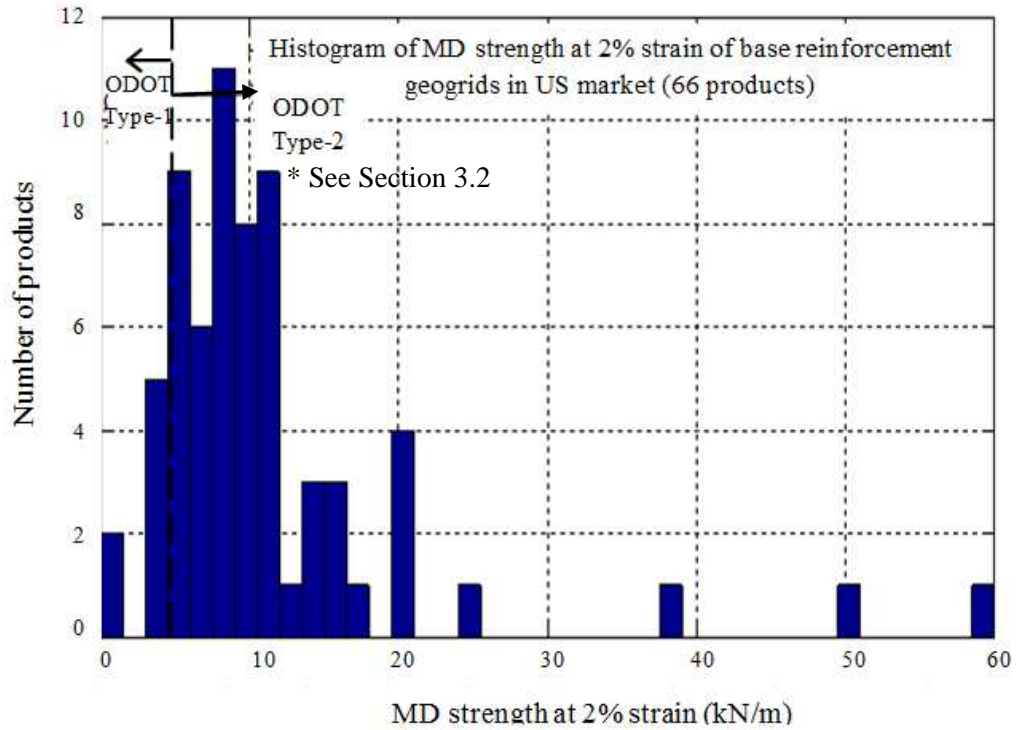


Figure 3.2. Distribution of MD strength at 2% rib strain of **bi-axial geogrids** available on the market

Among the 66 geogrids that are represented in **Figure 3.2**, a total of 31 geogrids were found to have either an aperture size or a 5%-strain rib strength value comparable to those of ODOT Type-1 and ODOT Type-2 geogrids as given in **Table 3.1**. The geogrid products discussed in this report are classified as extruded and non-extruded geogrids (EGG and NEGG, respectively). The NEGG category, in turn, includes woven and knitted geogrids (WGG and KGG, respectively).

Table 3.1. List of candidate geogrids with either aperture size or 5%-strain tensile strength comparable to those of ODOT Type-1 and Type-2 geogrids

Product Name	Aperture Size (mm)		Strength @ 5% Strain (kN/m)	
	MD	XD	MD	XD
ACE GG30-II	25	28	15	NP
ACE GG300-II	25	30	120	NP
BX1100*	25	33	8.5	13.4
BX 1120	25	33	8.5	13.4
BX1200**	25	33	11.8	19.6
BX-1220	25	33	11.8	19.6
BX 1500	25	31	17.5	20
BX 4100	25	33	8	10.5
BX-4200	25	33	10.5	14.6
Fornit 20	15	15	11	16
Fotracc 35	20	20	13	NA
LBO 202	28	38	9.5	13.5
MacGrid EB2	42	50	9	13.4
MacGrid EB3	42	50	13.5	19.6
MacGrid WB1	25	33	15.2	11.5
MacGrid WB2	25	33	15.2	16.5
MacGrid WB3	25	25	12.6	14.3
MacGrid WG3	25	28	15	NP
MacGrid WG5	24	28	28	NA
MacGrid WG8	24	28	40	NA
Mirafi BXG 11	25	25	13.4	13.4
Mirafi BXG 12	25	25	13.4	19.7
Miragrid 3XT	22	25	15.4	NA
MS 220	42	50	9	13.42
MS 330	42	50	13.5	19.6
MS 500	60	60	13.5	19.6
SF 11	25	25	15.2	11.5
SF 12	25	25	15.2	19.9
SF13	25	25	15.2	17
SF 15	25	25	17.5	20
StrataGrid SG150	25	24	9.1	6.2

Note: * ODOT Type-1 Geogrid; ** ODOT Type-2 Geogrid; NA: Not Applicable; NP: Not Provided; Products in green cells were ultimately selected for testing in this study

Based on the above survey and the selection criteria illustrated in **Figure 3.3**, a total of eight geogrids were selected as a final set for testing in this study (**Table 3.2**). All geogrid products, with the exception of the EGG2 geogrid, were tested in their as-supplied condition. The EGG2 geogrid is supplied by the manufacturer in the form of two layers that are stitched together using polyester ties in an offset arrangement (**Figure 3.4**). In practice, EGG2 is used as a double-layer geogrid. However, the mechanical properties of this product are determined for single-layer samples as recommended by the manufacturer. Also, in order to widen the range of material properties in the parametric study, the EGG2 geogrid was separated and tested as a single layer. Therefore, the EB2 results reported in this study are for single-layer geogrid specimens.

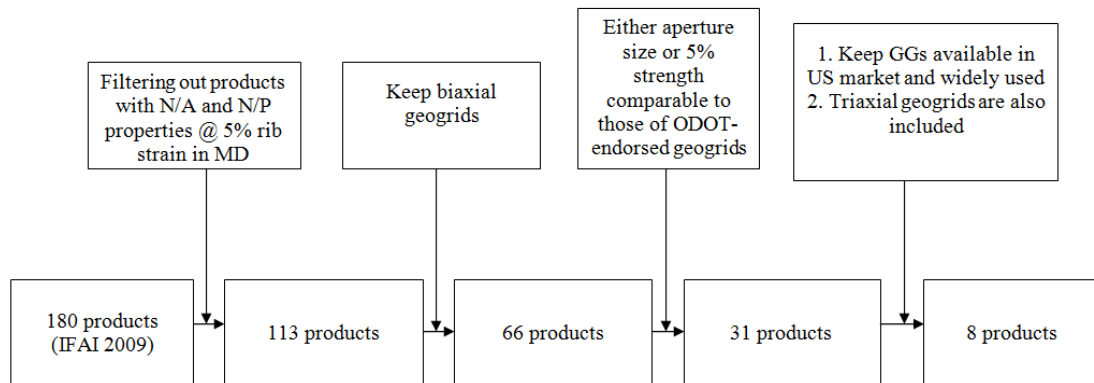


Figure 3.3. Procedure used to select geogrid products for testing in this study

Table 3.2. General information on geogrid products tested in this study

Geogrid Name	Designation in This Study	Fabrication Category	Manufacturer	Aperture size (mm)		Polymer	Normalized Price
				MD	XD		
BX1200	EGG1	EGG	Tensar	25	33	PP	1.00
EB2 (single layer) ⁽¹⁾	EGG2		Maccaferri	42	50		0.51
TX140	EGG3 ⁽²⁾		Tensar	40 ⁽³⁾	40 ⁽⁴⁾		1.00
TX160	EGG4 ⁽²⁾		Tensar	40 ⁽³⁾	40 ⁽⁴⁾		1.81
BXG11	WGG1	NEGG	TenCate-Mirafi	25.4	25.4	PET; PVC coating	0.85
BXG12	WGG2		TenCate-Mirafi	25.4	25.4		1.17
SF11	WGG3		Synteen	25	25		0.64
SG150	KGG1		Strata	25.4	24.1		PET; a proprietary UV stabilized coating

Notes:

BX: Biaxial, TX: Triaxial,

PP: Polypropylene, PET: Polyester, PVC: Polyvinyl Chloride, UV: Ultra Violet,

EGG: Extruded Geogrid, NEGG: Non-Extruded Geogrid, WGG: Woven Geogrid, KGG: Knitted Geogrid

⁽¹⁾ EGG2 geogrid was separated as a single layer in order to widen the range of the parametric study; though originally supplied by the manufacturer in the form of double-layer.

⁽²⁾ Triangular aperture geometry

⁽³⁾ Longitudinal rib

⁽⁴⁾ Diagonal rib

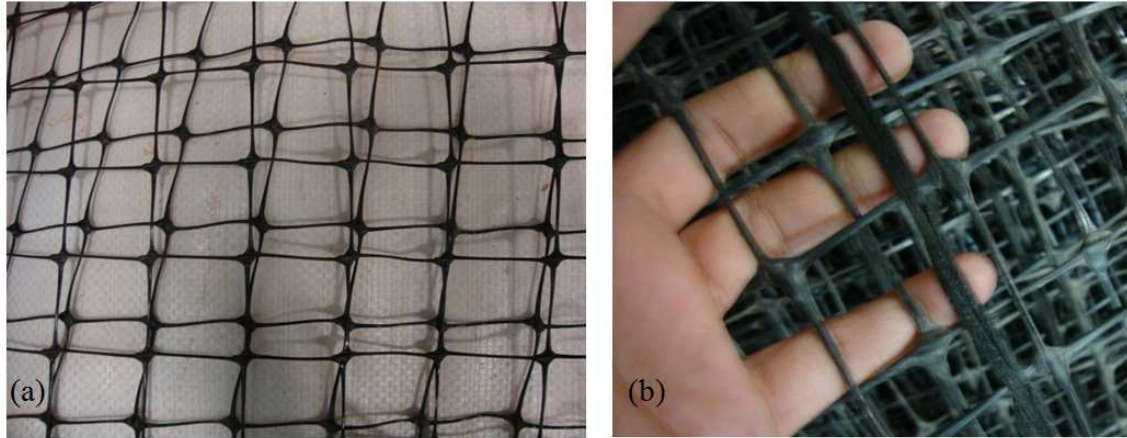


Figure 3.4. (a) EB2 geogrid, (b) Polyester ties which are used to stitched together the two layers of the geogrid

3.2. DOT Agencies Data

Table 3.3 shows a list of all 50 State DOTs in the United States that were surveyed with respect to their geogrid specifications. This survey revealed that those DOTs that have specifications for base reinforcement geogrids specify MD rib strength values at 2% elongation which vary between 3.0 kN/m and 10.0 kN/m. This range represents 62% of the biaxial geogrid products surveyed (i.e. 41 out of 66 products) within the lower end of tensile strength values (**Figure 3.1** and **Figure 3.2**). Stronger geogrids (especially of uniaxial type) are primarily used for reinforced soil walls, embankments and steepened slopes, which are outside the scope of this study. Based on the above survey, the geogrids listed in **Table 3.2** were grouped into categories shown in **Figure 3.5**. The 111 N split value for junction strength shown in **Figure 3.5** was selected based on the Holtz et al. (2008) requirement for minimum ultimate junction strength of geogrids. The split value for the 2%-strain rib strength was selected such

that ODOT Type-1 and ODOT Type-2 geogrids represent the weak rib (W_R) and strong rib (S_R) categories, respectively, with respect to this index property.

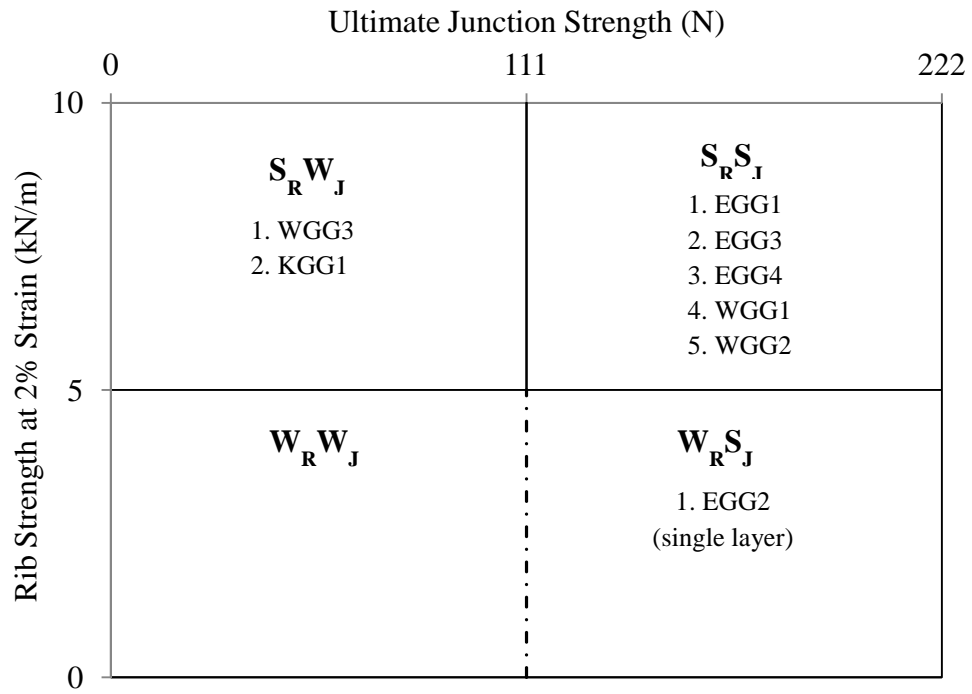
Table 3.3. State DOTs providing geogrid specifications for base reinforcement

State	Specs.	No Specs.	Info. Source
Alabama		✓	🔗
Alaska*	✓		✉
Arizona		✓	🔗
Arkansas		✓	✉
California		✓	🔗
Colorado		✓	🔗
Connecticut		✓	🔗
Delaware		✓	🔗
Florida*	✓		🔗
Georgia		✓	🔗
Hawaii		✓	🔗
Idaho		✓	🔗
Illinois		✓	🔗
Indiana	✓		🔗
Iowa		✓	🔗
Kansas	✓		🔗
Kentucky	✓		🔗

State	Specs.	No Specs.	Info. Source
Louisiana		✓	✉
Maine		✓	🔗
Maryland		✓	✉
Massachusetts		✓	✉
Michigan		✓	✉
Minnesota	✓		🔗
Mississippi		✓	🔗
Missouri		✓	🔗
Montana		✓	🔗
Nebraska		✓	🔗
Nevada		✓	🔗
New Hampshire		✓	🔗
New Jersey		✓	🔗
New Mexico		✓	🔗
New York		✓	🔗
North Carolina		✓	🔗
North Dakota		✓	🔗

State	Specs.	No Specs.	Info. Source
Ohio	✓		🔗
Oklahoma*	✓		🔗
Oregon	✓		🔗
Pennsylvania		✓	🔗
Rhode Island	✓		🔗
South Carolina		✓	🔗
South Dakota		✓	🔗
Tennessee	✓		🔗
Texas	✓		🔗
Utah		✓	🔗
Vermont	✓		🔗
Virginia		✓	🔗
Washington		✓	🔗
West Virginia		✓	🔗
Wisconsin*	✓		🔗
Wyoming	✓		🔗

🔗 DOT Agency Website
 ✉ Correspondence with Agency
 * States that Endorse Specific Products



Note: EGG: Extruded Geogrid
 NEGG: Non Extruded Geogrid
 $S_R W_J$ = Strong Rib Weak Junction
 $S_R S_J$ = Strong Rib Strong Junction
 $W_R W_J$ = Weak Rib Weak Junction
 $W_R S_J$ = Weak Rib Strong Junction

Figure 3.5. Classification of the geogrid products used in the study

CHAPTER FOUR

DETERMINATION OF JUNCTION STRENGTH PROPERTIES

4.1. Fabrication of Junction Strength Testing Clamps

A total of eighty (80) junction strength tests were carried out on geogrids listed in **Figure 3.5** in both MD and XD directions according to the GRI GG2 test method. A minimum of five replicate samples of each product were prepared and tested. In these tests, a junction clamp firmly gripped the transverse ribs on each side of the junction (**Figure 4.1**) and the specimen was subjected to a monotonic tensile load until the junction failed. In addition to obtaining junction strength values for the geogrid products, these tests helped us to evaluate the performance of the fabricated clamps and apply necessary modifications to improve their performance. Due to the manufacturing technique and comparatively low junction strength, the strain magnitudes of the non-extruded geogrids (NEGG) were too low for meaningful analysis. Therefore it was decided to study only the ultimate junction strength of these products. Digital imagery technique was used to determine the strain in extruded geogrid (EGG) products (Wang 2009).

Figure 4.2 and **Figure 4.3** show the tensile testing machine and an example output plot from the in-isolation tests, respectively. **Figure 4.4** shows different failure modes observed in the junction tests on the extruded geogrid (EGG) products.

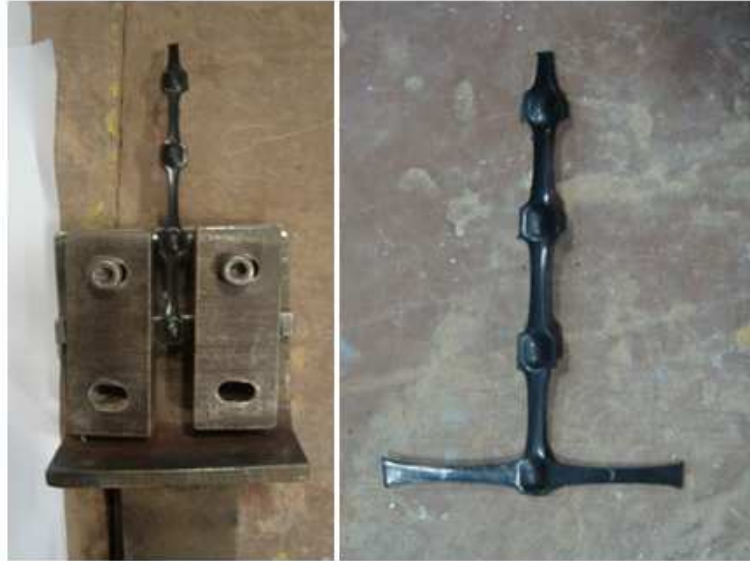


Figure 4.1. Clamp and example test specimen used in junction tests (junctions in the specimen shown are one inch apart from each other)



Figure 4.2. Tensile testing frame for testing rib and junction strength of geogrid specimens

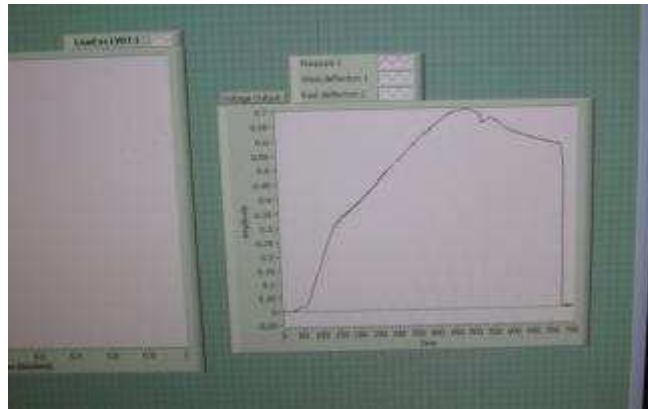


Figure 4.3. Specimen failure as captured on the data acquisition system screen

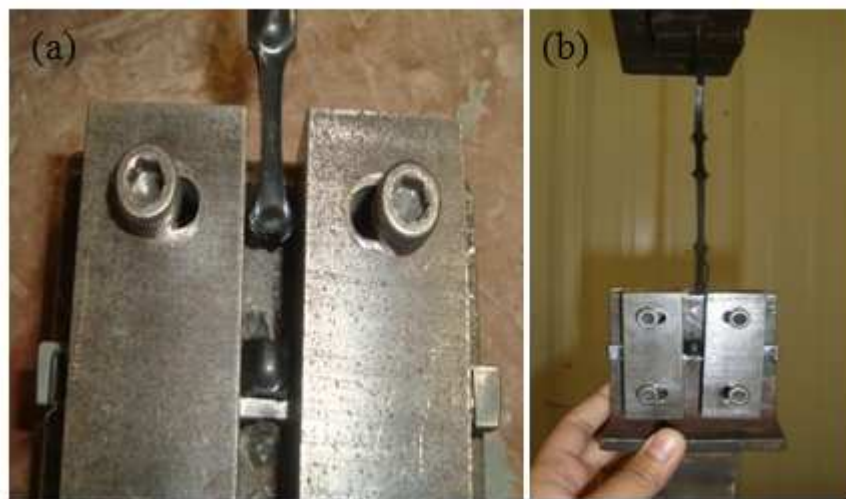


Figure 4.4. Different failure modes observed in junction testing of extruded geogrids:
 (a) Brittle failure (b) Ductile failure

4.2. Junction Strength Test Results

Samples of the eight different geogrids examined in this study (**Table 3.2**) are shown in **Figure 4.5** through **Figure 4.12**, respectively. **Figure 4.13** shows an EGG4 geogrid specimen in the junction test setup before and after failure.

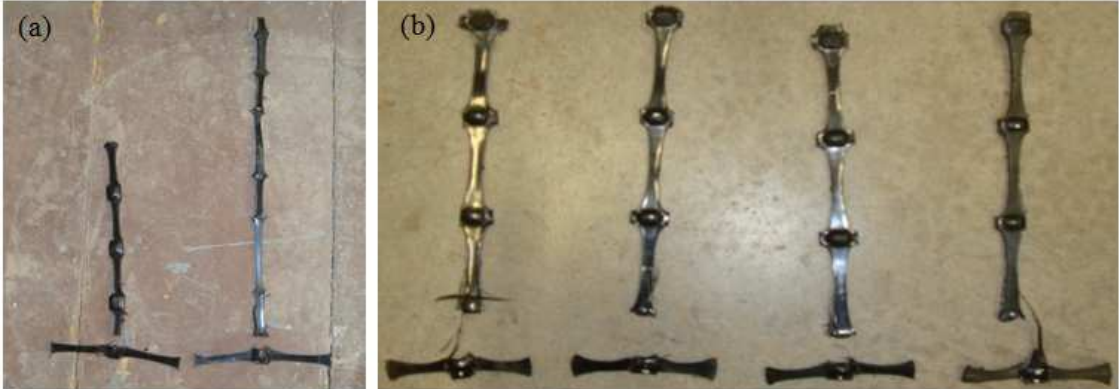


Figure 4.5. EGG1 geogrid junction strength specimens after the test (a) MD, (b) XD

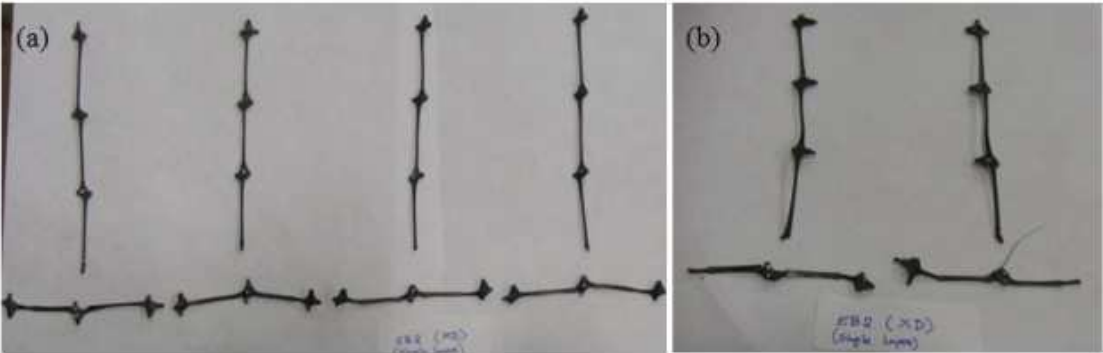


Figure 4.6. EGG2 (single layer) geogrid junction strength specimens after the test: (a) in MD and (b) in XD

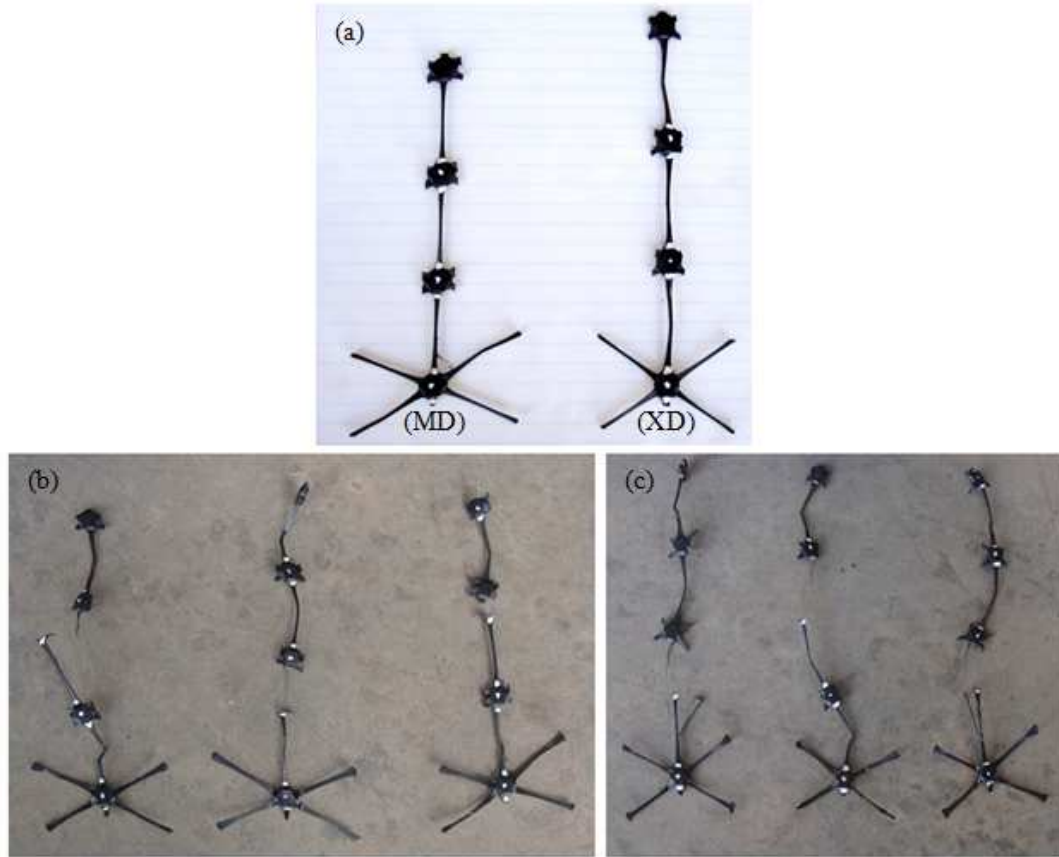


Figure 4.7. EGG3 geogrid junction strength specimens: (a) before the test, (b) after failure (MD), (c) after failure (XD)

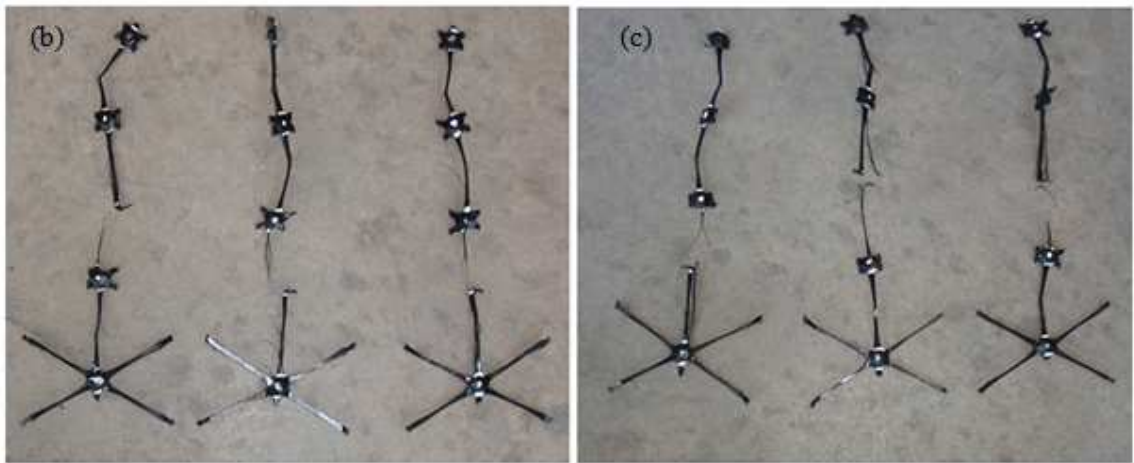
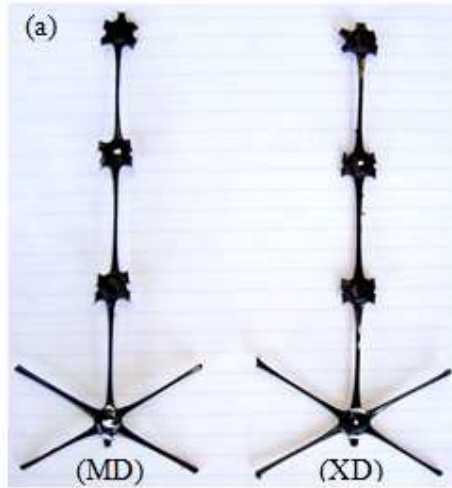


Figure 4.8. EGG4 geogrid junction strength specimens: (a) before the test, (b) after failure (MD), (c) after failure (XD)

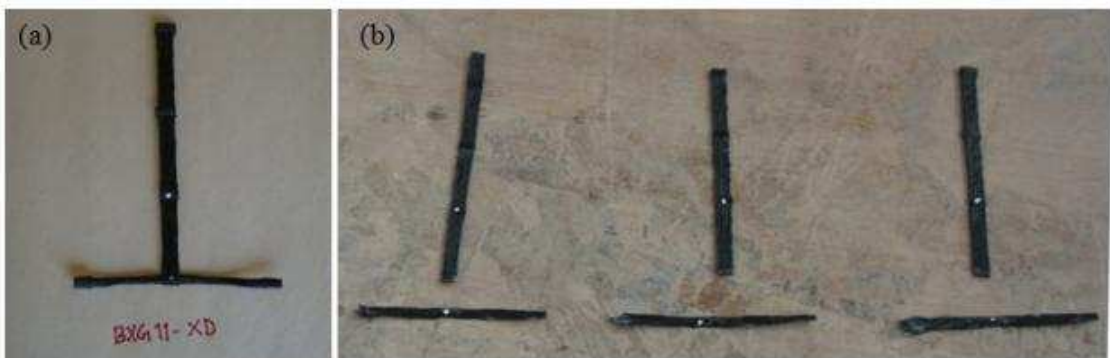


Figure 4.9. WGG1 geogrid junction strength specimens in XD: (a) before failure, (b) after failure

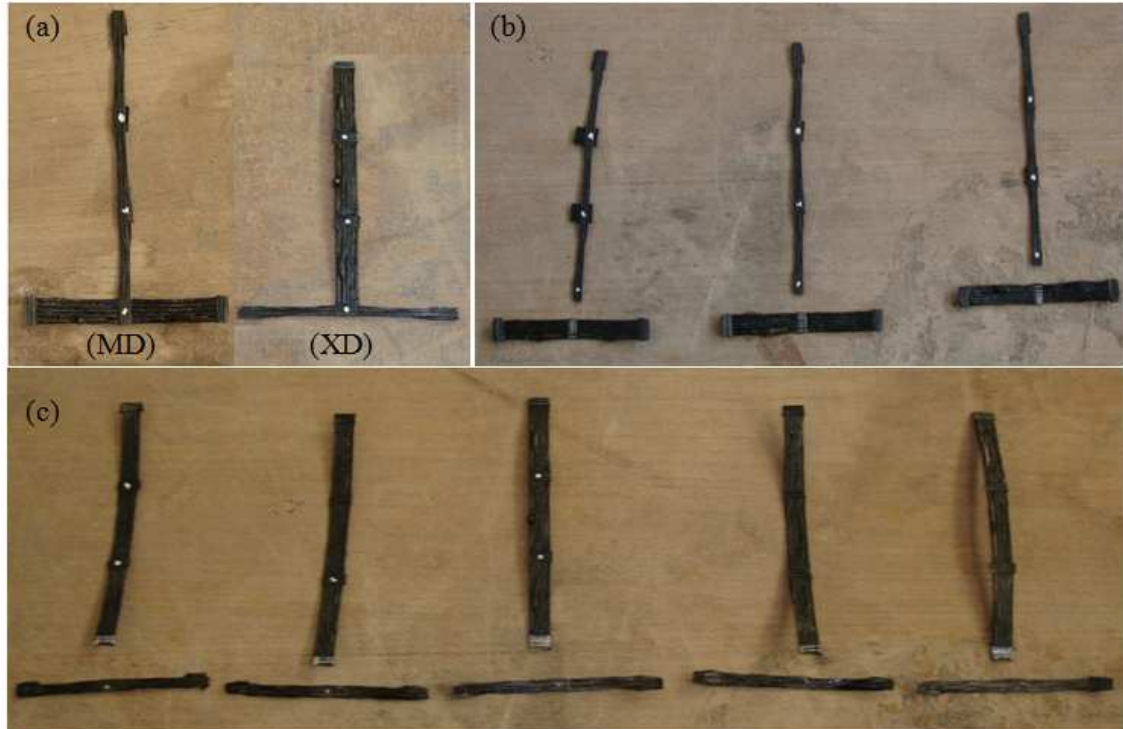


Figure 4.10. WGG2 geogrid junction strength specimens: (a) before the test, (b) after failure (MD), (c) after failure (XD)



Figure 4.11. WGG3 geogrid junction strength specimens (a) before the test, (b) after failure (MD), (c) after failure (XD)

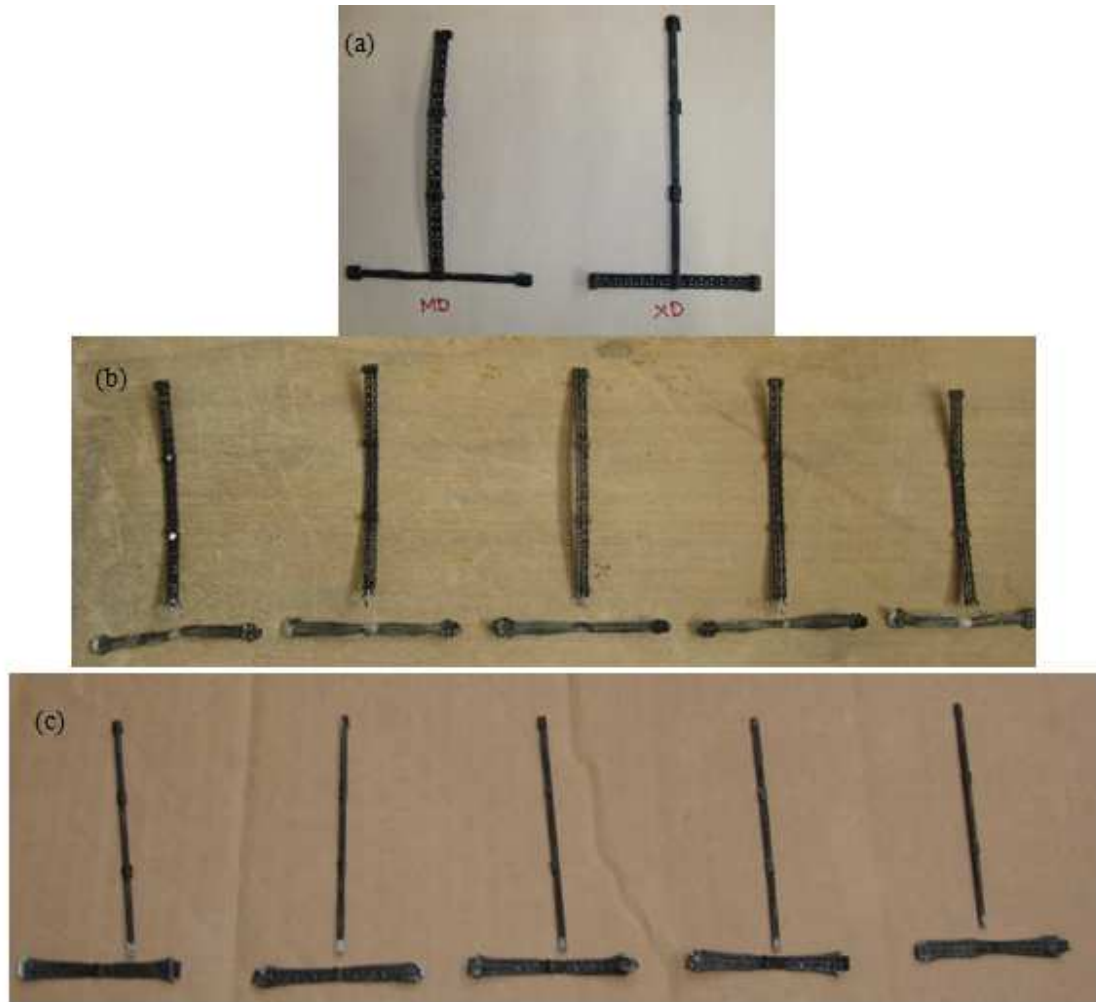


Figure 4.12. KGG1 geogrid junction strength specimens: (a) before the test, (b) after failure (MD), (c) after failure (XD)

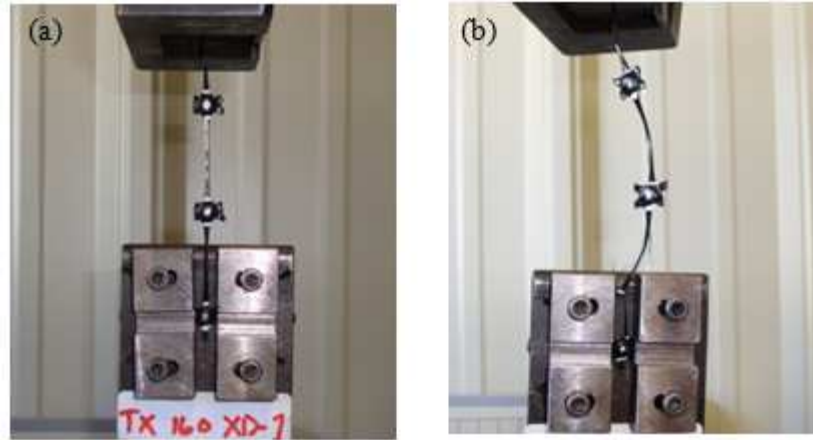


Figure 4.13. EGG4 specimen in junction strength test: (a) before test, (b) after failure

Junction test results for the eight different types of geogrids investigated (**Table 3.2**) are shown in **Figure 4.14** through **Figure 4.21**. In the cases of EGG3 and EGG4 geogrids in **Figure 4.16** and **Figure 4.17**, the “MD” notation refers to the ribs that are situated at 30° from the machine direction due to their triangular configuration. The test results for each geogrid product tested are summarized in **Table 4.1** and **Table 4.2**. In the results shown in these figures and tables, the outlier data points were discarded such that all the remaining data will fall within $\pm 5\%$ of the mean value.

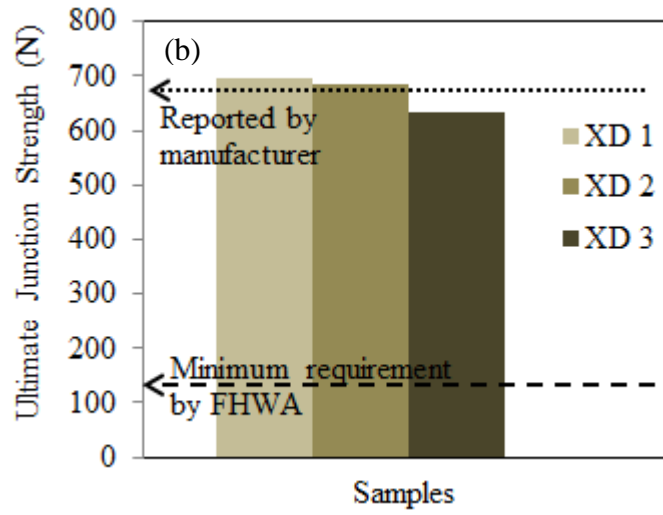
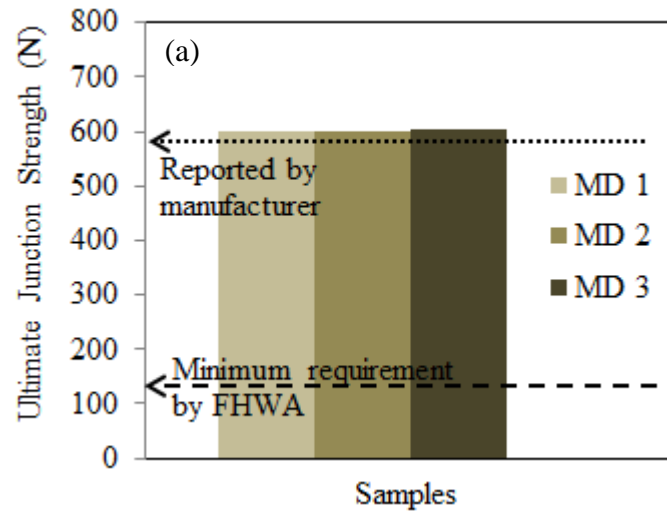


Figure 4.14. Junction strength test results for EGG1 test specimens (a) MD, (b) XD

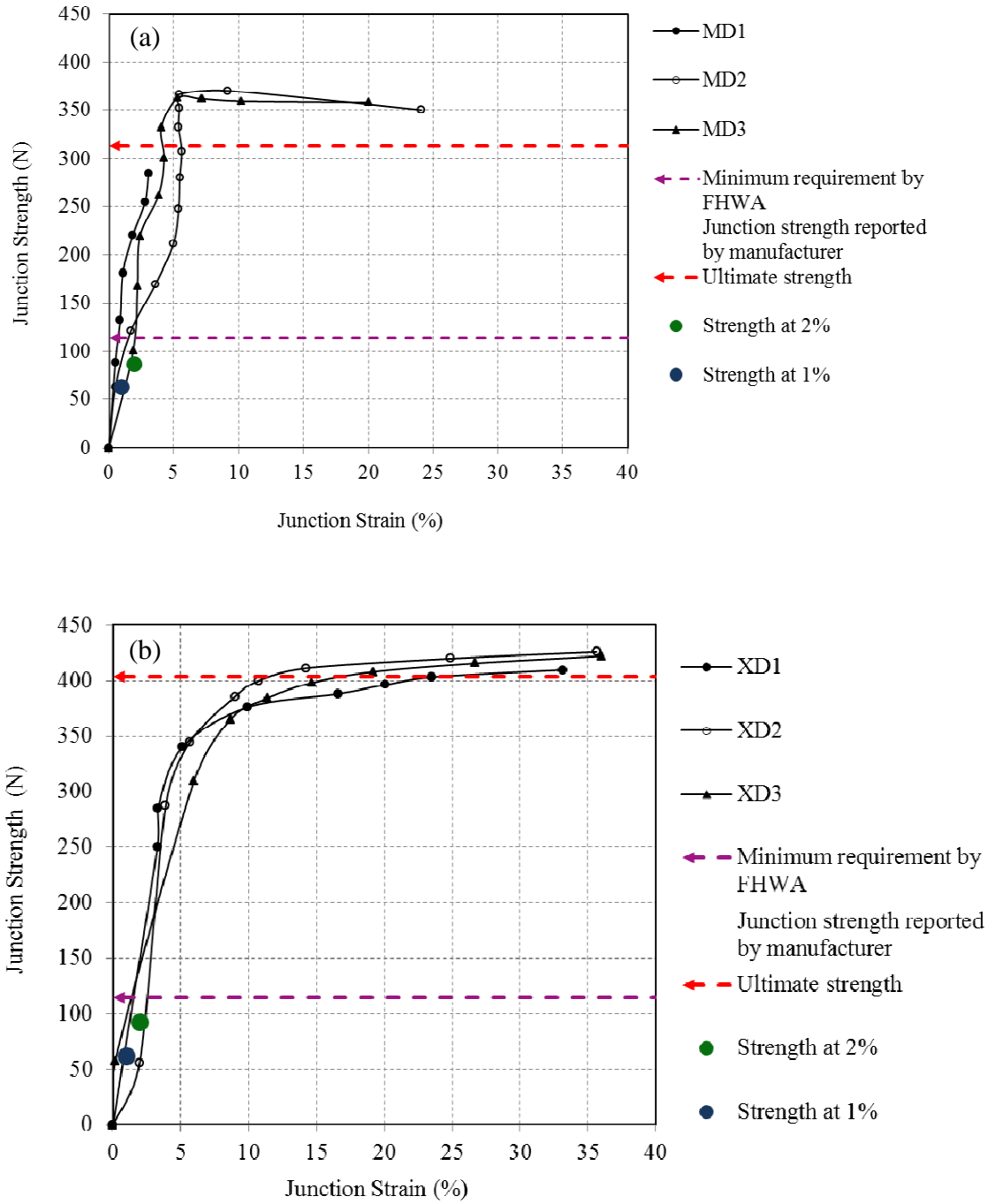


Figure 4.15. Junction strength test results for EGG2-single layer test specimens (a) MD, (b) XD

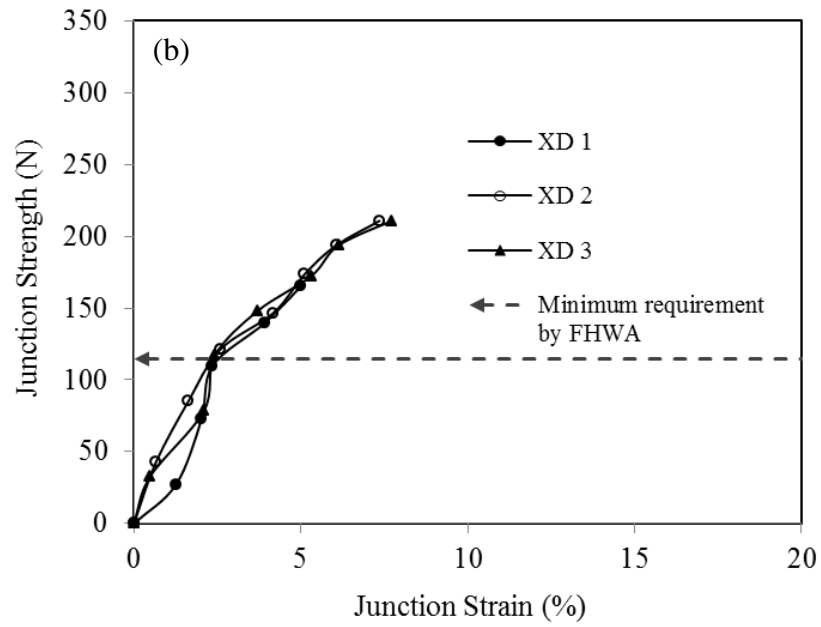
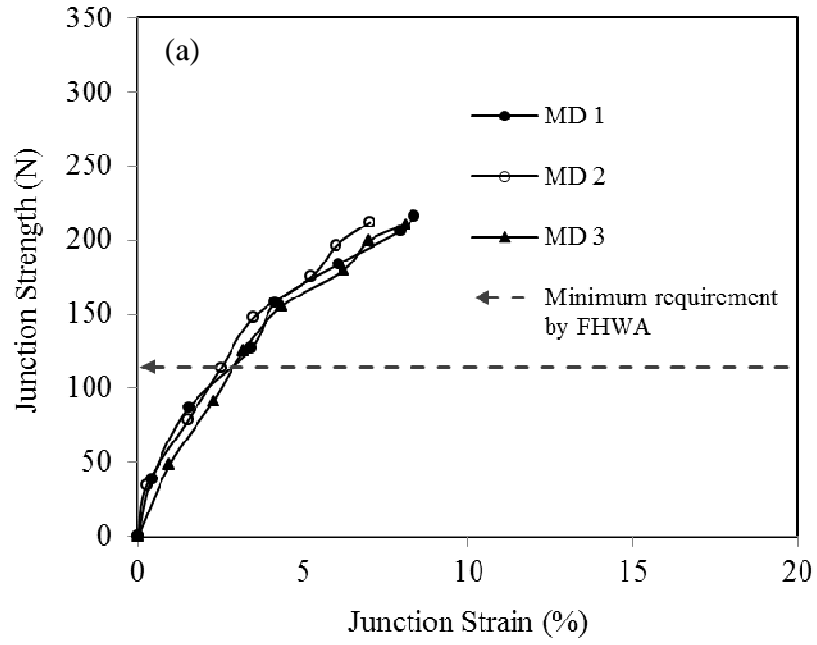


Figure 4.16. Junction strength test results for EGG3 test specimens (a) MD ribs (30° from MD), (b) XD

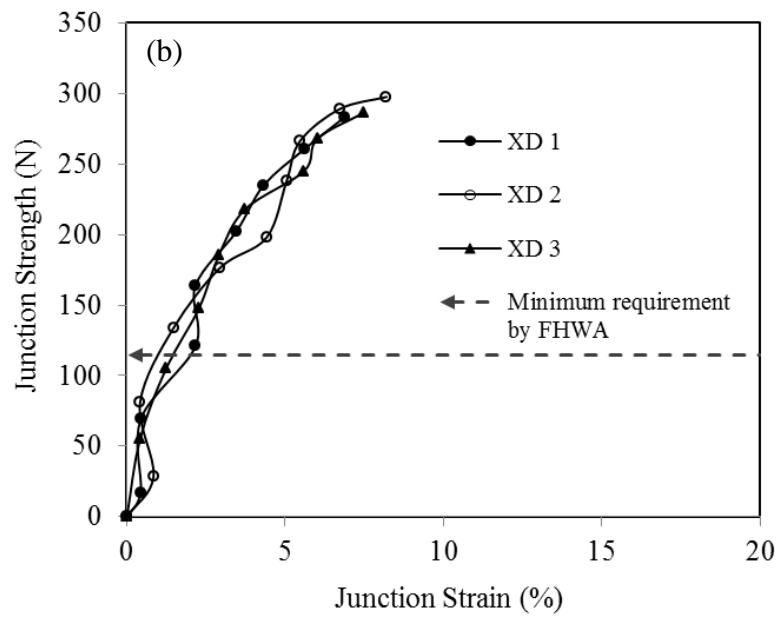
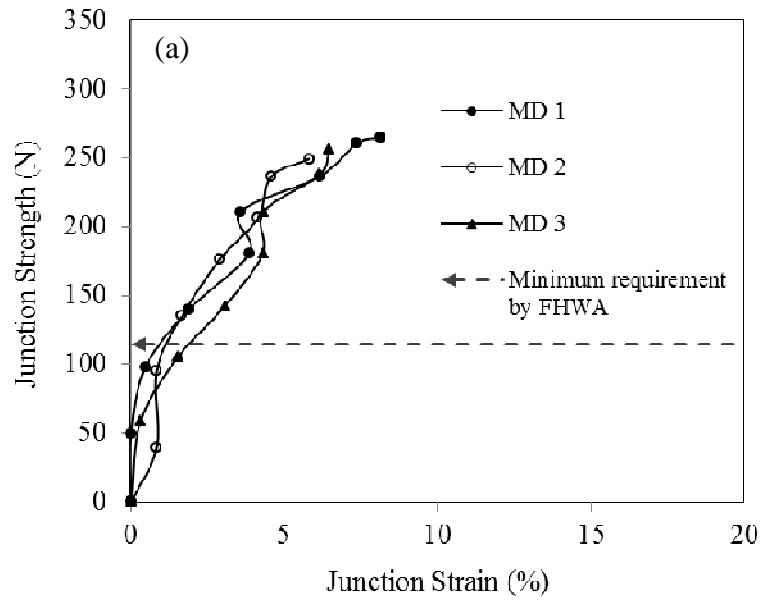


Figure 4.17. Junction strength test results for EGG4 test specimens (a) MD ribs (30° from MD), (b) XD

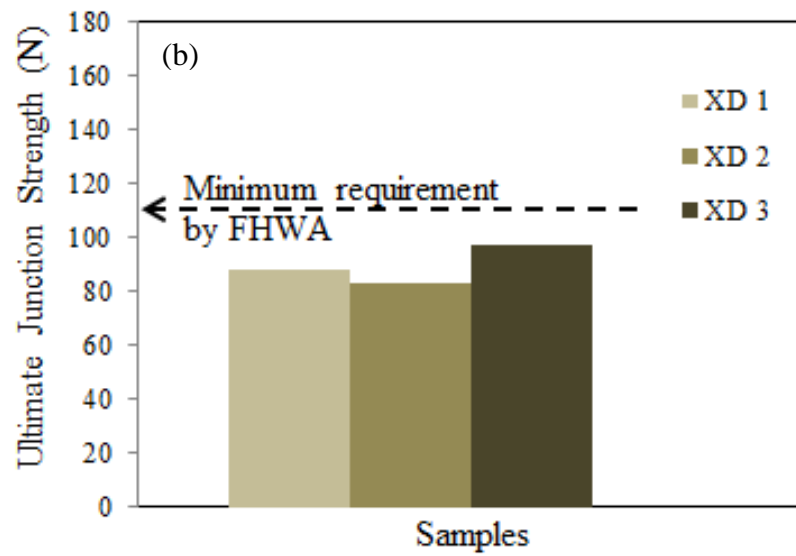
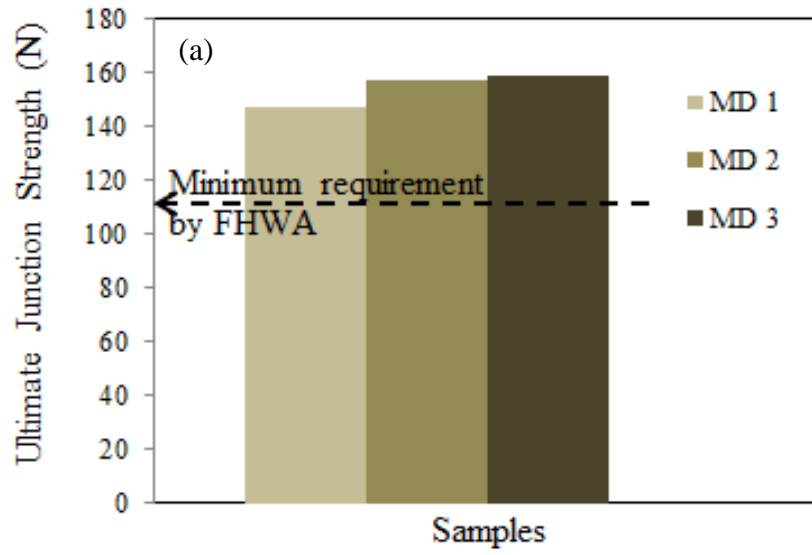


Figure 4.18. Junction strength test results for WGG1 test specimens (a) MD, (b) XD

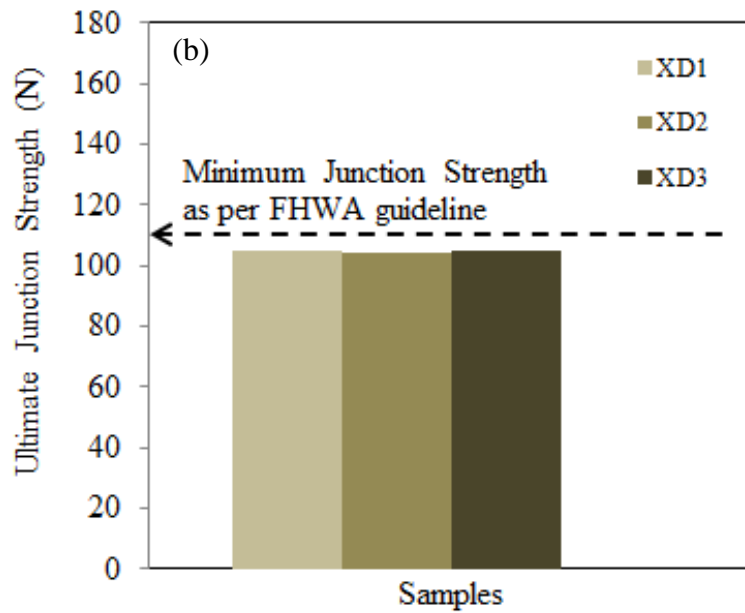
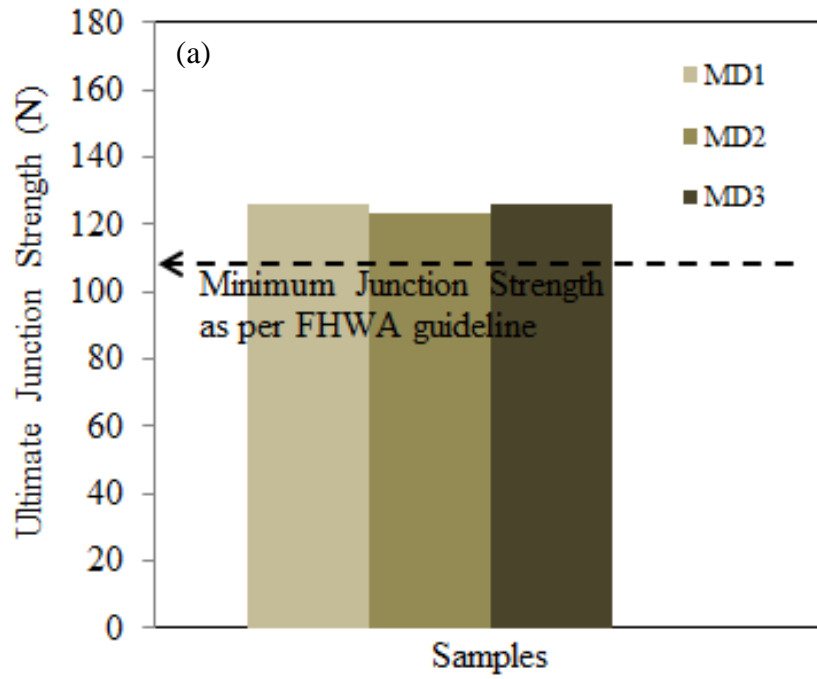


Figure 4.19. Junction strength test results for WGG2 test specimens (a) MD, (b) XD

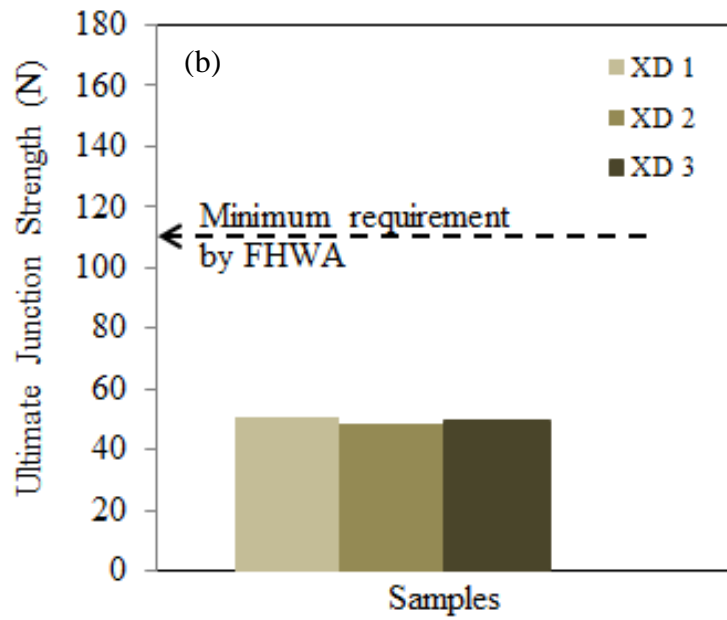
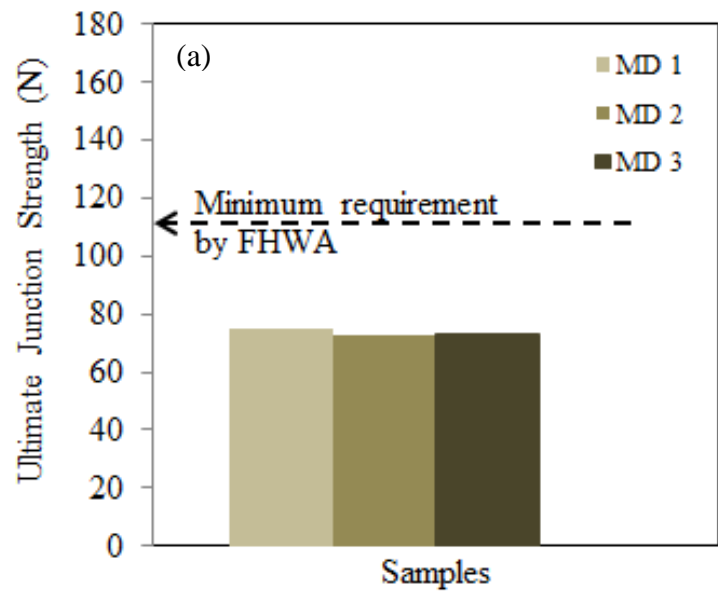


Figure 4.20. Junction strength test results for WGG3 test specimens (a) MD, (b) XD

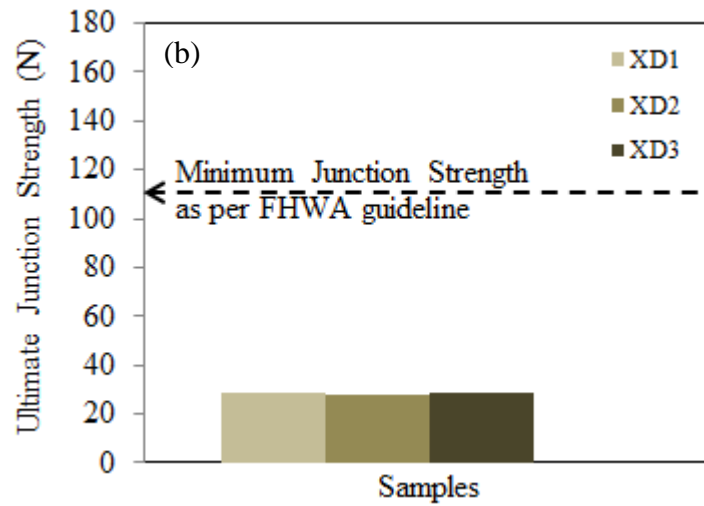
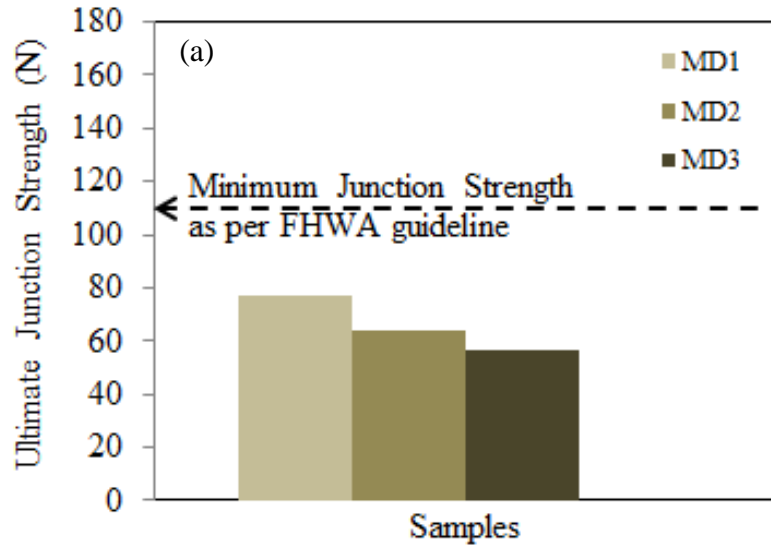


Figure 4.21. Junction strength test results for KGG1 test specimens (a) MD, (b) XD

Table 4.1. Summary of junction strength test results in MD

Geogrid	Type	Junction Strength in Machine Direction (N)								
		1	2	3	4	5	Mean (μ)	Standard Deviation (σ)	Coefficient of Variation, COV (%)	MARV value from manufacturer
EGG1	$S_R S_J$ Biaxial Extruded	600.48	600	[587.2]	604.48		601.65	2.01	0.33	451.60
EGG2 (single layer)	$W_R S_J$ Biaxial Extruded	[284]	369.00	362.00	368.84	353.19	363.26	3.26	0.90	313.75
EGG3	$S_R S_J$ Triaxial Extruded	210.00	210.00	215.00			211.67	2.36	1.11	NP
EGG4	$S_R S_J$ Triaxial Extruded	250.00	250.00	260.00			253.33	4.71	1.86	NP
WGG1	$S_R S_J$ Biaxial Woven	[183.58]	158.49	157.42	146.97		154.29	5.20	3.37	133.44
WGG2	$S_R S_J$ Biaxial Woven	125.70	125.75	123.08	126.11	[177.48]	125.16	1.21	0.97	133.44
WGG3	$S_R W_J$ Biaxial Woven	74.68	72.90	73.25	72.81	72.86	73.30	0.71	0.96	264.22
KGG1	$S_R W_J$ Biaxial Woven	76.91	45.55	64.10	56.98		60.89	11.37	18.68	135.66

Cell background color key:

Green: Junction meets minimum Holtz et al. (2008) requirement

Pink: Junction does not meet minimum Holtz et al. (2008) requirement

[---] Outlier value

NP Not provided by the manufacturer

Table 4.2. Summary of junction strength test results in XD

Geogrid	Type	Junction Strength in Cross-Machine Direction (N)								
		1	2	3	4	5	Mean (μ)	Standard Deviation (σ)	Coefficient of Variation, COV (%)	MARV value from manufacturer
EGG1	$S_R S_J$ Biaxial Extruded	695.34	683.42	[558.74]	634.5		671.09	26.32	3.92	679.13
EGG2 (single layer)	$W_R S_J$ Biaxial Extruded	425.84	404.43	403.20	422.07	434.32	417.97	12.23	2.93	403.20
EGG3	$S_R S_J$ Triaxial Extruded	210.00	210.00	200.00			206.67	4.71	2.28	NP
EGG4	$S_R S_J$ Triaxial Extruded	300.00	290.00	290.00			293.33	4.71	1.61	NP
WGG1	$S_R S_J$ Biaxial Woven	88.29	82.60	96.84	[128.15]		89.24	5.85	6.55	133.44
WGG2	$S_R S_J$ Biaxial Woven	104.67	104.31	[171.83]	105.00		104.66	0.28	0.27	133.44
WGG3	$S_R W_J$ Biaxial Woven	50.40	48.62	[28.65]	49.46		49.49	0.73	1.47	211.73
KGG1	$S_R W_J$ Biaxial Woven	29.89	29.89	29.89	28.47		29.54	0.62	2.09	90.30

Cell background color key:

Green: Junction meets minimum Holtz et al. (2008) requirement

Pink: Junction does not meet minimum Holtz et al. (2008) requirement

[---] Outlier value

NP Not provided by the manufacturer

CHAPTER FIVE

DETERMINATION OF RIB STRENGTH PROPERTIES

Several preliminary tensile strength tests were carried out on selected geogrids according to the ASTM D6637 test protocol. However, the existing clamping mechanism for single rib specimens was found to be problematic; either the specimens would pull out of the clamps or the measured tensile strength values for different specimens were not consistent. Therefore, new clamps were fabricated to improve the test results as described in the following sections.

The new clamps were successfully tried on both ODOT Type-1 and Type-2 geogrids. Afterwards, these clamps were used to carry out a total of 80 in-isolation rib strength tests to determine the 2%-strain, 5%-strain and ultimate tensile strength values of the geogrids listed in **Table 3.2** in both machine (MD) and cross-machine (XD) directions. Five tests were carried out in MD and five in XD for each geogrid products.

5.1. Fabrication of Rib Strength Testing Clamps for EGG

Two 102 mm × 102 mm × 6 mm steel plates were fabricated as rib strength test clamps. In order to grip the geogrid ribs properly, a clamping system was developed that utilized frictional and interlocking forces using two layers of sandpapers mounted on the inside edges of each clamp. A piece of No. 100 wood sandpaper was fixed on the

edge of the clamp using superglue as a permanent frictional layer as shown in **Figure 5.1**. A 25 mm × 25 mm piece of sandpaper was placed on the middle of each fixed sandpaper layer as a disposable pad. These pieces were replaced after each test because they would lose their roughness during testing.



Figure 5.1. Rib strength test clamp for extruded geogrids and accessories

Specimen preparation steps for rib strength tests of geogrids are discussed below:

1. A piece of geogrid was cut according to ASTM D6637 test standard (each specimen should consist of 3 junctions or 300 mm long). Then, the initial length of the geogrid specimen was measured and its junctions were marked using a white marker.

2. The two clamps were aligned as shown in **Figure 5.2(a)**. The test specimen and additional dummy (spacer) pieces of geogrid were placed on the clamps at equal distances from the center of the bolts as shown in **Figure 5.2(b)**. Spacer pieces of

geogrid were used to keep the clamp plates parallel to each other which would help increase the grip of the clamp on the specimen during the application of tensile load.

3. Two additional small pieces (25 mm × 25 mm) of sandpaper were placed on the specimen inside the clamp. Clamp bolts were inserted into the holes. During the assembly of the clamps, each nut was uniformly tightened one turn at a time until the geogrid was completely secured in the clamps [Figure 5.3(a)].

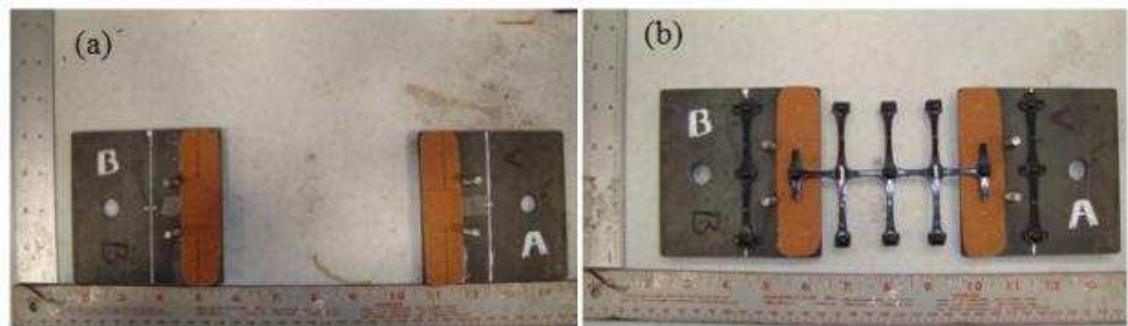


Figure 5.2. (a) Sandpapers mounted on test clamps (b) alignment of test specimen and spacer pieces on clamps

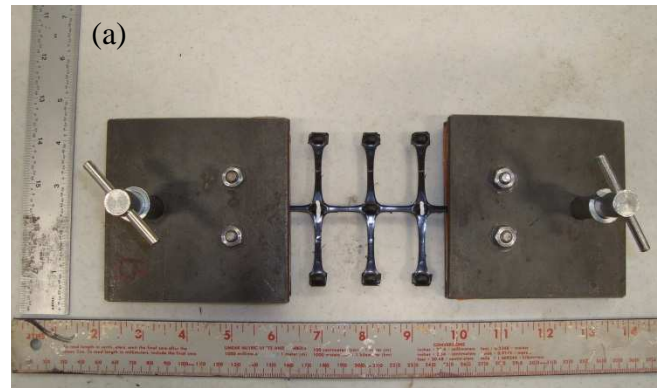


Figure 5.3. (a) Geogrid specimen secured in the clamps, (b) test setup mounted on the tension frame, (c) view from digital camera, ready to record the specimen deformation

4. The clamps and specimen assembly were carefully transported to and mounted on the testing frame as shown in **Figure 5.3(b)**. A digital camera was set up to record the specimen deformation during the test. The view frame of the camera was zoomed on the specimen such that the size of the specimen image was as large as

possible and yet, the two white marks on the specimen [**Figure 5.3(c)**] remained within the viewing range during the entire test until specimen failed.

5. The digital camera, the electric motor attached to the moving clamp and the data acquisition system were started simultaneously. The test continued until the specimen failed. This new clamping system was found to significantly improve the test success rate for extruded geogrids that offer very low surface friction.

6. The ASTM D6637 test protocol recommends placing three junctions across the width of the geogrid specimen inside the clamp. However, it was observed that placing three junctions in the clamped area prevented adequate pressure concentration on the middle junction, which resulted in increased risk of the test rib sliding out of the clamps. The new procedure followed in this study requires the placement of only one junction in a highly frictional clamped area which proved to be very effective in securing the specimen in its place throughout the test.

7. In all rib strength tests performed on the EGG1 specimens in the machine direction (MD), the specimens failed at the locations of mid-span junctions [**Figure 5.4(a)**], and the test was unable to capture the failure of the ribs. It was concluded that the ribs in machine direction are stronger than the junctions. This is explained by the fact that extruded geogrids such as EGG1 are manufactured using a punching and drawing technique. The ribs are stretched parts of a perforated polymer sheet during the manufacturing process, which in contrast to the junctions, experience strain hardening. As a result, the ribs become stronger than the junctions. These observations were

discussed with Tensar representatives and they acknowledged that failure of the mid-span junctions may likely occur while testing the rib samples. Nevertheless, the failure load recorded regardless of the location of the rupture in the mid-span is typically reported as the rib strength value. It therefore appears that using two aperture size-long specimens in the rib strength tests according to the ASTM D6637 test procedure makes it very difficult to measure the rib strength without rupturing the junction.

8. In order to investigate the influence of specimen size on junction failure as stated above and to eliminate any possible boundary effects (i.e. proximity of the failed junction to the clamps), samples with five aperture size length were tested. It was observed that the specimens still failed at their mid-span junction as shown in **Figure 5.4(b)**. This observation confirmed that the reason for junction failure in rib strength tests was indeed due to weaker junctions as compared to the ribs regardless of the specimen size. It also confirmed that the clamping system was robust and consistently resulted in failure at the specimen mid-span as opposed to a location near the clamps. The specimens tested in the cross-machine direction (XD) all failed at the connection between the ribs and junctions [**Figure 5.4(c)**].

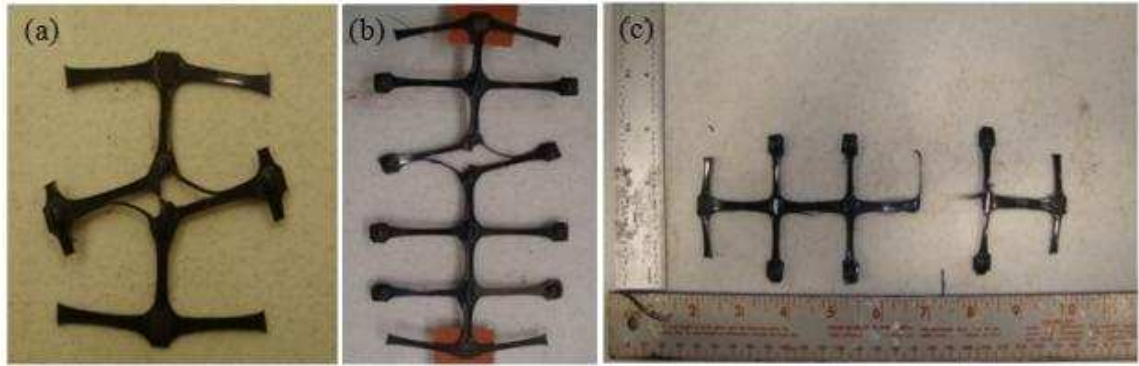


Figure 5.4. (a) and (b) Two- and five-aperture-size-long specimens which failed at their junctions in rib strength tests, (c) specimen failed in cross-machine direction

In addition to conventional biaxial geogrids, recently introduced triaxial products (EGG3 and EGG4) by Tensar were investigated. Currently, there are no standard test protocols for sample preparation, clamping requirements and in-isolation testing of triaxial products. ASTM D6637 test standard was largely followed for this purpose, which was originally developed for uniaxial and biaxial geogrids. **Figure 5.5** shows the geogrid samples prepared for the rib test according to ASTM D6637. **Figure 5.6** and **Figure 5.7** show the rib test setup for the EGG3 and EGG4 geogrids respectively, before and after failure.

In the case of EGG3 and EGG4 products, rib strength tests were carried out in the directions along the diagonal (MD) and transverse (XD) ribs. After comparing the measured results and the test data supplied by Tensar with the criteria given in **Figure 3.5**, both the EGG3 and EGG4 geogrids were classified in the strong rib and strong junction category.

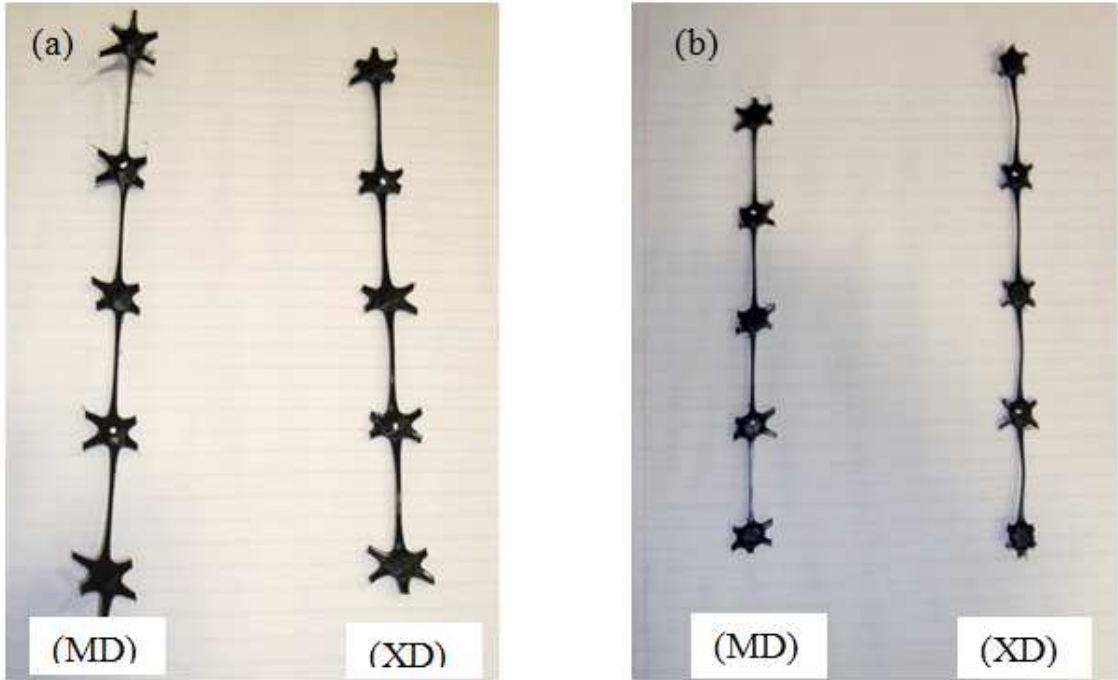


Figure 5.5. Geogrid specimens for rib strength tests (a) EGG3, (b) EGG4

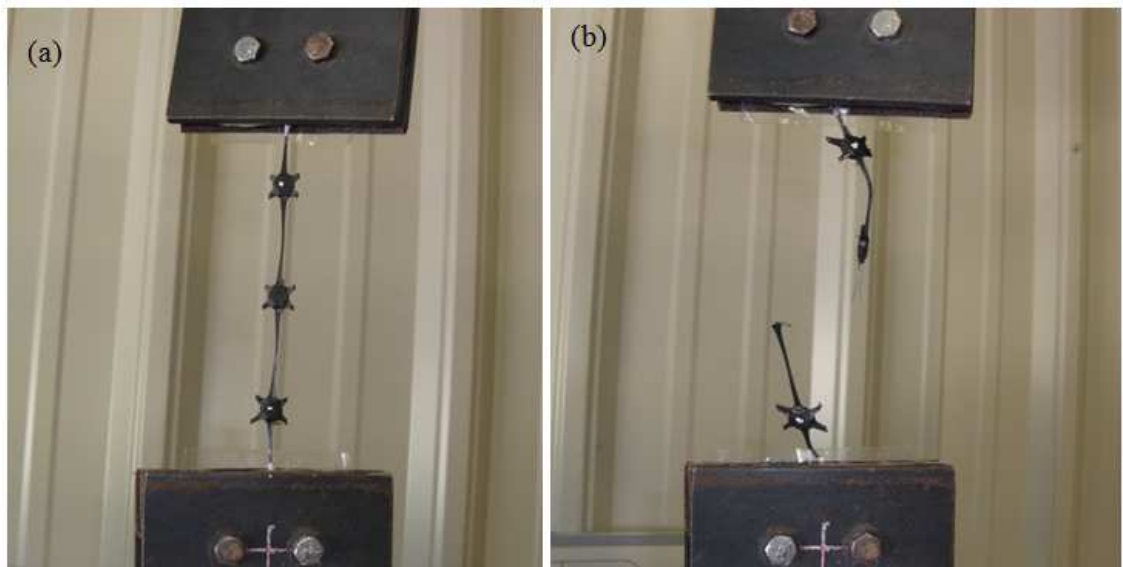


Figure 5.6. EGG3 geogrid sample for rib strength tests (a) before test, (b) after failure

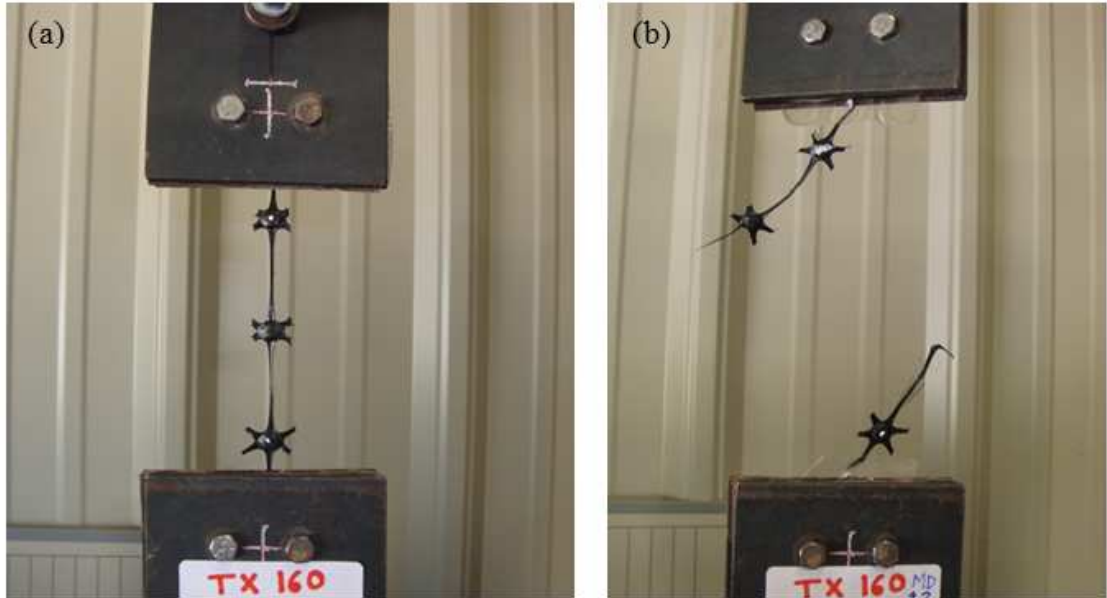


Figure 5.7. EGG4 geogrid sample for rib strength tests (a) before test, (b) after failure

5.2. Fabrication of Rib Strength Testing Clamps for NEGG

When PVC-coated polyester (PET) geogrids were tested using the above test setup, it was observed that in some specimens polyester yarns were pulled out of the PVC coating leaving a piece of the coating in the clamp. Based on this observation, a new clamping system was developed for non-extruded geogrids as shown in **Figure 5.8** and **Figure 5.9**. These clamps helped mitigate stress concentrations at the geogrid-clamp connections and therefore, prevented immature failure of the specimen. This type of clamp is comparable to Capstan clamps and roller grips discussed in the ASTM D4595 test protocol (ASTM 2009).



Figure 5.8. Clamping system fabricated to test non-extruded geogrids



Figure 5.9. Rib strength testing of non-extruded geogrid in progress

5.3. Rib Strength Test Results

Load-strain rib tensile strength test results for the geogrids listed in **Table 3.2** are shown in **Figure 5.10** through **Figure 5.17**.

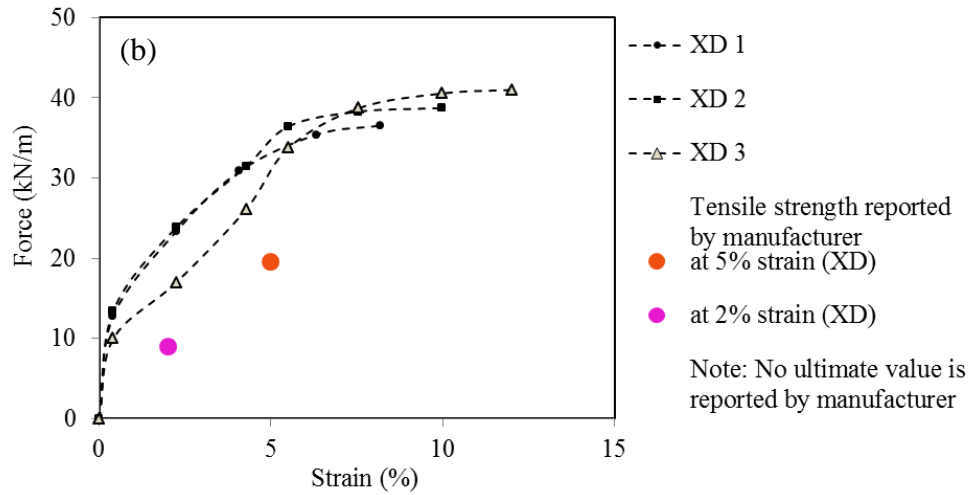
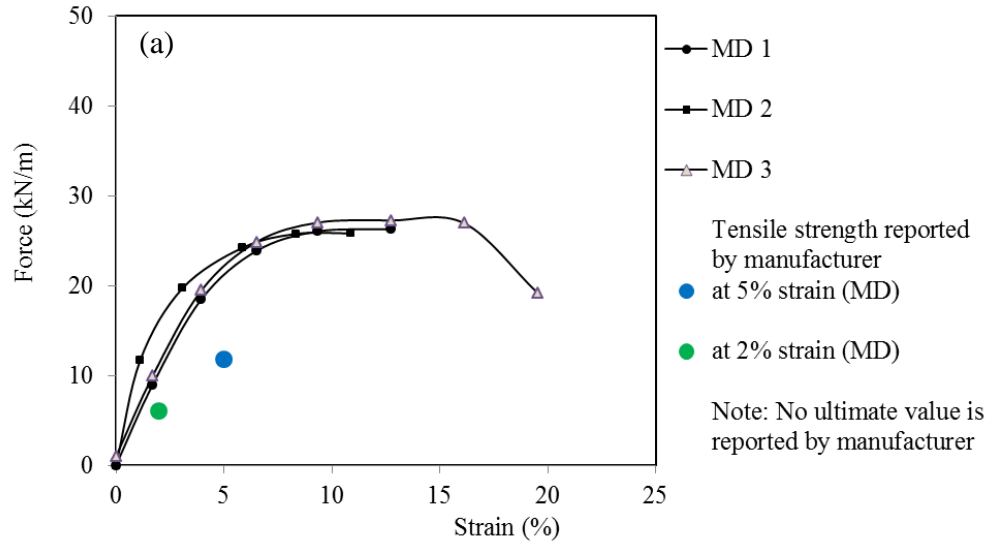


Figure 5.10. Tensile strength test results for EGG1 geogrid specimens (a) MD, (b) XD

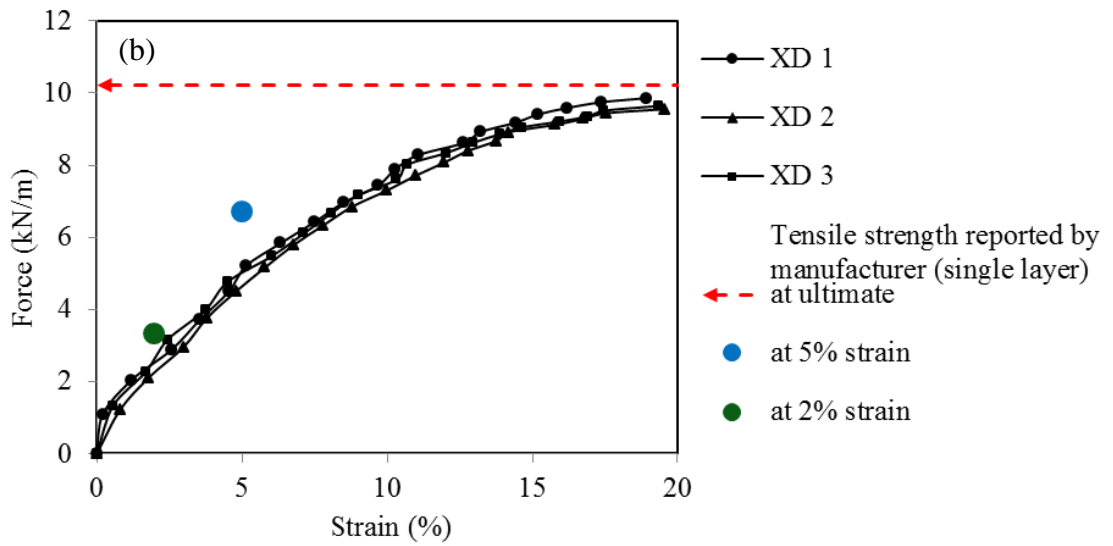
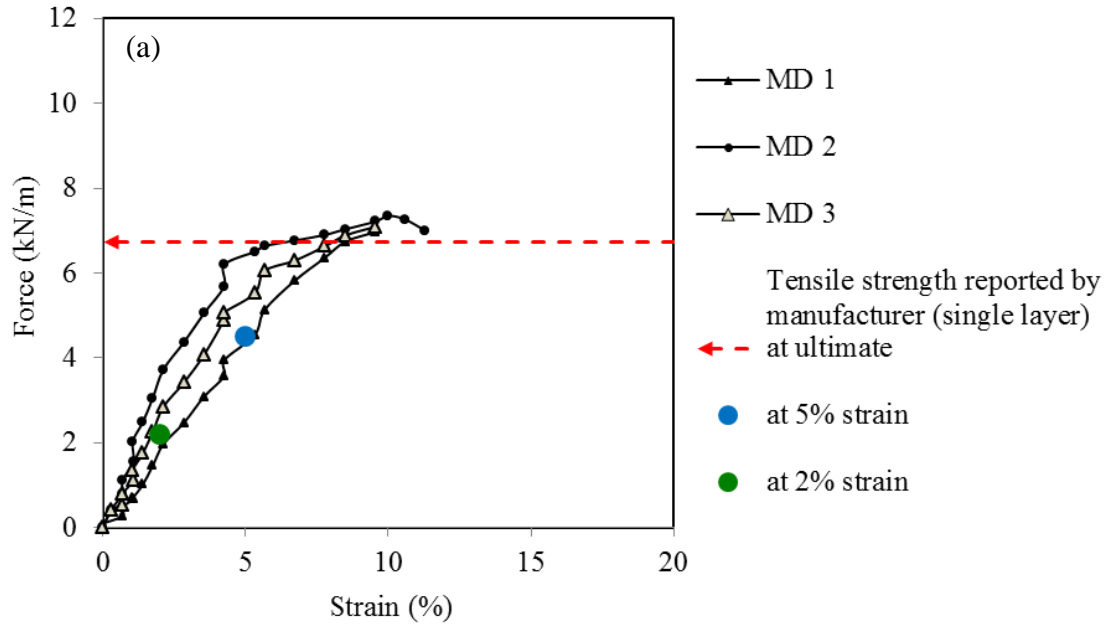


Figure 5.11. Tensile strength test results for EGG2 (single layer) geogrid specimens (a) MD, (b) XD

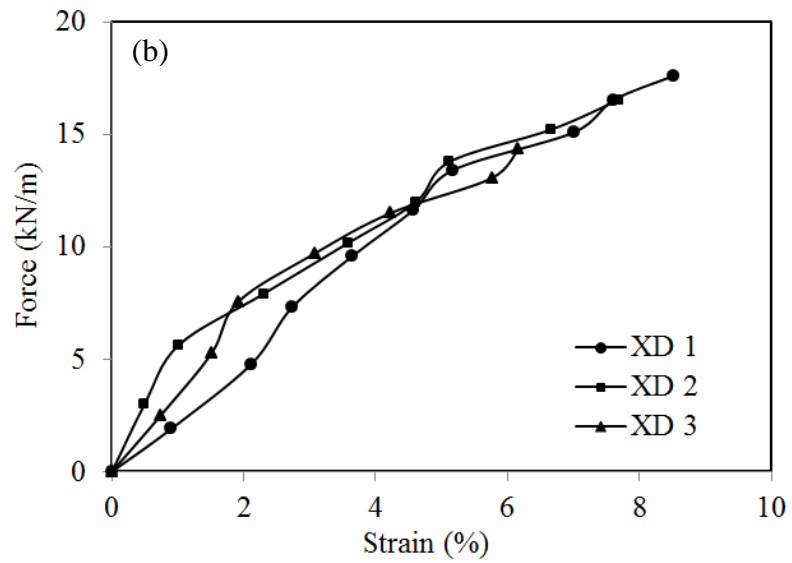
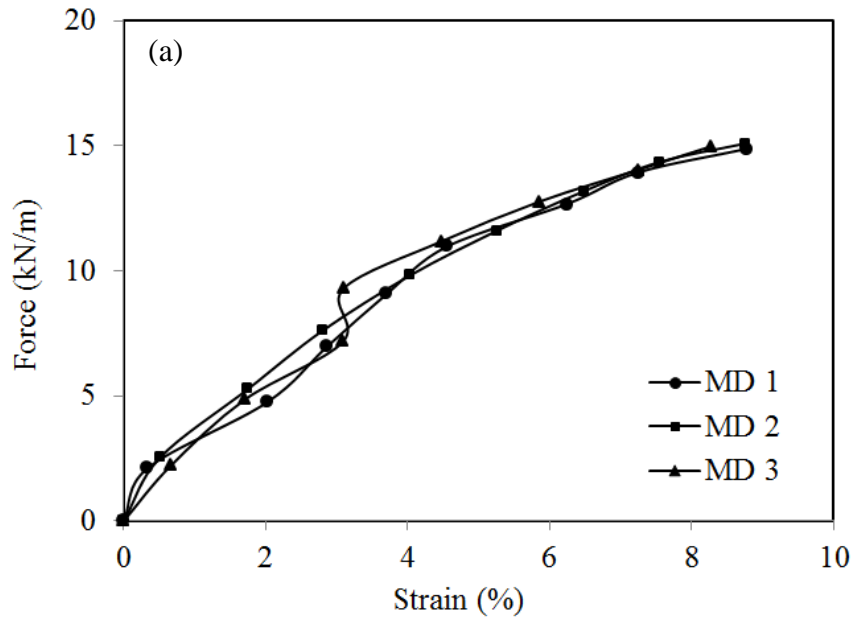


Figure 5.12. Tensile strength test results for EGG3 geogrid specimens (a) MD (30° from MD), (b) XD

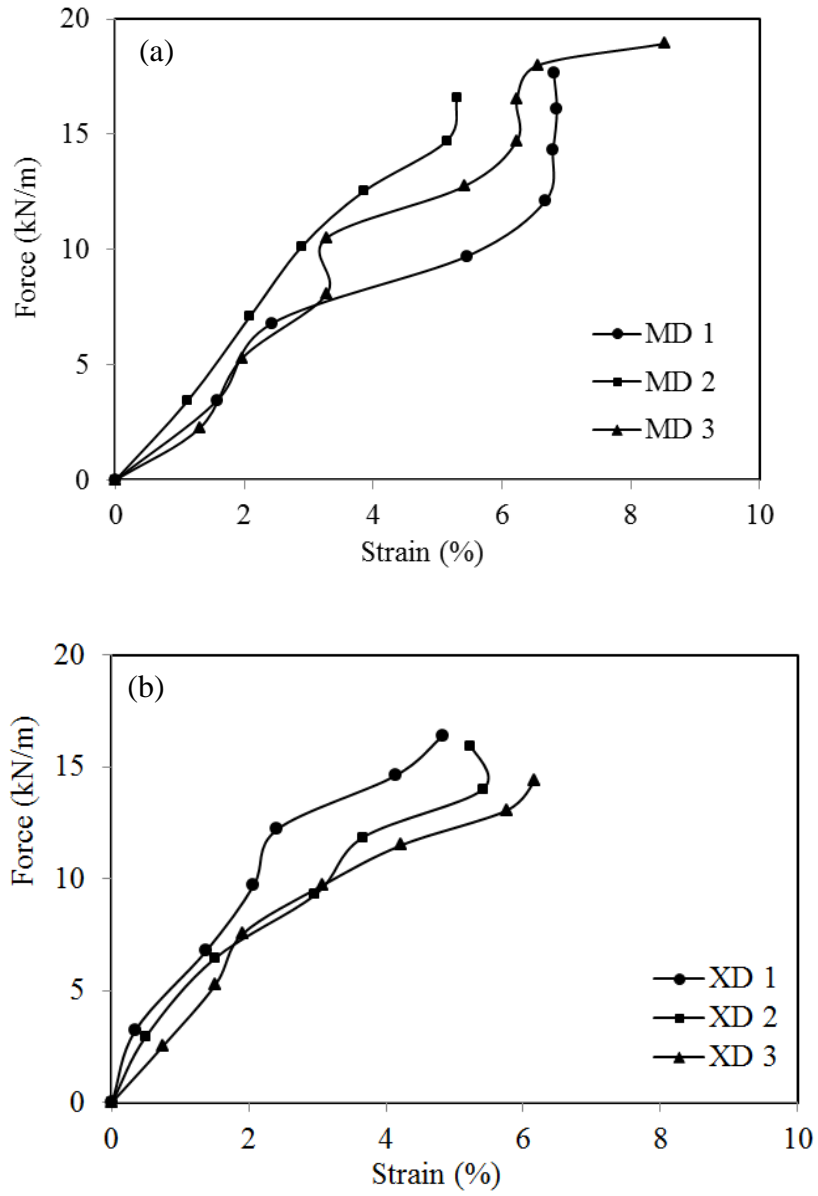


Figure 5.13. Tensile strength test results for EGG4 geogrid specimens (a) MD (30° from MD), (b) XD

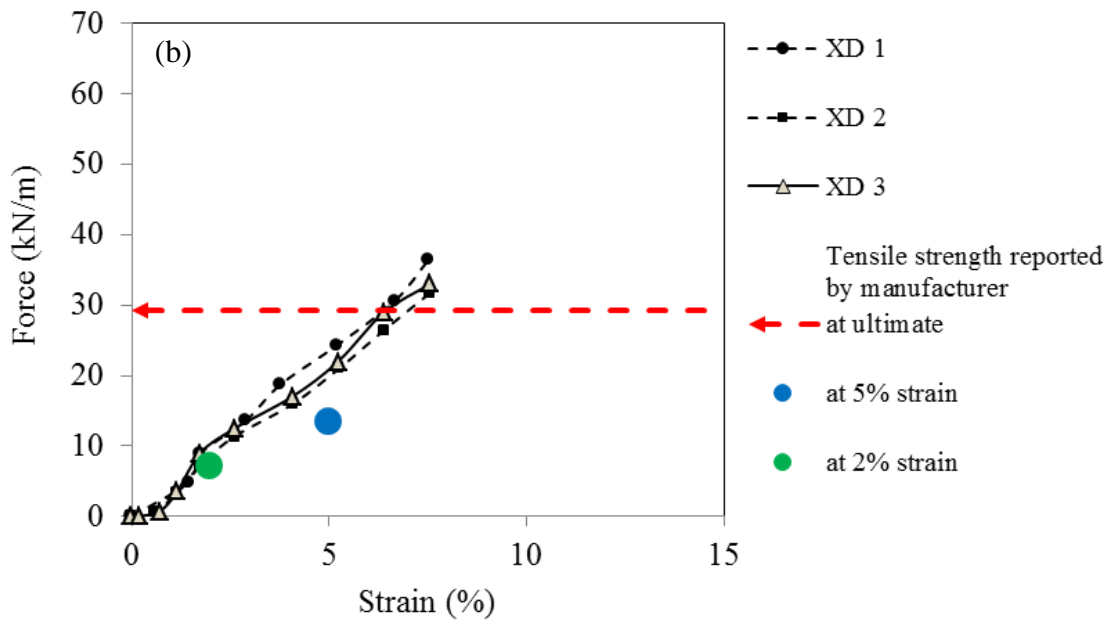
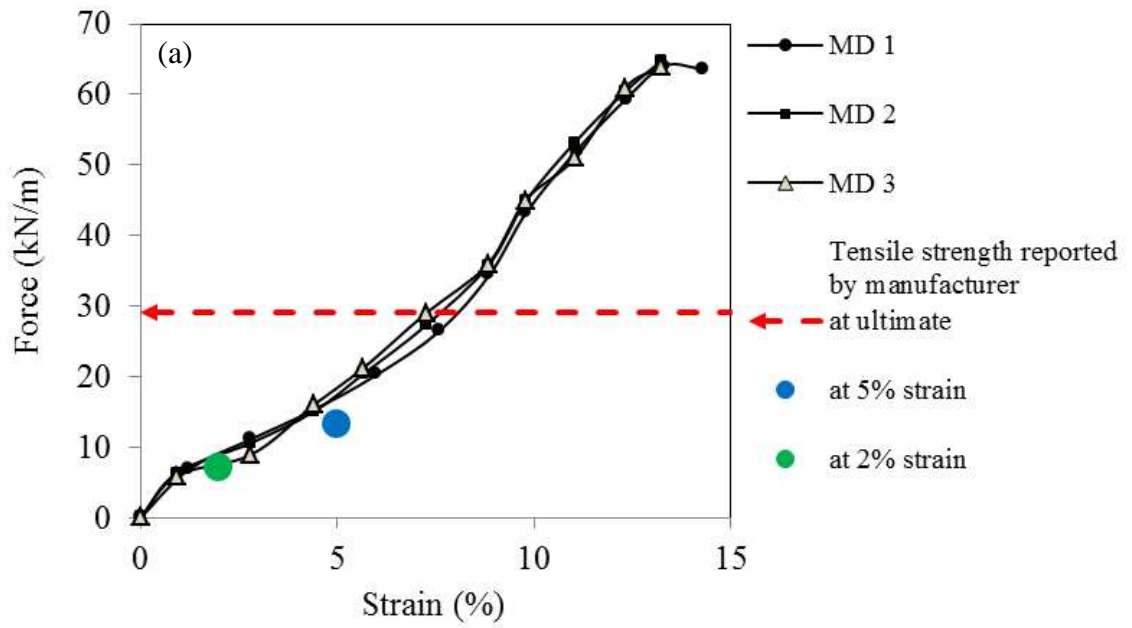


Figure 5.14. Tensile strength test results for WGG1 geogrid specimens (a) MD, (b) XD

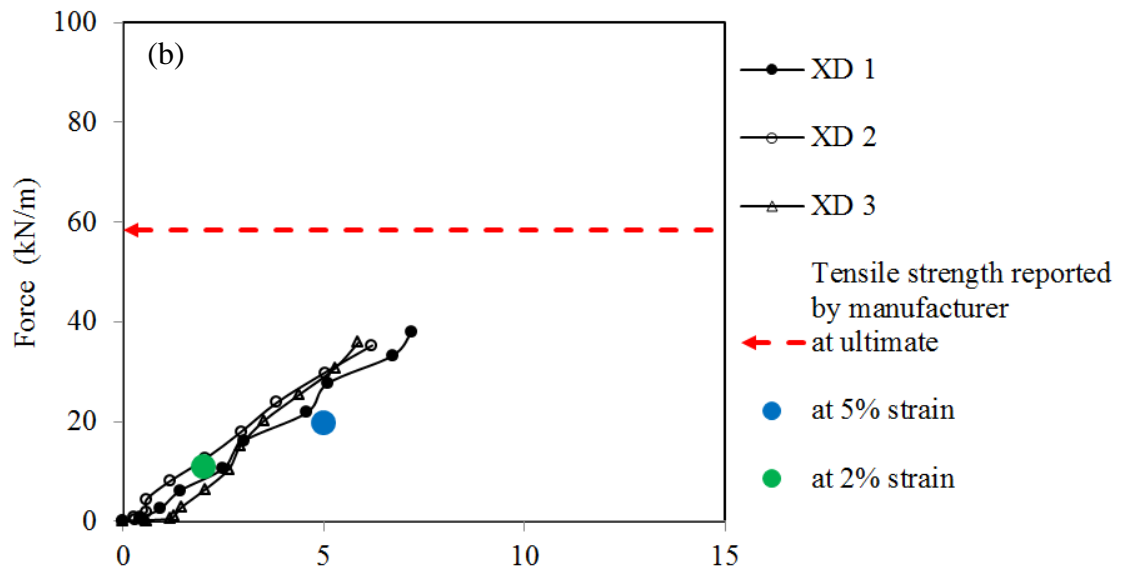
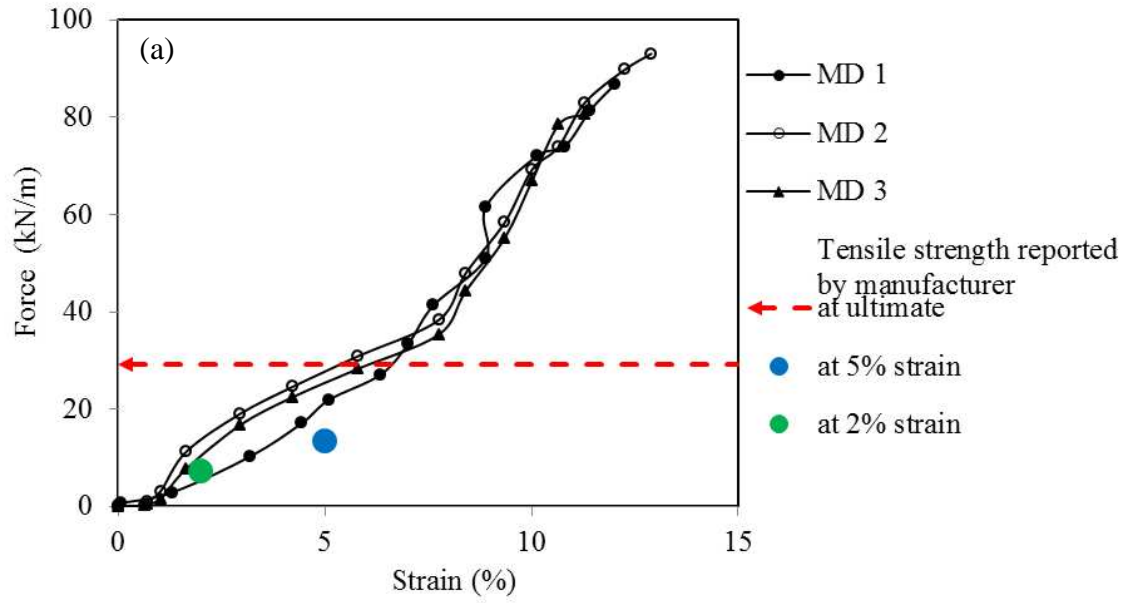


Figure 5.15. Tensile strength test results for WGG2 geogrid specimens (a) MD, (b) XD

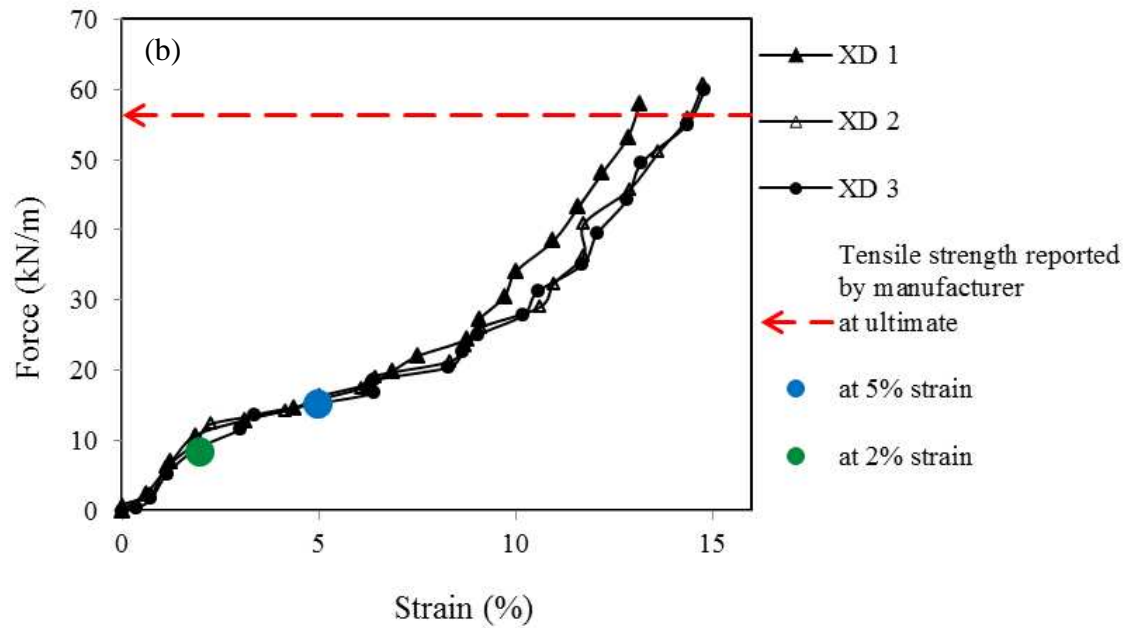
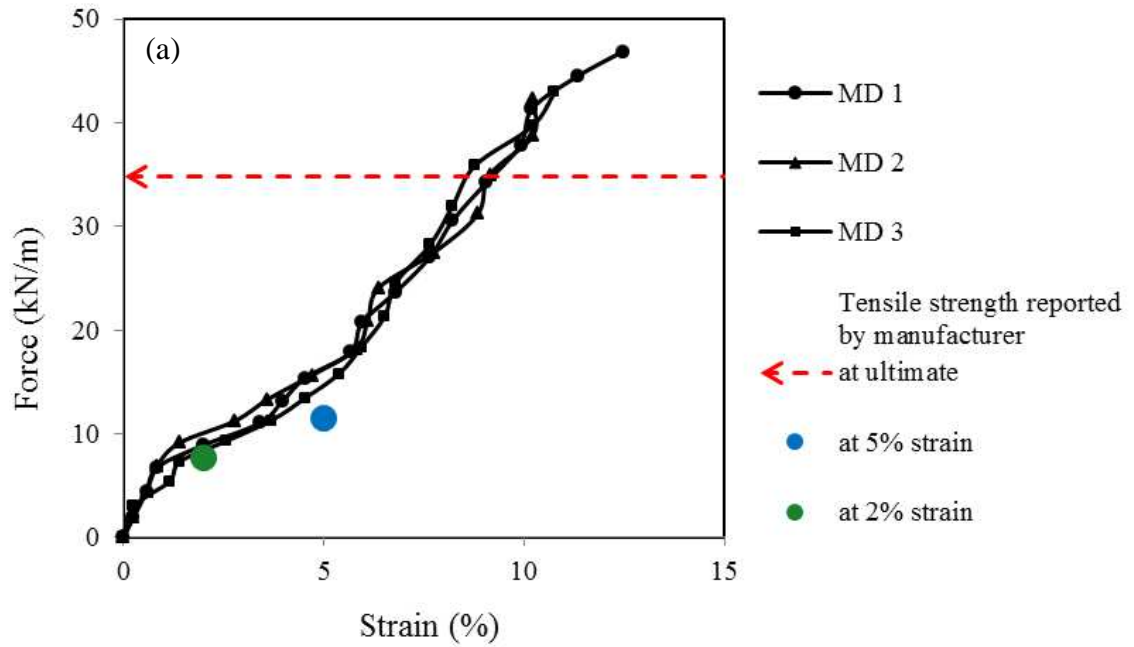


Figure 5.16. Tensile strength test results for WGG3 geogrid specimens (a) MD, (b) XD

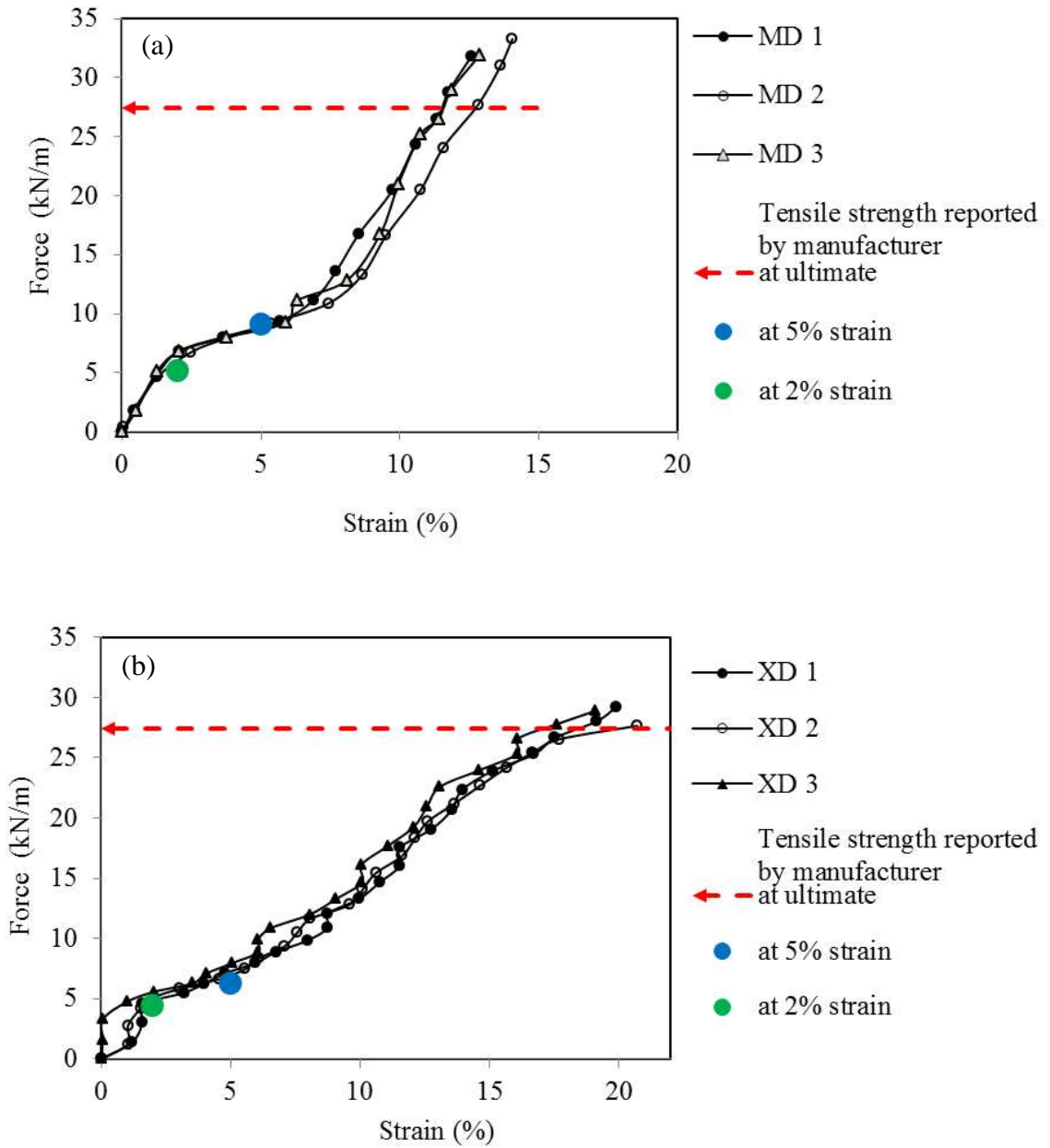


Figure 5.17. Tensile strength test results for KGG1 geogrid specimens (a) MD, (b) XD

Rib tensile strength values at 2% strain in MD and XD are summarized in **Table 5.1** and **Table 5.2**, respectively. In **Table 5.1**, the 2% rib strength values of the extruded biaxial geogrids (i.e. EGG1, WGG1, WGG2 and EB2) from this study are slightly higher than the MARV (Minimum Average Roll Value) values reported by the corresponding manufacturers. This is not unexpected because the MARV values theoretically represent two standard deviations below the mean value of a large population of samples with an assumed bell-curve distribution (e.g. Koerner 2005). The FHWA guidelines (Holtz et al. 2008) also stipulate that the test results from any sampled roll in a lot should meet or exceed the minimum values reported by the manufacturers. The overall summary of the rib strength test results for all geogrids tested are given in **Table 5.1** through **Table 5.6**.

Table 5.1. Summary of rib tensile strength values at 2% strain in MD

Geogrid	Type	2% Rib Strength in Machine Direction (kN/m)						
		MD 1	MD 2	MD 3	Mean (μ)	Standard Deviation (σ)	Coefficient of Variation, COV (%)	MARV value from manufacturer
EGG1	S _R S _J Biaxial Extruded	10.2	16.0	11.0	12.4	2.6	20.7	6.0
EGG2 (single layer)	W _R S _J Biaxial Extruded	1.8	3.5	2.5	2.6	0.7	26.3	2.2
EGG3	S _R S _J Triaxial Extruded	4.9	5.2	5.8	5.3	0.4	7.1	NP
EGG4	S _R S _J Triaxial Extruded	7.0	5.0	5.5	5.8	0.8	14.6	NP
WGG1	S _R S _J Biaxial Woven	9.0	9.0	8.7	8.9	0.1	1.6	7.3
WGG2	S _R S _J Biaxial Woven	[19]	14.0	10.0	12.0	2.0	16.7	7.3
WGG3	S _R W _J Biaxial woven	9.0	10.0	8.5	9.2	0.6	6.8	7.7
KGG1	S _R W _J Biaxial Knitted	6.0	7.0	7.0	6.7	0.5	7.1	5.1

Notes:

S_RS_J: Strong Rib Strong Junction

S_RW_J: Strong Rib Weak Junction

W_RS_J: Weak Rib Strong Junction

NP: Not provided by the manufacturer

[---] Outlier value

Table 5.2. Summary of rib tensile strength values at 2% strain in XD

Geogrid	Type	2% Rib Strength in Cross-Machine Direction (kN/m)							
		XD 1	XD 2	XD 3	XD 4	Mean (μ)	Standard Deviation (σ)	Coefficient of Variation, COV (%)	MARV value from manufacturer
EGG1	$S_R S_J$ Biaxial Extruded	22.0	22.2	16.0		20.1	2.9	14.3	9.0
EGG2 (single layer)	$W_R S_J$ Biaxial Extruded	2.6	2.2	2.6		2.5	0.2	7.0	3.3
EGG3	$S_R S_J$ Triaxial Extruded	4.5	7.3	7.7		6.5	1.4	21.9	NP
EGG4	$S_R S_J$ Triaxial Extruded	7.5	7.5	9.2		8.1	0.8	9.9	NP
WGG1	$S_R S_J$ Biaxial Woven	9.0	10.0	10.0		9.7	0.5	4.9	7.3
WGG2	$S_R S_J$ Biaxial Woven	12.0	8.0	6.0	[3]	8.7	2.5	28.8	10.9
WGG3	$S_R W_J$ Biaxial woven	11.0	11.0	13.0		11.7	0.9	8.1	8.4
KGG1	$S_R W_J$ Biaxial Woven	5.5	5.5	5.5	5.5	5.5	0.0	0.1	4.4

Notes:

$S_R S_J$: Strong Rib Strong Junction

$S_R W_J$: Strong Rib Weak Junction

$W_R S_J$: Weak Rib Strong Junction

NP: Not provided by the manufacturer

[---] Outlier value

Table 5.3. Summary of rib tensile strength values at 5% strain in MD

Geogrid	Type	5% Rib Strength in Machine Direction (kN/m)						
		MD 1	MD 2	MD 3	Mean (μ)	Standard Deviation (σ)	Coefficient of Variation, COV (%)	MARV value from manufacturer
EGG1	$S_R S_J$ Biaxial Extruded	21.3	23.2	24.0	22.8	1.1	5.0	11.8
EGG2 (single layer)	$W_R S_J$ Biaxial Extruded	4.4	6.4	5.3	5.4	0.8	15.2	4.5
EGG3	$S_R S_J$ Triaxial Extruded	11.2	11.5	11.8	11.5	0.2	2.1	NP
EGG4	$S_R S_J$ Triaxial Extruded	9.0	12.0	14.5	11.8	2.2	19.0	NP
WGG1	$S_R S_J$ Biaxial Woven	17.0	18.0	18.0	17.7	0.5	2.7	13.4
WGG2	$S_R S_J$ Biaxial Woven	[34]	28.0	26.0	27.0	1.0	3.7	13.4
WGG3	$S_R W_J$ Biaxial woven	14.8	16.2	16.2	15.7	0.7	4.2	11.5
KGG1	$S_R W_J$ Biaxial Woven	9.0	9.1	9.0	9.0	0.0	0.5	9.1

Notes:

$S_R S_J$: Strong Rib Strong Junction

$S_R W_J$: Strong Rib Weak Junction

$W_R S_J$: Weak Rib Strong Junction

NP: Not provided by the manufacturer

[---] Outlier value

Table 5.4. Summary of rib tensile strength values at 5% strain in XD

Geogrid	Type	5% Rib Strength in Cross-Machine Direction (kN/m)							
		XD 1	XD 2	XD 3	XD 4	Mean (μ)	Standard Deviation (σ)	Coefficient of Variation, COV (%)	MARV value from manufacturer
EGG1	$S_R S_J$ Biaxial Extruded	33.2	35.2	30.0		32.8	2.1	6.5	19.6
EGG2 (single layer)	$W_R S_J$ Biaxial Extruded	5.2	4.6	5.0		4.9	0.2	5.1	6.7
EGG3	$S_R S_J$ Triaxial Extruded	12.0	13.0	13.5		12.8	0.6	4.9	NP
EGG4	$S_R S_J$ Triaxial Extruded	12.0	13.5	16.5		14.0	1.9	13.4	NP
WGG1	$S_R S_J$ Biaxial Woven	23.8	20.0	22.0		21.9	1.6	7.1	13.4
WGG2	$S_R S_J$ Biaxial Woven	27.0	28.0	30.0	30.0	28.8	1.3	4.5	13.7
WGG3	$S_R W_J$ Biaxial Woven	15.8	15.9	16.0		15.9	0.1	0.5	15.2
KGG1	$S_R W_J$ Biaxial Woven	7.5	7.0	8.0	7.7	7.6	0.4	4.8	6.2

Notes:

$S_R S_J$: Strong Rib Strong Junction

$S_R W_J$: Strong Rib Weak Junction

$W_R S_J$: Weak Rib Strong Junction

NP: Not provided by the manufacturer

Table 5.5. Summary of ultimate rib tensile strength values in MD

Geogrid	Type	Ultimate Rib Strength in Machine Direction (kN/m)						
		MD 1	MD 2	MD 3	Mean (μ)	Standard Deviation (σ)	Coefficient of Variation, COV (%)	MARV value from manufacturer
EGG1	$S_R S_J$ Biaxial Extruded	26.3	25.8	27.0	26.4	0.5	1.9	NP
EGG2 (single layer)	$W_R S_J$ Biaxial Extruded	7.0	7.3	6.0	6.8	0.6	8.3	6.7
EGG3	$S_R S_J$ Triaxial Extruded	15.0	15.0	15.1	15.0	0.0	0.3	NP
EGG4	$S_R S_J$ Triaxial Extruded	17.0	18.0	19.0	18.0	0.8	4.5	NP
WGG1	$S_R S_J$ Biaxial Woven	64.0	64.9	63.0	64.0	0.8	1.2	29.2
WGG2	$S_R S_J$ Biaxial Woven	36.7	42.0	30.6	36.4	4.6	12.7	29.2
WGG3	$S_R W_J$ Biaxial woven	46.9	42.3	43.0	44.0	2.0	4.6	34.9
KGG1	$S_R W_J$ Biaxial Woven	32.0	33.0	30.0	31.7	1.2	3.9	27.4

Notes:

$S_R S_J$: Strong Rib Strong Junction

$S_R W_J$: Strong Rib Weak Junction

$W_R S_J$: Weak Rib Strong Junction

NP: Not provided by the manufacturer

Table 5.6. Summary of ultimate rib tensile strength values in XD

Geogrid	Type	Ultimate Rib Strength in Cross-Machine Direction (kN/m)							
		XD 1	XD 2	XD 3	XD 4	Mean (μ)	Standard Deviation (σ)	Coefficient of Variation, COV (%)	MARV value from manufacturer
EGG1	$S_R S_J$ Biaxial Extruded	36.6	38.7	40.0		38.4	1.4	3.7	NP
EGG2 (single layer)	$W_R S_J$ Biaxial Extruded	9.9	9.6	9.6		9.7	0.1	1.3	10.3
EGG3	$S_R S_J$ Triaxial Extruded	14.0	16.5	17.5		16.0	1.5	9.2	NP
EGG4	$S_R S_J$ Triaxial Extruded	14.0	16.0	16.5		15.5	1.1	7.0	NP
WGG1	$S_R S_J$ Biaxial Woven	36.4	31.7	28.0		32.1	3.4	10.7	29.2
WGG2	$S_R S_J$ Biaxial Woven	45.0	35.3	38.1	41.0	39.8	3.6	9.1	58.4
WGG3	$S_R W_J$ Biaxial woven	58.0	60.9	59.9		59.6	1.2	2.0	56.5
KGG1	$S_R W_J$ Biaxial Woven	27.6	29.6	28.0	28.0	28.3	0.8	2.7	27.4

Notes:

$S_R S_J$: Strong Rib Strong Junction

$S_R W_J$: Strong Rib Weak Junction

$W_R S_J$: Weak Rib Strong Junction

NP: Not provided by the manufacturer

CHAPTER SIX

LABORATORY TESTING OF SAND AND AGGREGATE

6.1. Gradation Analysis

ODOT Type-A aggregate was purchased from Dolese's quarry in Oklahoma City and transported to the Fears laboratory at OU (University of Oklahoma). Type-A aggregate is the most commonly used type of aggregate in ODOT projects. Sieve tests were performed on the aggregate at the OU Broce Laboratory according to the ASTM C136-06 test standard (**Figure 6.1**).



Figure 6.1. Sieve analysis equipment at the OU Broce Laboratory

Two representative gradation curves from the sieve analyses are shown in **Figure 6.2**. It is observed that gradation curves from the two trials are reasonably close to each other and both fall within the upper and lower limits of the range defining ODOT Type-A aggregates (ODOT 2009). These aggregates were used in the pullout and plate load tests carried out in this study. The sieve analysis of aggregate was repeated after every four pullout and plate load tests to ensure that their gradation curve fell within the upper and lower limits of the ODOT Type-A aggregate. If that was not the case, the aggregates were discarded and new aggregates were used for the following tests.

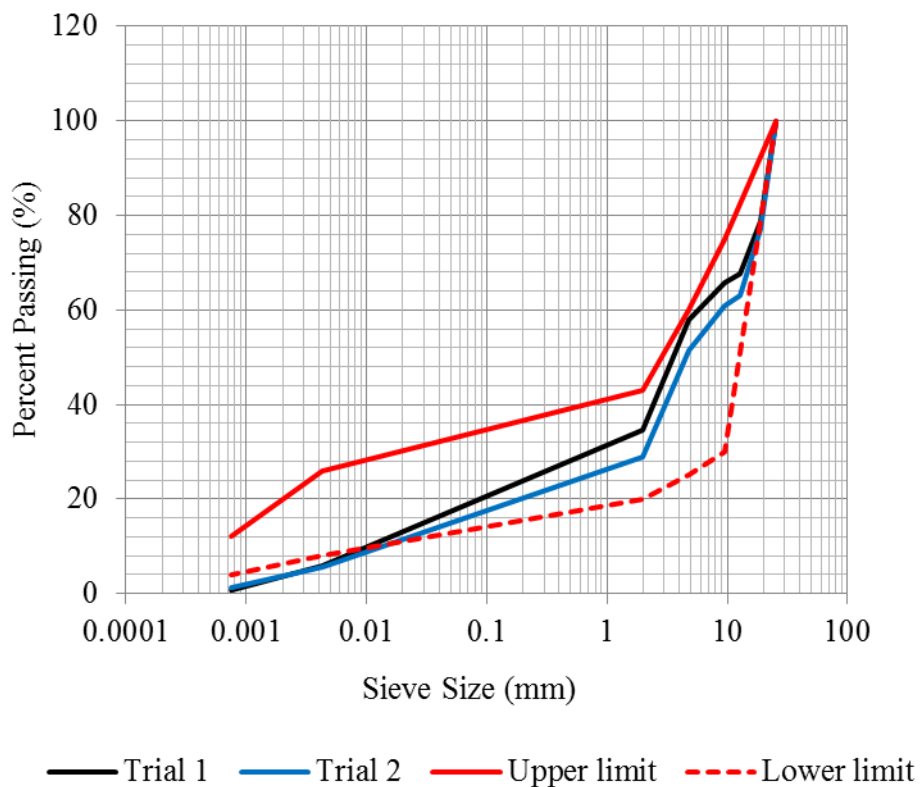


Figure 6.2. Gradation curves for the ODOT Type-A aggregates used in this study

6.2. Durability Analysis

A series of LA (Los Angeles) abrasion tests were carried out on ODOT Type-A aggregates as per the ASTM C131-06 test standard to determine their durability (**Figure 6.3**). This test has been widely used as an indicator of the relative quality of various sources of aggregate having similar mineral compositions. This test also measures the degradation of aggregate minerals due to loading over a project service life. A rotational grinding drum that contained 11 steel balls was used and underwent 500 revolutions to perform the LA abrasion tests. Aggregates were washed and their dry weight was measured after 24 hours. The amount of aggregate weight loss was used to determine the LA abrasion values (**Table 6.1**).



Figure 6.3. Los Angeles (LA) abrasion tests

Table 6.1. LA abrasion test results for ODOT Type-A aggregate

Aggregate Type	Grading Type ¹	% of Loss	% Max Allowable Loss ²
ODOT Type-A (ODOT Specification)	B	20	50
ODOT Type-A (This Study)	B	21	50

Notes:

¹ Type B grading in ASTM C131-01 test standard requires the use of eleven (11) steel balls. Each load of aggregate for testing should have a mass of 4584 ± 15 grams.

² Maximum allowable loss according to ODOT requirements for base aggregates (ODOT 2009, Specification 703.01 C).

6.3. Small-Scale Direct Shear Tests (DST) on Sand

6.3.1. Material Properties and Test Setup

Three small-scale direct shear tests (DST) were carried out on the subgrade sand which was collected from ‘Dover Sand Plant’ located in Dover, Oklahoma. The sand called “Washed Dover Sand” met the ASTM C33 specifications for concrete mix. The DST tests were carried out to determine the shear strength parameters of the subgrade sand used in the cyclic plate load tests (**Sections 9.1** and **9.2**). The moisture content and unit weight of the sand in the DST were 0.2% and 16.25 kN/m^3 , respectively. Wang (2009) reported the minimum and maximum dry unit weights of this sand to be equal to 10.98 kN/m^3 and 16.61 kN/m^3 , respectively. Hence, the relative density of the sand used

in the DST was 95.7%. The unit weight and relative density of the sand for final cyclic plate load tests were also 16.25 kN/m^3 and 95.7%, respectively.

The size of the test cell in the small-scale DST was $60 \text{ mm} \times 60 \text{ mm}$. A porous stone was placed at the bottom of the test cell which was covered with the sand that was placed and compacted in three lifts (**Figure 6.4**). The sand was compacted by a combination of vibration (e.g. tapping the test cell gently against the table) and manual compaction (using a tamping rod). The porous stone and top cap were then placed on the top of the compacted sand.



Figure 6.4. Dover sand in the test cell of the small-scale DST machine

The desired overburden pressure on the sand specimen was applied by placing weights on a hanging platform attached to a lever arm that applied a vertical load on the

specimen through an aluminum cap. The tests were carried out until the measured shear stress in the soil became practically constant. **Figure 6.5** shows a final test setup.



Figure 6.5. Final setup of the test cell the DST machine

6.3.2. Direct Shear Test Results

Small-scale direct shear test results for the subgrade sand at $\gamma = 16.25 \text{ kN/m}^3$ are presented in **Figure 6.6** through **Figure 6.9**. From **Figure 6.9**, the peak friction angle of the sand was determined as 46 degrees.

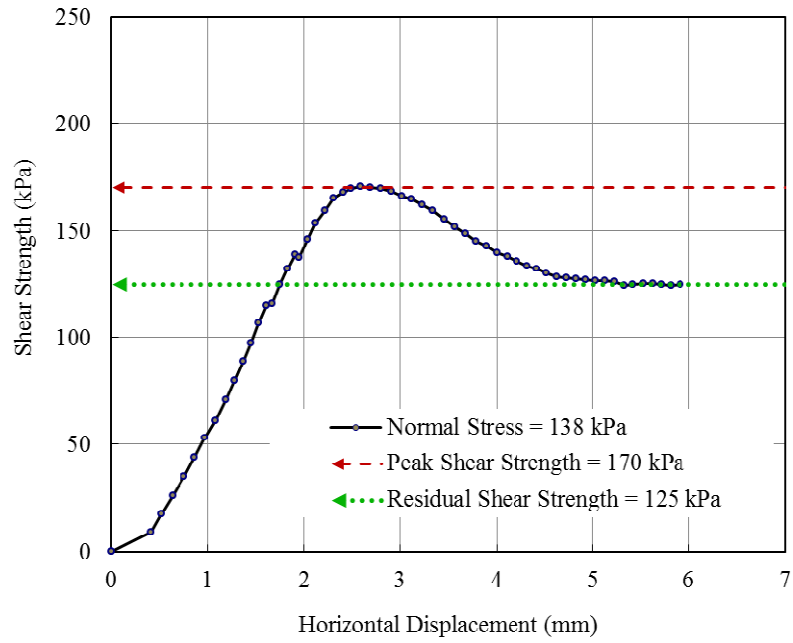


Figure 6.6. Small-scale test results on the subgrade sand at 138 kPa overburden pressure ($\gamma = 16.25 \text{ kN/m}^3$)

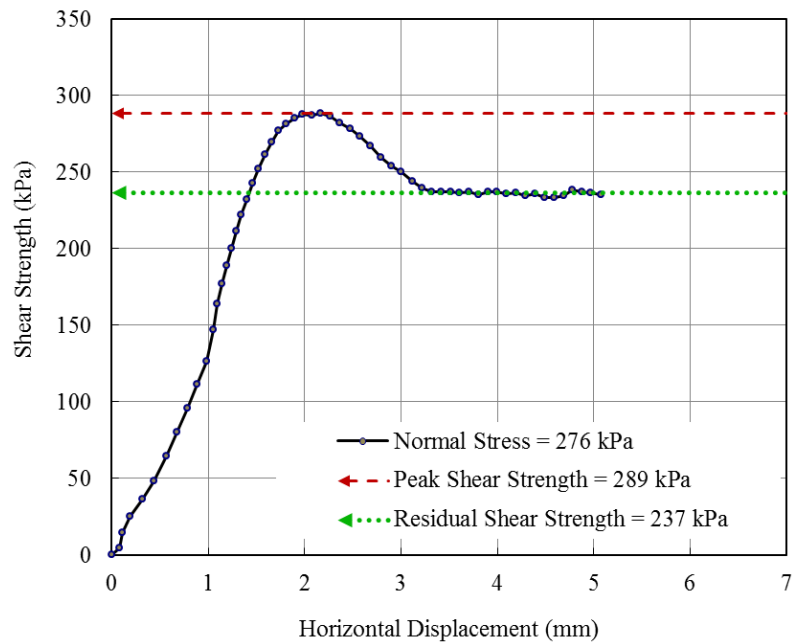


Figure 6.7. Small-scale test results on the subgrade sand at 276 kPa overburden pressure ($\gamma = 16.25 \text{ kN/m}^3$)

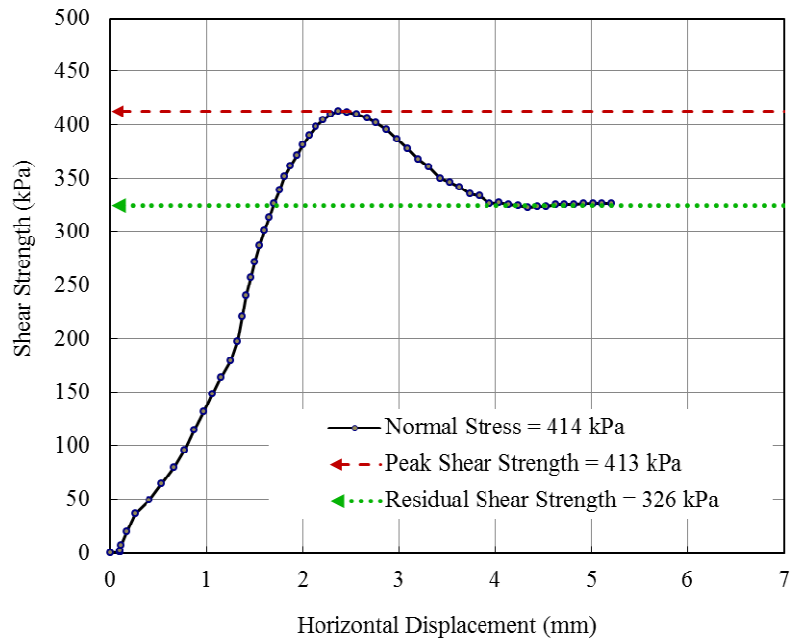


Figure 6.8. Small-scale test results on the subgrade sand at 414 kPa overburden pressure ($\gamma = 16.25 \text{ kN/m}^3$)

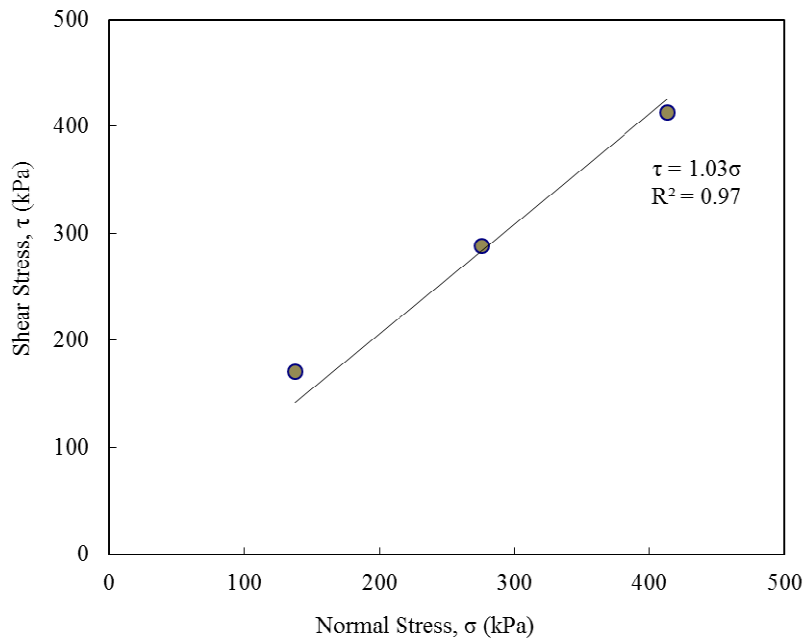


Figure 6.9. Mohr-Coulomb failure envelope for the sand (small-scale DST)

6.4. Large Scale Direct Shear Tests (DST) on Sand and Aggregate

6.4.1. Preparation of the Soil Samples

A series of large-scale direct shear tests was carried out on the subgrade sand and the ODOT Type-A aggregate using a ShearTrac-III Machine (and ancillary software) manufactured by GeoComp Corporation (**Figure 6.10**). The dimensions of the shear box were 305 mm (L) \times 305 mm (W) \times 203 mm (H).

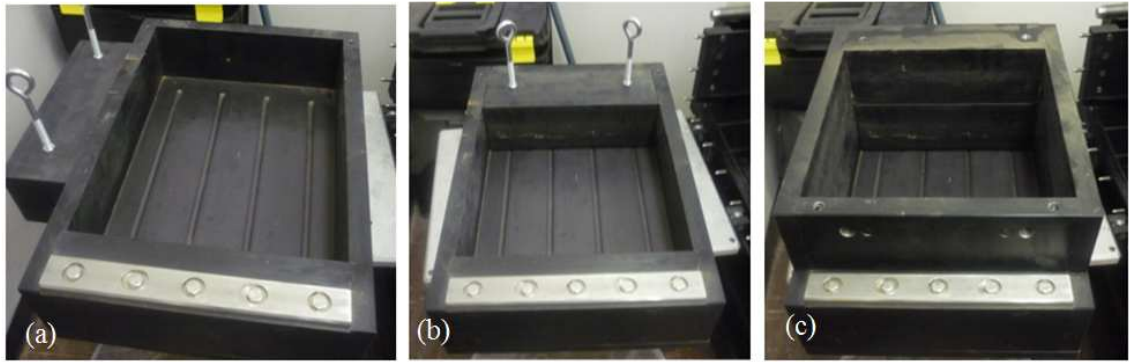


Figure 6.10. Assembly of the large-scale shear box: (a) the lower half, (b) the spacer, (c) the upper half

The moisture content and unit weight of the sand in these tests were 0.2% and 16.25 kN/m³, respectively. The shear box was filled with seven layers of sand (**Figure 6.11**). Each layer of sand was compacted manually using a mallet. In the case of aggregate, the shear box was filled with three layers of aggregate (**Figure 6.12**). The moisture content and unit weight of the aggregate were 0.11% and 20.41 kN/m³, respectively.



Figure 6.11. Setting up the large-scale DST machine to test sand specimens



Figure 6.12. (a) Placing of first layer of aggregate in the shear box, (b) Compaction of first layer of aggregate with a mallet, (c) Second layer of aggregate after compaction, (d) Third (i.e. final) layer of aggregate after compaction

After filling the shear box, the top cap was placed above the sand or aggregate specimen. The top cap was handled with two studs which were screwed in the threads inside the cap (**Figure 6.13**).

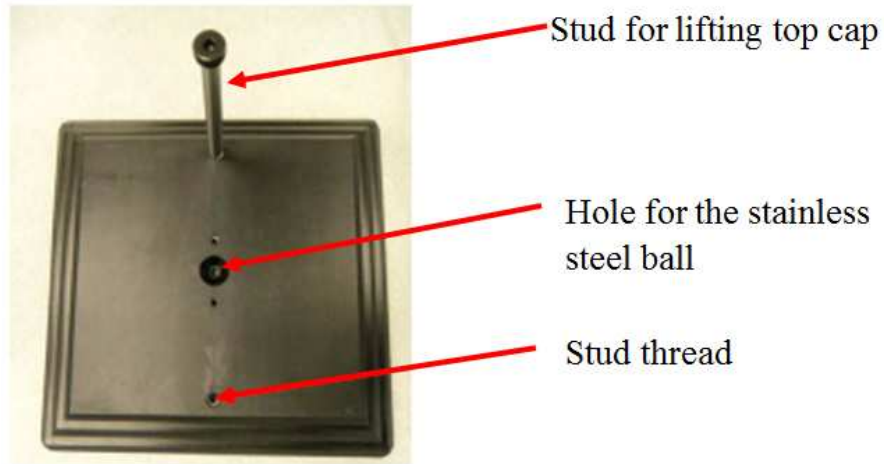


Figure 6.13. The top cap with stud

The vertical load cell needed to be positioned on the stainless steel ball on the top cap carefully so that there was a little gap between the loading cell and the steel ball. The proper positioning of the vertical load cell could be ensured by observing the green light on the front panel display of the DST machine (**Figure 6.14**). Before starting the shearing phase of the test, the two bolts connecting the two halves of the test cell were removed to allow the upper box to slide horizontally. A complete test setup is shown in **Figure 6.15**.



Figure 6.14. (a) Front panel of the DST machine (b) Positioning of the vertical load cell on the test cell



Figure 6.15. Large-scale direct shear test setup

6.4.2. Shear Test Results

The large scale shear test results of sand are presented in **Figure 6.16** through **Figure 6.19**. From **Figure 6.19**, the peak friction angle of the sand was determined to be 34 degrees. **Figure 6.20** shows the combined results of small-scale and large-scale shear tests. The difference in the calculated sand friction angle at the same nominal unit weight and moisture content could be attributed the scale effects between the two tests. The friction angle value from the large-scale DST is believed to represent the sand used as a substrate in the cyclic plate load tests more closely.

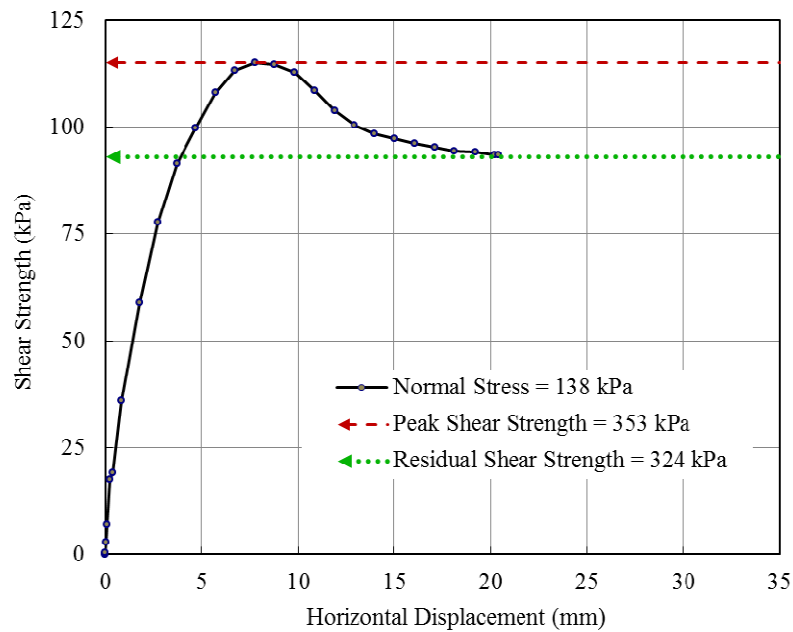


Figure 6.16. Large-scale test results on the subgrade sand at 138 kPa overburden pressure ($\gamma = 16.25 \text{ kN/m}^3$)

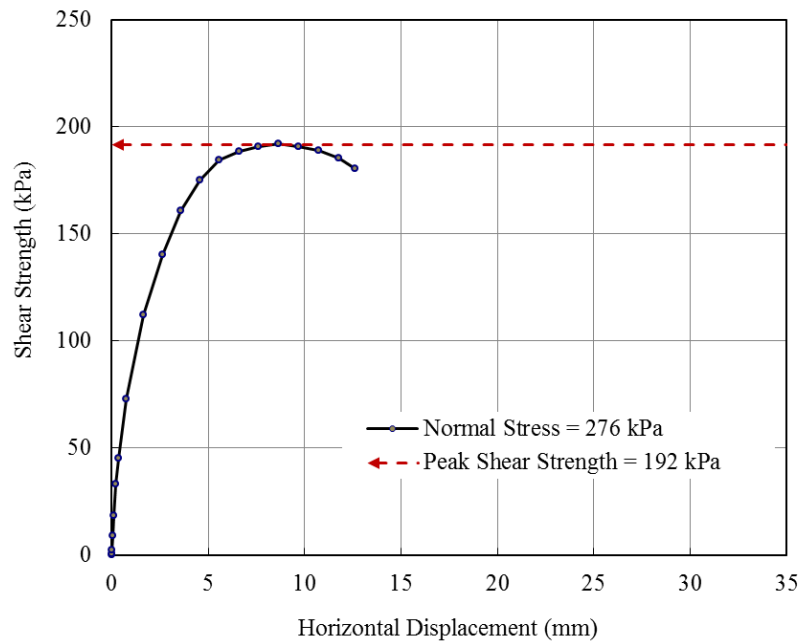


Figure 6.17. Large-scale test results on the subgrade sand at 276 kPa overburden pressure ($\gamma = 16.25 \text{ kN/m}^3$)

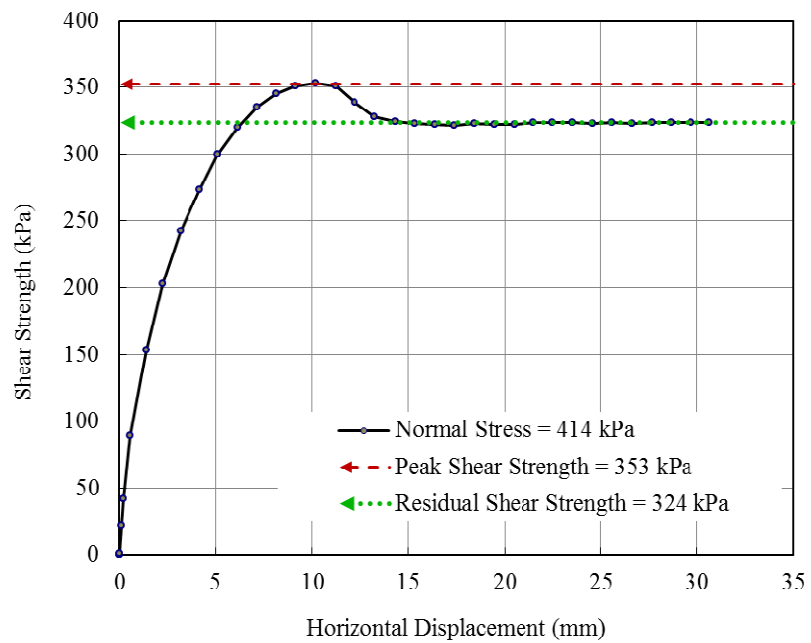


Figure 6.18. Large-scale test results on the subgrade sand at 414 kPa overburden pressure ($\gamma = 16.25 \text{ kN/m}^3$)

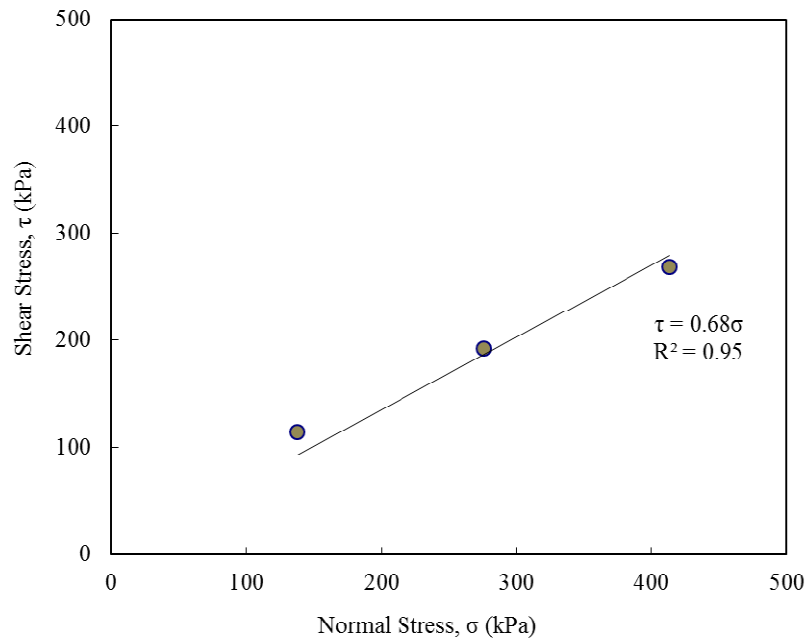


Figure 6.19. Mohr-Coulomb failure envelope for the sand (large-scale DST)

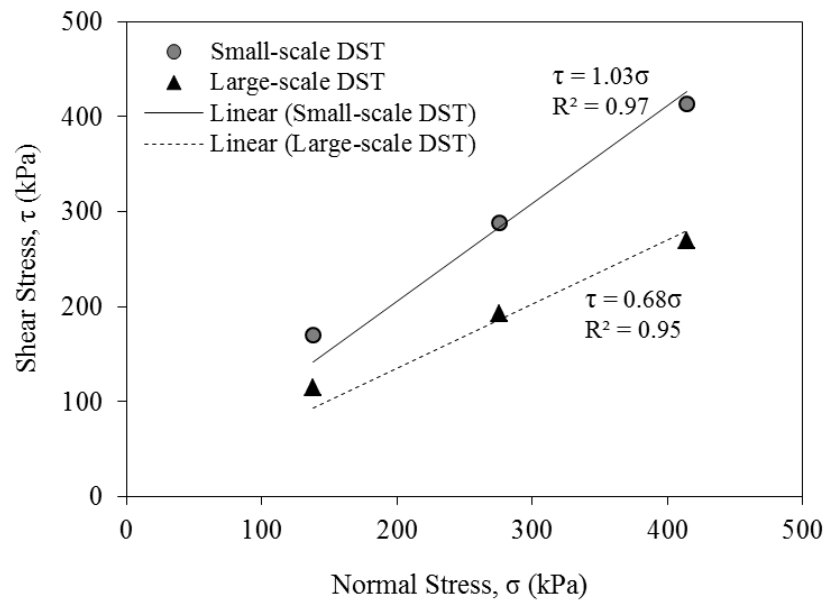


Figure 6.20. Mohr-Coulomb failure envelopes of the sand at different scale DST

The large-scale shear test results for the ODOT Type-A aggregate are shown in **Figure 6.21** through **Figure 6.23**. The aggregate specimens were tested at smaller overburden pressures as compared to sand specimens in order to avoid reaching the capacity of the large DST machine in former case. The peak friction angle of the aggregate ($\gamma = 20.4 \text{ kN/m}^3$) with assumption of zero cohesion from the data shown in **Figure 6.24** is calculated as 69 degrees. Therefore, it is recommended that more large-scale DSTs should be carried out to obtain a more reasonable friction angle value for the ODOT Type-A aggregate.

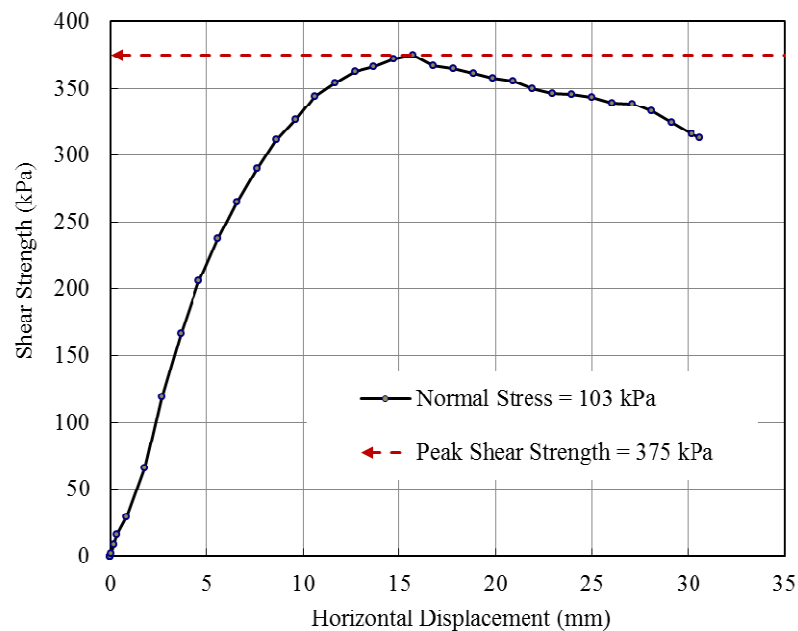


Figure 6.21. Large-scale test results on ODOT Type-A aggregate at 103 kPa overburden pressure ($\gamma = 20.41 \text{ kN/m}^3$)

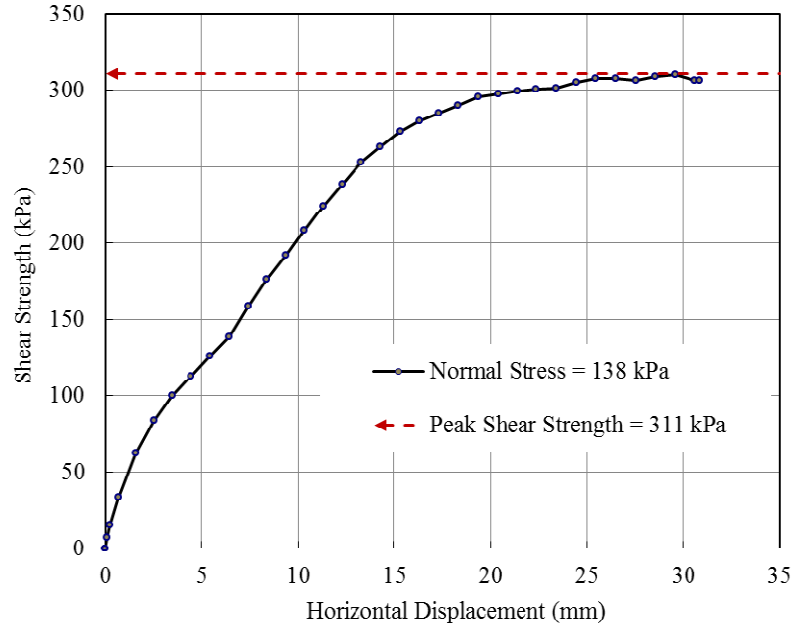


Figure 6.22. Large-scale test results on ODOT Type-A aggregate at 138 kPa overburden pressure ($\gamma = 20.41 \text{ kN/m}^3$)

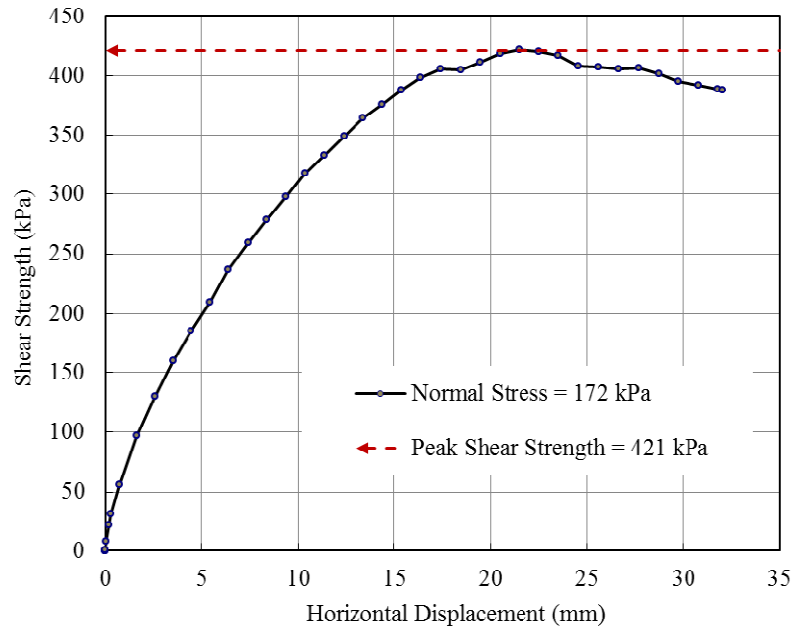


Figure 6.23. Large-scale test results on ODOT Type-A aggregate at 172 kPa overburden pressure ($\gamma = 20.41 \text{ kN/m}^3$)

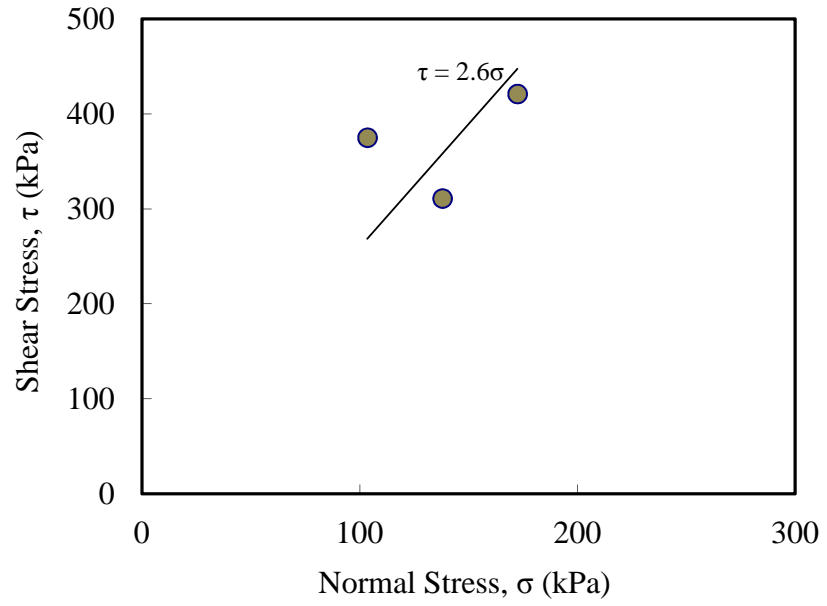


Figure 6.24. Mohr-Coulomb failure envelope for the ODOT Type-A aggregate (large-scale DST)

CHAPTER SEVEN

INSTALLATION DAMAGE TESTING OF GEOGRIDS

7.1. General

Stresses on geogrid reinforcement can be especially high during construction when geogrids are subjected to significant loading by the construction equipment. Therefore, survivability tests such as installation damage tests are important to understand the significance of geogrid index properties during construction of pavements. In this study, two large-scale field installation damage tests were carried out on the extruded and non-extruded geogrids listed in **Table 3.2** in conformance with the ASTM D5818 and TRI 2006 test protocol to investigate their survivability during construction. According to the ASTM D5818 standard, “The geosynthetic should be installed in accordance with project-specific procedures. When project specific procedures and/or materials are not known, representative equipment, materials and procedures should be used and thoroughly documented.”

7.2. Summary of the Installation Damage Test Procedure

The following steps were taken to run the installation damage tests. Additional details of the installation damage procedure are given in the subsequent sections.

Step 1: A suitable site was selected for the test bed. Factors that were taken into consideration for this purpose included the evenness of the site surface and its proximity to the laboratory.

Step 2: The size of the test bed area and its depth were determined (**Section**

7.3. Size of the Test Bed Area

Step 3: Test area boundaries were marked and the surface vegetation was removed.

Step 4: Two 4.57 m long concrete beams were placed on the two sides of the cleared area. Soil was placed and compacted against the outside wall of each beam in order to support and secure it in place.

Step 5: An area near the test bed was cleared and prepared to store new aggregate.

Step 6: 11 metric tons of ODOT Type-A aggregate was purchased.

Step 7: Four steel plates were used to help with the exhumation of geogrid specimens after they were installed in the aggregate. 1 m-long chains were attached to each steel plate which facilitated lifting of the plates during the exhumation process.

Step 8: Different alternatives for the compaction equipment were examined and a compactor was selected.

Step 9: Steel plates were placed side-by-side along the test bed and were covered with 150 mm of aggregate. An aggregate ramp was built on both ends of the test bed so that the compactor equipment could access the main test area. The aggregate was compacted to 90% maximum dry density (as recommended in

ASTM D5818) using 4 passes of the 7056 kg steel drum compactor on the top of the aggregate. The number of passes for the compaction equipment was determined following the information reported in TRI (2006).

Step 10: Four geogrid specimens were prepared and placed in the test bed on the top of the first aggregate lift.

Step 11: The second 152 mm aggregate layer was placed and compacted in the test bed.

Step 12: The density of the aggregate in each lift was measured based on the as-placed thickness of the aggregate. In addition, a balloon testing apparatus was used to take additional density measurements (**Section 7.9**).

Step 13: Once the construction of the reinforced base model was completed, a forklift was used to lift the steel plates from underneath the base layer and tilt them to expose the geogrids. Afterwards, the aggregates on the top of the geogrid specimens were carefully removed and the specimens were taken to the laboratory for inspection and testing.

Step 14: The second installation damage test was carried out on four other geogrid products.

Step 15: In-isolation tests were carried out on damaged geogrid specimens to determine installation damage factors for their rib and junction strength properties.

7.3. Size of the Test Bed Area

A schematic site plan for installation damage tests outside the Fears laboratory at OU is shown in **Figure 7.1**. Selected data related to this site include:

Size of the test area: 3.66 m (L) x 2.44 m (W) (excluding the ramp)

Total length of the test section (including the ramp) = 7.32 m

Ramp slope = 3H : 1V

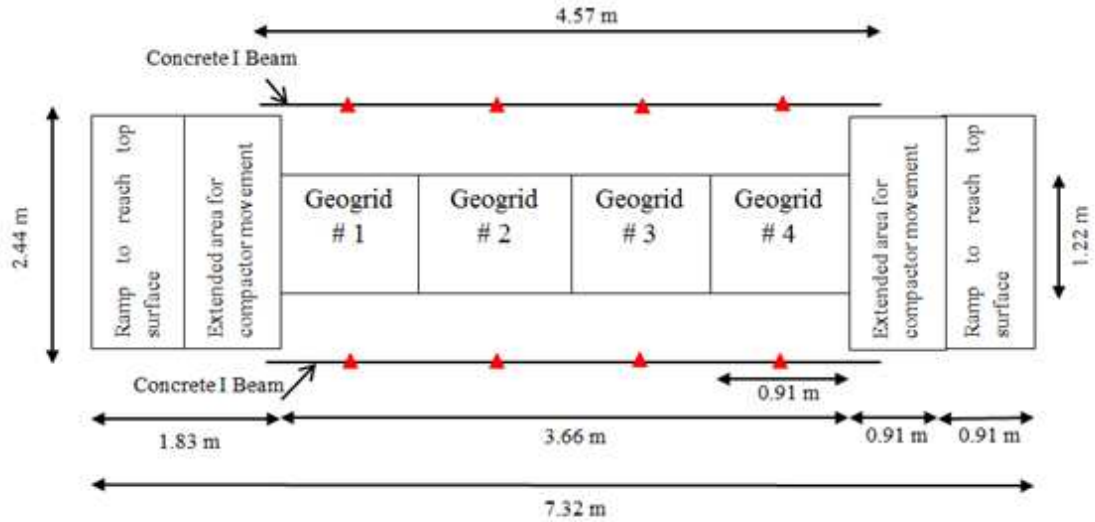
Length of the extended area for the compactor movement = 0.91 m

Length of the ramp = 0.91 m

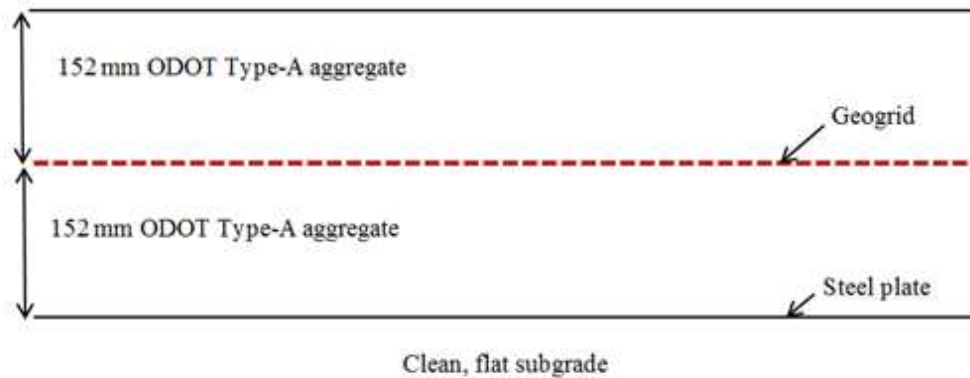
Length of the concrete side beams = 4.57 m

Height of the concrete side beams = 0.46 m

Height of the test section = 0.30 m



(a)



(b)

Figure 7.1. Schematic diagrams of the test bed for installation damage tests: (a) Plan view (Note: Solid triangles indicate the locations where the thickness of the aggregate layer was measured), (b) Elevation view (indicating the thicknesses of aggregate layers)

7.4. Geogrid Sampling and Specimen Preparation

Eight 0.91 m x 1.22 m geogrid specimens (one from each geogrid product) were prepared for the installation damage tests as shown in **Figure 7.2** through **Figure 7.11**.



Figure 7.2. Geogrid sample preparation

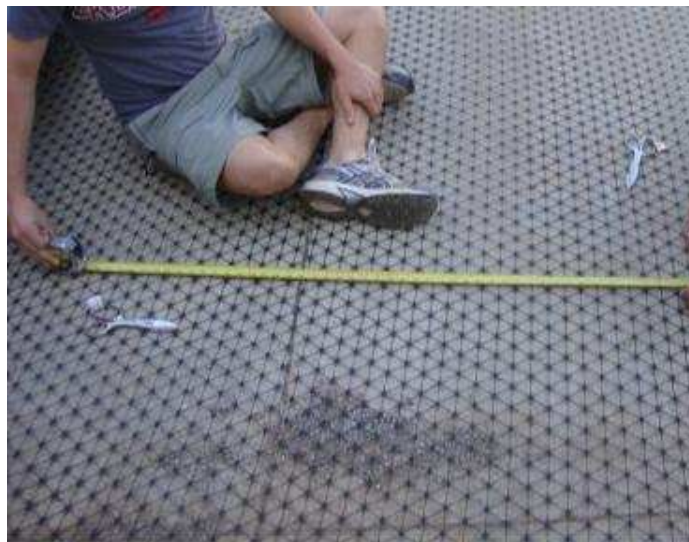


Figure 7.3. Preparing EGG4 geogrid specimen for installation damage tests

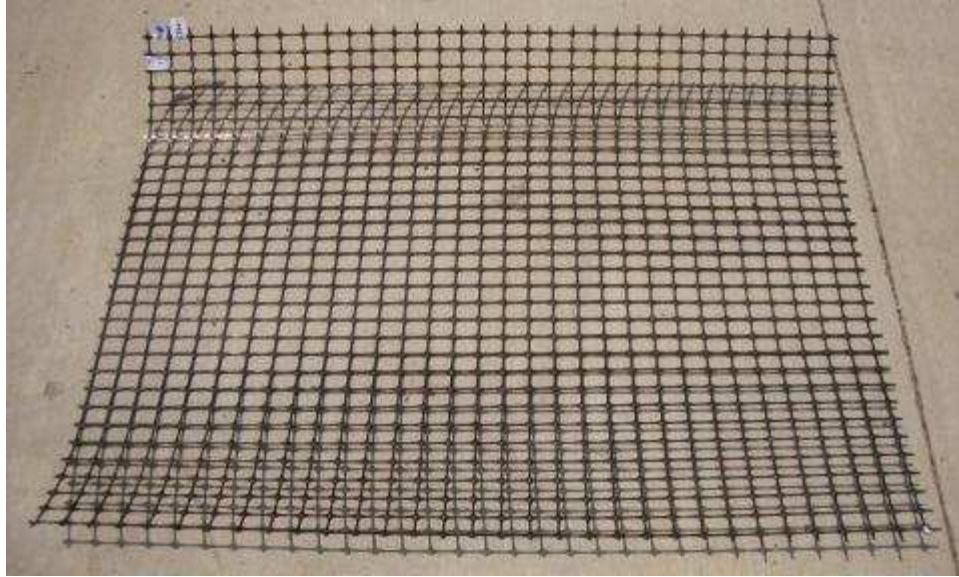


Figure 7.4. EGG1 geogrid specimen prepared for installation damage tests

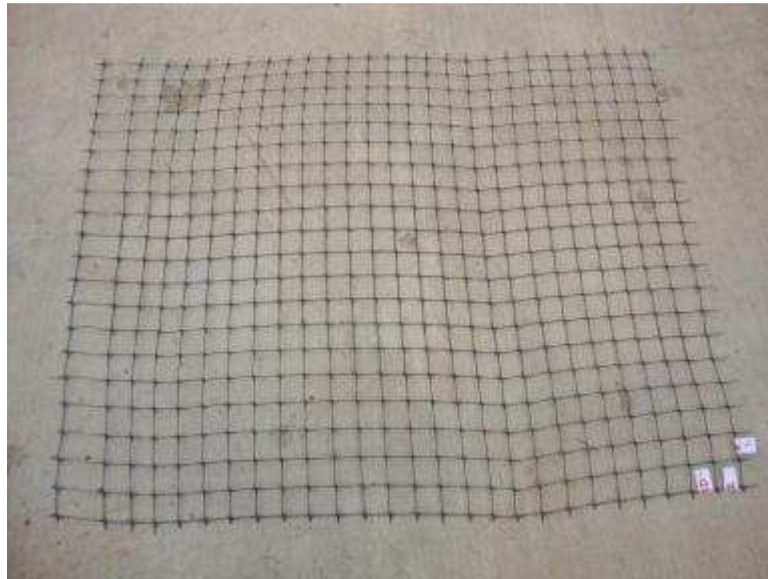


Figure 7.5. EGG2 geogrid specimen (single layer) prepared for installation damage tests

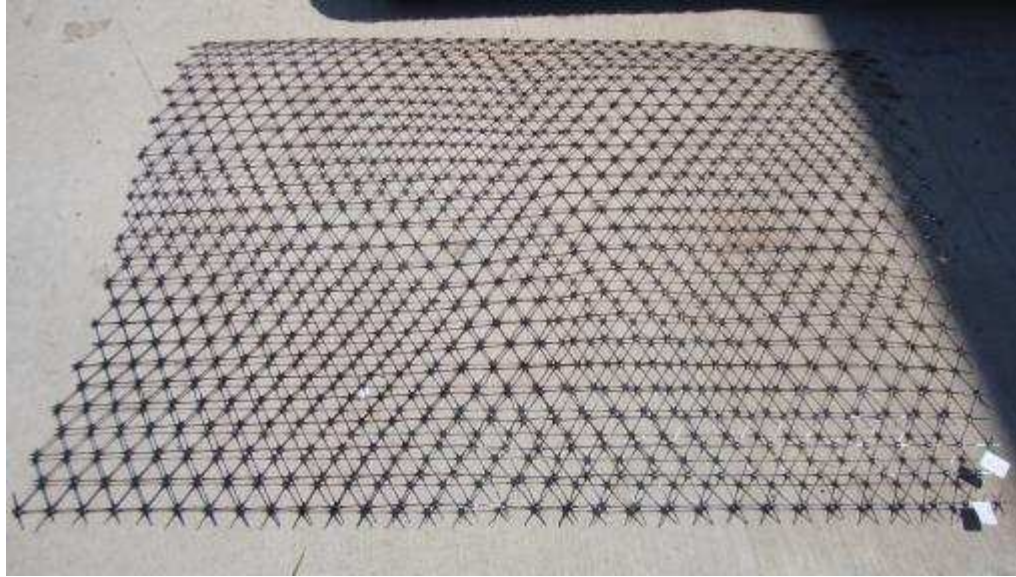


Figure 7.6. EGG3 geogrid specimen prepared for installation damage tests

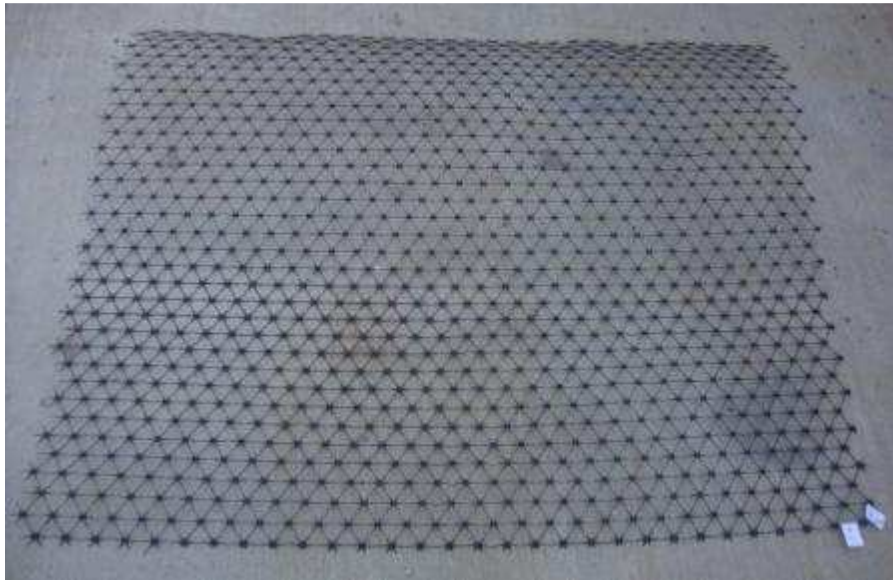


Figure 7.7. EGG4 geogrid specimen prepared for installation damage tests

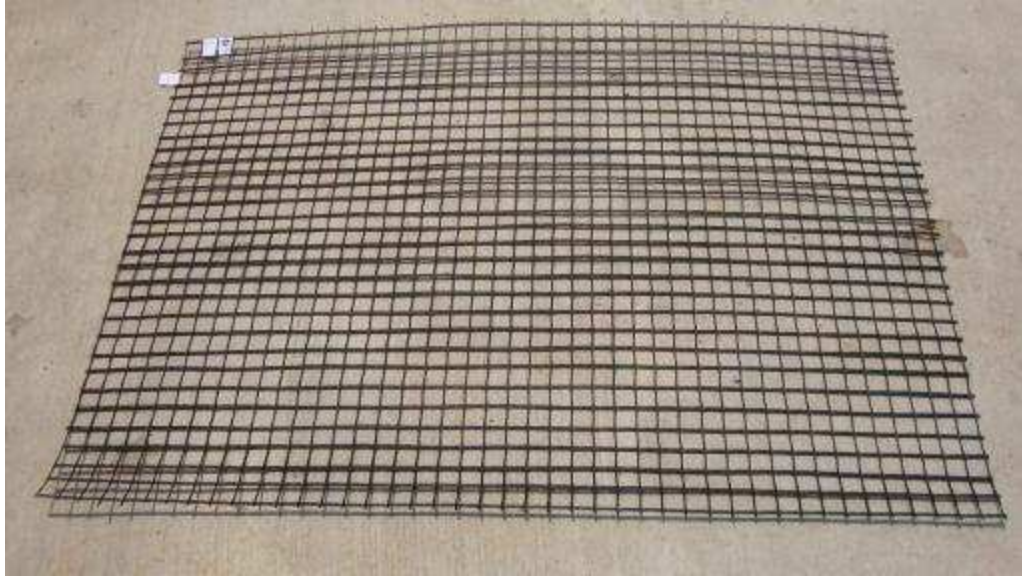


Figure 7.8. WGG1 geogrid specimen prepared for installation damage tests

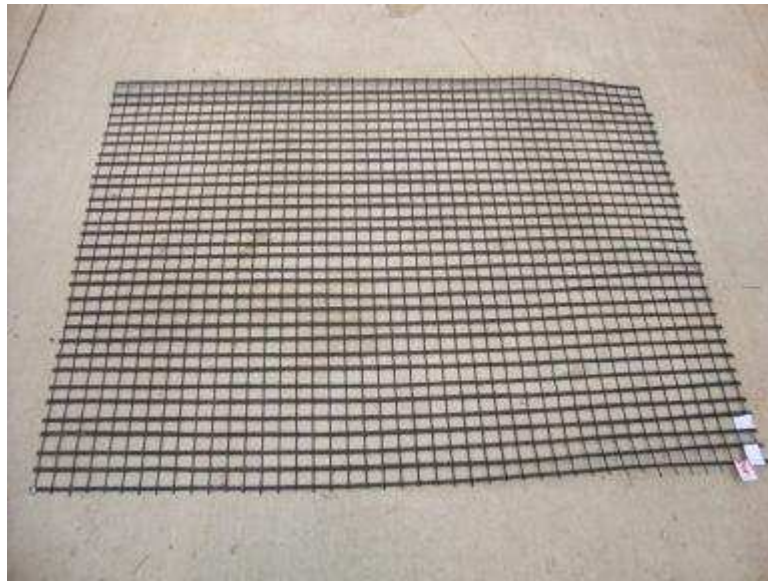


Figure 7.9. WGG2 geogrid specimen prepared for installation damage tests

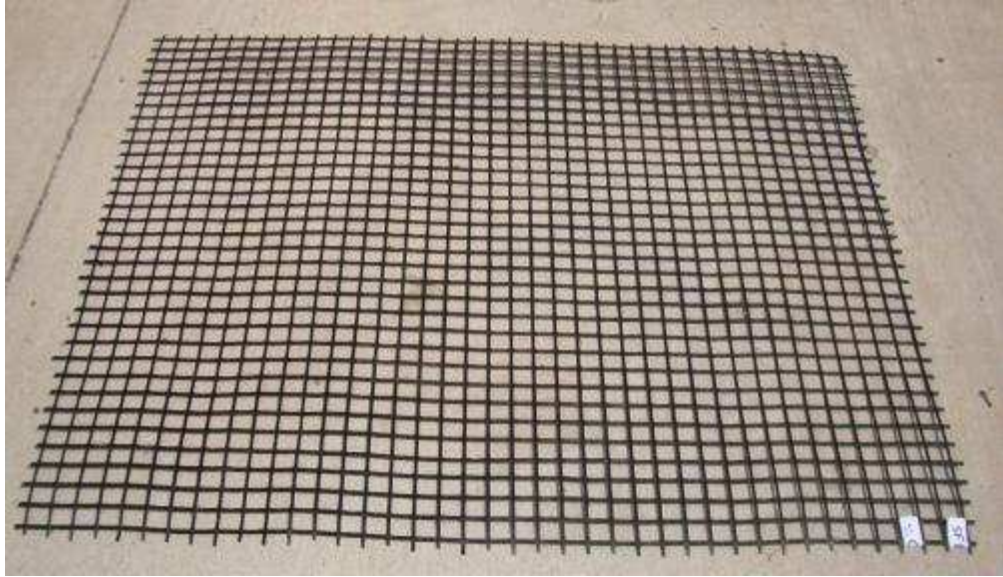


Figure 7.10. WGG3 geogrid specimen prepared for installation damage tests

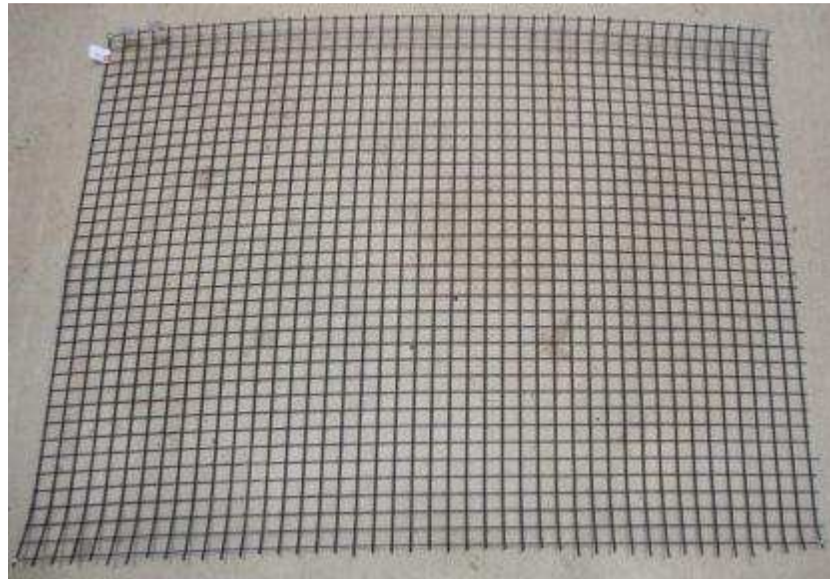


Figure 7.11. KGG1 geogrid specimen prepared for installation damage tests

The selected size of the geogrid specimens is comparable to that used in earlier similar studies (e.g. TRI 2006, Jeon and Bouazza 2008). It is also in agreement with the ASTM D5818 guidelines which state that: “The amount of geosynthetic to install in and retrieve from a test section is a function of the type and number of laboratory tests to be conducted for assessment of damage. An amount of material sufficient to obtain 20 tests on representative specimens for each type of test should be installed for each set of installation conditions.”

Two rounds of installation damage tests were carried out in this study. The extruded (EGG) and non-extruded (NEGG) geogrid specimens listed in **Table 3.2** were tested in the first and the second rounds of installation damage tests, respectively. The machine direction of each geogrid specimen was placed parallel to the running direction of the compaction equipment according to the ASTM D5818 test standard.

7.5. Compaction Equipment

A steel-wheeled vibratory roller compactor was used to compact the aggregates in the installation damage test bed. The compactor weight was more than 4500 kg, as recommended in ASTM D5818. Different companies in Oklahoma and Texas were contacted and the specifications and the rental and transportation costs of the available choices for the compactor equipment were compared to select a suitable compactor for the tests. Fortunately, a local company (Haskell Lemon) had a suitable compactor (**Figure 7.12**) and was able to loan it for this study. The compactor (Volvo Model

SD70D) was a single-drum vibratory roller compactor with the specifications as given in **Table 7.1**.



Figure 7.12. Compaction equipment (Source: <http://www.volvo.com>)

Table 7.1. Compactor Specifications

Weight	7056 kg
Recommended minimum weight of the compactor (ASTM D5818)	4500 kg
Width	1.87 m
Length	5.04 m
Height	2.88 m
Width of the roller drum	1.68 m

A forklift tractor (**Figure 7.13**) with a lifting capacity of 18 kN was used to lift the steel plates from underneath the aggregate layer in the test bed and initiate the exhumation process. A front-loader “bobcat” tractor was used to spread the aggregate in the test bed (**Figure 7.14**).



Figure 7.13. The forklift used in this study to lift the steel plates



Figure 7.14. The front-loader tractor used in this study

7.6. Steel Plates

Four steel plates were placed underneath the aggregate layer in the test bed on the cleared subgrade. Lifting chains were attached to the plates along one edge to facilitate their lifting and tilting during the exhumation process of the geogrid samples from underneath the compacted aggregate (**Figure 7.15** and **Figure 7.16**). The specifications of the steel plates are given in **Table 7.2**.



Figure 7.15. Steel plates with lifting chains



Figure 7. 16. Moving of the steel plates from the lab to the test site

Table 7.2. Specifications of steel plates used in the installation damage test bed

Number of steel plates	4
Length	1.07 m
Width	1.37 m
Thickness	12.7 mm
Weight	1.1 kN

7.7. Measuring Density of Compacted Aggregate

There are a number of ASTM standards for measuring the in-situ density of soils and aggregates as described below:

1. ASTM D 1556-07 “Standard Test Method for Density and Unit Weight of Soil in Place by Sand-Cone Method”: This test method is not suitable for soils

consisting of unbound granular materials, soils containing appreciable amounts of coarse-grained material larger than 38 mm, and granular soils having high void ratios. Therefore, sand cone method was not used in our tests.

2. ASTM D 4914-08 “Standard Test Methods for Density and Unit Weight of Soil and Rock in Place by the Sand Replacement Method in a Test Pit”: This test method is primarily suitable for rock, which is defined as aggregates that typically contain particles larger than 76 mm. Since ODOT Type-A particles are significantly smaller than 76 mm this method was not used to measure the as-placed density of the aggregates.

3. ASTM D 2167-08 “Standard Test Method for Density and Unit Weight of Soil in Place by the Rubber Balloon Method”: This test method is recommended for aggregates. Therefore, ASTM D 2167-08 method was used to measure the in-situ unit weight of the ODOT Type-A aggregate in the installation damage tests of this study (**Section 7.9**).

7.8. Site Preparation

A 7.32 m × 2.44 m area was marked outside the Fears laboratory on the OU south campus. The marked area was cleared of the existing vegetation and two concrete beams were placed on its side boundaries and secured in place by placing and compacting soil against the outside walls of the beams (**Figure 7.17** through **Figure 7.20**).



Figure 7.17. Test site for the installation damage tests of geogrids outside the Fears Laboratory



Figure 7.18. Marking the boundaries of the test site



Figure 7.19. Clearing the test area from existing vegetation



Figure 7.20. Concrete beams placed on both sides of the test section with soil support on the outside

7.9. Key Steps in the Field

Prior to the placement of aggregates, a grid was drawn on the inside wall of each beam using a red marker. Each grid was comprised of horizontal and vertical lines at 152 mm intervals. For each lift, after more than 152 mm of aggregate was placed in the test bed and compacted, its final thickness was measured at eight locations along the length of the test section using a ruler (**Figure 7.21**). For this purpose, the lift thickness was calculated by measuring the distance between the aggregate surface and the marked horizontal line on the beam sidewall immediately above it. The compaction of each aggregate lift was carried out using four passes of the compaction equipment (TRI 2006). **Figure 7.21** through **Figure 7.33** illustrate the key steps followed to carry out the installation damage tests.



Figure 7.21. Four steel plates were placed in the test bed to facilitate the exhumation process of geogrids after they were covered by compacted aggregate



Figure 7.22. Aggregate was taken from a nearby stockpile using a front-loader tractor



Figure 7.23. Spreading ODOT Type-A aggregate in the test bed



Figure 7.24. First layer of aggregate in the test bed before compaction



Figure 7.25. Compacting the first layer of aggregate with a vibratory roller compactor

The as-placed unit weight of the aggregate in each lift was measured according to ASTM D2167-08 using a model HM-310 Voluvessel densometer (**Figure 7.26**), which was found to vary between 20.41 kN/m^3 and 21.20 kN/m^3 . Comparison of these values with the maximum unit weight of the ODOT Type-A aggregate used in the study (with a maximum dry unit weight equal to 23 kN/m^3 from the modified proctor tests according to the AASHTO T 180-01 test method; Kazmee 2010) indicated that the unit weight of the aggregate in the test bed was approximately 90% of its maximum modified Proctor value during the tests.

The aggregate moisture content was also determined according to the ASTM D4643 test method. The moisture content values were in the range between 0.25% and 0.30%, which meant that the aggregate was in an essentially dry condition.



Figure 7.26. Measuring the in-situ density of aggregates (a) Model HM-310 Voluvessel Rubber Balloon densometer, (b) The densometer in use on the test bed



Figure 7.27. Four extruded geogrids placed on the first layer of compacted aggregate



Figure 7.28. Spreading the second layer of aggregate in the test bed



Figure 7.29. Compaction of the second layer of aggregate with the vibratory roller compactor



Figure 7.30. The top (second) layer of aggregate in the test bed after compaction

To exhume the geosynthetic specimens, the forklift tractor was used to lift the chains that were attached to one edge of the steel plates underneath the compacted aggregate. Each plate was lifted and tilted to an angle of nearly 45° from horizontal using the lifting chains (**Figure 7.31** and **Figure 7.32**). Afterwards, the upper part of the aggregate on the top of the geogrid was initially removed using a shovel (**Figure 7.33**). However, deeper aggregate closer to the geogrid was carefully removed by hand. If necessary, the plate was struck with a mallet to loosen the fill and facilitate the exhumation process without any contact with the geogrid.



Figure 7.31. Forklift connected to the lifting chains



Figure 7.32. Tilting of steel plates from underneath the compacted aggregate



Figure 7.33. Tilting of steel plates and removing of aggregates to facilitate exhumation process

The summary of the two installation damage tests are presented in **Table 7.3**.

Table 7.3. Summary of installation damage tests on geogrids in ODOT Type-A aggregate

Test No.	Geogrid	First Lift				Second Lift			
		Unit Weight (kN/m ³)	Moisture Content (%)	No. of Passes	Final Thickness (mm)	Unit Weight (kN/m ³)	Moisture Content (%)	No. of Passes	Final Thickness (mm)
1	EGG1, EGG2 (single layer), EGG3, EGG4	20.88	0.25	4	147	20.41	0.25	4	160
2	WGG1, WGG2, WGG3, KGG1	21.20	0.30	4	152	20.72	0.3	4	157

7.10. Geogrid Samples after Exhumation

The geogrid samples after exhumation were brought to the laboratory where they were cleaned using a soft brush. Afterwards, the samples were tagged and stored in a secure place in the laboratory. Photographs of geogrid samples after exhumation are shown in **Figure 7.34** through **Figure 7.41**.

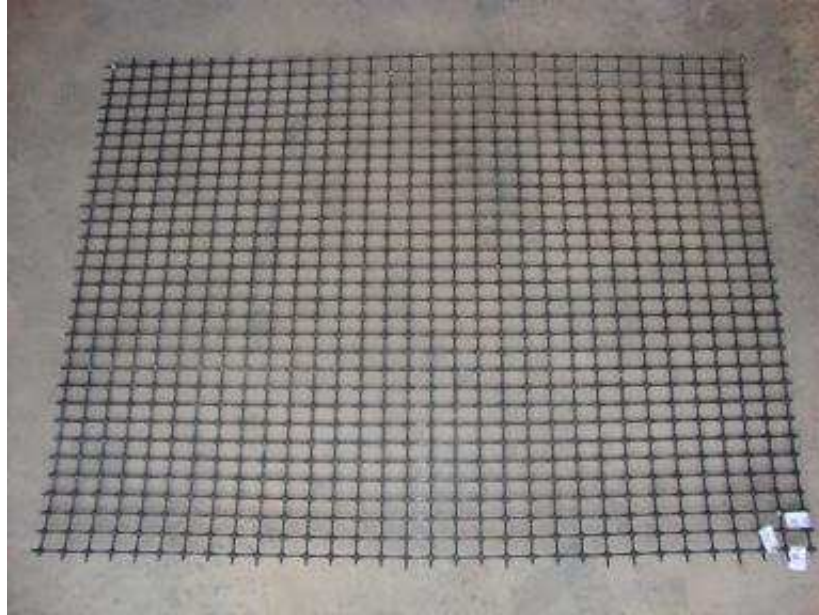


Figure 7.34. EGG1 geogrid specimen after exhumation

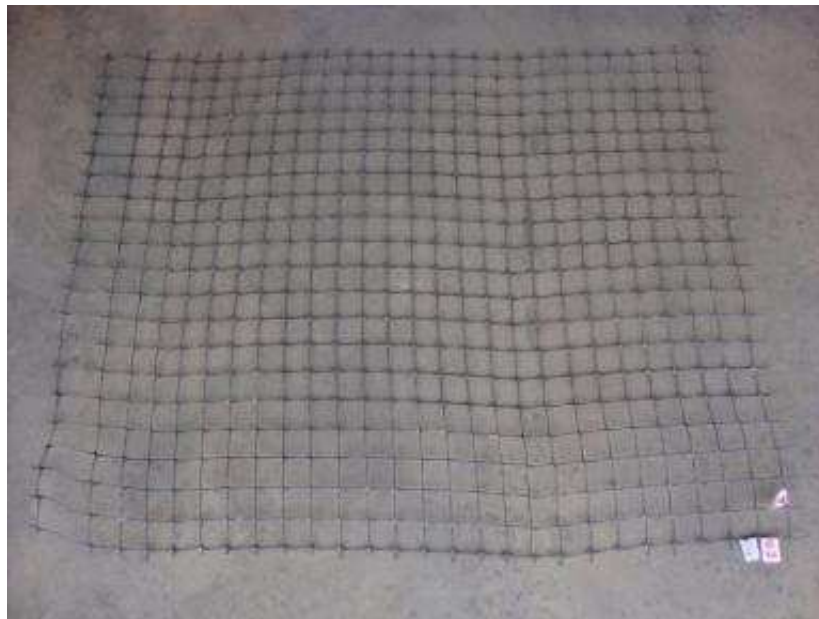


Figure 7.35. EGG2 geogrid specimen (single layer) after exhumation

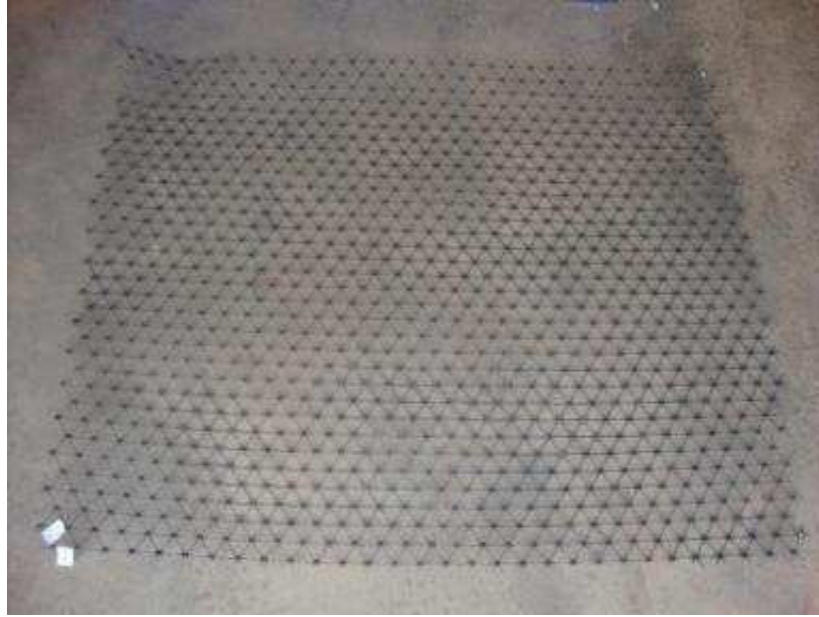


Figure 7.36. EGG3 geogrid specimen after exhumation

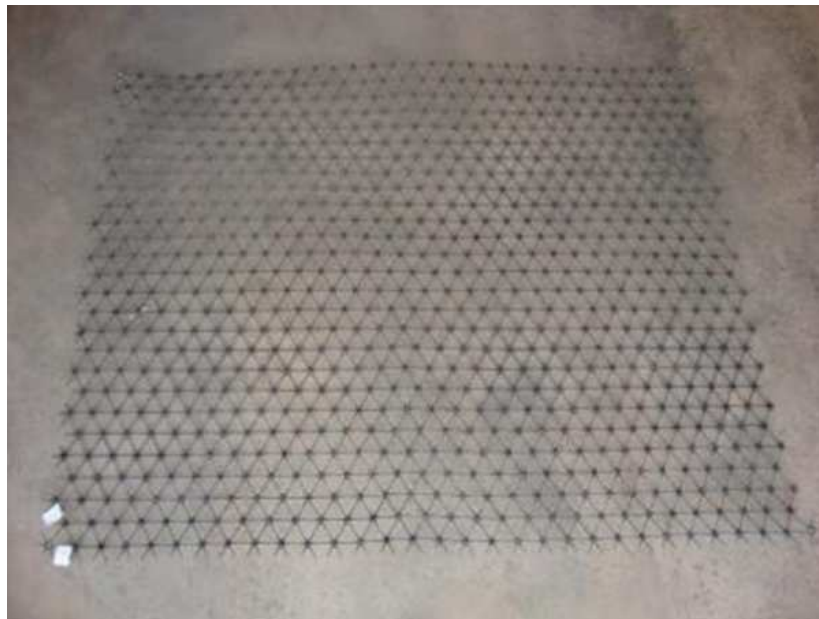


Figure 7.37. EGG4 geogrid specimen after exhumation



Figure 7.38. WGG1 geogrid specimen after exhumation

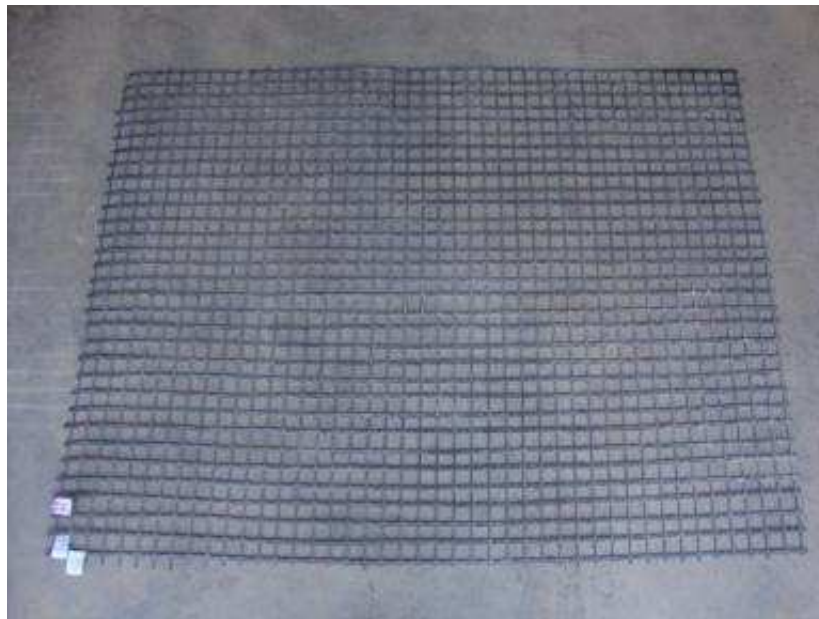


Figure 7.39. WGG2 geogrid specimen after exhumation



Figure 7.40. WGG3 geogrid specimen after exhumation



Figure 7.41. KGG1 geogrid specimen after exhumation

7.11. Obtaining Representative Test Specimens from Exhumed Samples

Following the ASTM D5818 test standard, areas of the geosynthetic samples that were damaged during removal were identified, spray painted and designated as being non-representative of installation damage. Consequently, these parts of the geogrids were excluded from sampling for installation damage evaluation. The “non-representative area of installation damage” for EGG1, EGG2- single layer, EGG3, EGG4 and KGG1 geogrid samples, painted in red, are shown in **Figure 7.42** through **Figure 7.46**.

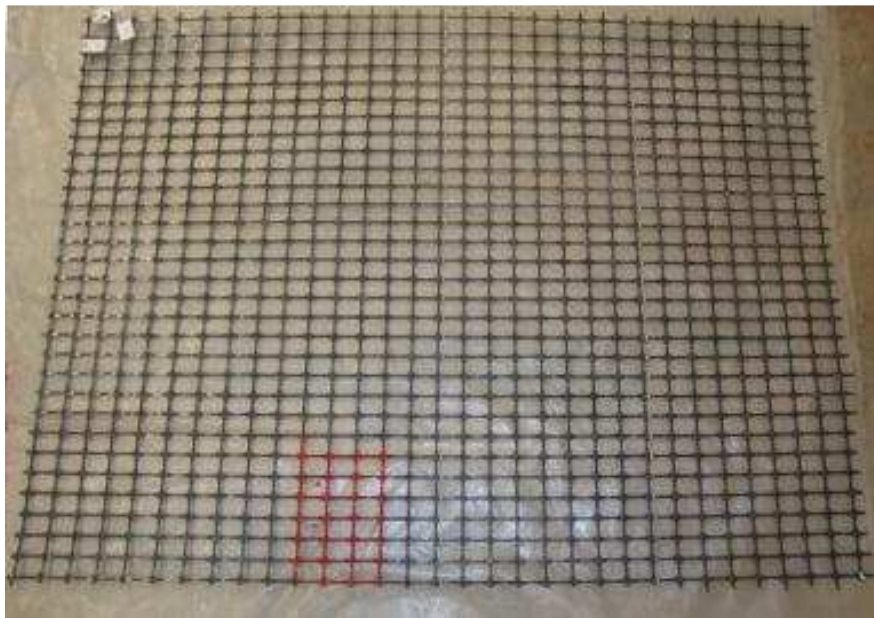


Figure 7.42. EGG1 geogrid sample with marked damaged area

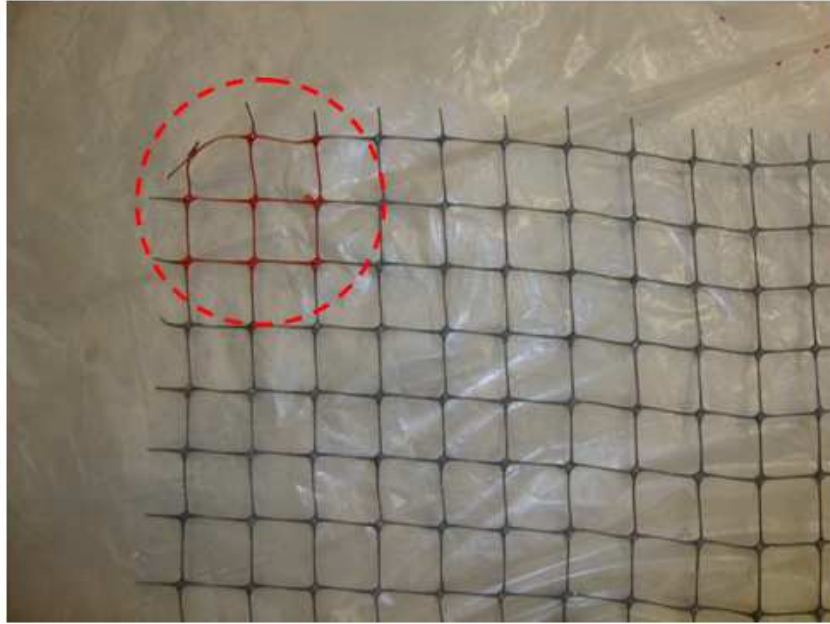


Figure 7.43. EGG2 geogrid sample (single layer) with marked damaged area

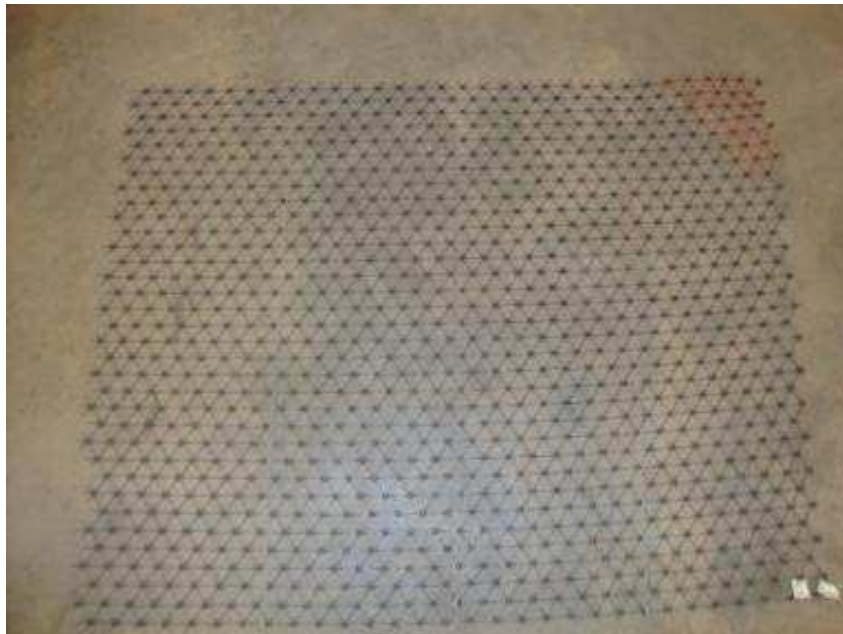


Figure 7.44. EGG3 geogrid sample with marked damaged area

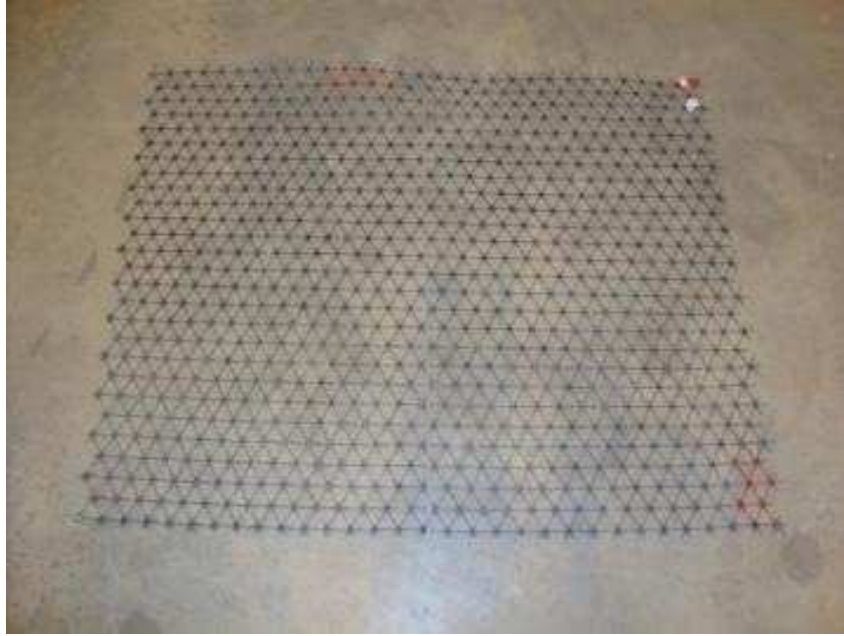


Figure 7.45. EGG4 geogrid sample with marked damaged area



Figure 7.46. KGG1 geogrid sample with marked damaged area

Following the ASTM D5818 test protocol and the TRI (2006) sampling procedure guidelines, each exhumed geogrid sample was divided into four sections (indicated as Sections A, B, C and D in **Figure 7.47**). This was done in order to obtain representative specimens from the entire area of geogrid samples and thereby eliminate any potential bias in specimen selection. Eight specimens were cut out from each section for in-isolation tests. As a result, a total of thirty two (32) representative specimens were obtained from each geogrid sample to carry out rib and junction strength tests in both machine and cross-machine directions (MD and XD) (**Figure 7.47**). From each group of eight specimens, five specimens were randomly selected to run the in-isolation tests.

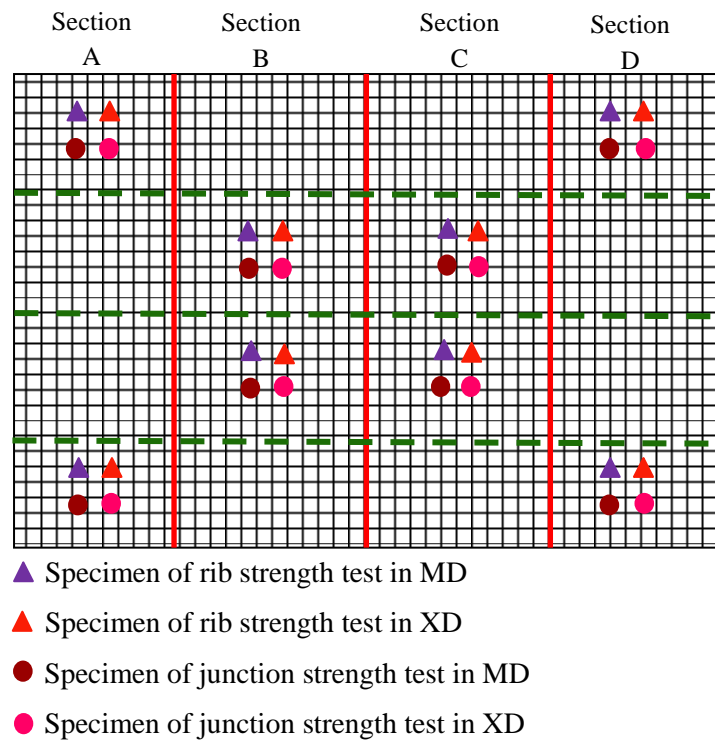


Figure 7.47. Layout of specimens obtained from each geogrid sample

7.12. Junction Strength Tests on Damaged Geogrid Specimens

A total of eighty (80) junction strength tests (i.e. five in MD and five in XD for each of the final eight geogrid products that were shortlisted in **Table 3.2**) were carried out on damaged geogrid specimens according to ASTM D7737. Due to the fabrication method of the non-extruded geogrids (NEGG), the magnitude of the junction strain before failure was very low. Therefore, only the ultimate junction strength of the NEGG products was determined (**Section 4.1. Fabrication of Junction Strength Testing Clamps**). However, digital imagery technique (Wang 2009, Hatami et al. 2011a) was used to determine the local strain in each junction for extruded geogrid (EGG) products. **Figure 7.48** shows damaged EGG1 geogrid specimens that were prepared for junction strength tests.

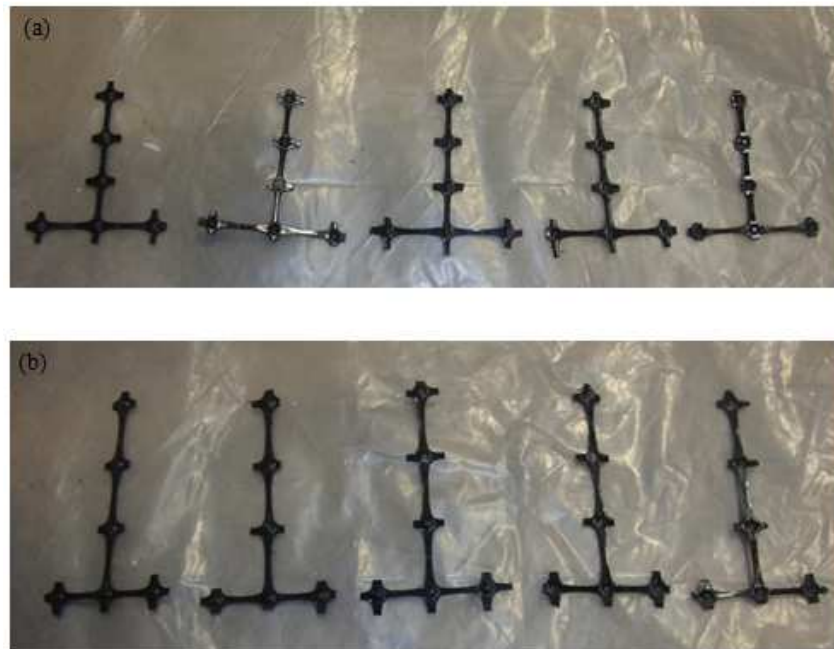


Figure 7.48. Damaged EGG1 geogrid junction strength test specimens before the test:

(a) MD specimens, (b) XD specimens

7.13. Rib Strength Tests on Damaged Geogrid Specimens

A total of eighty (80) rib strength tests (i.e. five in MD and five in XD for each of the final eight geogrid products that were shortlisted in **Table 3.2**) were carried out according to the ASTM D 6637 test standard. The gauge length on each specimen was marked and a non-contact digital imagery technique (Wang 2009, Hatami et al. 2011a) was used to measure the rib extension of extruded geogrids (**Figure 7.53**).

Figure 7.49 and **Figure 7.50** show damaged specimens of the EGG2 geogrid (single layer) before and after the rib strength tests. **Figure 7.51** and **Figure 7.52** show images of a KGG1 test specimen before and after the tests.

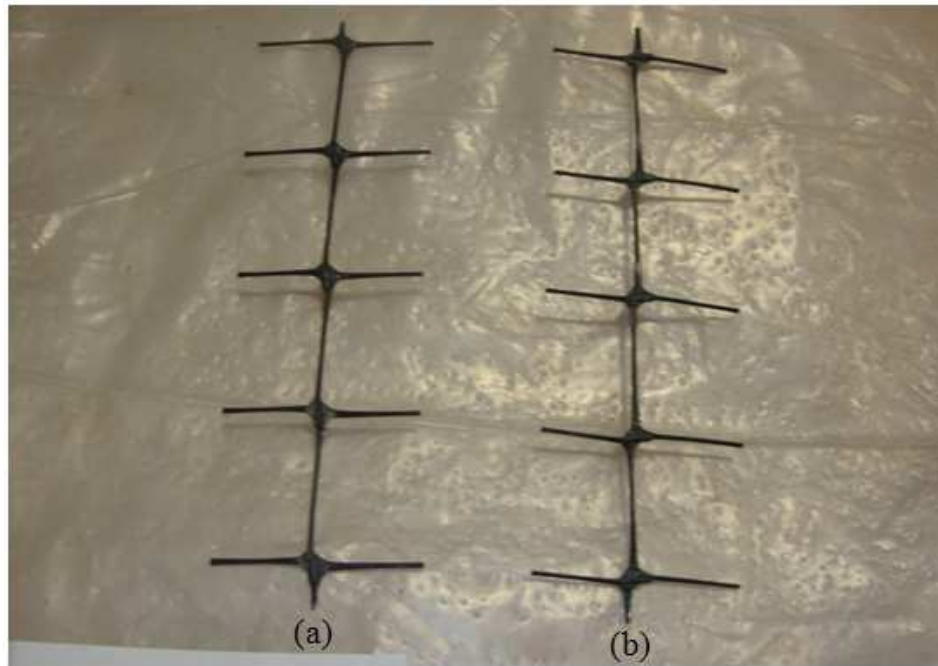


Figure 7.49. Damaged EGG2 (single layer) geogrid rib strength test specimens before the test: (a) MD specimens, (b) XD specimens

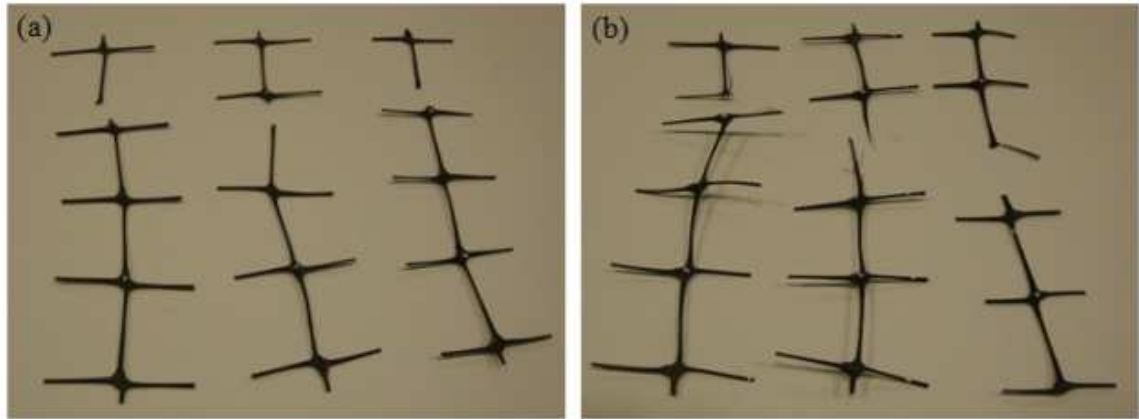


Figure 7.50. Damaged EGG2 (single layer) geogrid rib strength test specimens after the test: (a) MD specimens, (b) XD specimens

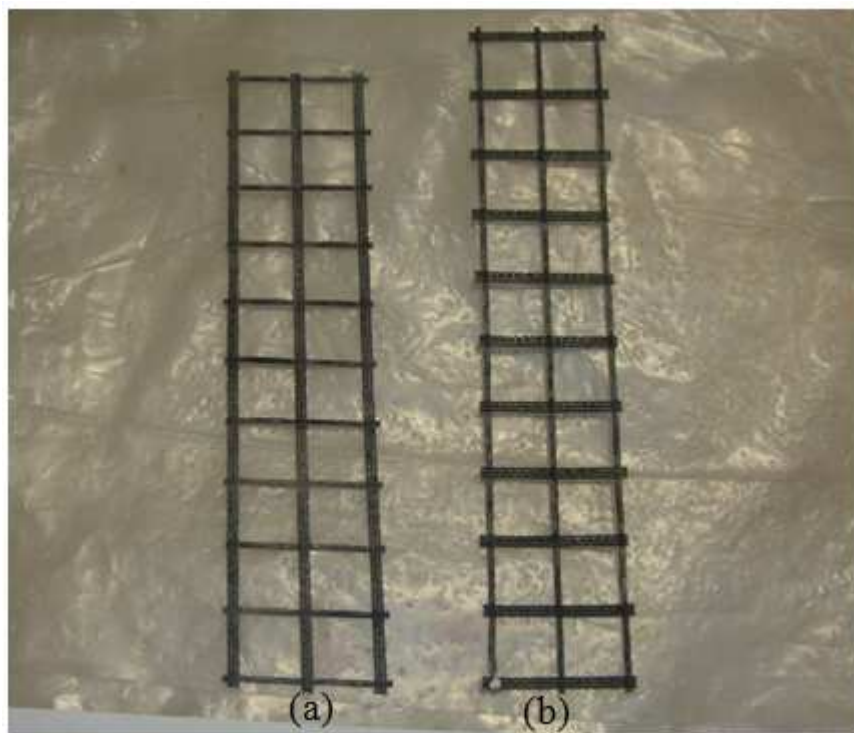


Figure 7.51. Damaged KGG1 geogrid rib strength test specimens before the test: (a) MD specimens, (b) XD specimens

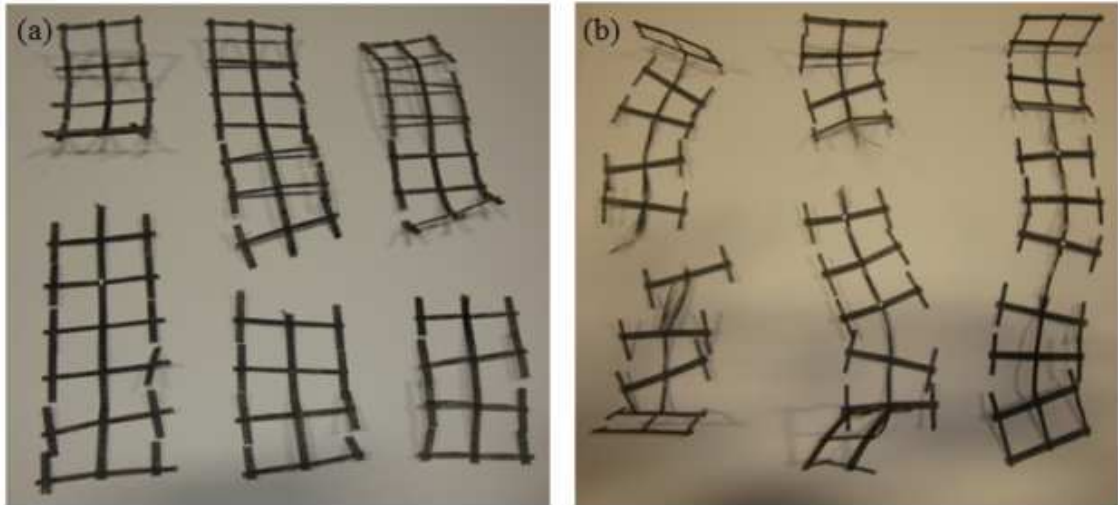


Figure 7.52. Damaged KGG1 geogrid rib strength test specimens after the test: (a) MD specimens, (b) XD specimens

The EGG and NEGG specimens were tested using the clamping systems described in **Sections 5.1**. Fabrication of Rib Strength Testing Clamps for and **Section 5.2**. Fabrication of Rib Strength Testing Clamps for NEGG, respectively. **Figure 7.53** and **Figure 7.54** show the rib strength test setup for the EGG and NEGG products, respectively.

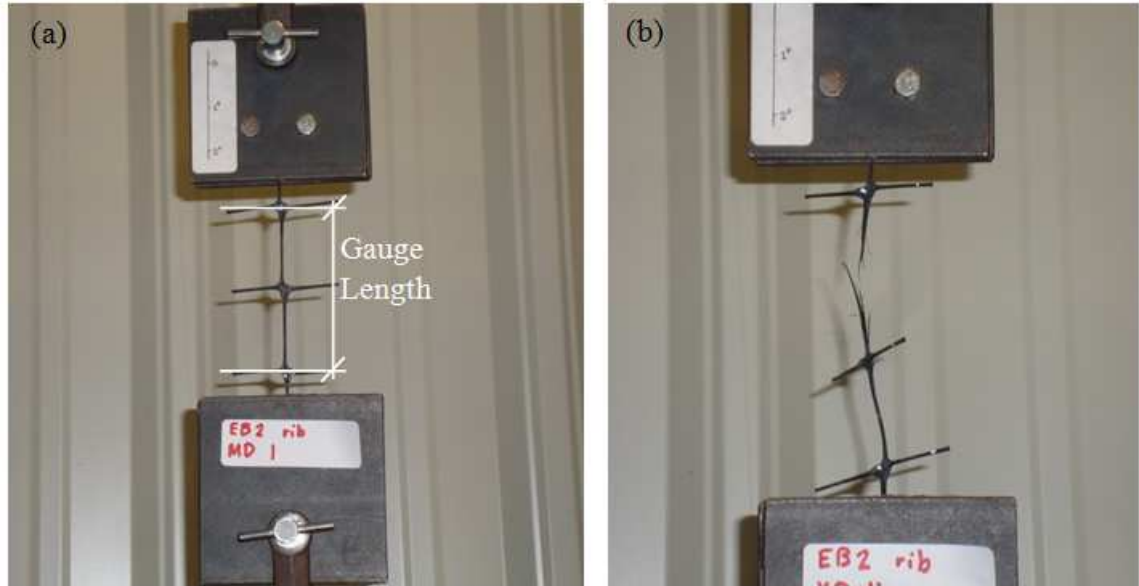


Figure 7.53. Rib strength testing of an extruded [EGG2 (single layer)] geogrid product: (a) before the test, (b) after the test

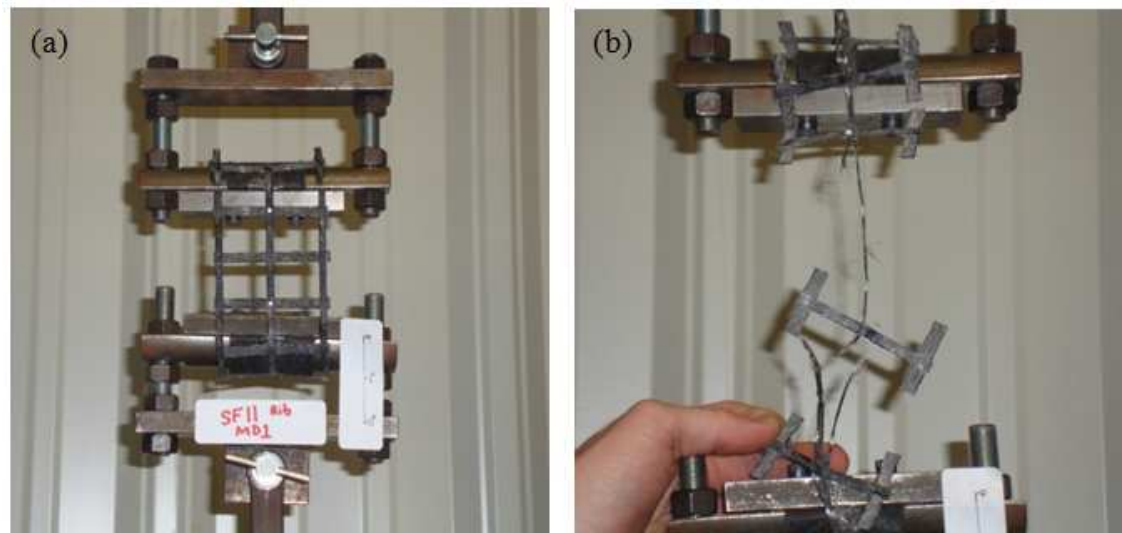


Figure 7.54. Rib strength testing of a non-extruded (WGG3) geogrid product: (a) before the test, (b) after the test

7.14. Installation Damage Reduction Factors

The retained properties (e.g. rib strength and junction strength) of geogrid specimens, after they were carefully exhumed from the test bed, were compared with the corresponding values of virgin specimens (**Section 4.2. Junction Strength Test Results** and **Section 5.3. Rib Strength Test Results**). Installation damage reduction factors for the eight geogrids tested in ODOT Type-A aggregate are listed in **Table 7.4**.

Koerner (2005) reports a range of recommended installation damage reduction factors (RF_{ID}) for unpaved roads, which vary between 1.1 and 2 for geotextiles. In this study, the range of installation damage factors for geogrids was found to vary between 1 and 2. The RF_{ID} values for the rib tensile strength at 2% strain were found to be larger than those for the ultimate strength. Overall, larger RF_{ID} values were obtained for extruded geogrid products as compared to non-extruded geogrid products. The EGG3 and EGG4 products overall showed greater RF_{ID} values compared to other products tested.

The installation damage factors for the EGG1 and EGG2 geogrids were compared with the values provided by the manufacturers. Manufacturers' data on installation damage factors were not found for other geogrid products listed in this study. However, TRI (1998) reported installation damage factors for some other geogrids comparable to EGG3. The range of installation damage factors they reported was 1.01 to 1.17. This range is also comparable with the installation damage factors calculated for EGG3 geogrid in this study (**Table 7.4**). According to the manufacturers'

data, the installation damage factors for EGG1 and EGG2 are 1.16 and 1.11, respectively, when used with gravel. These values are comparable with the values reported in **Table 7.4**. However, it should be noted that the geogrids RF_{ID} values depend on the type of materials/aggregate used in the tests. In addition, RF_{ID} values are reported for ultimate strength values only, whereas the results given in **Table 7.4** indicate that different RF_{ID} values should be used for different index properties of geogrids. However, such data are typically not available for low-strain rib tensile strength or junction strength of geogrid products.

Table 7.4. Installation damage factors of the geogrids tested in this study

Geogrid		Installation Damage Reduction Factors (RF_{ID})							
		RF_{ID} for rib strength at 2% strain		RF_{ID} for rib strength at 5% strain		RF_{ID} for ultimate rib strength		RF_{ID} for ultimate junction strength	
		MD	XD	MD	XD	MD	XD	MD	XD
EGG	EGG1 (ODOT Type-2)	1.7	1.3	1.2	1.1	1.1	1.1	1.0	1.0
	EGG2 (single layer)	1.3	1.2	1.1	1.2	1.0	1.0	1.0	1.0
	EGG3	1.1	1.5	1.3	1.5	1.6	1.8	1.0	1.0
	EGG4	1.1	1.2	1.1	1.2	1.4	1.3	1.0	1.0
NEGG	WGG1	1.0	1.0	1.0	1.3	1.5	1.1	1.0	1.0
	WGG2	1.1	1.0	1.3	1.1	1.0	1.0	1.0	1.0
	WGG3	1.3	1.0	1.0	1.2	1.0	1.0	1.3	1.0
	KGG1	2.0	1.1	1.2	1.0	1.0	1.0	1.1	1.0

CHAPTER EIGHT

INFLUENCE OF IN-ISOLATION PROPERTIES OF GEOGRIDS ON THEIR PULLOUT PERFORMANCE

8.1. General

Geogrids used in aggregate base reinforcement applications can be subjected to significant compaction-induced stresses during the construction stage. Pullout tests can provide a methodic means to study geogrid-aggregate interactions at different stress levels under controlled conditions. In addition, pullout tests can help to isolate the tensile performance of geogrids in the anchorage zone outside the pressure bulb of the tire from its out-of-plane membrane behavior when the geogrid is subjected to the vertical load of traffic (Hatami et al. 2011a).

8.2. Fabrication of a New Pullout Box

A new pullout test box with the dimensions 1.83 m (H) \times 0.91 m (W) \times 0.76 m (H) was fabricated in the Fears laboratory to carry out pullout tests on geogrids in aggregates (**Figure 8.1**).



Figure 8.1. Newly fabricated pullout test box at the OU Fears laboratory

8.3. Pullout Test Setup and Procedure

A total of 33 pullout tests were carried out on the eight geogrid products listed in **Table 3.2** as per the ASTM D6706 test protocol (ASTM 2009) to investigate the influence of geogrid index properties on their in-aggregate performance. The pullout tests were carried out in ODOT Type-A aggregate which is a widely used dense-graded aggregate in ODOT projects.

The pullout tests were conducted at 3.3 kPa, 6.6 kPa and 11.5 kPa overburden pressures. These overburden pressures on the geogrid-aggregate interface were primarily due to the weight of a compacted aggregate layer with different heights on the top of the interface in the pullout box. The overburden pressures 3.3 kPa and 6.6 kPa

were generated using aggregate thicknesses of 0.15 m and 0.3 m, respectively. In the case of the 11.5 kPa overburden pressure, an airbag was used on the top of a 0.3 m thick aggregate layer to apply the additional pressure needed. These pressure levels resemble field conditions (outside the tire pressure bulb) where pullout (as opposed to geogrid rupture) would be the likely failure mechanism. Pullout tests on biaxial and triaxial geogrid specimens were carried out in the machine direction. However, due to the distinctive geometry of triaxial products (i.e. EGG3 and EGG4), the MD geogrid ribs are actually at 30° angles diagonally from the machine direction on both sides.

Different steps of the pullout tests are illustrated in **Figure 8.2** through **Figure 8.15**. The pullout force was applied to the geogrid specimen using a servo-controlled hydraulic actuator. The geogrid specimen was connected to the actuator through a roller clamp (**Figure 8.12**). Displacement of the geogrid specimen was measured and recorded in four different locations along their length using wire potentiometers.

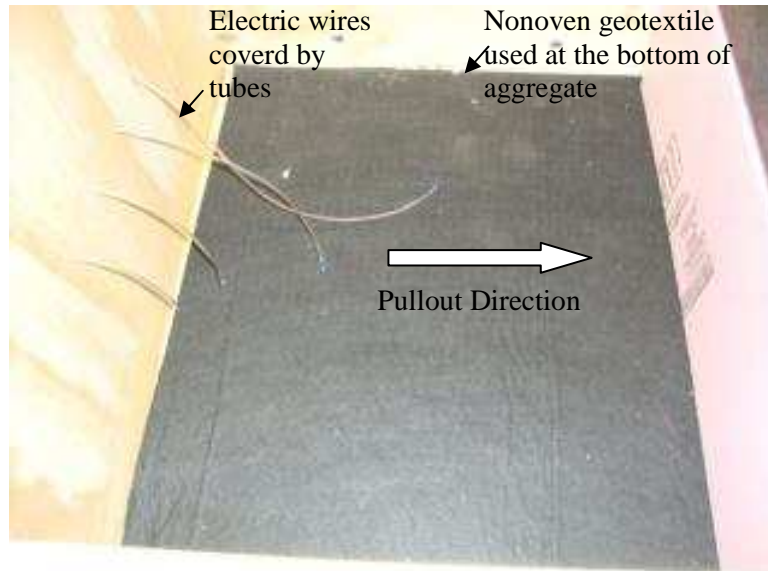


Figure 8.2. Pullout test box before placing the aggregate



Figure 8.3. Compacted aggregate in the pullout box (the 203 mm-wide lower steel sleeve can be seen in the foreground)



Figure 8.4. Drilling of the geogrid junctions to connect the extensometers



Figure 8.5. Connecting wires to geogrid specimen



Figure 8.6. Tell-tale wires connected to wire potentiometers



Figure 8.7. Top surface of the aggregate



Figure 8.8. A separator geotextile was placed on the top of the aggregate



Figure 8.9. An earth pressure cell was placed on a 25 mm sand layer on top of the aggregate



Figure 8.10. Air bag was used (if necessary) to generate additional overburden pressure on the geogrid-aggregate interface



Figure 8.11. Closing of the pullout test box before the test



Figure 8.12. Geogrid was connected to the roller clamp



Figure 8.13. Geogrid attachment to the roller clamp



Figure 8.14. Completed pullout test setup before the test



Figure 8.15. A pullout test in progress

Figure 8.16 through **Figure 8.23** show the conditions of geogrid products before and after the completion of pullout tests.

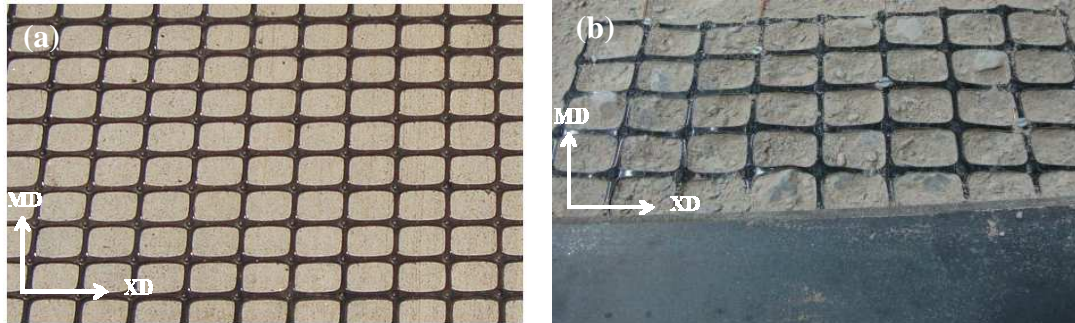


Figure 8.16. EGG1 geogrid (a) before pullout test, (b) after pullout test

Three pullout tests were carried out on EGG2 (single layer) geogrid with 0.61 m embedded length at 3.3 kPa, 4.95 kPa and 6.6 kPa overburden pressures (**Figure 8.17**). Four pullout tests were carried out on EGG3 geogrid specimens (**Figure 8.18**). Three of the tests were carried out on 0.61 m embedded length long specimens subjected to 3.3 kPa, 4.95 kPa and 6.6 kPa overburden pressures. One test was carried out at 3.3 kPa overburden pressure with 356 mm embedded length.

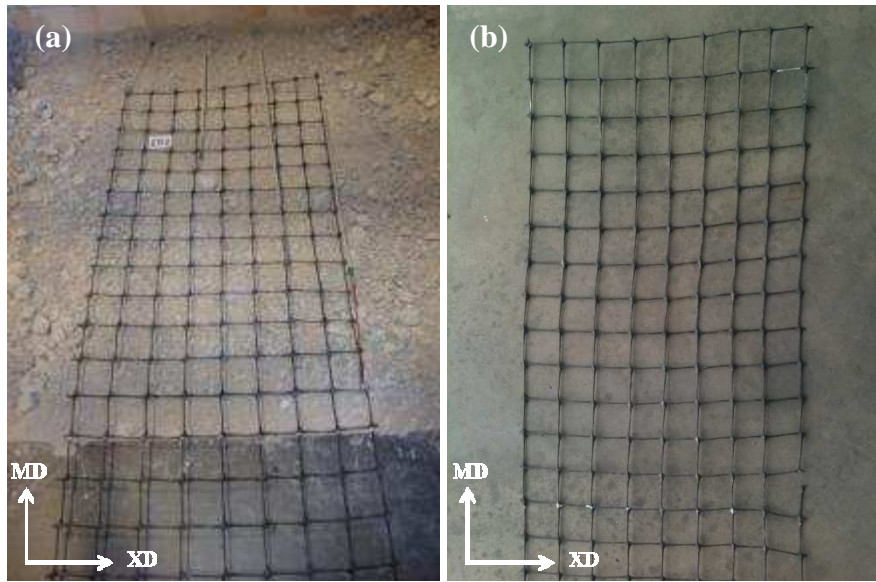


Figure 8.17. EGG2 (single layer) geogrid (a) before pullout test, (b) after pullout test

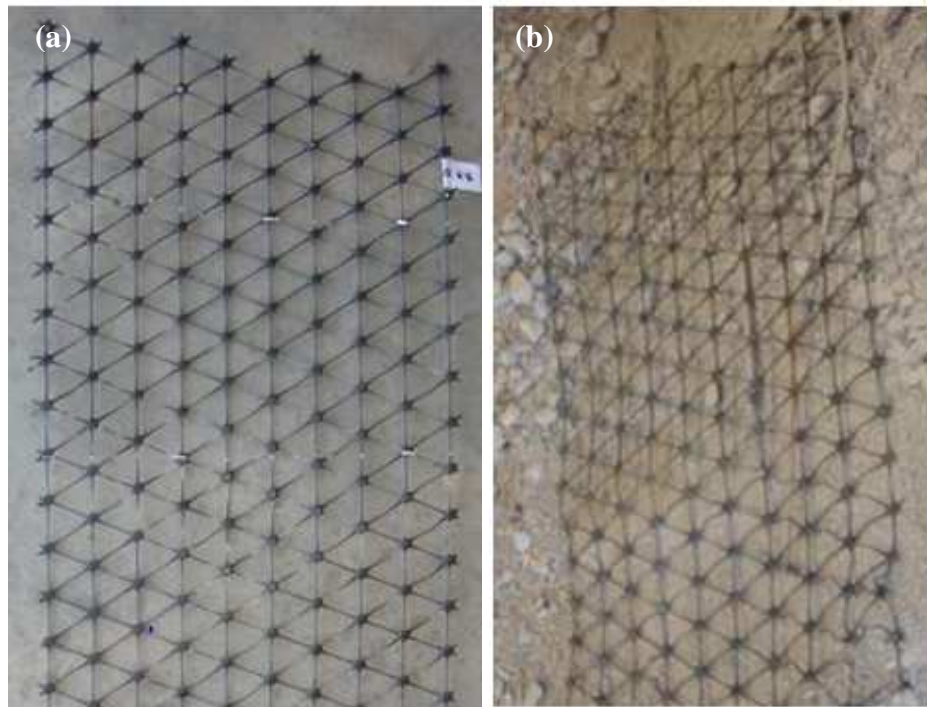


Figure 8.18. EGG3 geogrid (a) before pullout test, (b) after pullout test

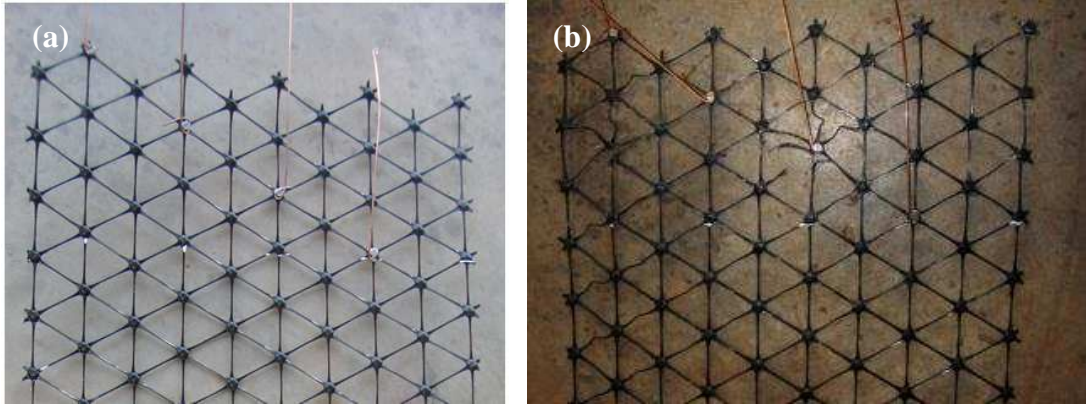


Figure 8.19. EGG4 geogrid (a) before pullout test, (b) after pullout test

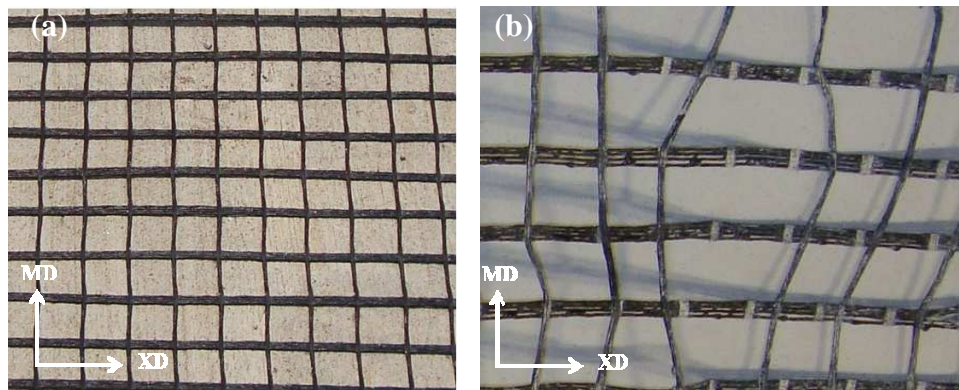


Figure 8.20. WGG1 geogrid (a) before pullout test, (b) after pullout test

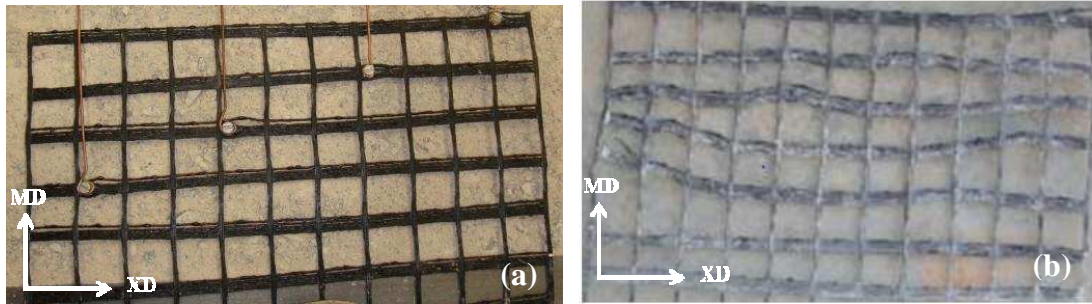


Figure 8.21. WGG2 geogrid (a) before pullout test, (b) after pullout tes

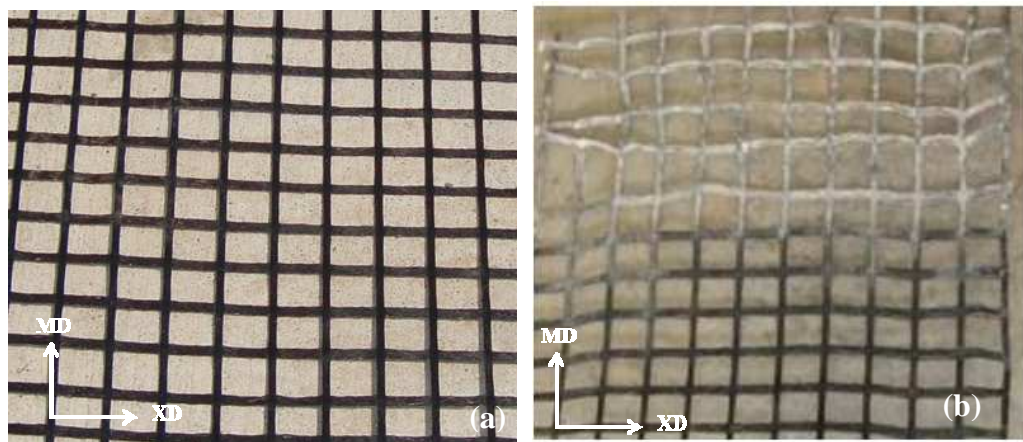


Figure 8.22. WGG3 geogrid (a) before pullout test, (b) after pullout test

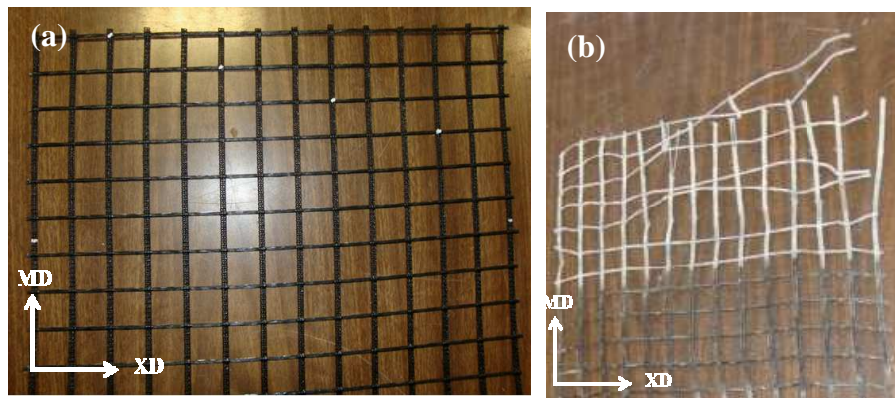


Figure 8.23. KGG1 geogrid (a) before pullout test, (b) after pullout test

Two additional pullout tests were carried out on 0.61 m-long (embedded length) EGG1 and WGG1 geogrid specimens at 3.3 kPa overburden pressure. A summary of all pullout tests on geogrid products in this study is given in **Table 8.1**.

Table 8.1. Summary of pullout tests on geogrids in this study

Geogrid	Type	Embedded Length, L_c (mm)	Overburden Pressure (kPa)			Total Overburden Pressure on Geogrid (kPa)	Equivalent Aggregate Thickness (mm)
			Aggregate	Sand	EPC		
EGG1	$S_R S_J$ Biaxial Extruded	152	3.30	0	0	3.30	152
		152	6.60	0.45	0	7.05	305
		152	6.60	0.45	4.25	11.30	522
		610	3.30	0	0	3.30	152
EGG2 (single layer)	$W_R S_J$ Biaxial Extruded	610	3.30	0	0	3.30	152
		610	4.95	0	0	4.95	229
		610	6.60	0	0	6.60	305
EGG3	$S_R S_J$ Triaxial Extruded	610	3.30	0	0	3.30	152
		610	4.95	0	0	4.95	229
		610	6.60	0	0	6.60	305
		356	3.30	0	0	3.30	152
EGG4	$S_R S_J$ Triaxial Extruded	365	3.30	0	0	3.30	152
		365	4.95	0	0	4.95	229
		365	6.60	0	0	6.60	305
WGG1	$S_R S_J$ Biaxial Woven	152	3.30	0	0	3.30	152
		152	6.60	0	0	6.60	305
		152	6.60	0.45	4.45	11.50	531
		610	3.30	0	0	3.30	152
WGG2	$S_R S_J$ Biaxial Woven	152	3.30	0	0	3.30	152
		152	4.95	0	0	4.95	229
		152	5.50	0	0	5.50	254
		152	6.60	0	0	6.60	305
		152	6.60	0.45	4.45	11.50	531
WGG3	$S_R W_J$ Biaxial Woven	152	3.30	0	0	3.30	152
		152	4.95	0	0	4.95	229
		152	6.60	0	0	6.60	305
		152	6.60	0.45	4.91	11.96	552
KGG1	$S_R W_J$ Biaxial Woven	152	3.30	0	0	3.30	152
		152	6.60	0	0	6.60	305
		152	6.60	0.45	4.45	11.50	531

Notes: $S_R S_J$: Strong Rib Strong Junction, $S_R W_J$: Strong Rib Weak Junction, $W_R S_J$: Weak Rib Strong Junction

8.4. Pullout Test Results and Analysis

Pullout responses of the geogrid products listed in **Table 8.1** subjected to different confining pressures are shown in **Figure 8.24** through **Figure 8.50**.

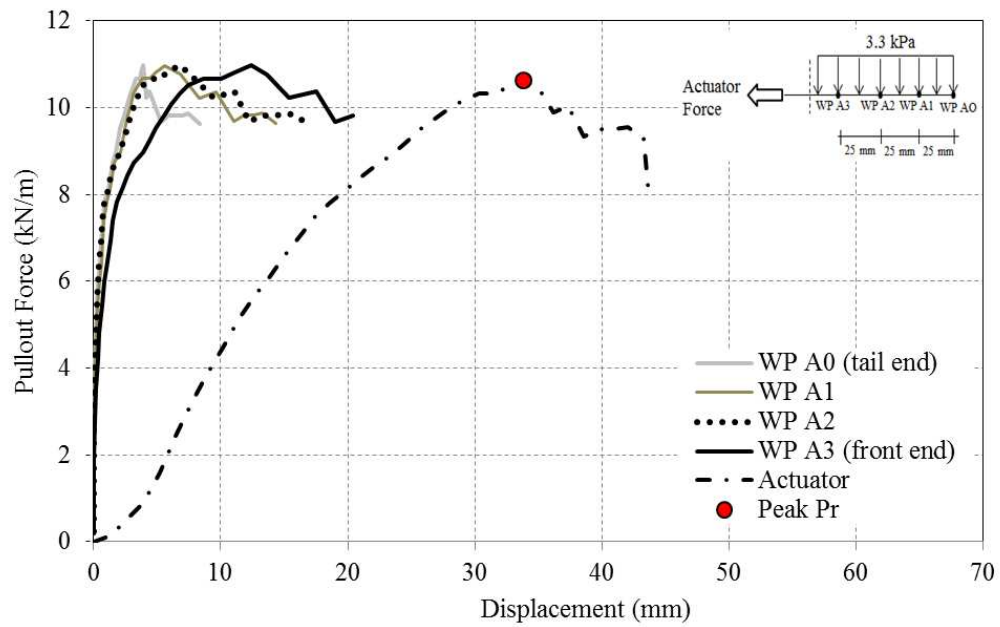


Figure 8.24. Pullout response results of EGG1 geogrid in ODOT Type-A aggregate subjected to 3.30 kPa overburden pressure (WP: Wire-line Potentiometers)

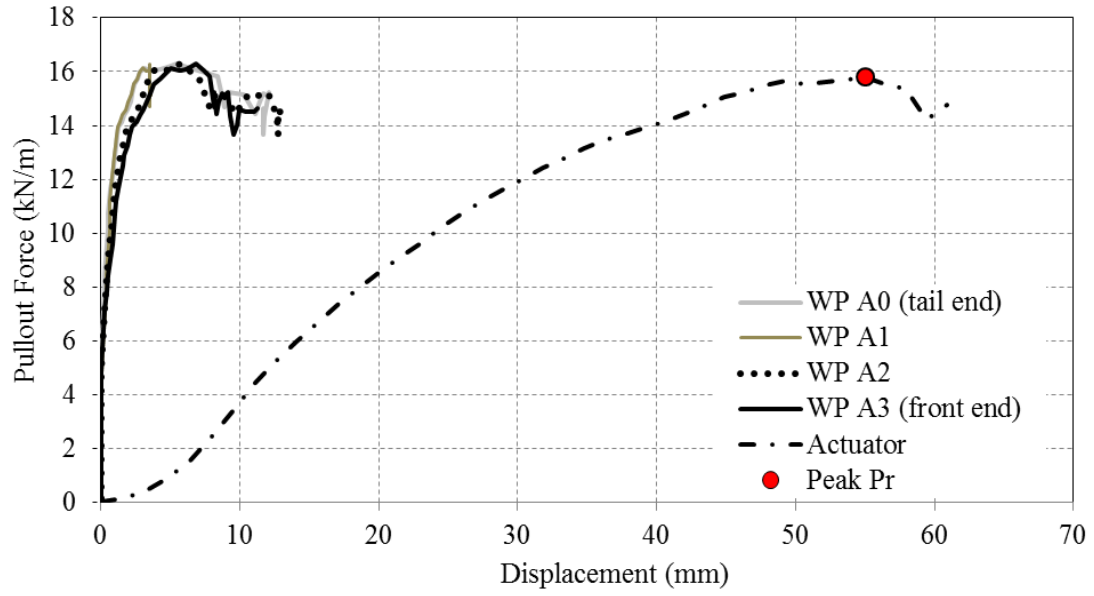


Figure 8.25. Pullout response results of EGG1 geogrid in ODOT Type-A aggregate subjected to 7.07 kPa overburden pressure

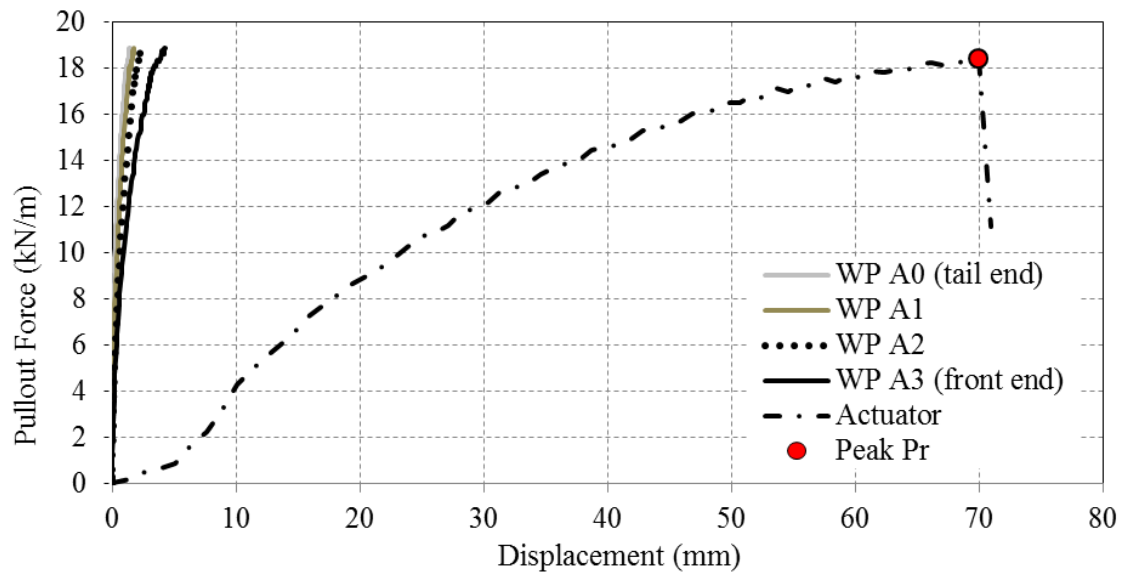


Figure 8.26. Pullout response results of EGG1 geogrid in ODOT Type-A aggregate subjected to 11.65 kPa overburden pressure

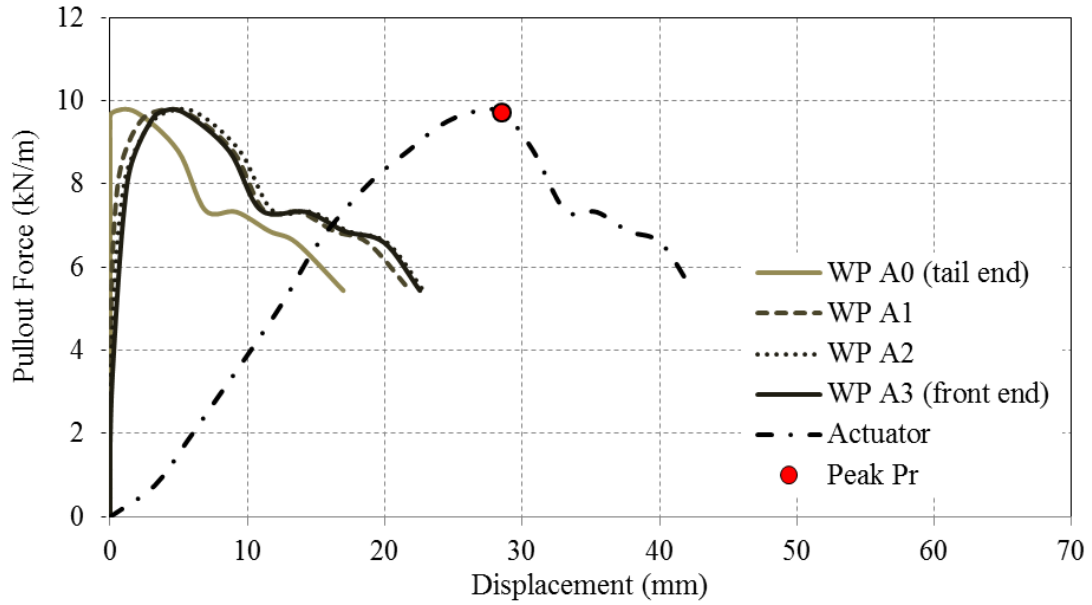


Figure 8.27. Pullout response results of EGG1 geogrid in ODOT Type-A aggregate subjected to 3.3 kPa overburden pressure (0.6 m embedment length)

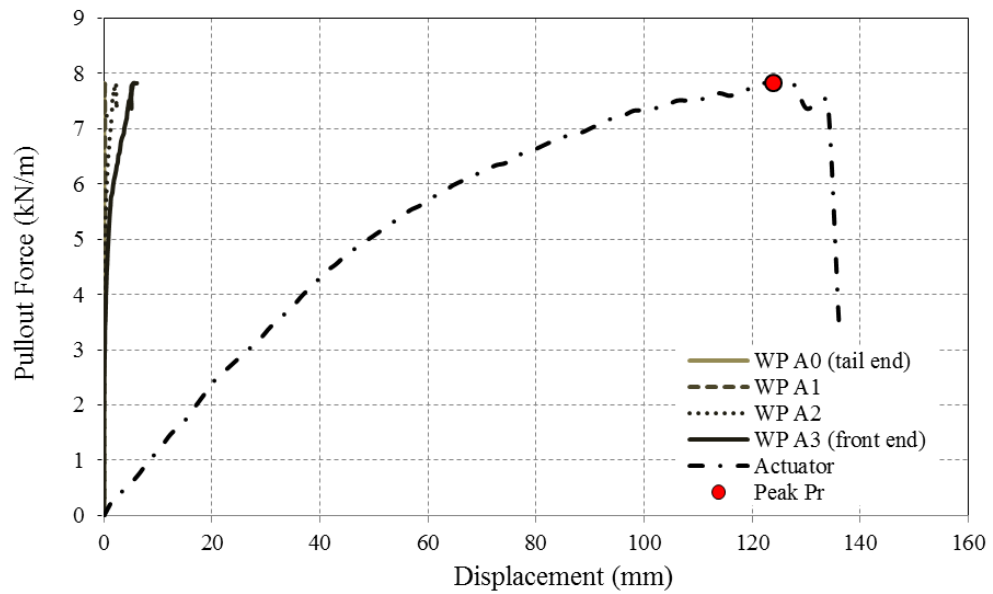


Figure 8.28. Pullout response results of EGG2 (single layer) geogrid in ODOT Type-A aggregate subjected to 4.95 kPa overburden pressure

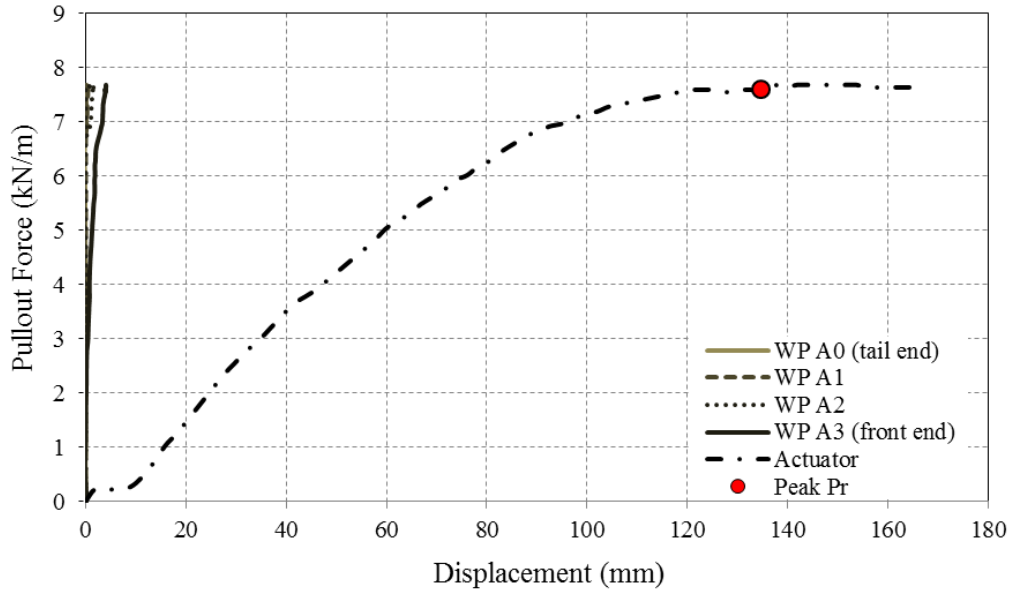


Figure 8.29. Pullout response results of EGG2 (single layer) geogrid in ODOT Type-A aggregate subjected to 6.6 kPa overburden pressure

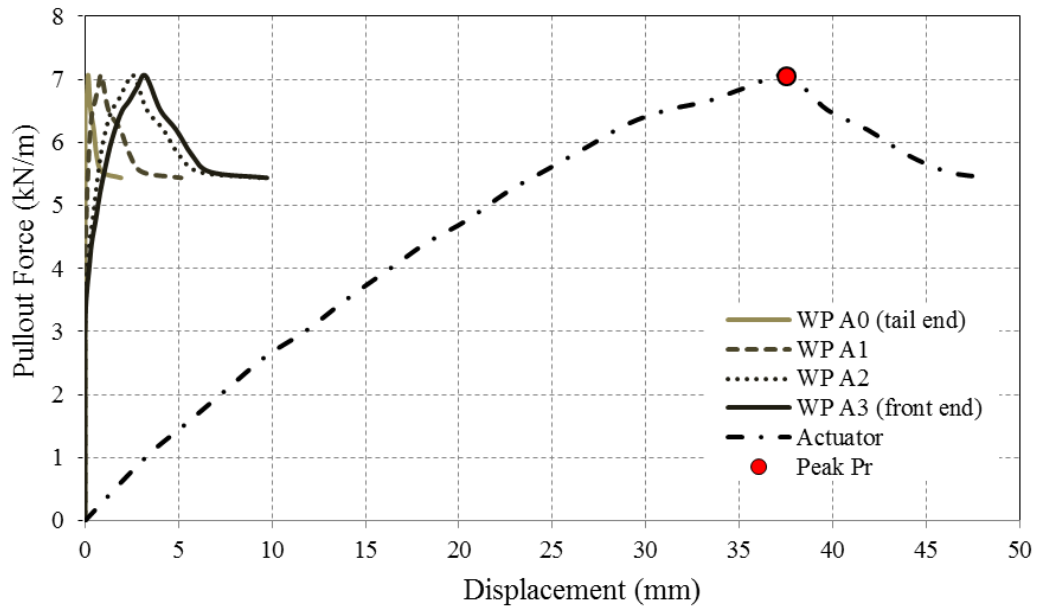


Figure 8.30. Pullout response results of EGG3 geogrid in ODOT Type-A aggregate subjected to 3.3 kPa overburden pressure

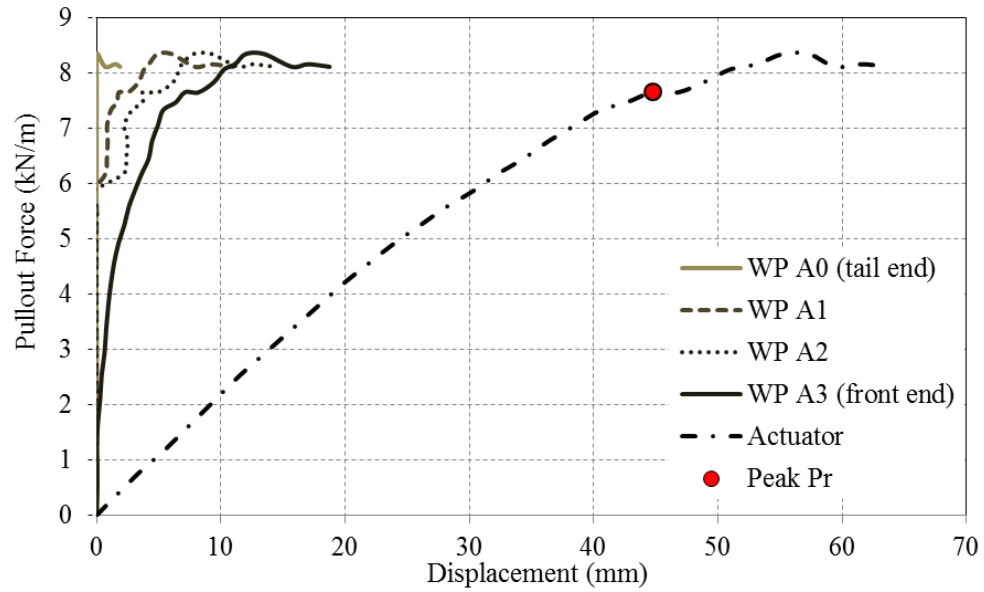


Figure 8.31. Pullout response results of EGG3 geogrid in ODOT Type-A aggregate subjected to 3.3 kPa overburden pressure (0.6 m embedded length)

It should be noted that in two test cases [i.e. EGG3 subjected to 4.95 kPa overburden pressure (**Figure 8.32**) and EGG4 subjected to 6.6 kPa overburden pressure (**Figure 8.36**)], the peak value of the pullout force recorded was due to premature rupture of the geogrid inside the aggregate.

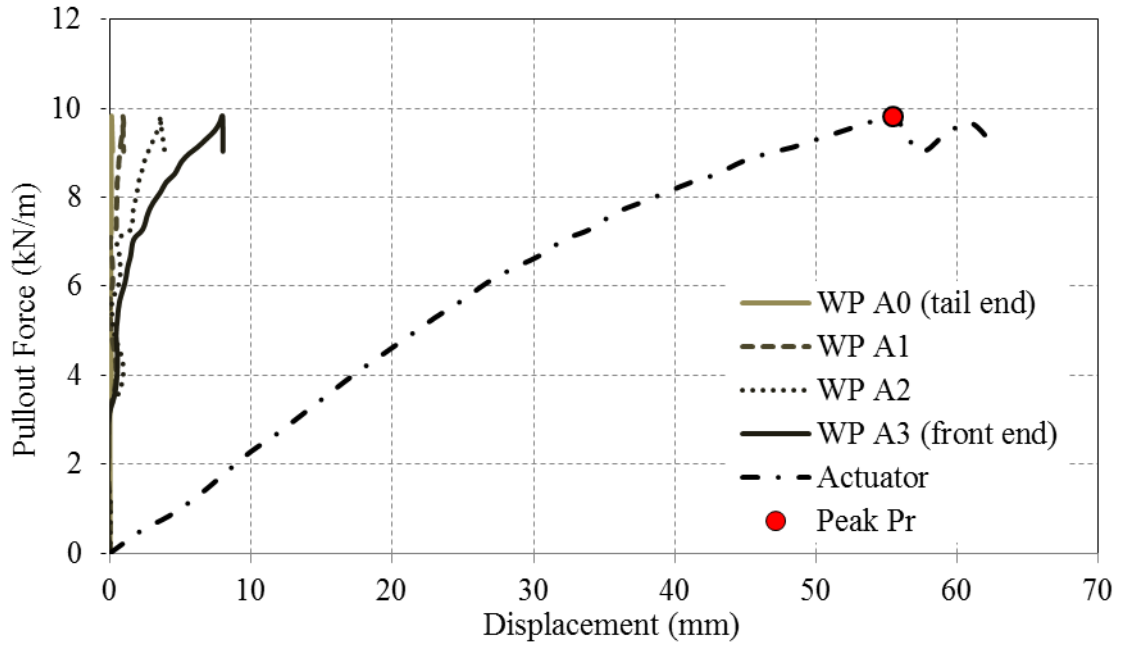


Figure 8.32. Pullout response results of EGG3 geogrid in ODOT Type-A aggregate subjected to 4.95 kPa overburden pressure (0.6 m embedment length)

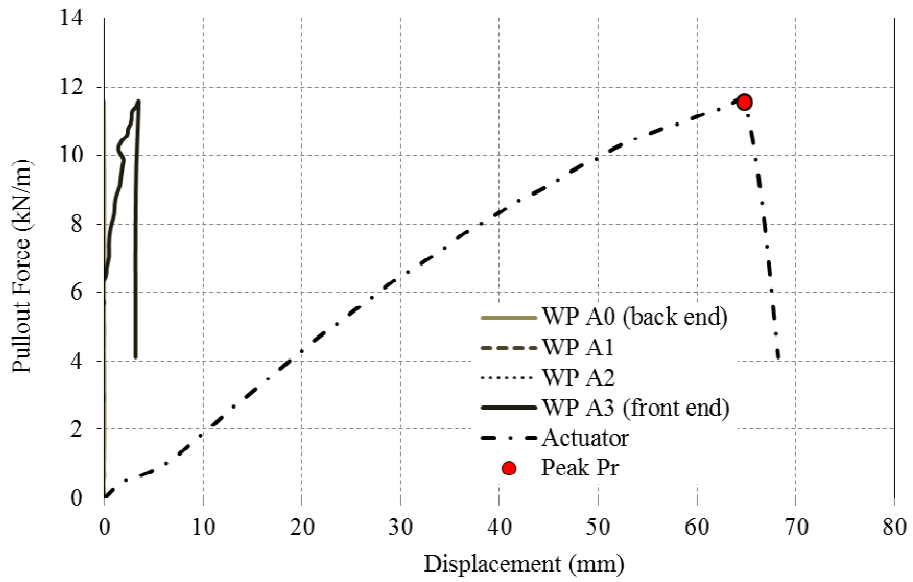


Figure 8.33. Pullout response results of EGG3 geogrid in ODOT Type-A aggregate subjected to 6.6 kPa overburden pressure (0.6 m embedment length)

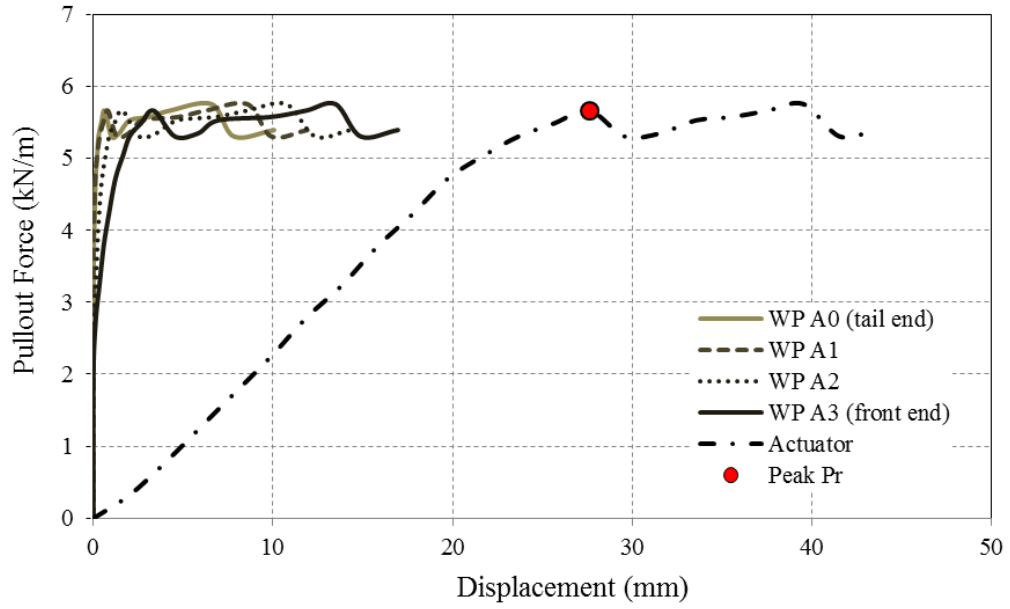


Figure 8.34. Pullout response results of EGG4 geogrid in ODOT Type-A aggregate subjected to 3.3 kPa overburden pressure

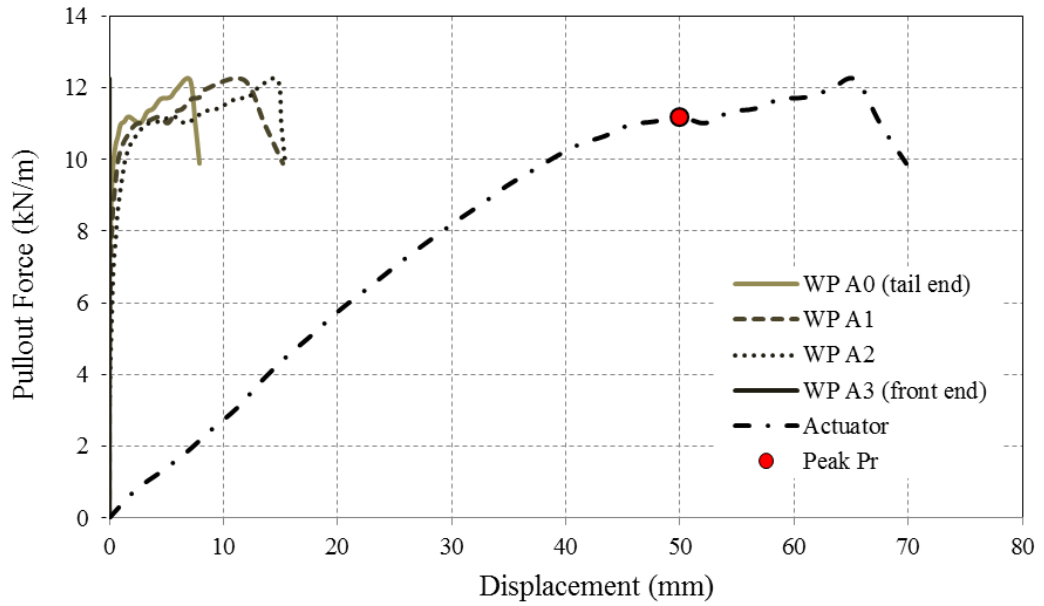


Figure 8.35. Pullout response results of EGG4 geogrid in ODOT Type-A aggregate subjected to 4.95 kPa overburden pressure

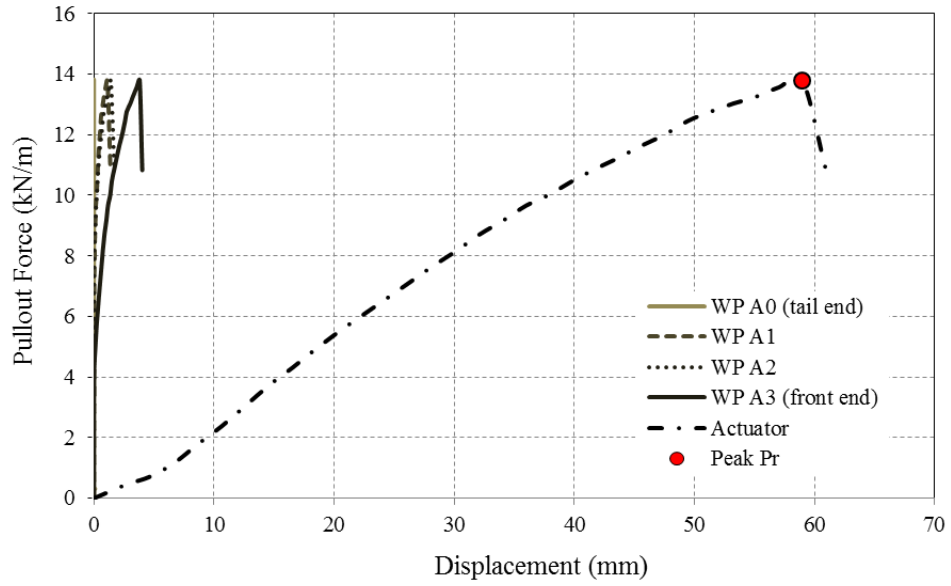


Figure 8.36. Pullout response results of EGG4 geogrid in ODOT Type-A aggregate subjected to 6.6 kPa overburden pressure

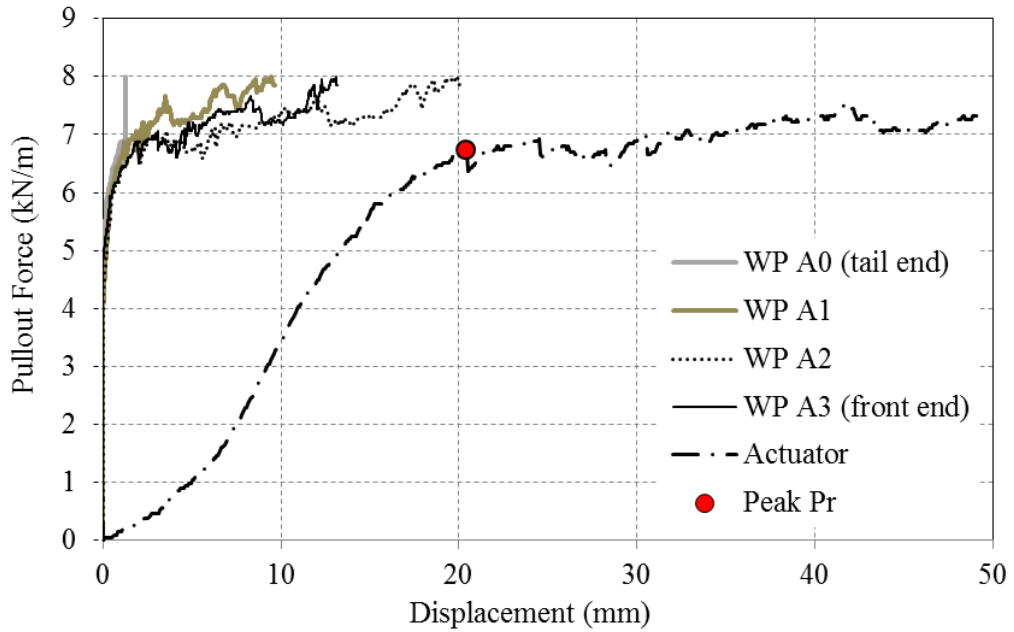


Figure 8.37. Pullout response results of WGG1 geogrid in ODOT Type-A aggregate subjected to 3.3 kPa overburden pressure

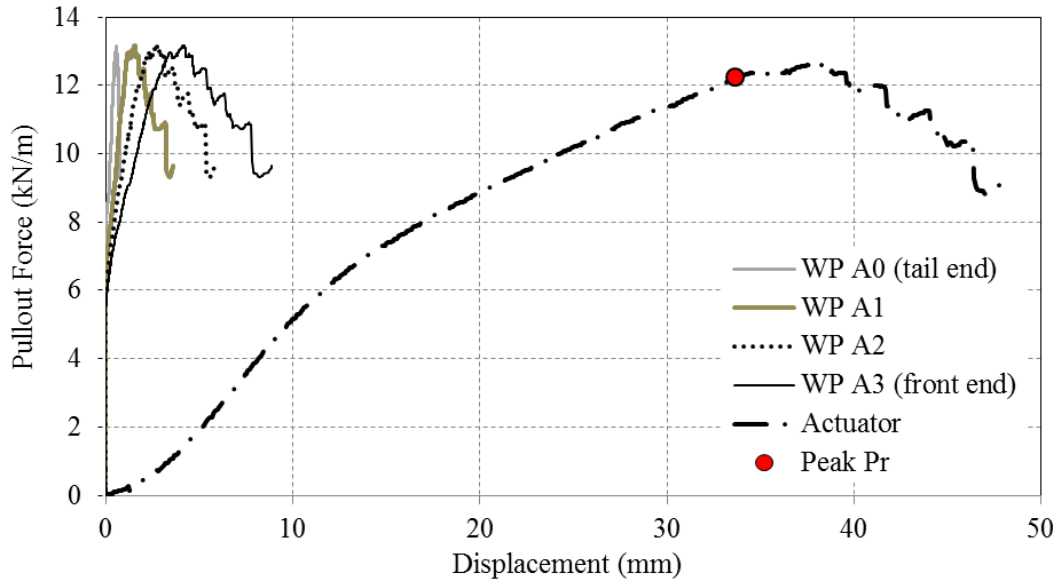


Figure 8.38. Pullout response results of WGG1 geogrid in ODOT Type-A aggregate subjected to 6.60 kPa overburden pressure

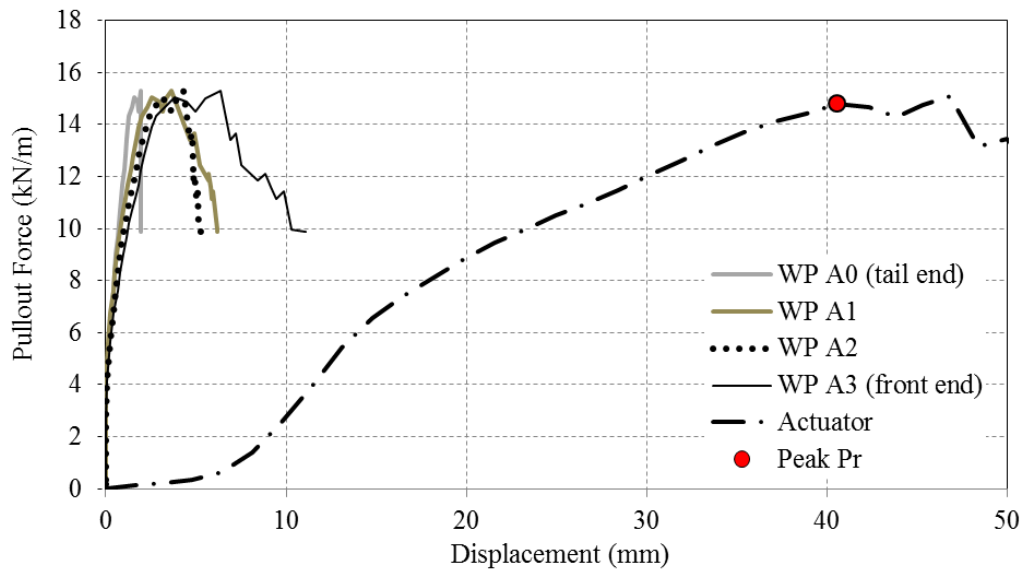


Figure 8.39. Pullout response results of WGG1 geogrid in ODOT Type-A aggregate subjected to 11.61 kPa overburden pressure

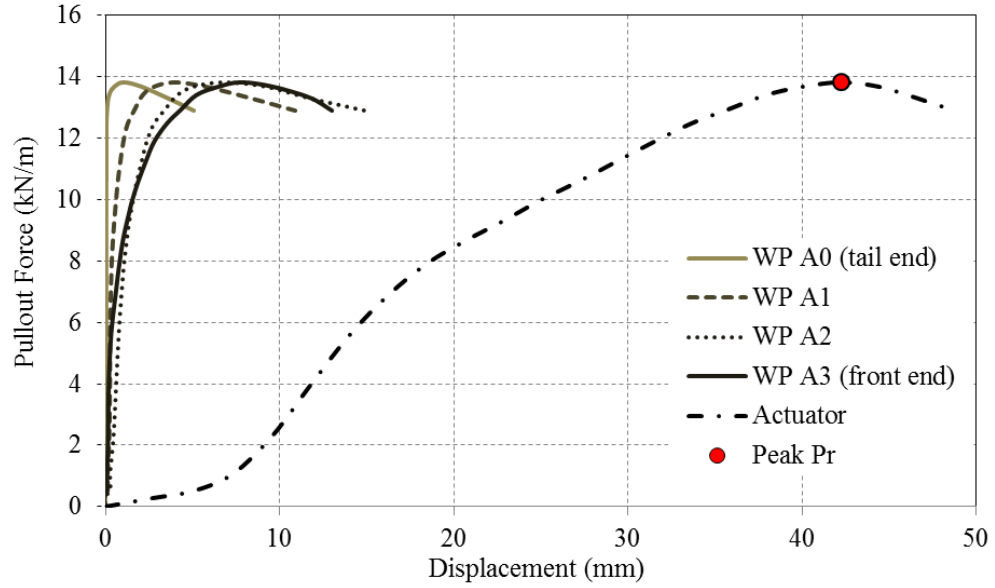


Figure 8.40. Pullout response results of WGG1 geogrid in ODOT Type-A aggregate subjected to 3.3 kPa overburden pressure (0.6 m embedment length)

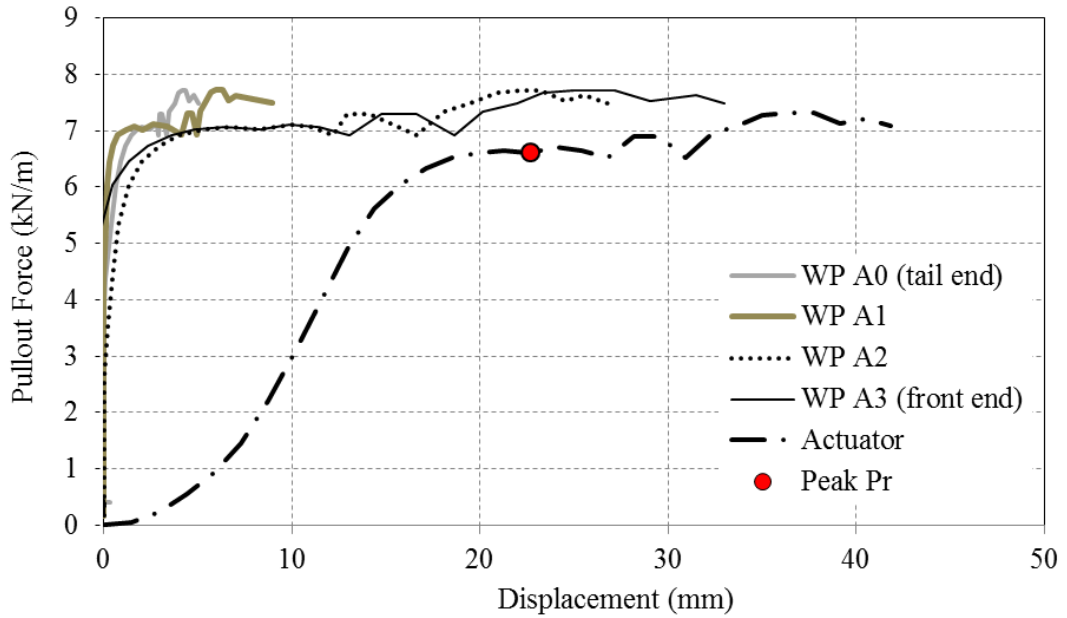


Figure 8.41. Pullout response results of WGG2 geogrid in ODOT Type-A aggregate subjected to 3.30 kPa overburden pressure

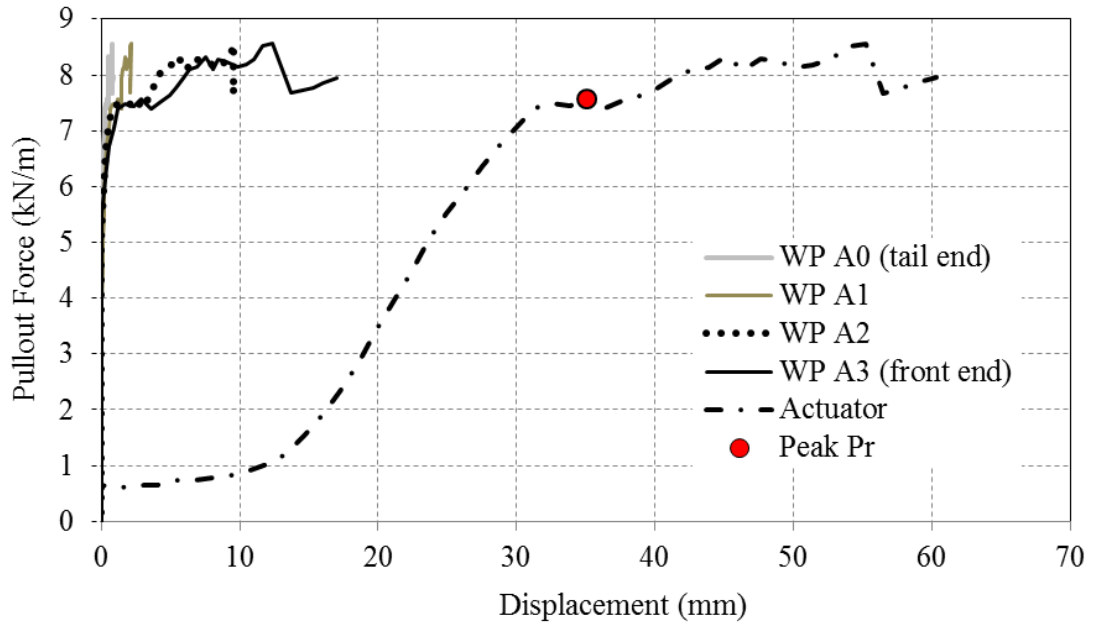


Figure 8.42. Pullout response results of WGG2 geogrid in ODOT Type-A aggregate subjected to 4.95 kPa overburden pressure

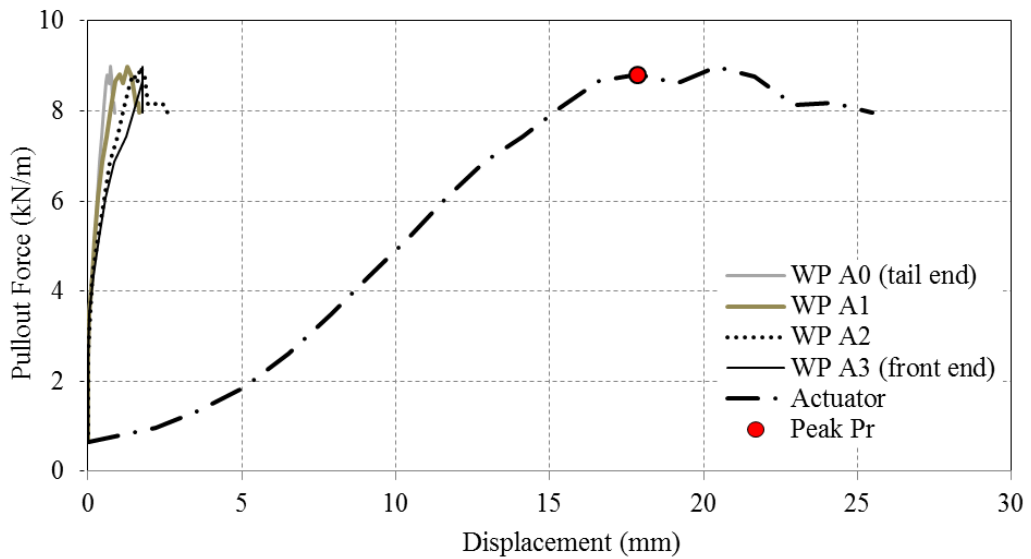


Figure 8.43. Pullout response results of WGG2 geogrid in ODOT Type-A aggregate subjected to 6.60 kPa overburden pressure

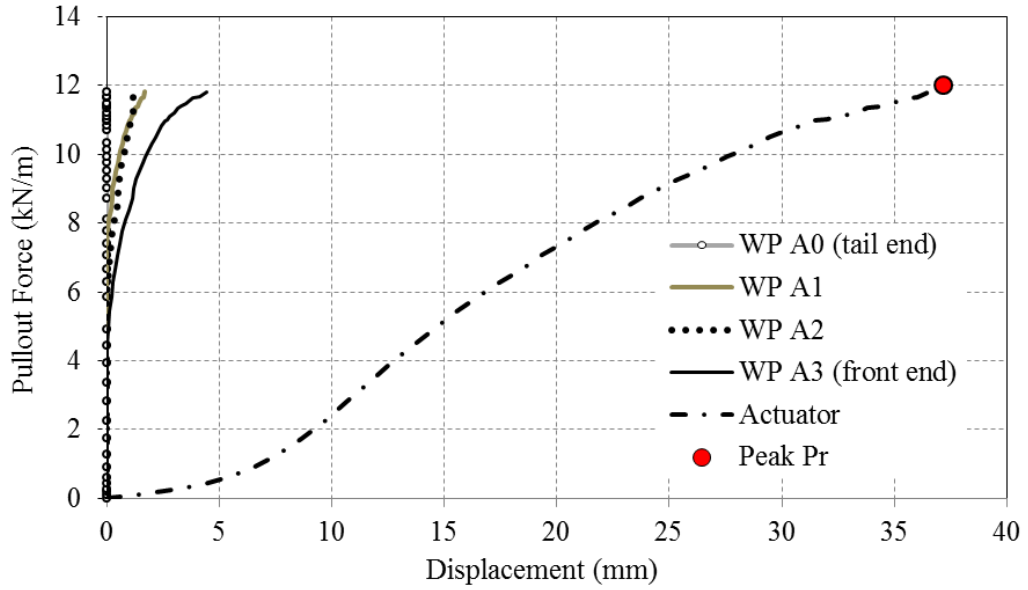


Figure 8.44. Pullout response results of WGG2 geogrid in ODOT Type-A aggregate subjected to 11.5 kPa overburden pressure

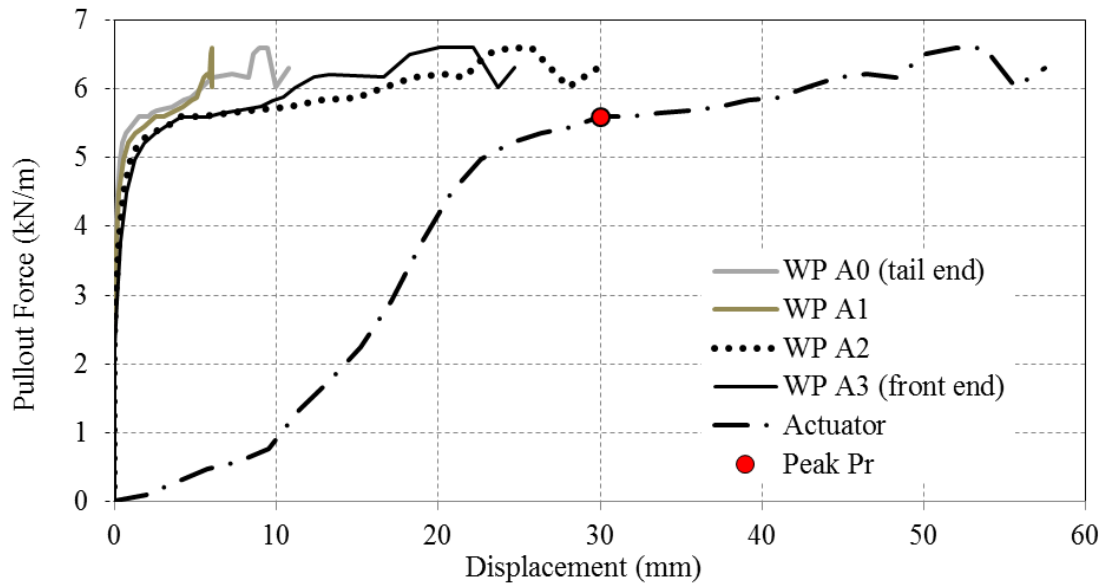


Figure 8.45. Pullout response results of WGG3 geogrid in ODOT Type-A aggregate subjected to 3.30 kPa overburden pressure

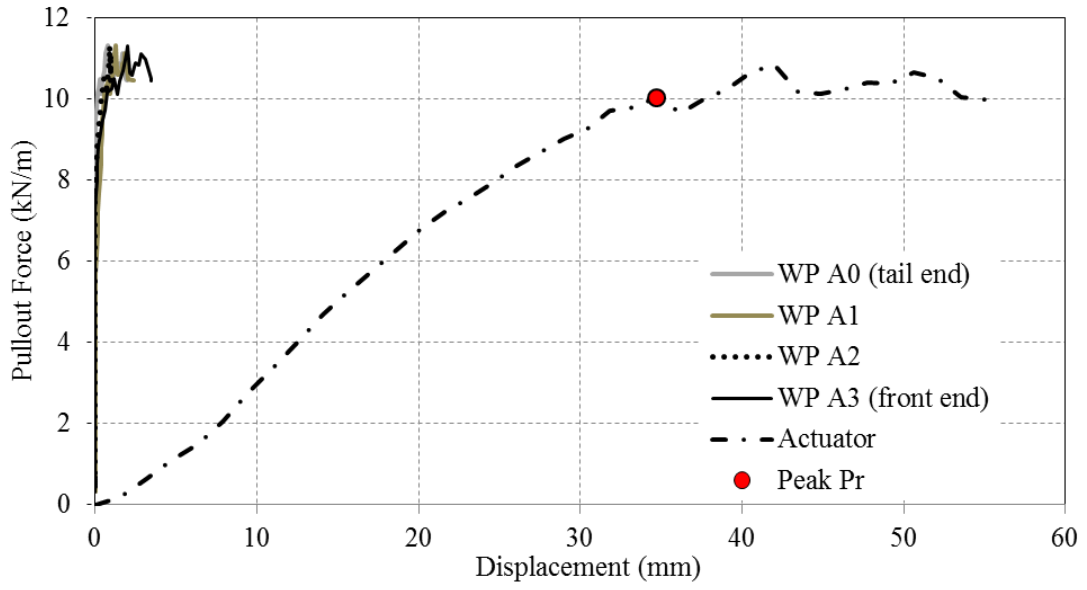


Figure 8.46. Pullout response results of WGG3 geogrid in ODOT Type-A aggregate subjected to 6.6 kPa overburden pressure

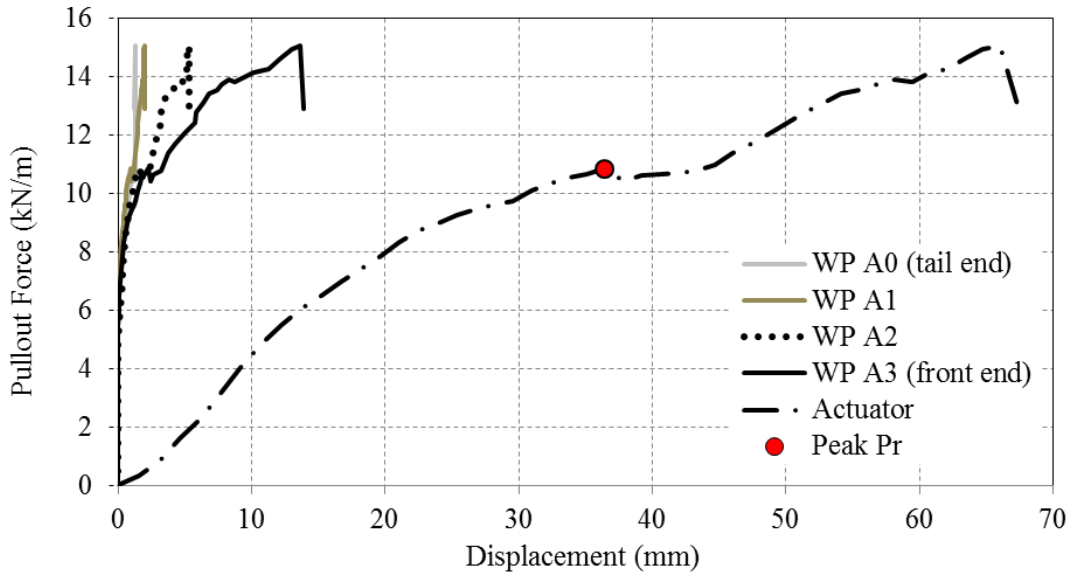


Figure 8.47. Pullout response results of WGG3 geogrid in ODOT Type-A aggregate subjected to 11.96 kPa overburden pressure

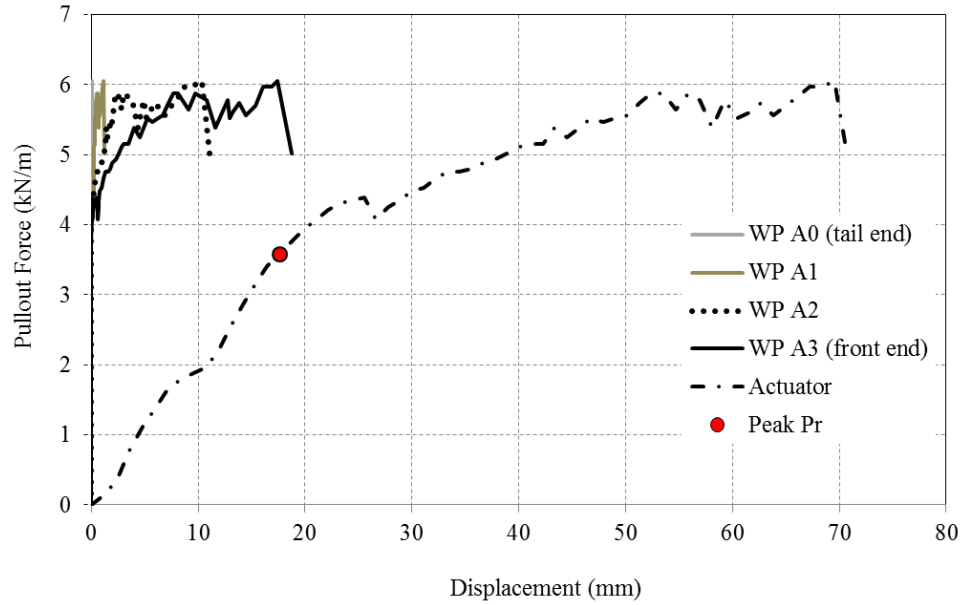


Figure 8.48. Pullout response results of KGG1 geogrid in ODOT Type-A aggregate subjected to 3.3 kPa overburden pressure

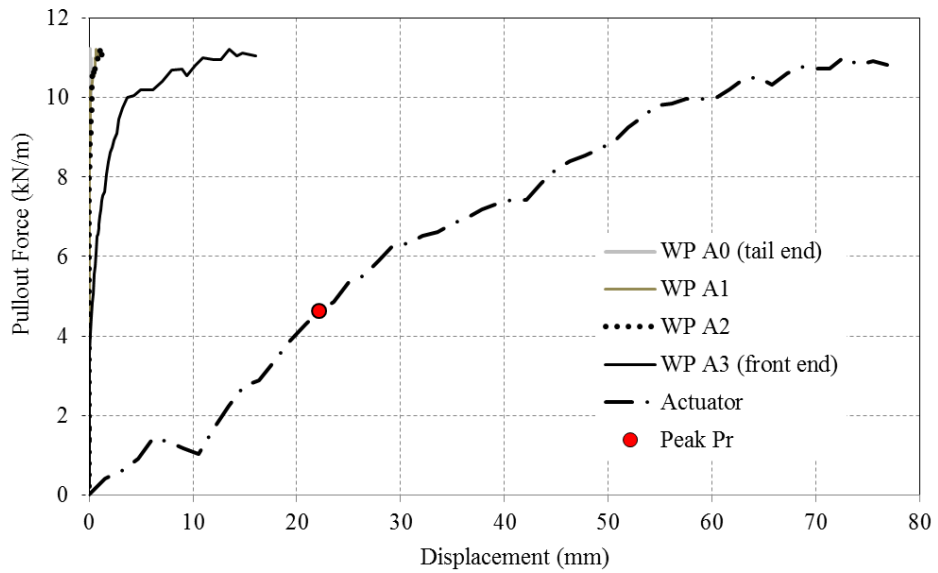


Figure 8.49. Pullout response results of KGG1 geogrid in ODOT Type-A aggregate subjected to 6.6 kPa overburden pressure

After the pullout test on the KGG1 geogrid at 11.5 kPa was completed (**Figure 8.50**), it was noticed that some junctions (especially those which were connected to the brass wires) had been failed. However, no ribs were found to have been ruptured. This failure pattern of KGG1 geogrid is consistent with its classification in **Figure 3.5** as a comparatively weak-junction but strong-rib geogrid.

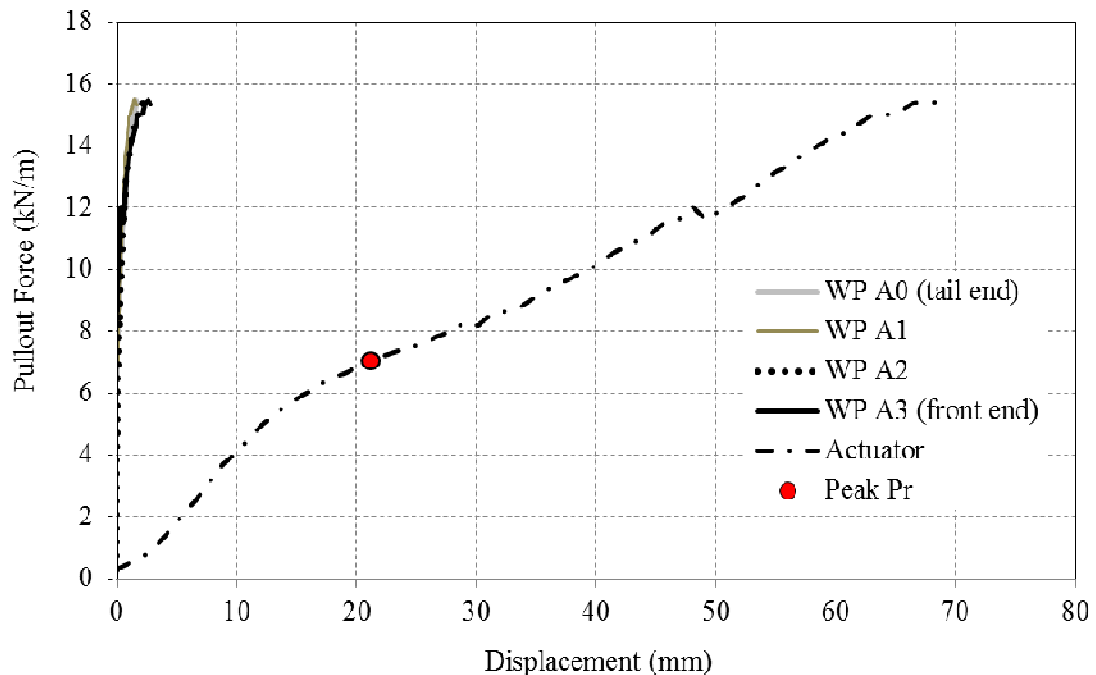


Figure 8.50. Pullout response results of KGG1 geogrid in ODOT Type-A aggregate subjected to 11.5 kPa overburden pressure

8.5. Determination of the Peak Pullout Resistance

According to ASTM D6706, the maximum pullout resistance measured during the test should be reported to indicate the pullout resistance of a geosynthetic reinforcement material. However, obtaining consistent pullout test data and getting a

well-defined peak for geogrids in aggregates is challenging due to significant interlocking that develops between these materials. In the pullout test data presented in this paper, the ultimate pullout resistance, P_r , for each test case had to be determined by inspection. In several cases, this value was determined as the first peak in the pullout response curve that preceded a plateau, followed by subsequent peaks or a monotonic increase in the pullout load. These strain-hardening features at larger displacements were attributed to the likely influence of the front boundary condition and were therefore dismissed. This was done even though the test box included a pair of 200 mm-long sleeves and Styrofoam blocks on the inside of its front wall to minimize the influence of an otherwise rigid front boundary on the test results. The magnitude of the peak pullout resistance, P_r , is presented in terms of the load per unit reinforcement width in this study.

8.6. Relationship between Peak P_r and Overburden Pressure

Figure 8.51 compares the relationship between the peak pullout resistance, P_r , and the overburden pressure, σ_n , for all geogrid products tested in this study. Results in **Figure 8.51** indicate that the EGG1 geogrid with the largest 5%-strain rib strength and comparatively larger junction strength values resulted in the largest pullout resistance among all geogrids tested. The triaxial geogrid (EGG4), with the largest ultimate junction strength values both in MD (795 N) and XD (792 N) showed the largest increase in its pullout resistance with overburden pressure among all the geogrids examined. Conversely, the KGG1 geogrid with the smallest junction and rib strength

values showed the weakest pullout characteristics (i.e. resistance and slope). Basic statistical information related to the results shown in **Figure 8.51** is given in **Table 8.2**.

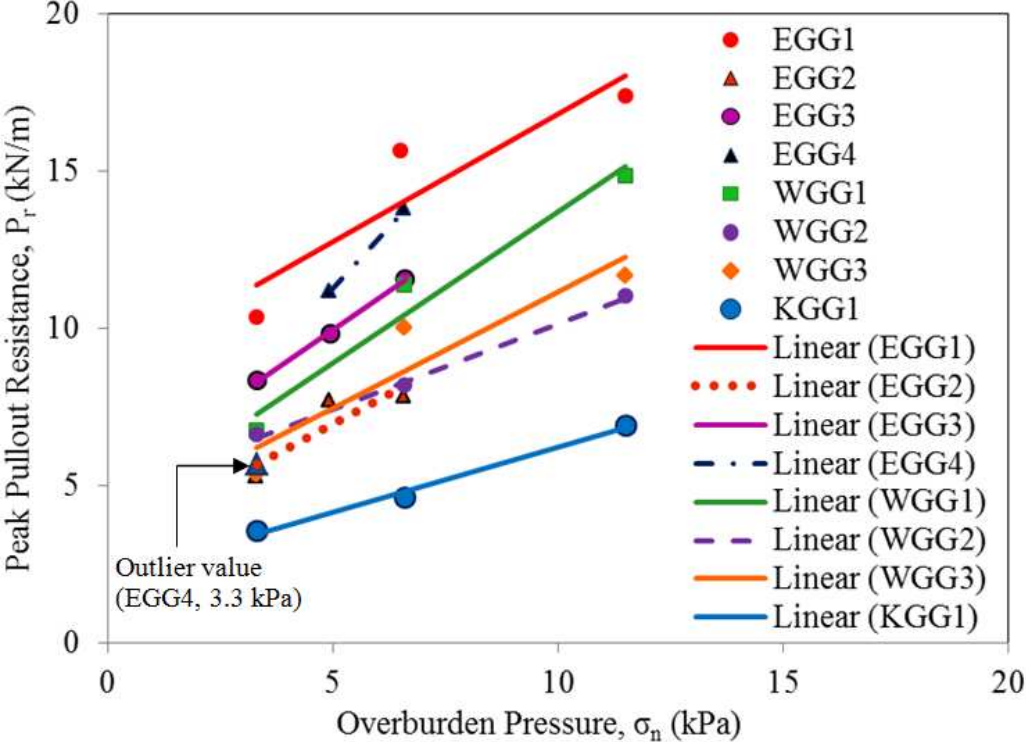


Figure 8.51. Peak pullout resistance of geogrids tested in this study as a function of overburden pressure

Table 8.2. Statistical data for the results shown in **Figure 8.51**

Geogrid	Linear Regression Equation	R ² -value	Slope, m	Comment
EGG1	$P_r = 0.82\sigma + 8.66$	0.84	0.82	
EGG2	$P_r = 0.76\sigma + 3.16$	0.79	0.76	
EGG3	$P_r = 0.98\sigma + 5.07$	1.00	0.98	
EGG4	$P_r = 1.58\sigma + 3.36$	1.00	1.58	Largest gradient
WGG1	$P_r = 0.96\sigma + 4.11$	0.96	0.96	
WGG2	$P_r = 0.54\sigma + 4.74$	1.00	0.54	
WGG3	$P_r = 0.74\sigma + 3.76$	0.86	0.74	
KGG1	$P_r = 0.42\sigma + 2.07$	0.99	0.42	Smallest gradient

8.7. Correlations between Peak P_r and Geogrid Strength Properties

Figure 8.52 shows the correlations between the measured pullout resistance and index strength properties in the machine direction for the geogrids tested. Results shown in **Figure 8.52a,b** indicate that the in-aggregate performances of the geogrids examined show a reasonable correlation with their rib strength at 2% and 5% strain within the range of overburden pressures examined (i.e. 3.3 kPa - 11.5 kPa). However, rib strength at 2%-strain appears to be more influential than rib strength at 5%-strain and ultimate rib strength because the slopes of the corresponding regression lines are the greatest (1.09 for 11.5 kPa, 0.41 for 6.6 kPa and 0.43 for 3.3 kPa). Tang et al. (2008) also observed that the pullout coefficients of interaction of the geogrids tested increased with their rib tensile strength at 2% strain.

Statistical regression of the data shown in **Figure 8.52c** indicates that there is no convincing correlation between the geogrid ultimate rib strength and its maximum

pullout resistance if the manufacturing technique is not taken into account. In contrast, the results in **Figure 8.52d** show a comparatively good correlation between the geogrid ultimate junction strength and its pullout performance ($R^2 > 0.6$). Tang et al. (2008) also showed that the pullout coefficients of interaction of the geogrids tested increased with their junction strength. Chehab et al. (2007) found that wide-width tensile strength and junction strength were the most significant properties of the geogrids influencing their in-aggregate performance.

More careful inspection of the data shown in **Figure 8.52** indicates that geogrid pullout resistance shows a stronger correlation with the properties investigated if examined separately in the EGG and NEGG categories. **Figure 8.53** shows the same data as in **Figure 8.52** with the regression lines plotted separately for the EGG and NEGG categories. It can be observed that the R^2 value for each geogrid property investigated is significantly greater than the corresponding value in **Figure 8.52**.

Figure 8.53 shows the correlations between the measured pullout resistance and index strength properties in the cross-machine direction of the geogrids tested. By and large, results in **Figure 8.53** on the XD index properties are consistent with those obtained for the MD direction (**Figure 8.52**). The geogrids low-strain rib strength (i.e. 2%-strain and 5%-strain strengths) in XD and ultimate junction strength show convincing influences on their pullout performance. Similar to the MD results, the XD tensile strength at 2% strain (with the slopes of the regression lines equal to 0.54 for 11.5 kPa, 0.5 for 6.6 kPa and 0.31 for 3.3 kPa) is more influential than the strength at 5% strain (with the slopes of the regression lines equal to 0.31 for 11.5 kPa, 0.22 for 6.6

kPa and 0.18 for 3.3 kPa) on the pullout performance of the geogrids examined. Cuelho and Perkins (2009) also found that XD rib strength at 2% strain had a more significant role in the in-aggregate performance of the geogrids than their rib strength at 5% strain.

It should be noted that the MD and XD ultimate junction strength values for each of the geogrids tested are comparable. Therefore, the consistency between the results (i.e. statistical regression parameters) shown in **Figure 8.52d** and **Figure 8.53d** are to be expected. On the other hand, the relationships between the geogrid rib strength properties in MD and XD and its MD pullout performance are different. In MD, a greater low-strain rib strength value provides a more confining effect on the aggregate and also controls the longitudinal deformations of the geogrid during the pullout test. In comparison, a combination of high XD-direction rib strength and strong junctions, in addition to the aforementioned MD effects, results in significant interlocking capabilities for the geogrid (i.e. large passive resistance) which contributes to a greater pullout performance. Also, the importance of the 2%-strain rib strength of a geogrid on its in-aggregate performance can be explained by noting that a large value of rib strength at low strains helps to generate significant confining pressure and locked-in stresses on the aggregate during the compaction period.

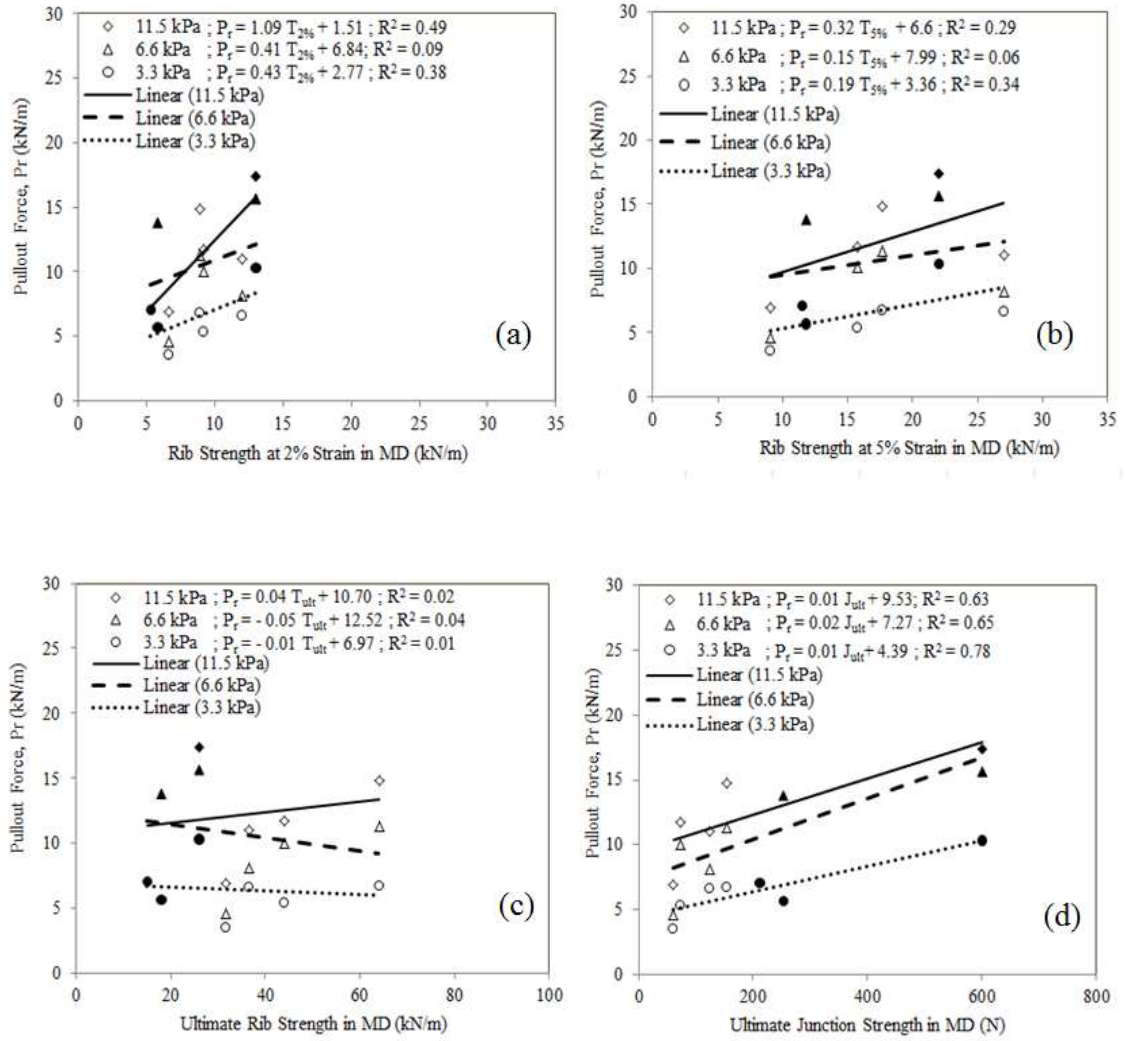


Figure 8.52. Correlations between pullout force and rib tensile strengths in MD at (a) 2% strain, (b) 5% strain and (c) Ultimate rib strengths and (d) Ultimate junction strengths of geogrids examined in this study (EGG: represented by solid markers, NEGG: represented by hollow markers)

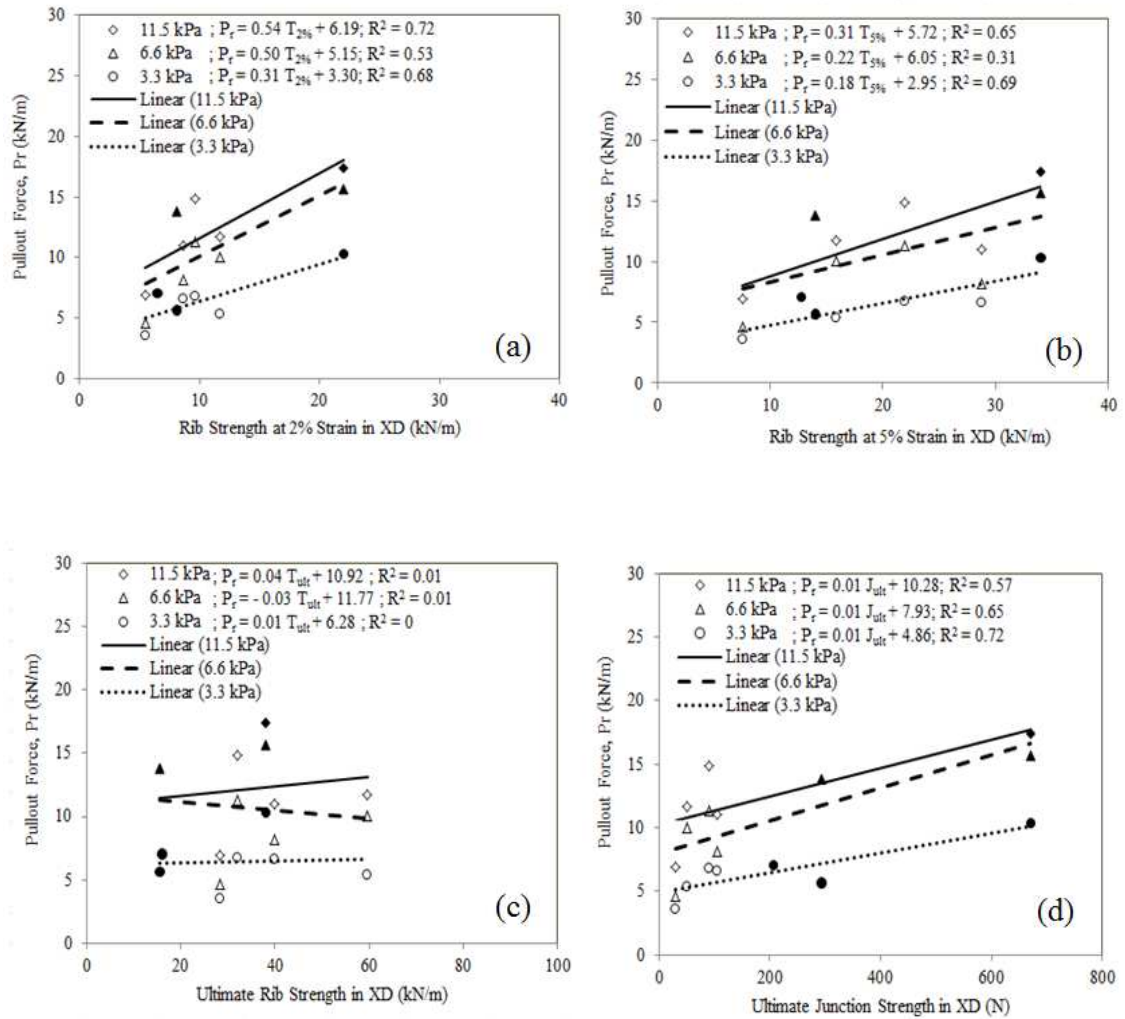


Figure 8.53. Correlation between pullout force and rib tensile strengths in XD at (a) 2% strain, (b) 5% strain and (c) Ultimate rib strengths and (d) Ultimate junction strengths of geogrids examined in this study (EGG: represented by solid markers, NEGG: represented by hollow markers)

Figure 8.54 shows the correlations between the measured pullout resistance and index strength properties in the machine direction of NEGG products. 2%-strain and 5%-strain strength values in MD show convincing influences on their pullout performance (**Figure 8.54a** and **Figure 8.54b**). The tensile strength at 2% strain (with the slopes of the regression lines equal to 0.65 for 11.5 kPa, 0.55 for 6.6 kPa and 0.56 for 3.3 kPa) is more influential than the strength at 5% strain (with the slopes of the regression lines equal to 0.2 for 11.5 kPa, 0.16 for 6.6 kPa and 0.17 for 3.3 kPa) on the pullout performance of the geogrids examined. **Figure 8.54c** indicates that the ultimate rib strength value in MD is an influential parameter in peak pullout performance for NEGG products. **Figure 8.54d** indicates that at all overburden pressures, the ultimate geogrid junction strength has a significant influence on its pullout resistance.

Figure 8.55 shows the correlations between the XD rib and junction properties and the measured pullout resistance in MD for the NEGG products. The geogrids low-strain rib strength (i.e. 2%-strain and 5%-strain strengths in XD) and ultimate junction strength show convincing influences on their pullout performance. Similar to the MD results, the XD tensile strength at 2% strain (with the slopes of the regression lines equal to 0.94 for 11.5 kPa, 0.99 for 6.6 kPa and 0.35 for 3.3 kPa) is more influential than the strength at 5% strain (with the slopes of the regression lines equal to 0.23 for 11.5 kPa, 0.18 for 6.6 kPa and 0.15 for 3.3 kPa) on the pullout performance of the geogrids examined.

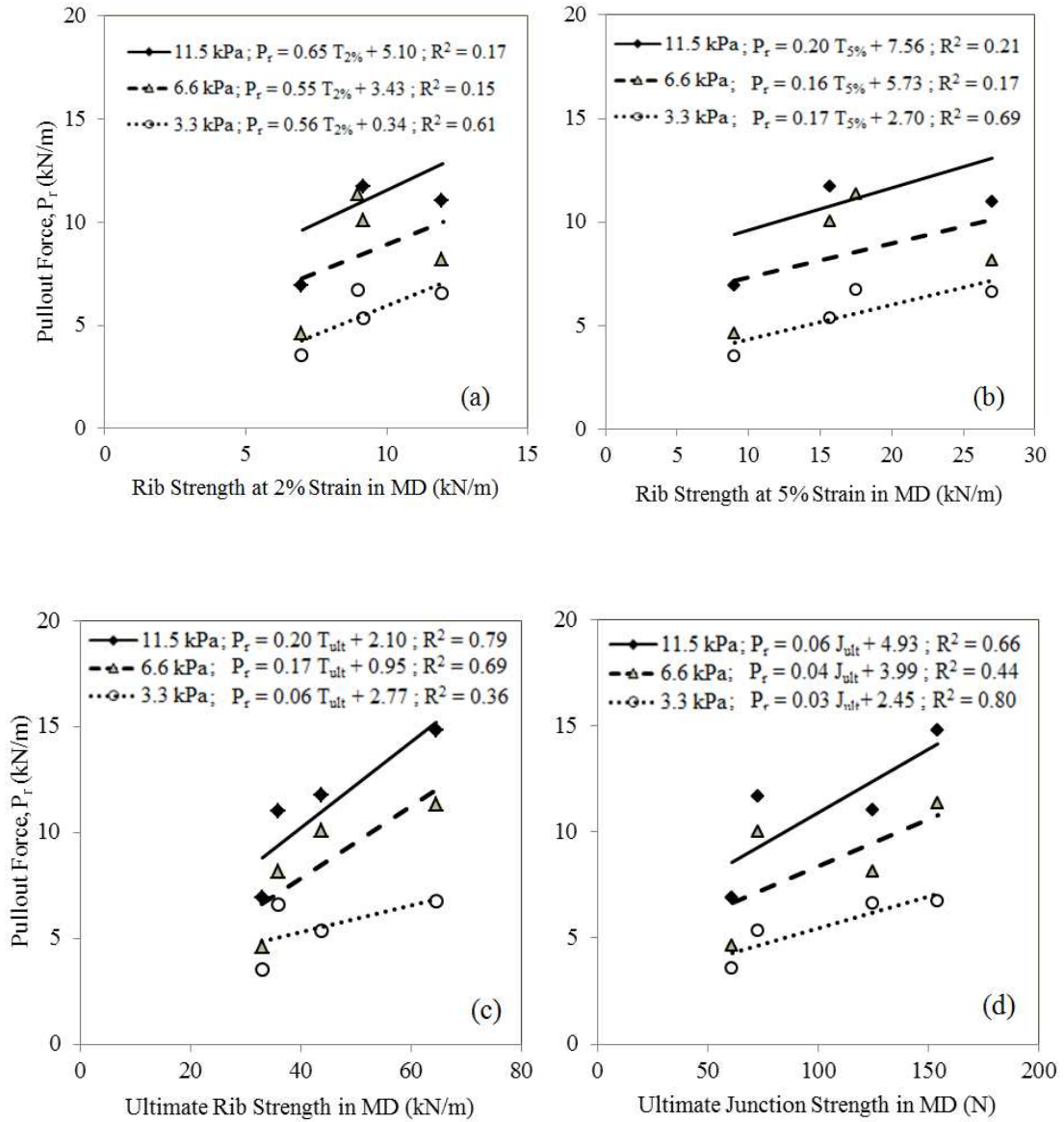


Figure 8.54. Correlation between pullout force and rib tensile strengths in MD at (a) 2% strain, (b) 5% strain and (c) Ultimate rib strengths and (d) Ultimate junction strengths of NEGG geogrids

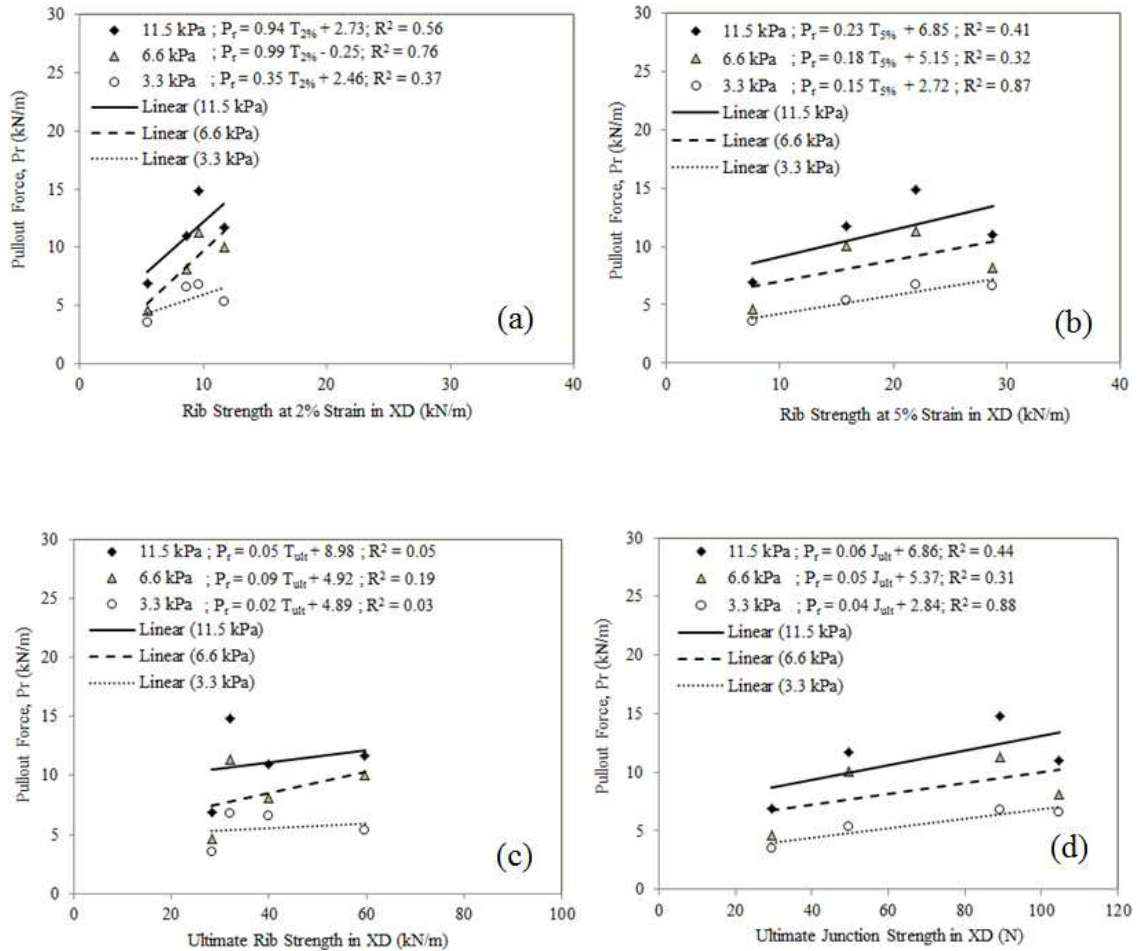


Figure 8.55. Correlation between pullout force and rib tensile strengths in XD at (a) 2% strain, (b) 5% strain and (c) Ultimate rib strength and (d) Ultimate junction strengths of NEGG geogrids

The correlations between pullout resistance and index strength properties in MD and XD of EGG products at 3.3 kPa are shown in **Figure 8.56** and **Figure 8.57**, respectively. Sufficient data points are not available to plot correlations at 6.6 and 11.5 kPa for the EGG geogrids. Nevertheless, 2%-strain and 5%-strain strength values show convincing influences on their pullout performance. Similar to what was observed in the case of NEGG geogrids, the tensile strength of EGG products at 2% strain is more

influential in their pullout performance than their strength at 5% strain. The ultimate rib strength and junction strength of the geogrids both in MD and XD are also correlated reasonably well with their peak pullout performance. Comparison of the regression analysis parameters given in **Figure 8.56** and **Figure 8.57**, indicate that in the case of EGG products, the rib strength properties in MD are slightly more influential in their MD pullout performance than those in XD.

In summary, the low-strain rib strength (i.e. strength at 2% strain and 5% strain) and the ultimate junction strength were found to be important properties of geogrids that influence their pullout performance. The rib strength at 2% strain was found to play a more important role than rib strength at 5% strain, in both MD and XD. The ultimate rib strength also shows a reasonable correlation, when EGG and NEGG products were studied separately. The findings of this study as reported in this chapter are beneficial in understanding the significance of in-isolation properties of geogrids in their pullout performance.

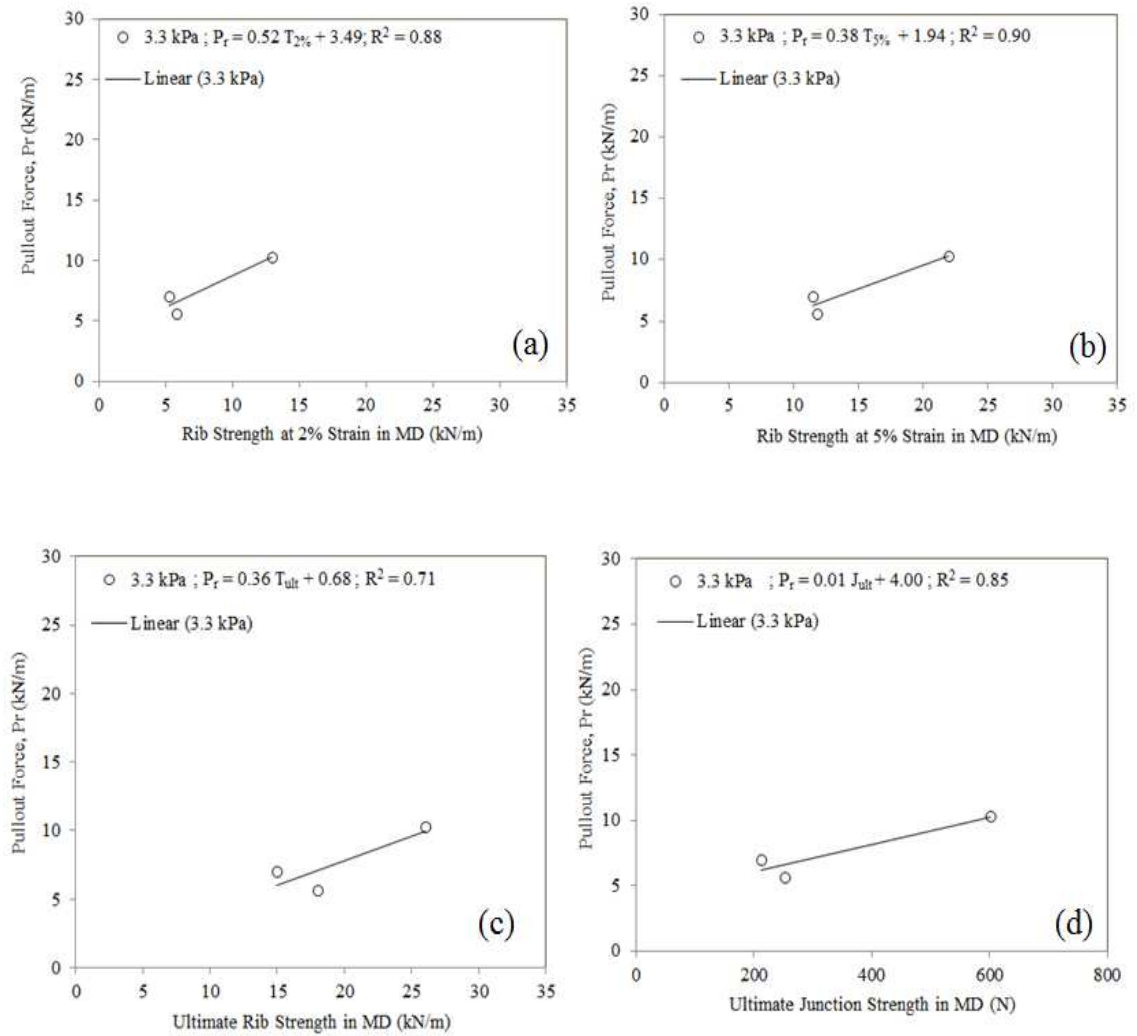


Figure 8.56. Correlation between pullout force and rib tensile strengths in MD at (a) 2% strain, (b) 5% strain and (c) Ultimate rib strengths and (d) Ultimate junction strengths of EGG geogrids

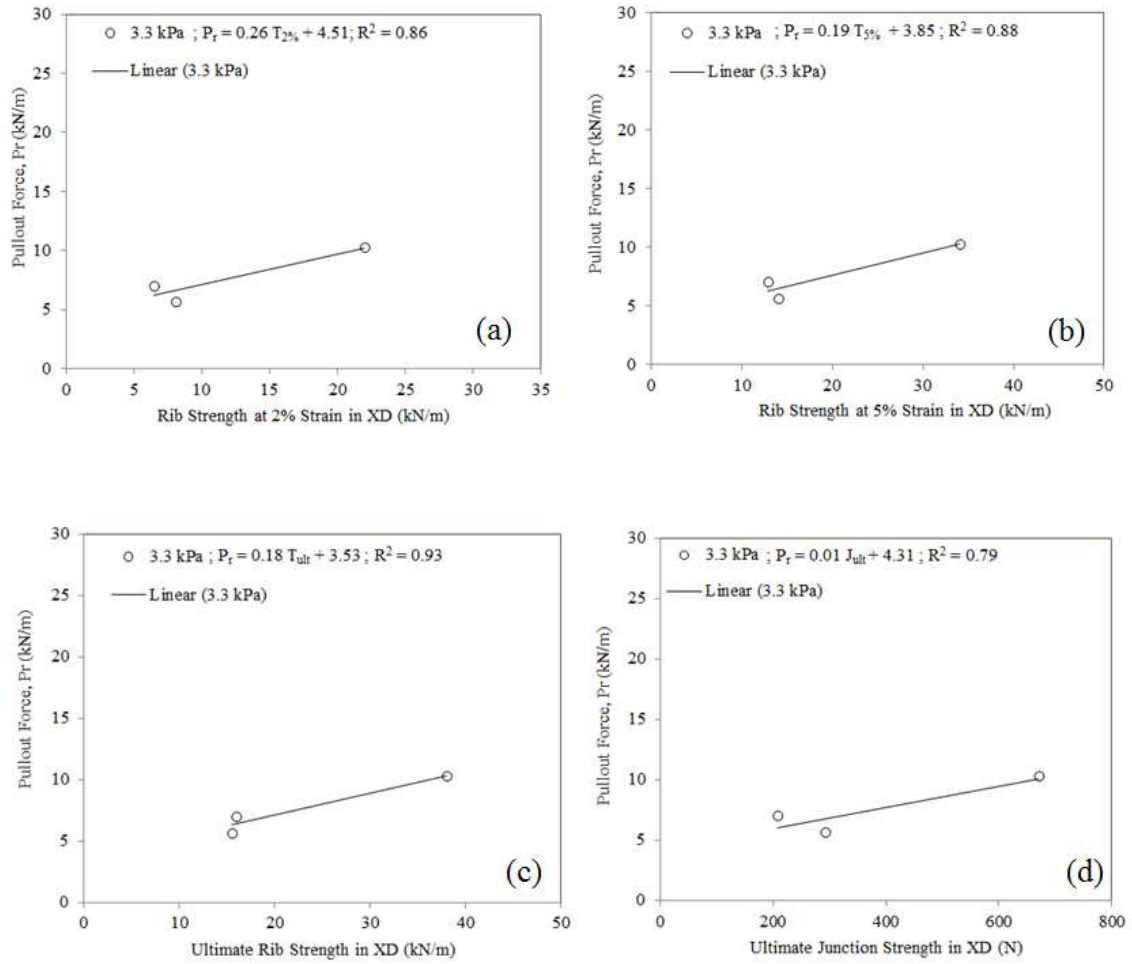


Figure 8.57. Correlation between pullout force and rib tensile strengths in XD at (a) 2% strain, (b) 5% stain and (c) Ultimate rib strengths and (d) Ultimate junction strengths of EGG geogrids

CHAPTER NINE

RESPONSE OF GEOGRID-REINFORCED AGGREGATE-SUBSTRATE SPECIMENS TO SIMULATED WHEEL LOAD

A series of monotonic and cyclic plate load tests was carried out to examine the in-aggregate performance of the selected geogrids when subjected to vertical load simulating tire pressure. The primary objective of the plate load tests was to compare the reinforcing performance of different geogrids subjected to vertical load in nominally identical conditions (as opposed to simulating any specific subgrade soils). The static plate load tests were carried out to determine the influence of test setup (e.g. use of geotextile separator and location of the geogrid within the base layer) on the test results. The cyclic plate load tests were carried out to study the influence of geogrids index properties on their in-aggregate response under repetitive wheel loading simulating traffic load on flexible pavements.

9.1. Static Plate Load Tests

A total of six static plate load tests were carried out to determine the influence of geogrid reinforcement layer and geotextile separator arrangement at the interface between the base course and the sand substrate on the performance of the reinforced base models. The tests were carried out in a 1.83 m (L) \times 1.22 m (W) \times 0.61 m (H) test box. Styrofoam panels were placed against the walls of the test box on the inside to mitigate boundary effects against the lateral movement of aggregates in the box.

The test box was filled with 356 mm of loose sand (unit weight of 12.13 kN/m³ and relative density of 28%) as the subgrade and 203 mm of base aggregate layer. 1.21 m (L) × 1.21 m (W) EGG1 geogrid specimens and non-woven geotextile (**Figure 9.1**) were cut and placed in the test box for these tests. The static plate load test setup and test box are shown in **Figure 9.2** and **Figure 9.3**. Details of the plate load test setup, instrumentation and procedure are given by Wang (2009). Different cases of static plate load tests carried out in this study are summarized in **Table 9.1**.



Figure 9.1. Preparation of the geogrid and geotextile specimen for a static plate load test

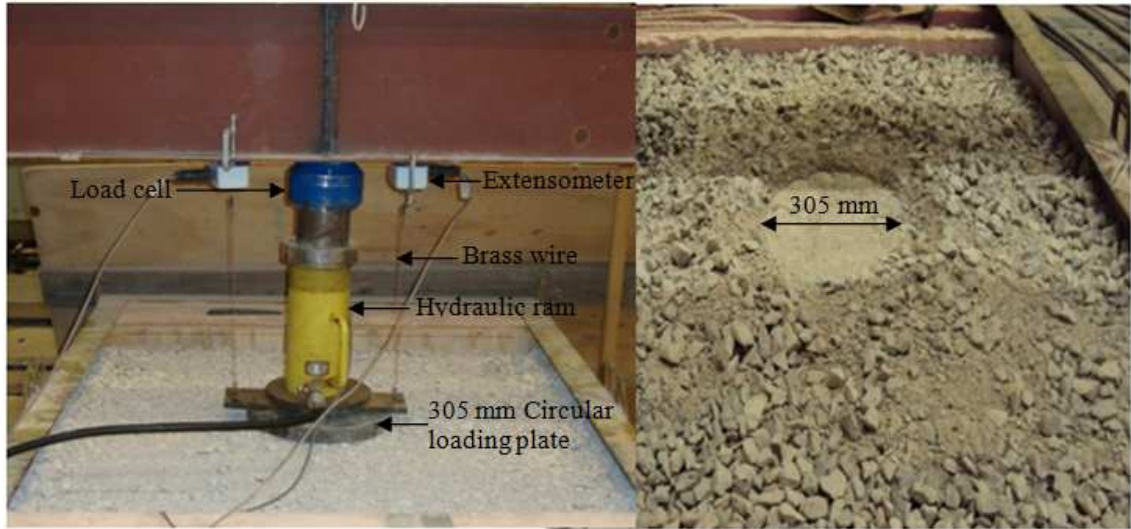


Figure 9.2. Static plate load test setup



Figure 9.3. Test box used for the static plate load tests

Table 9.1. Summary of static plate load tests

Plate Load Test Number	Geotextile Separator	Type of Geogrid	Location of Geogrid	Comments
1	Yes	Not Used	-	This test was done only for compaction verification purposes
2	Yes	Not Used	-	-
3	No	EGG1	On Sand	-
4	Yes	EGG1	25 mm above geotextile	25 mm aggregate was placed on geotextile
5	No	Not Used	-	-
6	Yes	EGG1	Directly on geotextile	Geogrid and geotextile were in contact with each other

Notes:

Sand Thickness = 356 mm

Aggregate Thickness = 203 mm

Figure 9.4 shows the load-settlement results for the test cases listed in **Table 9.1**. These results indicate that: 1) the geotextile separator did not provide any significant reinforcing effect within the conditions of the test setup; 2) placing the geogrid at the aggregate-substrate interface without the separator layer in contact with it improved the interface strength properties and helped mobilize the tensile capacity of geogrid from the start of the test. In other words, adequate interlocking with aggregates is key to achieving effective reinforcement; and 3) placement of a thin aggregate layer

between the geogrid and geotextile layers could be an effective way in the laboratory to simulate the rugged interface that invariably exists between the aggregate base course and the underlying subgrade in the field, which allows the geogrid reinforcement to properly interlock with the aggregate.

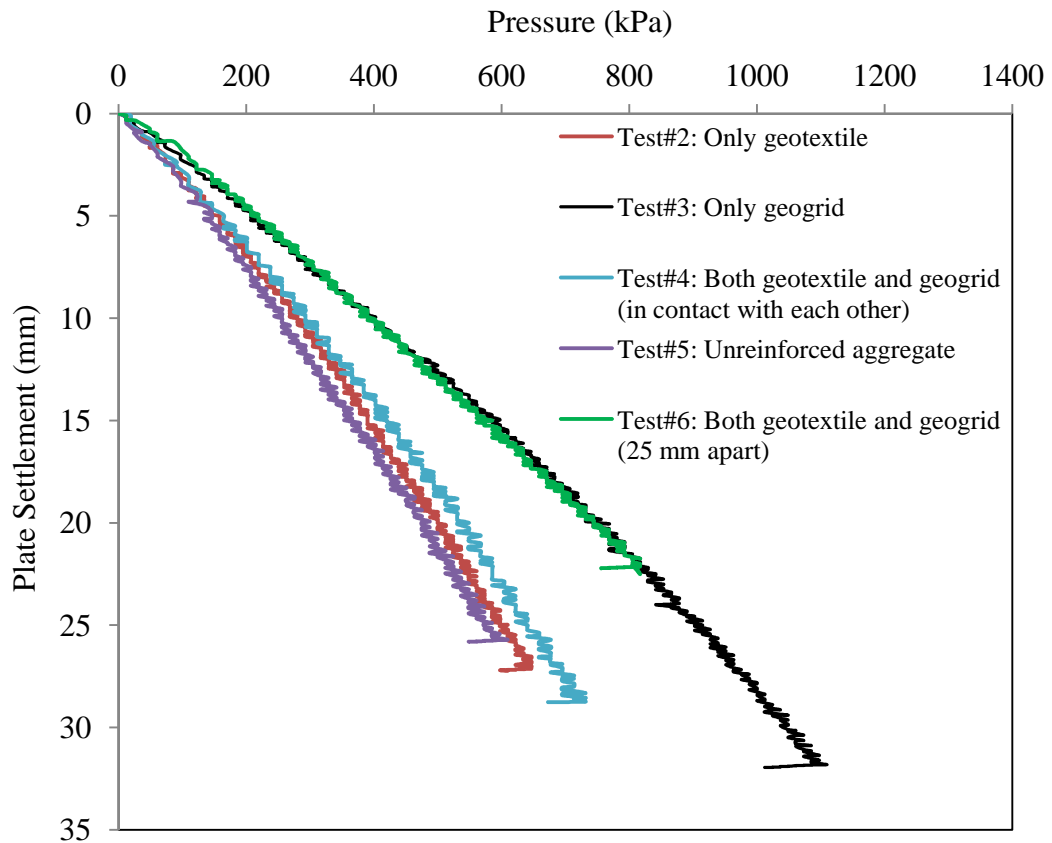


Figure 9.4. Load-settlement responses of aggregate-sand substrate models

9.2. Cyclic Plate Load Tests

9.2.1. Preparation of New Test Setup for Cyclic Plate load Tests

A new data acquisition system (**Figure 9.5**) with LabVIEW 2010 software was purchased for the instrumentation used in plate load tests. The required program for the instruments (e.g. load cell, LVDTs, wire potentiometers and strain gauges) was installed and calibrated.



Figure 9.5. The new Data Acquisition System used in the cyclic plate load tests

The existing loading frame was redesigned and retrofitted to achieve added safety and precision for the cyclic loading tests in this study (**Figure 9.6**). A new and larger test box [with inside dimensions of 1.78 m (L) x 1.78 m (W) x 1.07 m (H)] was also designed and fabricated at the OU Fears Laboratory (**Figure 9.7**).



Figure 9.6. Redesigned and retrofitted steel loading frame at the Fears Laboratory



Figure 9.7. The newly fabricated large steel test box for cyclic plate load tests

A new automated FlexTest 40 dynamic controller unit with a new computer and application software was purchased (**Figure 9.8**). The system was calibrated and tuned. A trial cyclic plate load test was carried out to ensure that the controller system was in a good operating condition.



Figure 9.8. Cyclic loading tests on reinforced base-substrate models using the new controller system

9.2.2. Strain Gauge Attachment Technique

Strains in geosynthetic reinforcement were measured using model YEFLA-5-3L foil strain gauges (manufactured by Tokyo Sokki Kenkyujo Co., Ltd.) with a gauge factor of $2.14 \pm 2\%$ and a gauge length of 5 mm. These strain gauges are capable of measuring large strains up to 15%. Wang (2009) found that these foil strain gauges are suitable to measure strains in both extruded and non-extruded geogrids. The strain

gauge installation procedure used for extruded PP (Polypropylene) geogrids is as follows:

a. The geogrid specimen was placed on a smooth and dry surface. The surface of the geogrid rib where the strain gauge needed to be attached was prepared. The outline of the strain gauge was marked on the rib. The surface was cleaned using industrial tissue and/or cotton swabs (**Figure 9.9**).

b. A piece of sandpaper was used to roughen the geogrid surface (**Figure 9.10**). The surface was then cleaned from any dust and residues due to abrasion using a fine brush (**Figure 9.11**).

c. A poly-primer (**Figure 9.12**) was used to clean the geogrid surface at the strain gauge location.

d. The strain gauge was aligned carefully in its position. A piece of Scotch tape was applied to the gauge backing and Cyanoacrylate (CN) adhesive was applied to the gauge (**Figure 9.13** and **Figure 9.14**). The Scotch tape helped to fix the gauges in place and to adjust their location as necessary (**Figure 9.15**). The gauges were centered on the prepared ribs and held in place with the Scotch tape while the adhesive was cured.

e. Direct pressure was applied to the gauge (**Figure 9.16**) for at least one minute and the adhesive was allowed to cure for approximately five minutes before the tape was peeled off the backing (**Figure 9.17**).

f. The gauge surface was covered with the coating material, M-Coat A (Air-drying Polyurethane coating; **Figure 9.18**). Plastic wire ties were used to hold the strain gauge wires in position (**Figure 9.19** and **Figure 9.20**). The strain gauges were left in air for at least 24 hours.

g. Silicon sealant was injected into a length of flexible tubing (**Figure 9.21**) that was split open along its length and extended beyond the gauge and its terminal strip.

h. The silicon-filled tube was placed around the gauge (**Figure 9.22**). It was left for 24 hours in order to dry fully (**Figure 9.23**). Strain gauge lead wires were then ready to be connected to the readout device.



Figure 9.9. Cleaning the surface of geogrid with industrial tissue or cloth



Figure 9.10. Abrasive paper was used to roughen the surface of the extruded geogrid



Figure 9.11. A brush was used to remove dust due to abrasion



Figure 9.12. Adhesive, primer and sealant used in this study



Figure 9.13. Application of adhesive material to the geogrid



Figure 9.14. Application of adhesive material to the back of the strain gauge base



Figure 9.15. Gauges were held in place with the Scotch tape while the adhesive was cured



Figure 9.16. Pressure was applied to the gauge to cure



Figure 9.17. The tape was peeled off carefully from the strain gauge



Figure 9.18. The gauge surface was covered with coating material



Figure 9.19. Wire tie was used to hold the strain gauge wire in position



Figure 9.20. Geogrid with strain gauges attached



Figure 9.21. Flexible rubber tube was used to cover strain gauges



Figure 9.22. Siliocon rubber sealant was applied on the strain gauge



Figure 9.23. Geogrid sample left for 24 hours in order for the adhesive and sealant materials to dry out

The strain gauge installation procedure used on the polyester geogrid (i.e. WGG1) was slightly different. A small steel wire brush was used to remove the PVC coating of the geogrid. Then the strain gauge was directly attached to the polyester yarns of the geogrid following the same attachment procedure described for extruded geogrids.

Example geogrid specimens prepared for cyclic plate load tests are shown in **Figure 9.24**. Two 1.78 m \times 1.78 m woven geotextile layers (Mirafi HP 370) were also prepared (**Figure 9.25**). One layer of geotextile was placed underneath the subgrade layer in order to prevent sand from entering the Styrofoam area in the lower section of the test box. The other geotextile was placed at the subgrade-base interface.





Figure 9.24. Geogrid specimen used in a cyclic plate load tests before instrumentation:
(a) EGG1, (b) WGG1, (c) KGG1



Figure 9.25. Geotextile placed below the subgrade layer in the test box

Each geogrid specimen was instrumented with strain gauges for the cyclic plate load test. It took typically two days to prepare each specimen as pressure needed to be applied to the gauges to cure for 24 hours (**Figure 9.26**). It took another 24 hours for the silicon sealant inside the protective rubber tube to dry (**Figure 9.27a**). **Figure 9.27** show the EGG and NEGG geogrid specimens instrumented with strain gauges.



Figure 9.26. Pressure was applied to the gauges to cure their adhesive layer





Figure 9.27. Example geogrid specimens instrumented with strain gauges: (a) EGG1, (b) WGG3

9.2.3. Cyclic Plate Load Test Setup

A schematic elevation view of the test box and the instrumentation layout in the final cyclic plate load tests is presented in **Figure 9.28**. The following information was found useful in developing the instrumentation layout of the cyclic plate load tests: Abu-Farsakh and Chen (2011) found that largest tensile strains developed directly beneath the center of the cyclic loading plate (where the maximum lateral movement of the base course occurred), and became negligible at a certain distance from the loading plate. This distance was found to be approximately $1.5D$ (D is the diameter of the loading plate) from the center of the loading plate for the geogrid placed at the subgrade-base interface and nearly $1.0D$ from the center of the loading plate for the geogrid placed at the middle of the base layer. Wang (2009) also found that reinforcement strains become negligible at approximately $1.0D$ - $1.5D$ from the center of

the loading plate. Wang (2009) also reported that the settlement of aggregate layer at the surface was negligible beyond 1.25D from the center of the loading plate.

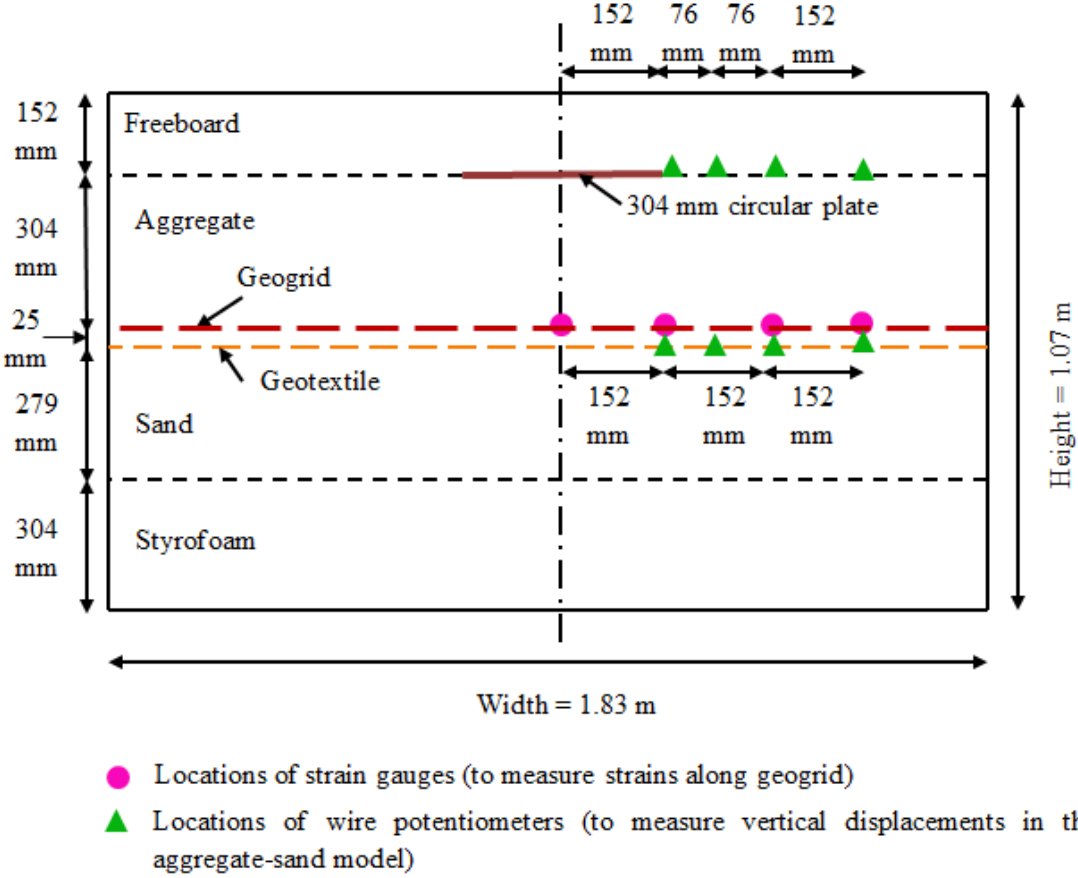


Figure 9.28. Schematic elevation view of the test box and the instrumentation layout in the final cyclic plate load tests

In the final cyclic plate load tests, the thicknesses of the aggregate and sand layers were 329 mm and 279 mm, respectively. A 25 mm layer of aggregate was placed below the geogrid to ensure sufficient interlocking between the geogrid and aggregate interface (**Section 9.1**). Afterwards, 304 mm of aggregate was placed and compacted in three equal lifts. The thickness of each lift was 100 mm. The total thickness of the base

layer in the test models was greater than the minimum 152 mm value recommended in the current FHWA guidelines (Holtz et al. 2008) for a geosynthetic reinforcement layer installed on a weak subgrade.

Figure 9.29 through **Figure 9.46** show different stages of setup and procedure for the large-scale cyclic plate load tests. A horizontal steel beam at the middle of the test frame and spanning the width of the test box served as a reaction beam to apply a concentric load on the test models (**Figure 9.29**). An actuator was positioned on the middle of the horizontal beam. It was connected to the hydraulic pump and the dynamic controller system. Before placing materials in the test box, a 305 mm-deep block of Styrofoam panels was placed at the bottom of the test box and 25 mm-thick panels were placed against the walls of the test box to mitigate the boundary effects against the lateral movement of aggregates (**Figure 9.30**). A geotextile layer was placed underneath the subgrade layer to prevent it from entering the Styrofoam block in the lower section of the test box (**Figure 9.31**).

The test box was then filled with uniformly graded loose sand as the subgrade and ODOT Type-A aggregate as the base layer. The sand and aggregate layers were separated using a layer of woven geotextile (Mirafi HP 370). The sand was compacted to a density that corresponded to a CBR value of 4 based on earlier CBR tests (**Section 6.3.1**). The density of subgrade and aggregate base layers were checked according to ASTM D2167-08 using a model HM-310 Voluvessel densometer (**Figure 9.32**). A 1.78

m (L) × 1.78 m (W) geogrid specimen was placed at 25 mm above the sand-aggregate interface inside the aggregate to allow for complete interlocking with the aggregate.

A 25 mm-thick, 305 mm-diameter circular steel loading plate was placed on the top of the aggregate layer directly beneath the actuator. The loading plate was attached to the actuator and a 100 kN load cell. The cyclic load was applied to the aggregate-substrate models and the settlement of the loading plate was measured using the displacement output from the dynamic controller system. In addition, a total of eight extensometers (wire potentiometers) were attached to the steel cross beam which supported the actuator. The calibration factors for each wire potentiometer were determined prior to the test.

Each reinforced test model was instrumented to measure the reinforcement strain, top surface deflection and settlements at the bottom of the aggregate layer. The instrumentation included eight wire potentiometers (WPs) and eight strain gauges. The strain gauges were attached to the bottom and the top the geogrid at each location to measure its tensile strains. Four WPs were mounted on the bottom side of the reaction beam and were connected to the loading plate and the separator geotextile through the aggregate layer at the radial distances of 152 mm, 228 mm, 304 mm and 456 mm from the center of the circular loading plate as shown in **Figure 9.33**. The distances are reported as shown on the figure because the WPs were attached to the bottom flange of one of the two reaction beams that flanked the central shaft that was rigidly attached to the loading plate.



Figure 9.29. The redesigned and retrofitted steel loading frame with the actuator, which is connected to the hydraulic pump and the controller system

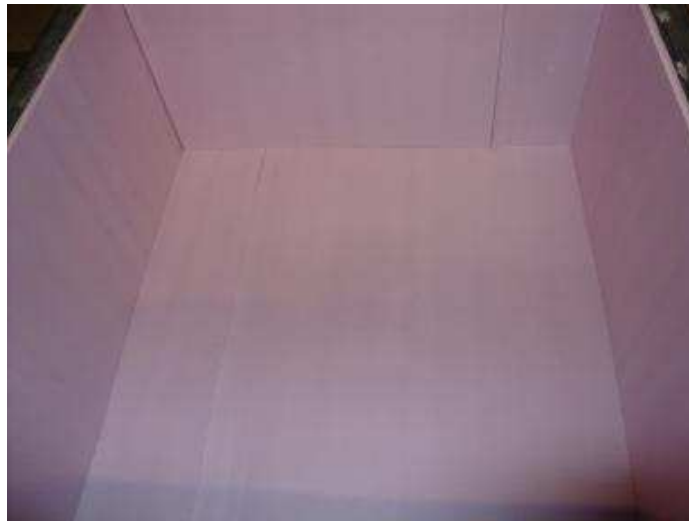


Figure 9.30. Styrofoam panels placed at the bottom and against the walls of the test box



Figure 9.31. Cyclic plate load test box after placing the geotextile separator on Styrofoam panels on the bottom of the test box

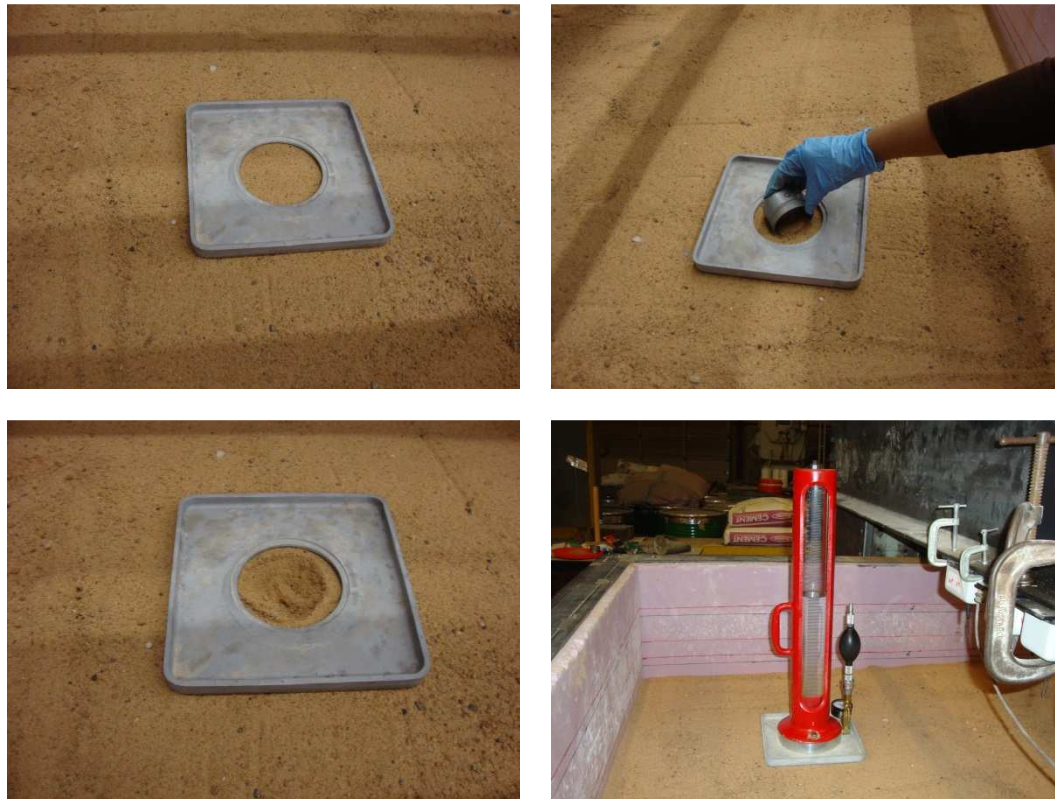


Figure 9.32. Measuring the in-situ density of sand by Model HM-310 Voluessel rubber balloon densometer

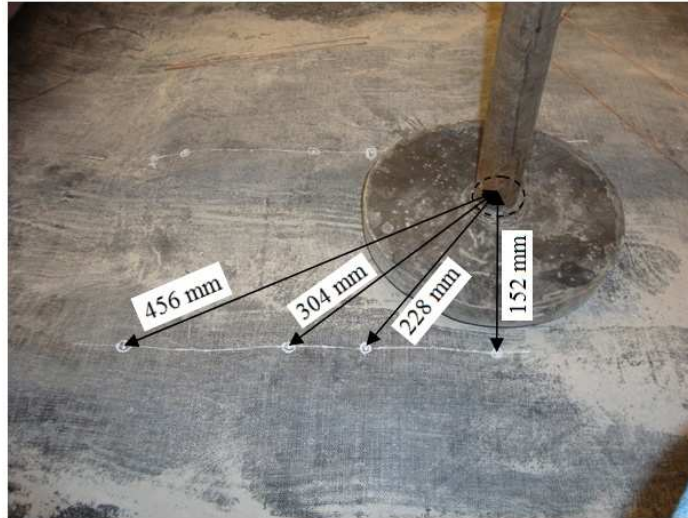


Figure 9.33. Marked locations of extensometer readings to measure deformation profile at the bottom of the aggregate layer due to cyclic loading



Figure 9.34. Attachment of brass wires to geotextile separator to measure its settlement



Figure 9.35. 25 mm-thick aggregate layer placed on the top of the geotextile separator



Figure 9.36. Placing geogrid reinforcement on the 25 mm-thick aggregate layer



Figure 9.37. Careful placement of aggregate on the geogrid layer



Figure 9.38. Compacted aggregate layer placed on the geogrid reinforcement



Figure 9.39. Brass wires connected to the wire potentiometers to measure the base layer deformation

Four additional extensometers (WPs) were placed on the other side of the reaction beam from the center of the loading plate at otherwise the same distances mentioned earlier in this section. The latter four WPs were attached to thin steel plates to form vertical tell-tales (**Figure 9.40**) to measure the settlement at the top of the aggregate layer at selected locations (**Figure 9.41**). The magnitudes of the cyclic load applied to the circular plate and its settlement were recorded during the tests using the dynamic controller system software. The deformation of the eight WPs and the elongation of the eight strain gauges with time during the tests were recorded using the program LabVIEW 2010 of the Data Acquisition System (**Figure 9.45**).



Figure 9.40. A telltale plate (50 mm × 50 mm) attached with brass wire to measure the surface deflection of the aggregate layer



Figure 9.41. Setup of the telltale plates on the top of the aggregate layer



Figure 9.42. Vertical telltale plate to measure the aggregate deformation near the circular loading plate



Figure 9.43. Connecting strain gauges to the DAS (Data Acquisition System)



Figure 9.44. Eight strain gauges connected to the DAS



Figure 9.45. Monitoring data in the Data Acquisition System while a cyclic plate load test is in progress



Figure 9.46. The position of the circular loading plate at the end of a test

9.2.4. Preliminary Plate Load Tests and Results

In the preliminary plate load tests, the test box was filled with 432 mm of uniformly graded loose sand as subgrade and 152 mm of ODOT Type-A aggregate for the base layer. The sand unit weight in as-placed condition was 12.13 kN/m^3 , equivalent to a relative density of 28%. The sand was placed in a loose condition to a uniform depth without any compaction to simulate a weak subgrade.

Prior to cyclic load tests, a preliminary static test was carried out to check the performance of the loading assembly, controller and the data acquisition system. The corresponding load-settlement data are shown in **Figure 9.47**. In this test, a total load of 40 kN was applied monotonically on a reinforced base-subgrade model in 10 equal increments using a 305 mm diameter circular steel plate. A 40 kN load was selected as the maximum applied load in these tests because it represented a tire inflation pressure

of 550 kPa which simulated dual tires under an equivalent 80 kN single-axle load (Abu-Farsakh and Chen 2011).

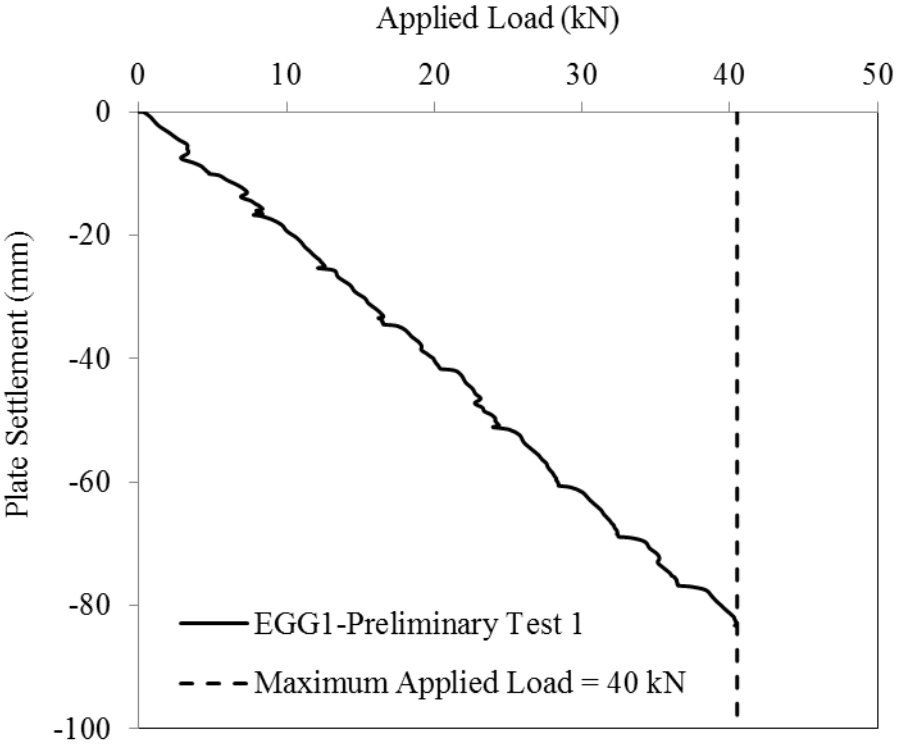


Figure 9.47. Load-settlement response of the aggregate-sand model subjected to a static (incremental static loading) plate load test in the large test box

Following the preliminary static test, two preliminary cyclic plate load tests were carried out on a reinforced model using one EGG (EGG1) and one NEGG (WGG3) geogrids as the geosynthetic reinforcement. A periodic load with the peak magnitude of 40 kN was applied on the model. The settlement of the aggregate layer at the surface, deformation of the base layer at the bottom, and the strain distribution in the geogrid reinforcement were measured. The following loading regime was used in the

cyclic plate load tests: First, the load was monotonically increased from an initial seating load of 2.2 kN to the final magnitude of 40 kN in 10 equal increments. Then, a 1-Hz force-controlled periodic load was applied, which included a 0.1-sec loading period followed by a 0.9-sec resting period. The periodic load amplitude varied between 2.2 kN and 40 kN for 1,000 load cycles. **Figure 9.48** and **Figure 9.49** show the load-settlement response data for the two preliminary periodic plate load tests. The magnitudes of the target seating load and maximum load are shown with vertical dashed lines on these figures.

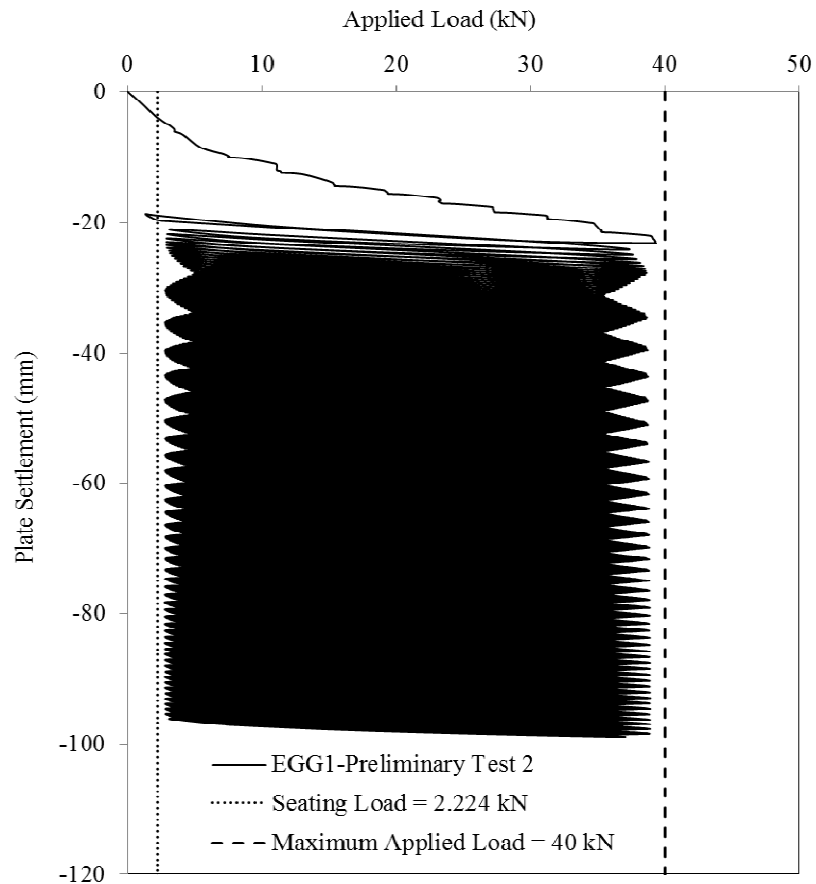


Figure 9.48. Load-settlement response of the preliminary periodic plate load tests with EGG1 geogrid

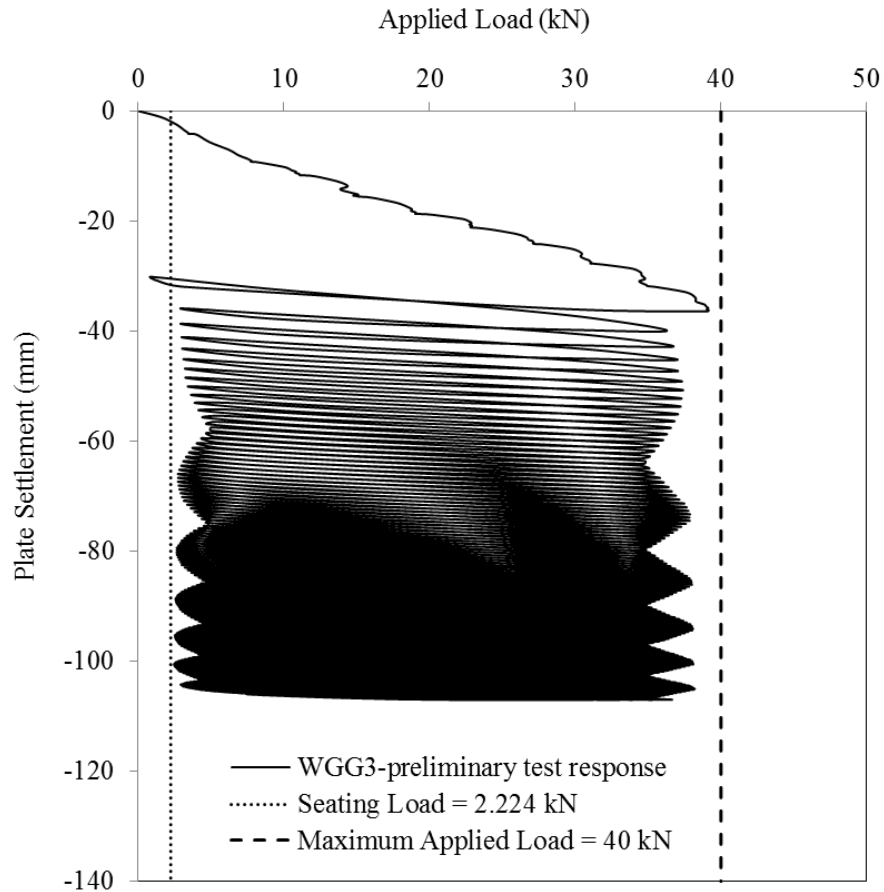


Figure 9.49. Load-settlement response of the preliminary periodic plate load tests with WGG3 geogrid

The preliminary tests indicated that the subgrade sand was too weak to support the 1000 loading cycles. Hence, a series of CBR tests was carried out on the subgrade sand at different compaction levels according to ASTM D1883-07 test protocol to determine a suitable CBR value for the subgrade sand. From the results of these CBR tests, it was found that a subgrade with CBR value equal to 4 would have adequate strength and stiffness to complete the cyclic plate load tests. **Figure 9.50** shows the CBR test results for the subgrade sand with a dry unit weight of 16.22 kN/m^3 .

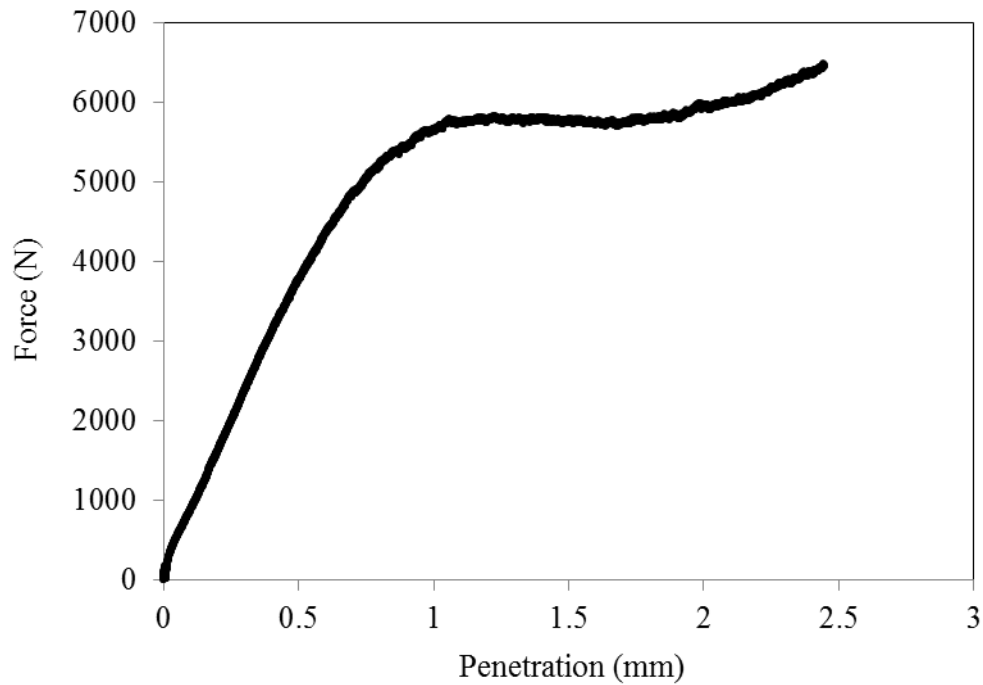


Figure 9.50. CBR test result of the subgrade sand with a dry unit weight of 16.22 kN/m^3

9.2.5. Final Cyclic Plate Load Tests and Results

Once a suitable CBR value for the subgrade sand was determined, nine (9) final cyclic plate load tests were carried out which included eight reinforced cases (i.e. using geogrids listed in **Table 3.2**) and an unreinforced case. The moisture content and unit weight of subgrade sand were 0.2% and 16.25 kN/m^3 (dry unit weight = 16.22 kN/m^3), respectively. The relative density of sand was 95.7%.

The following loading regime was used in the cyclic plate load tests: First, the load was monotonically increased from an initial seating load of 2.2 kN to the final magnitude of 40 kN in 10 equal increments. Then, a 1-Hz force-controlled periodic load

was applied, which included a 0.1-sec loading period followed by a 0.9-sec resting period. The periodic load amplitude varied between 2.2 kN and 40 kN for 1,000 load cycles. All final nine tests ran successfully. A total of 1000 load cycles were applied in each test without any interruption. The corresponding test results are shown in **Figure 9.51** through **Figure 9.59**.

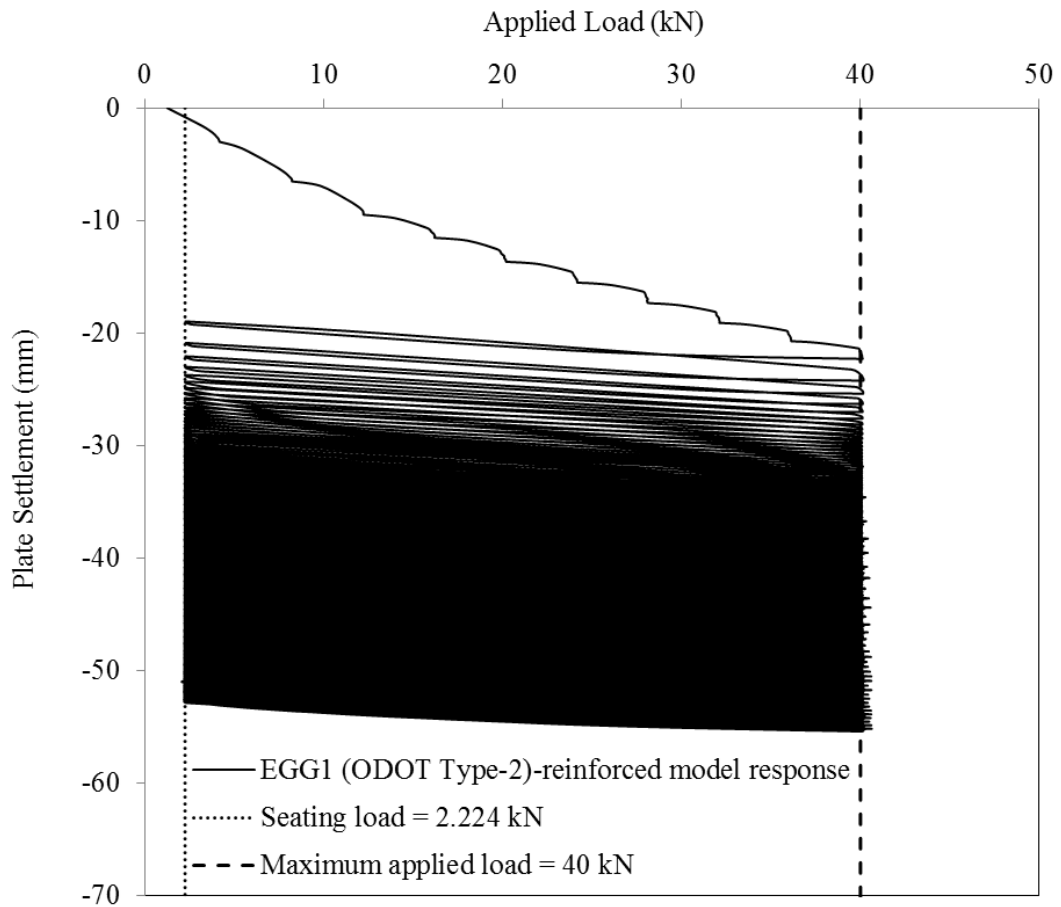


Figure 9.51. Plate load-settlement response of the aggregate-substrate model with EGG1 geogrid (1000 load cycles)

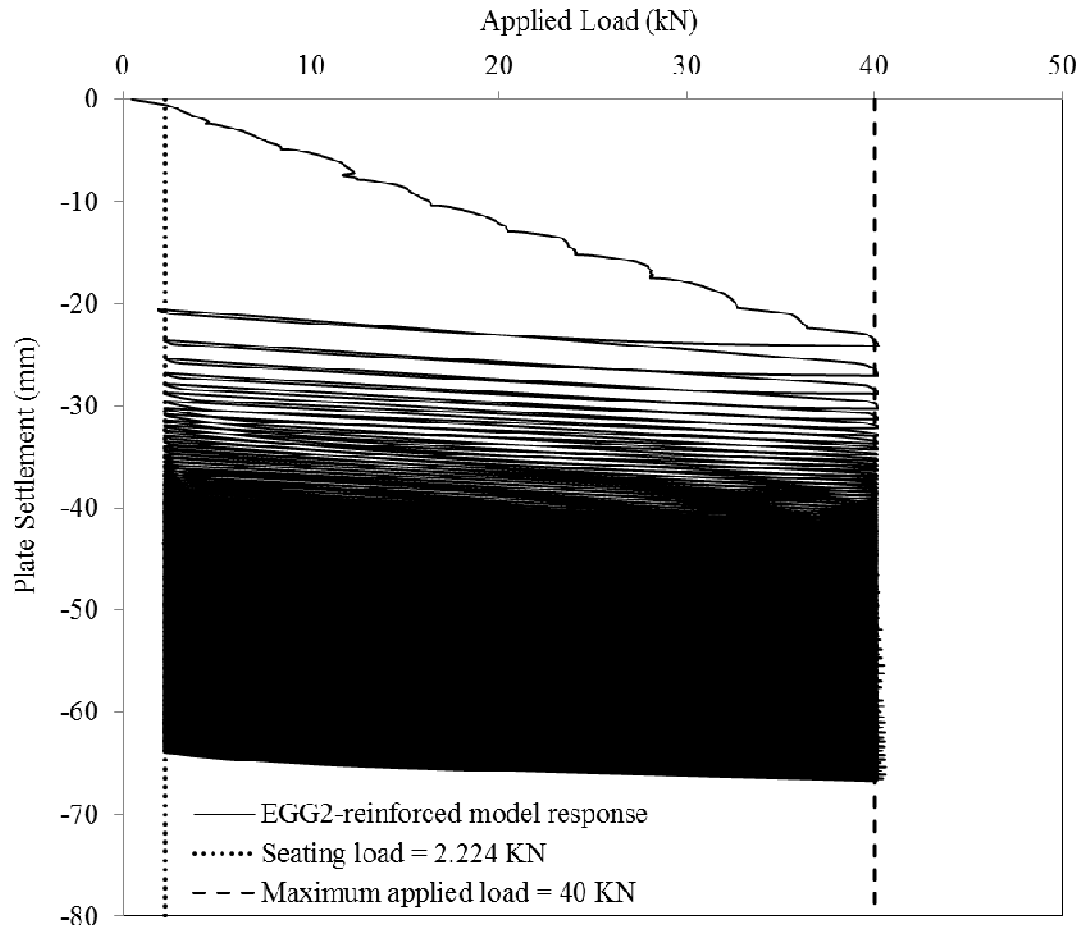


Figure 9.52. Plate load-settlement response of the aggregate-substrate model with EGG2-single layer geogrid (1000 load cycles)

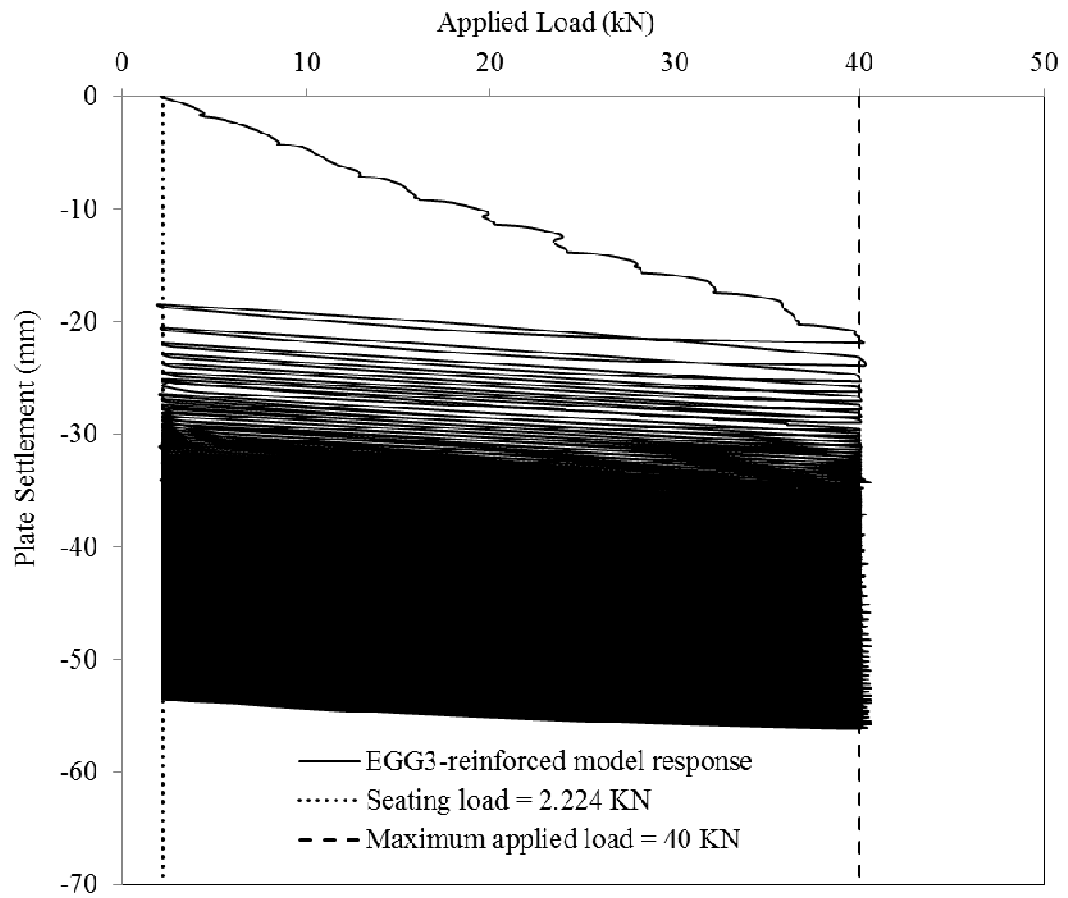


Figure 9.53. Plate load-settlement response of the aggregate-substrate model with EGG3 geogrid (1000 load cycles)

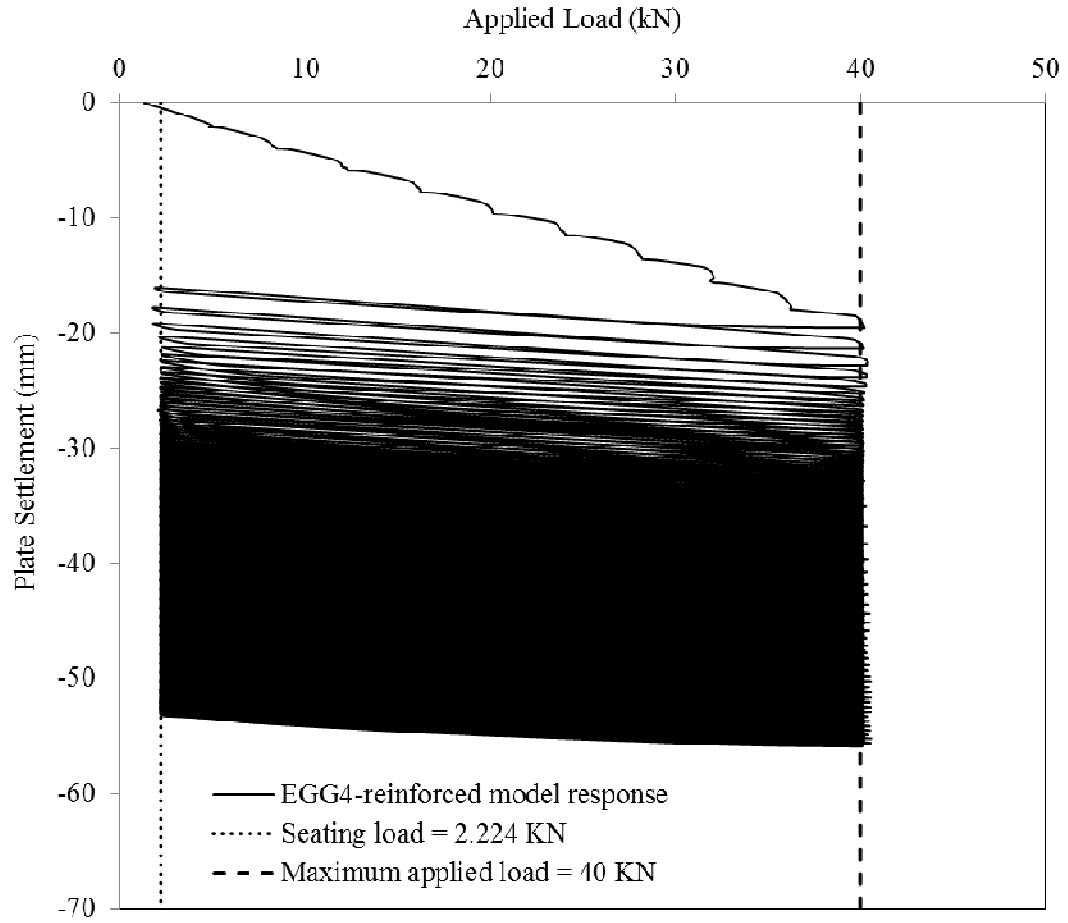


Figure 9.54. Plate load-settlement response of the aggregate-substrate model with EGG4 geogrid (1000 load cycles)

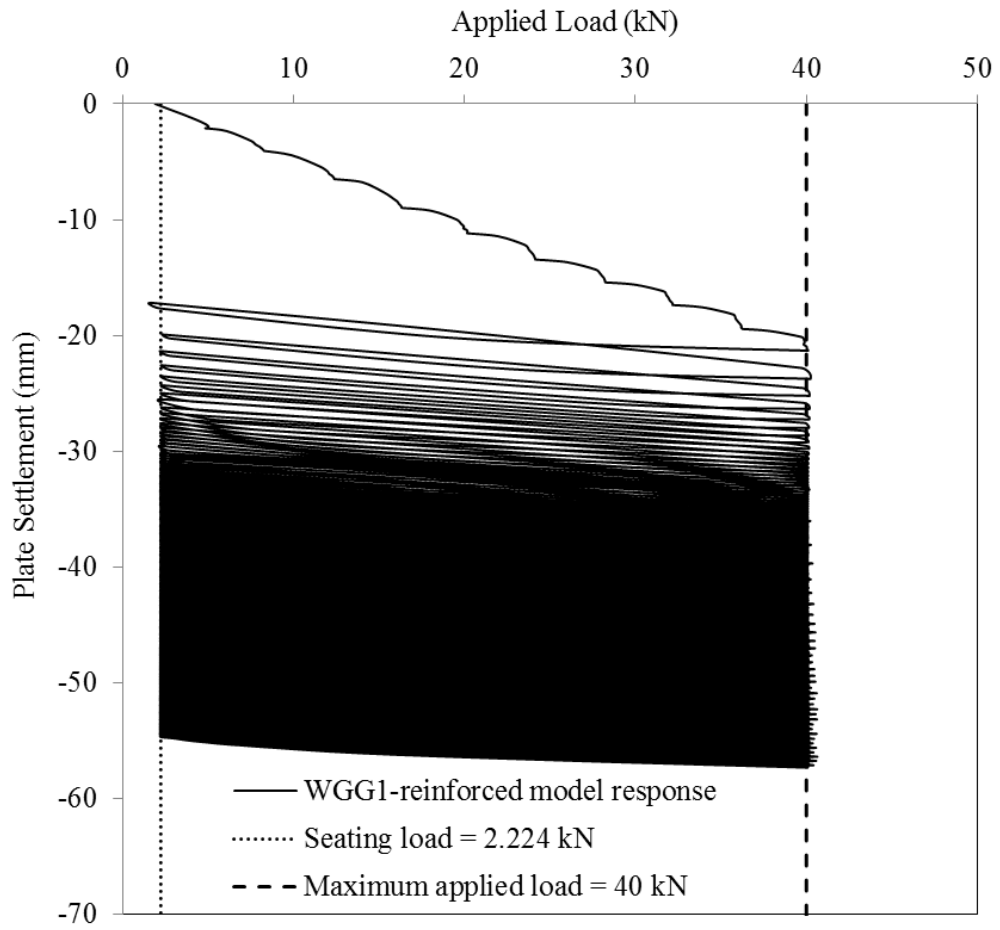


Figure 9.55. Plate load-settlement response of the aggregate-substrate model with WGG1 geogrid (1000 load cycles)

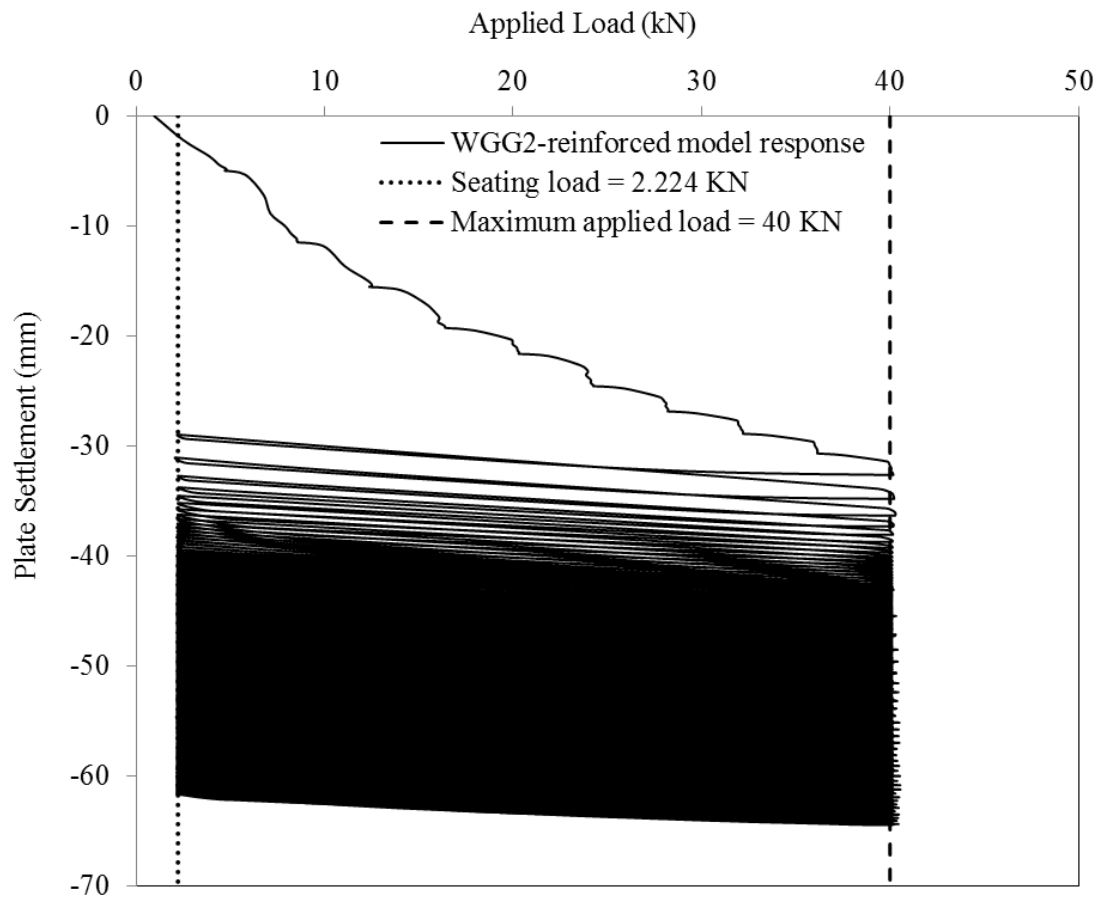


Figure 9.56. Plate load-settlement response of the aggregate-substrate model with WGG2 geogrid (1000 load cycles)

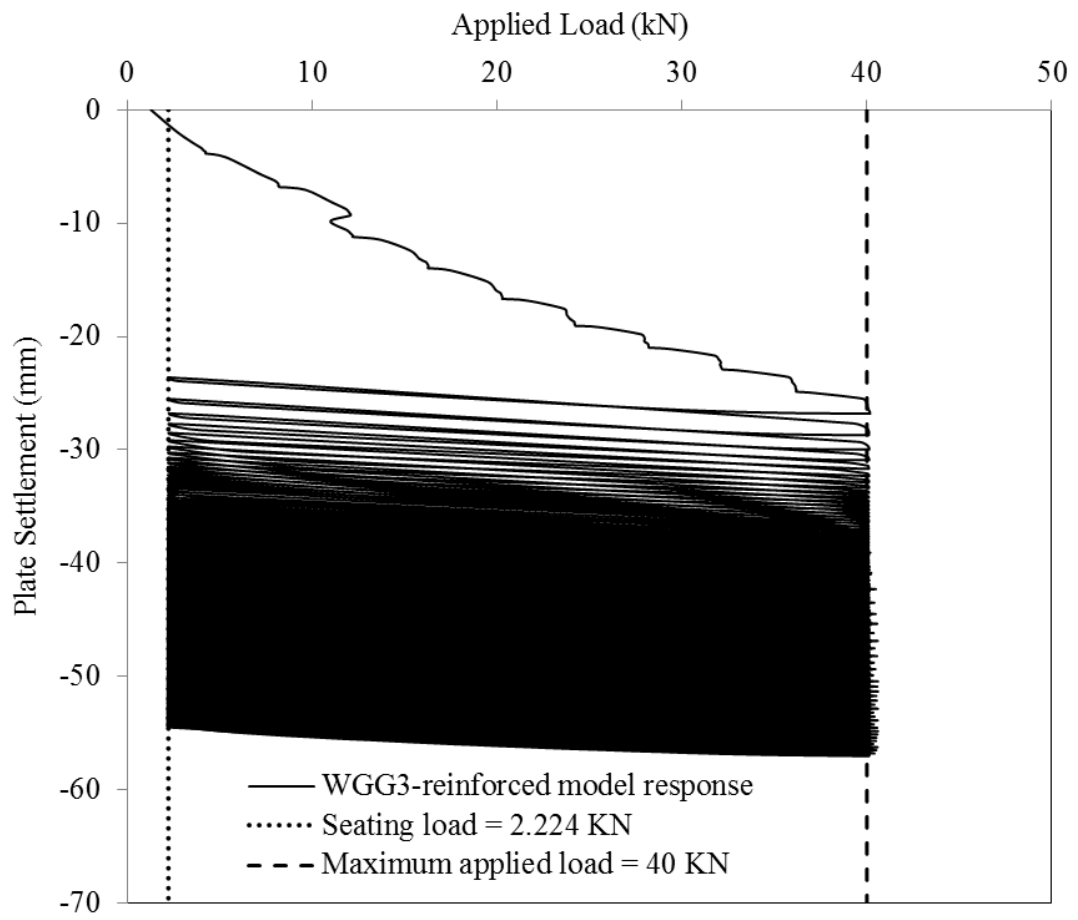


Figure 9.57. Plate load-settlement response of the aggregate-substrate model with WGG3 geogrid (1000 load cycles)

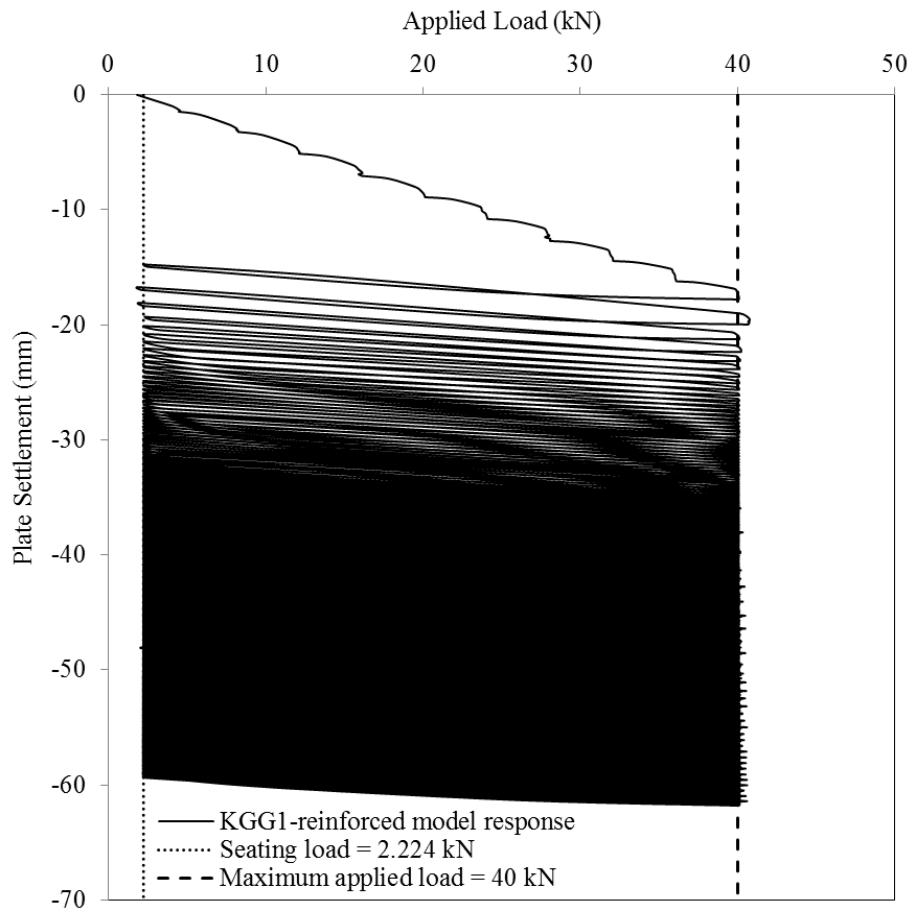


Figure 9.58. Plate load-settlement response of the aggregate-substrate model with KGG1 geogrid (1000 load cycles)

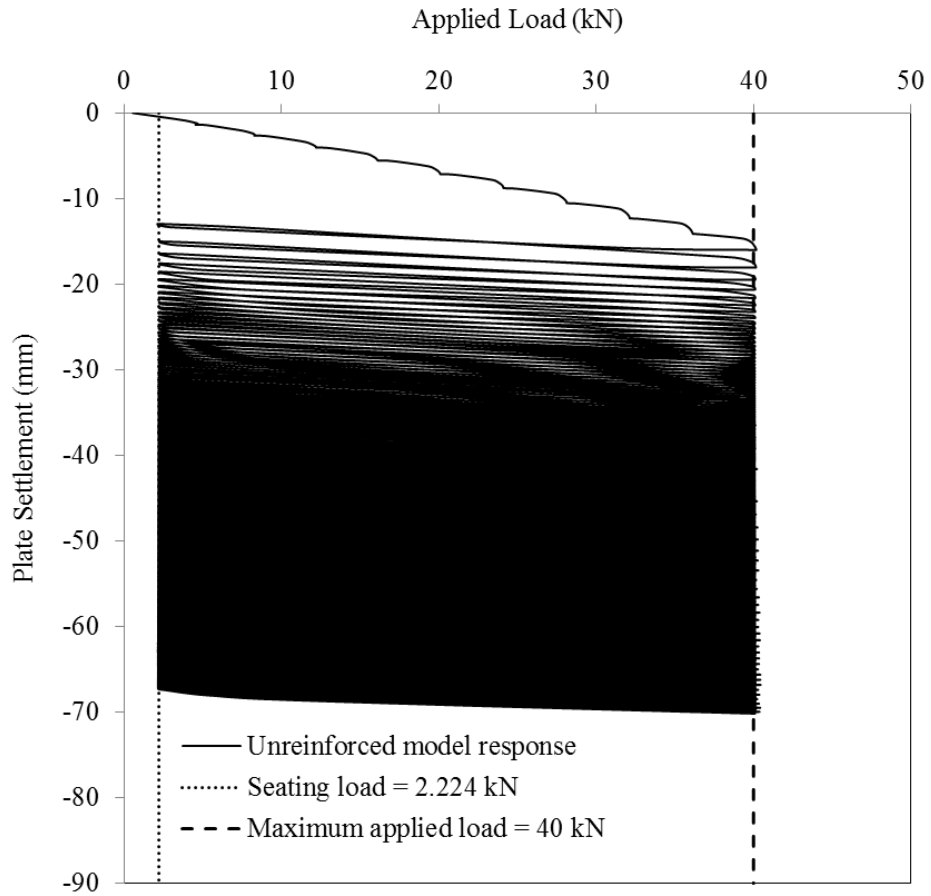


Figure 9.59. Plate load-settlement response of the aggregate-substrate model without any geogrid (1000 load cycles)

The geogrid specimens after each cyclic plate load tests are shown in **Figure 9.60** through **Figure 9.67**.



Figure 9.60. EGG1 geogrid specimen after the cyclic plate load test

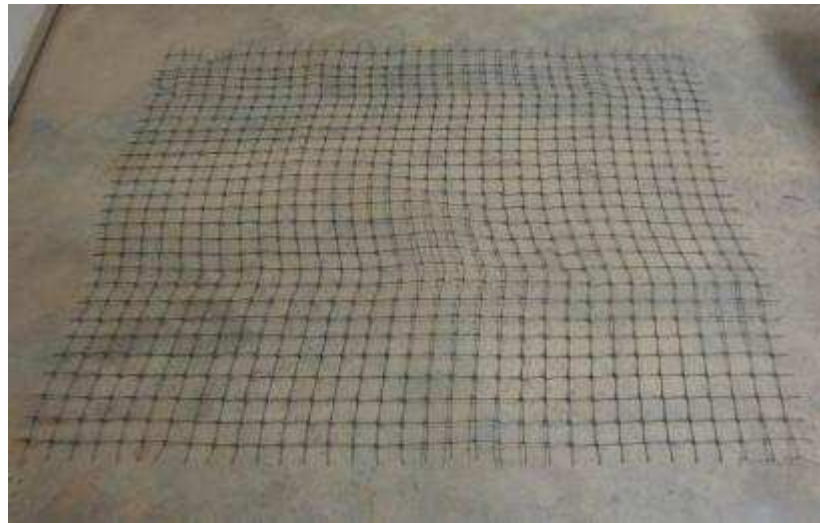


Figure 9.61. EGG2 geogrid specimen after the cyclic plate load test

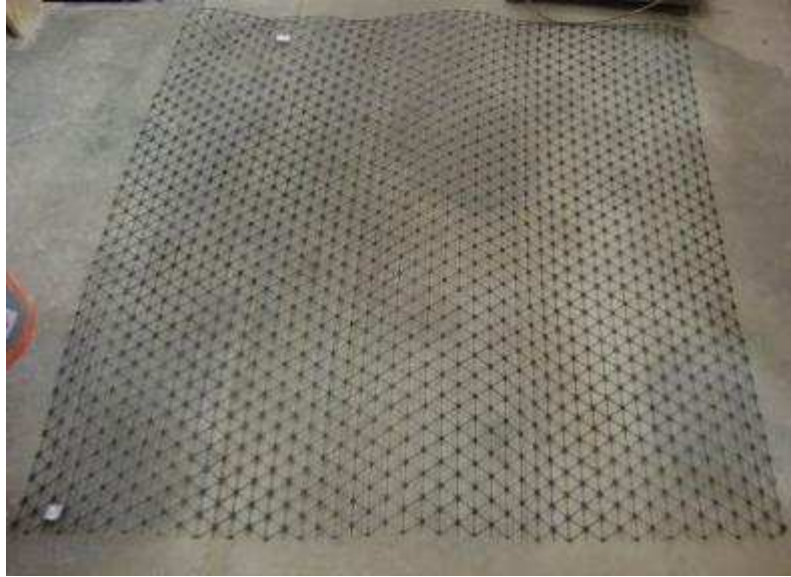


Figure 9.62. EGG3 geogrid specimen after the cyclic plate load test



Figure 9.63. EGG4 geogrid specimen after the cyclic plate load test



Figure 9.64. WGG1 geogrid specimen after the cyclic plate load test

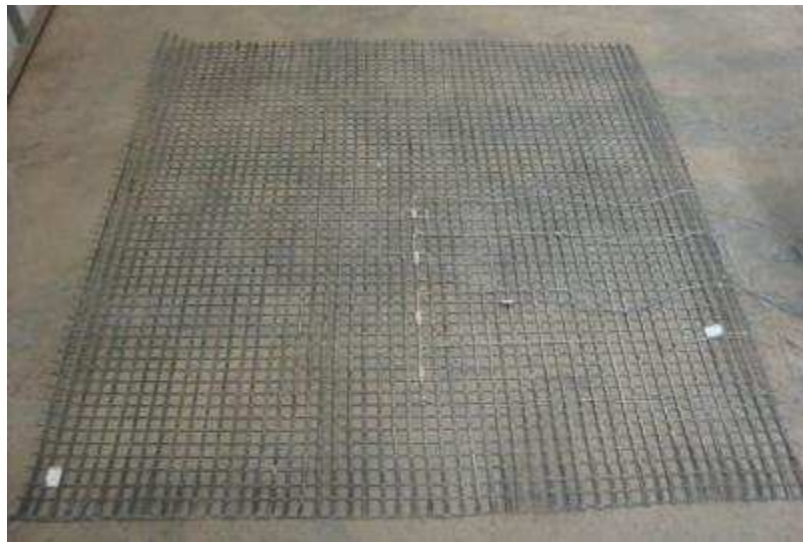


Figure 9.65. WGG2 geogrid specimen after the cyclic plate load test



Figure 9.66. WGG3 geogrid specimen after the cyclic plate load test



Figure 9.67. KGG1 geogrid specimen after the cyclic plate load test

Two terms were used in the present study to evaluate the benefits of using geogrids to reinforce aggregate base layers: The Settlement Reduction Factor (SRF) and the Traffic Benefit Ratio (TBR) (Berg et al. 2000, Christopher et al. 2010, Douglas et al. 2012). In this study, the SRF was defined as the ratio of the settlement of an unreinforced aggregate base test model (S_U) to that of an otherwise identical reinforced model (S_R) for a given applied load. Therefore, a higher SRF value indicates a more effective reinforcement.

$$SRF = S_U/S_R \quad (9.2.1)$$

The TBR is defined as the ratio between the number of load cycles on a reinforced section (N_R) to reach a defined failure state (e.g. a given rutting depth) and the number of load cycles on an unreinforced section (N_U) with the same geometry and material constituents that reaches the same defined failure state (Berg et al. 2000).

$$TBR = N_R/N_U \quad (9.2.2)$$

A greater TBR value also indicates a more effective reinforcement. **Figure 9.68a** shows that all reinforced cases performed better than the unreinforced case. However, it can be observed that the test section with EGG1 geogrid base reinforcement performed better than those with WGG1, KGG1 or EGG2 geogrid reinforcement. Overall, except for WGG3 and KGG1 cases, other geogrids performed comparable to the EGG1 geogrid. WGG2 and WGG3 products resulted in slightly smaller settlements in the test models. **Figure 9.68b** shows a comparison of SRF values corresponding to all geogrid products listed in this study. **Figure 9.69** shows a comparison of the

corresponding TBR values. The TBR values are larger than 1, which means that the reinforcement layer improved the bearing capacity of the aggregate-sand model.

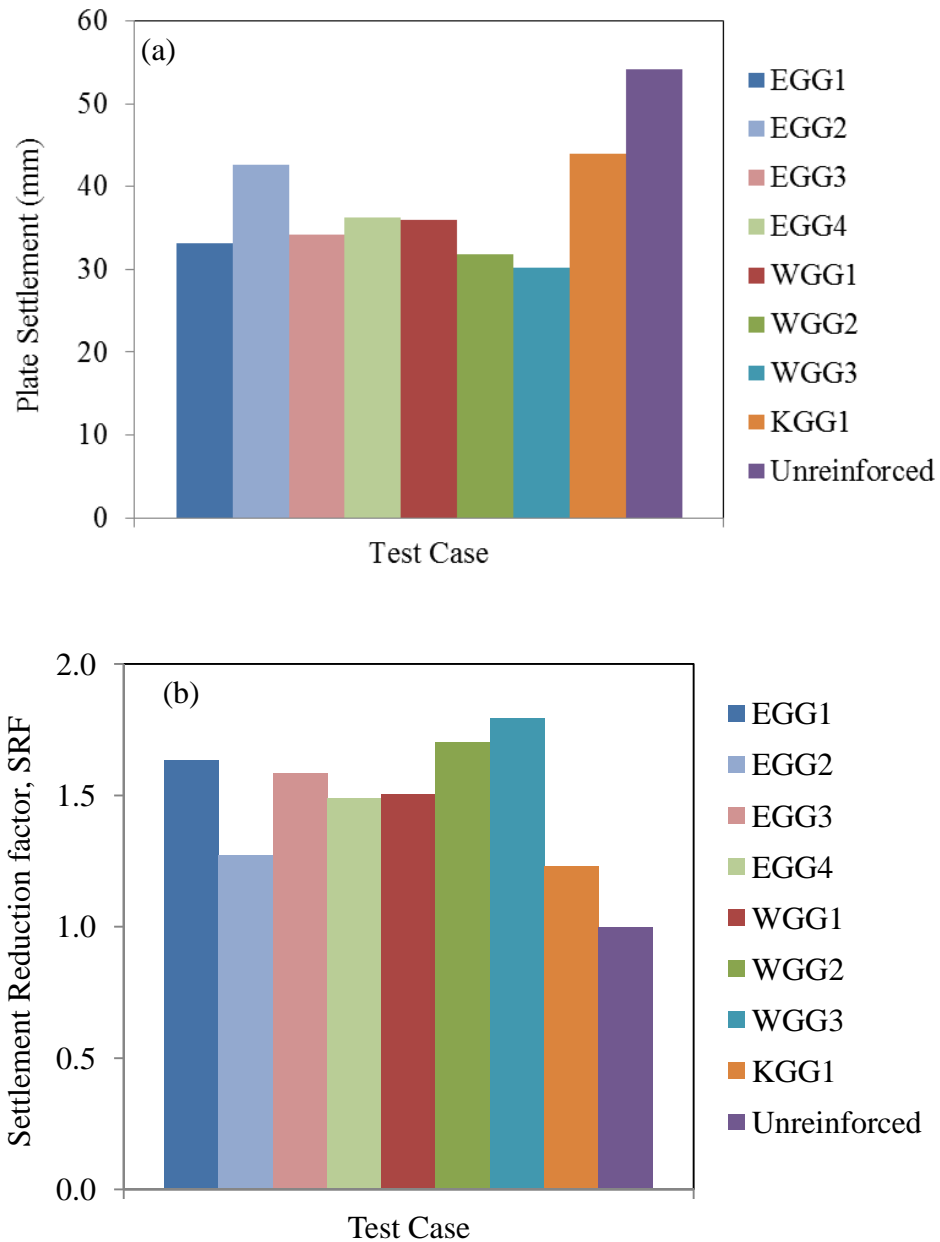


Figure 9.68. Comparison of (a) Maximum plate settlement under cyclic loading, (b) SRF values among test cases examined

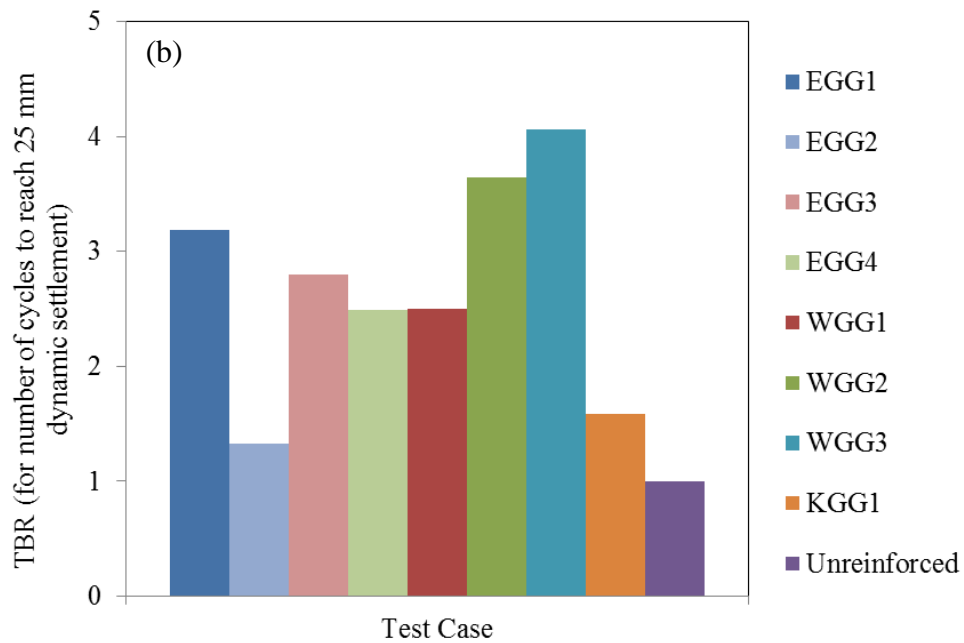
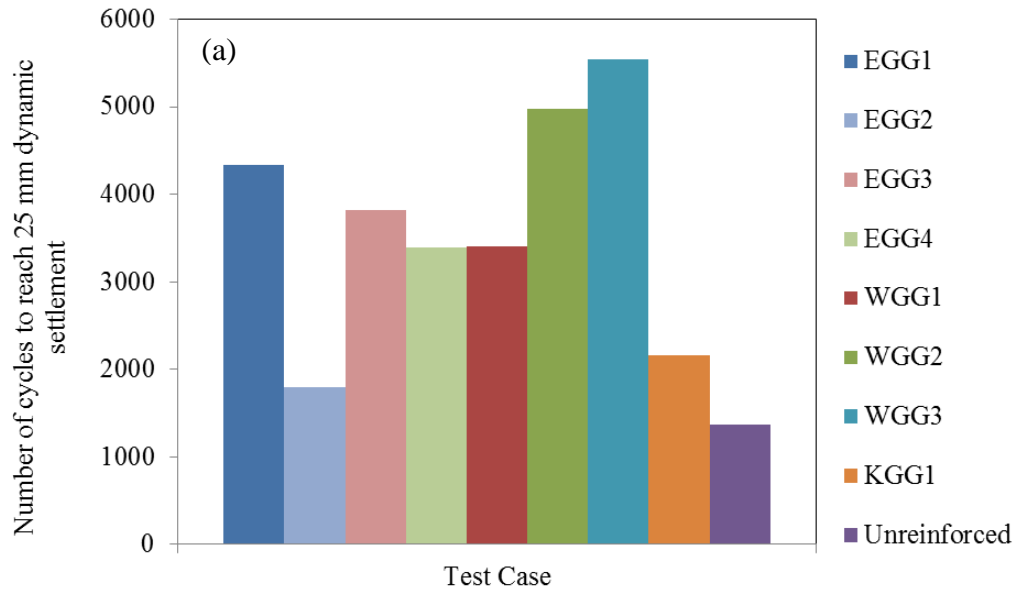


Figure 9.69. Comparison of (a) Number of cycles to reach 25 mm of settlement under cyclic loading, (b) Traffic Benefit Ratios (TBR) among test cases examined

Figure 9.70 shows a comparison of the top surface deflections at the end of 1000 cycles for different test cases. The results show that for the most part, the test

sections with extruded geogrid base reinforcement tend to result in smaller deformations than those with non-extruded geogrid reinforcement. It can also be seen that the maximum amount of top surface deformation occurred in the unreinforced case. The top surface deflection profiles reported in this study are consistent with those described by Abu-Farsakh and Chen (2011).

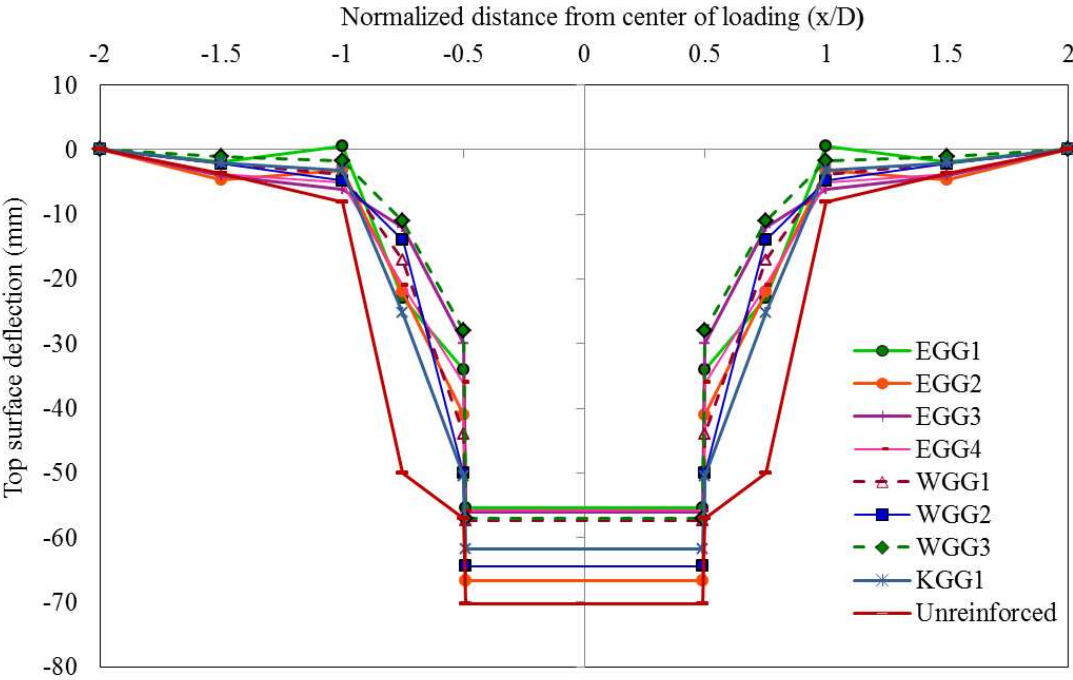


Figure 9.70. Comparison of top surface deflections in different cases at the end of 1000 cycles

Figure 9.71 shows a comparison of the subgrade deflection profiles in different test cases at the end of 1000 cycles. It was found that test sections with the WGG3 and EGG3 geogrid base reinforcement resulted in smaller subgrade deformations than the EGG1 geogrid case tested. The subgrade in the test section with EGG2 geogrid resulted in the largest deflection in the region beneath the loading plate. The EGG2 geogrid is

classified as the only ‘weak rib’ extruded geogrid in this study. It was also observed that, the largest subgrade deformation occurred in the unreinforced case.

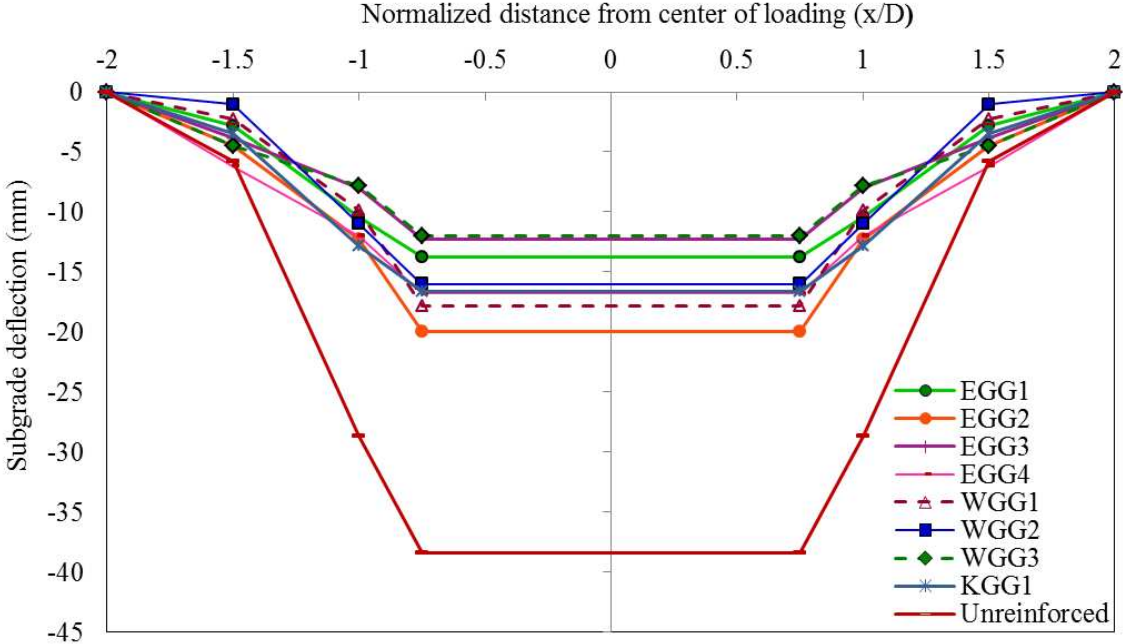


Figure 9.71. Comparison of subgrade deflection profiles in different test cases at the end of 1000 cycles

Strain distributions along the centerline of the EGG1, WGG2, WGG3 and KGG1 geogrids for different load cycles (i.e. after 100, 200, 300, 500, 700 and 1000 load cycles) are shown in **Figure 9.72** through **Figure 9.75**. It is observed that tensile strain in geogrids generally continued to increase with the number of loading cycles. It is also observed that the largest tensile strains developed directly beneath the center of the loading plate, where the maximum lateral movement of the base course was expected to occur. The strain magnitudes decrease farther away from the loading plate and become negligible (e.g. less than 5% of maximum value) at distances greater than

$x/D = 2$ (x is the horizontal distance from the center and D is the diameter of the circular loading plate equal to 304 mm). Geogrid strains for $x/D \geq 1$ were found to be negligible for extruded geogrids (e.g. less than 5% of maximum value). This distance for non-extruded geogrid was found to be closer to 1.5D. Abu-Farsakh and Chen (2011) also reported that tensile strains were negligible after 1.5D distance from the center of the loading plate for the geogrid placed at subgrade-base interface. However, in Abu-Farsakh and Chen's study, the base thickness was 320 mm (12.6 in) and a 60 mm (2.36 in)-thick layer of hot mix asphalt (HMA) was placed over the base course.

Figure 9.72 illustrates that the maximum strain developed in EGG1 geogrid (1.85%) was close to the serviceability limit (e.g. 2%; Christopher et al. 2008) but significantly smaller than the geogrid ultimate failure strain (i.e. greater than 8%). Results in **Figure 9.73** through **Figure 9.75** indicate that measured maximum strains in WGG2, WGG3 and KGG1 geogrids were well below the serviceability limit and therefore, significantly smaller than the geogrids failure strains. Similar strain distributions were reported by Miura et al. (1990), Perkins (1999) and Abu-Farsakh and Chen (2011).

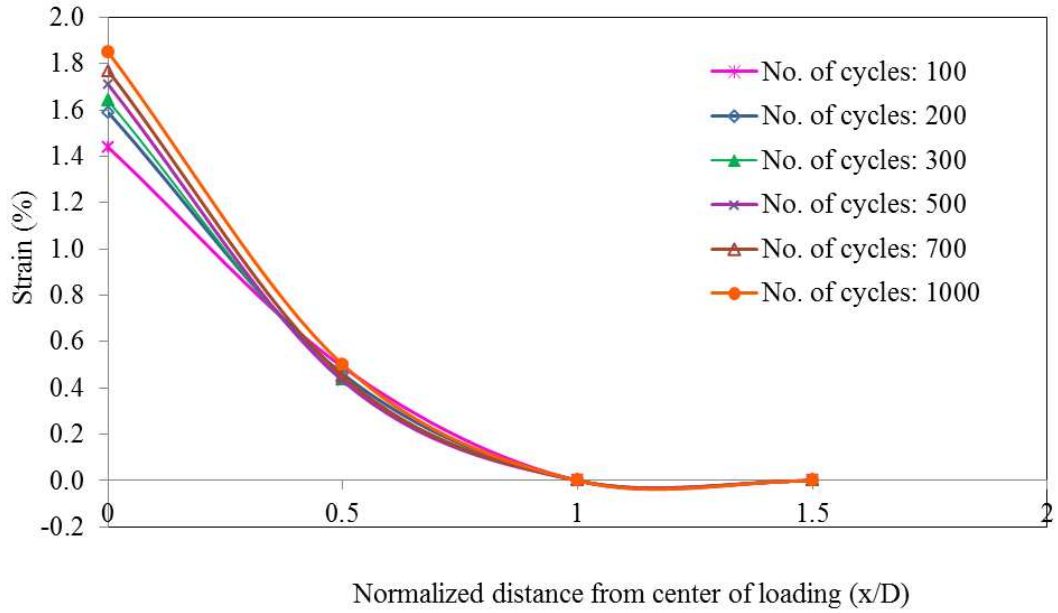


Figure 9.72. Strain distributions in the EGG1 geogrid

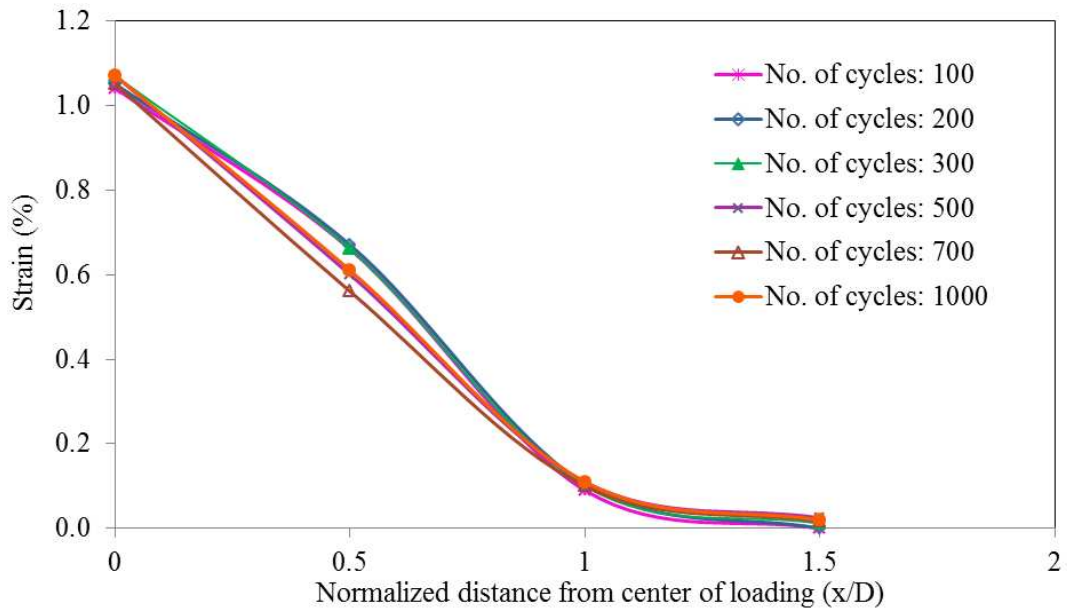


Figure 9.73. Strain distributions in the WGG2 geogrid

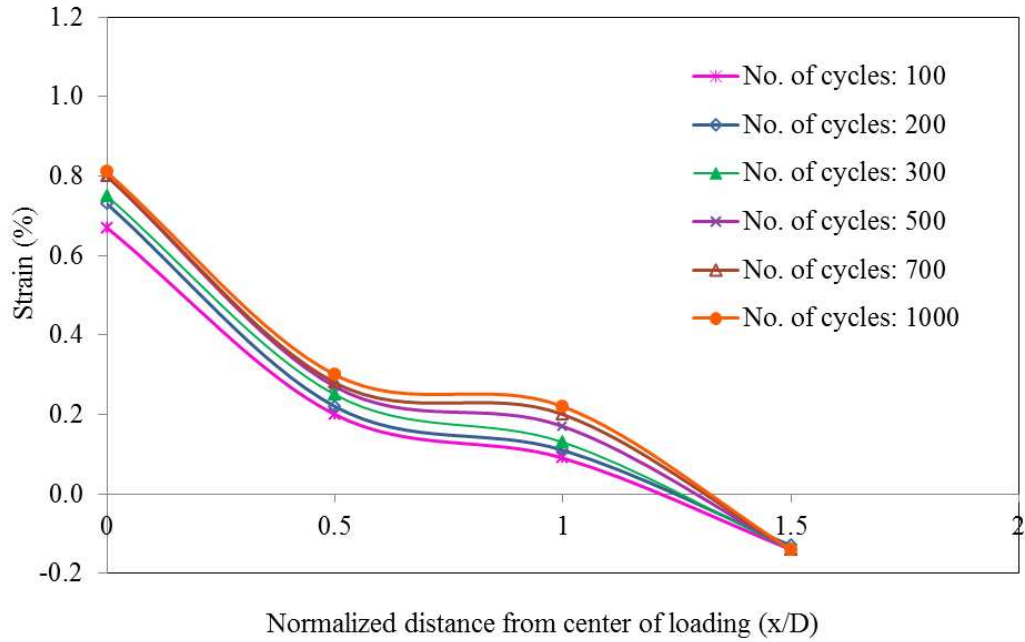


Figure 9.74. Strain distributions in the WGG3 geogrid

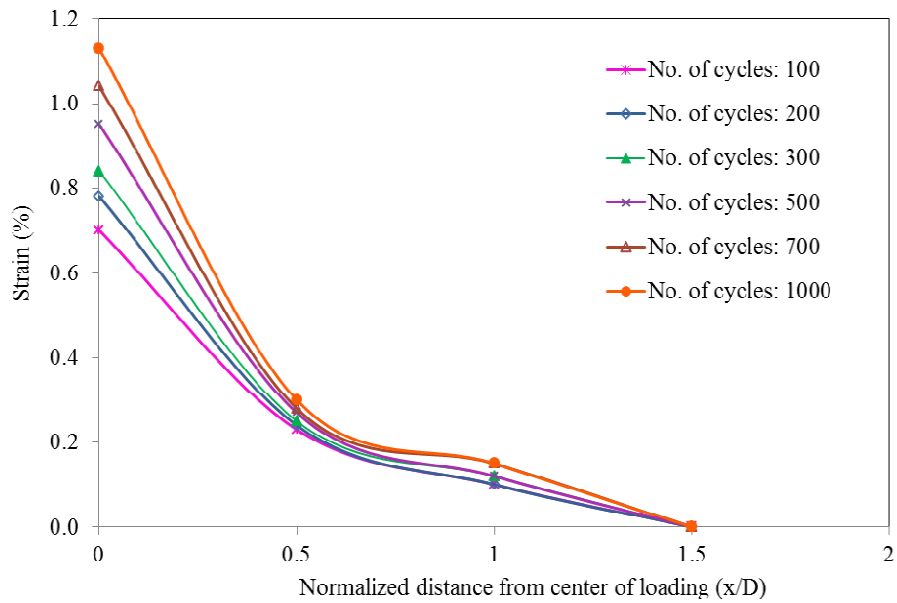
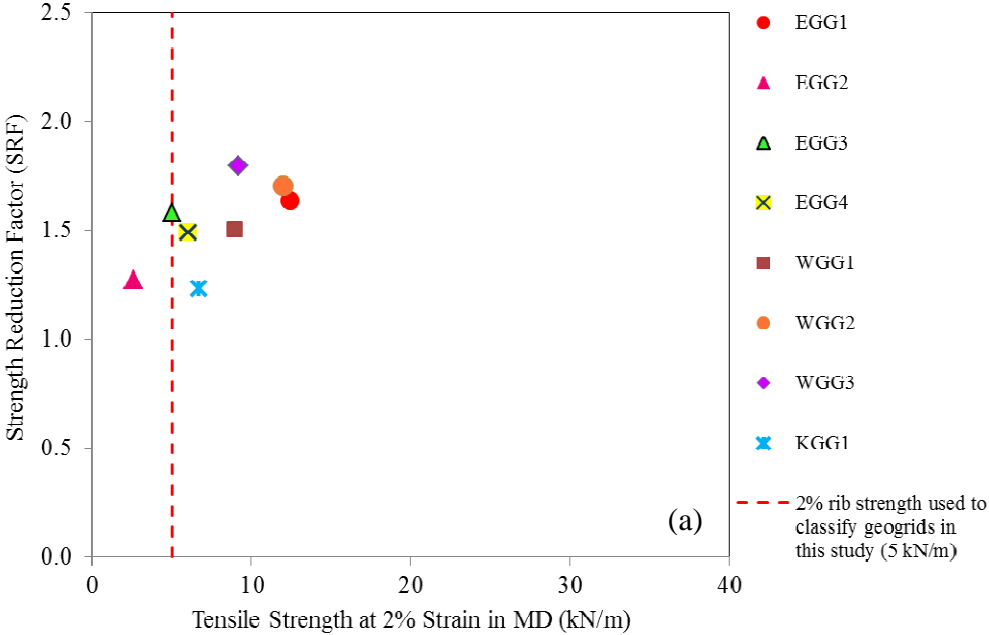
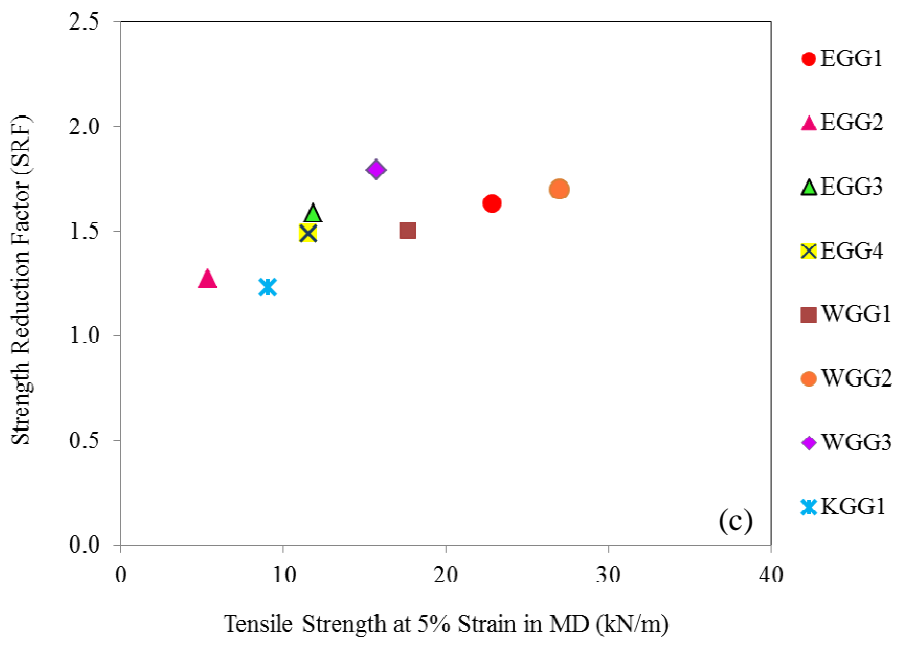
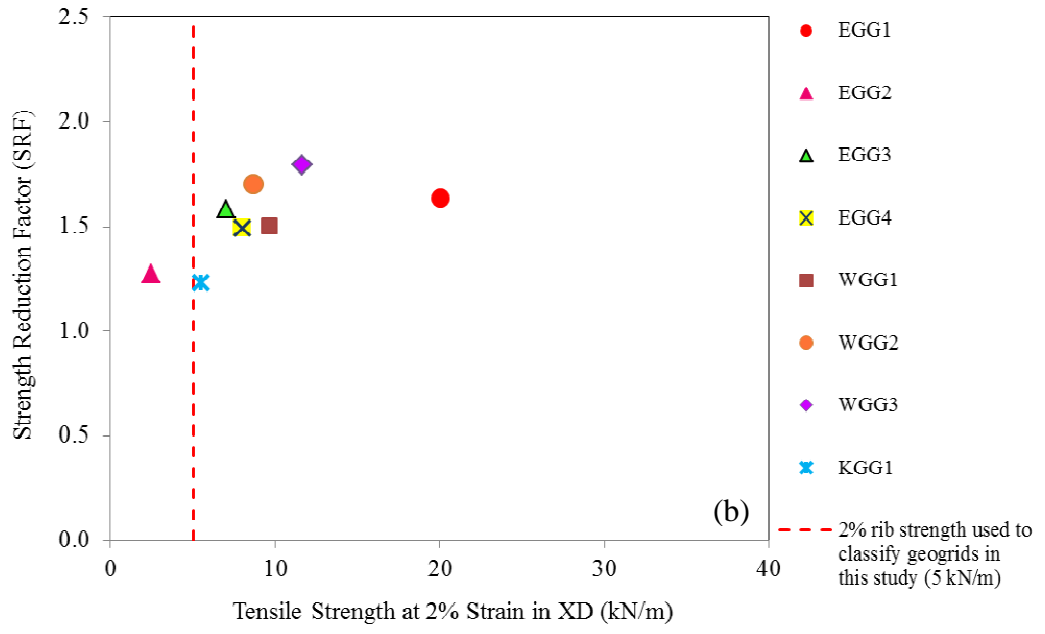


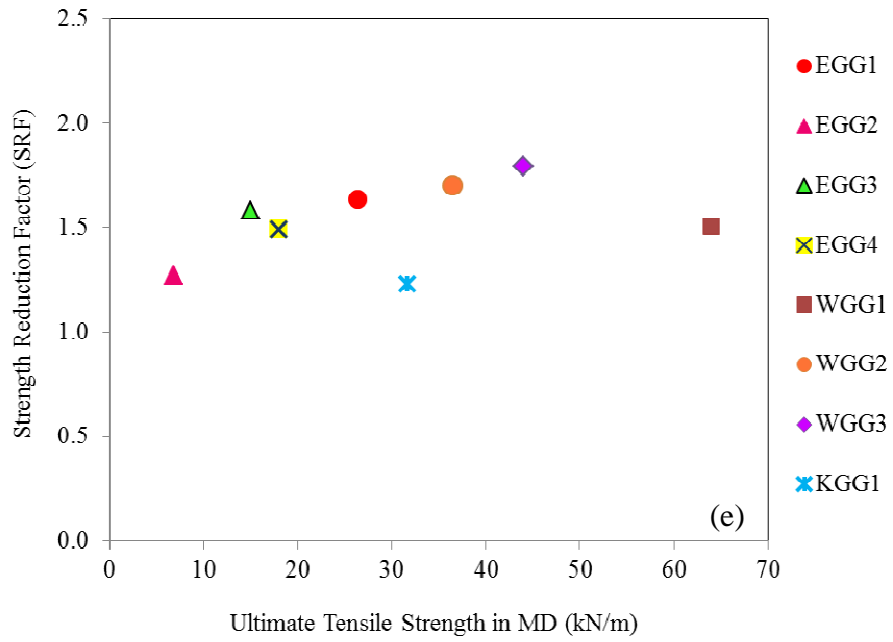
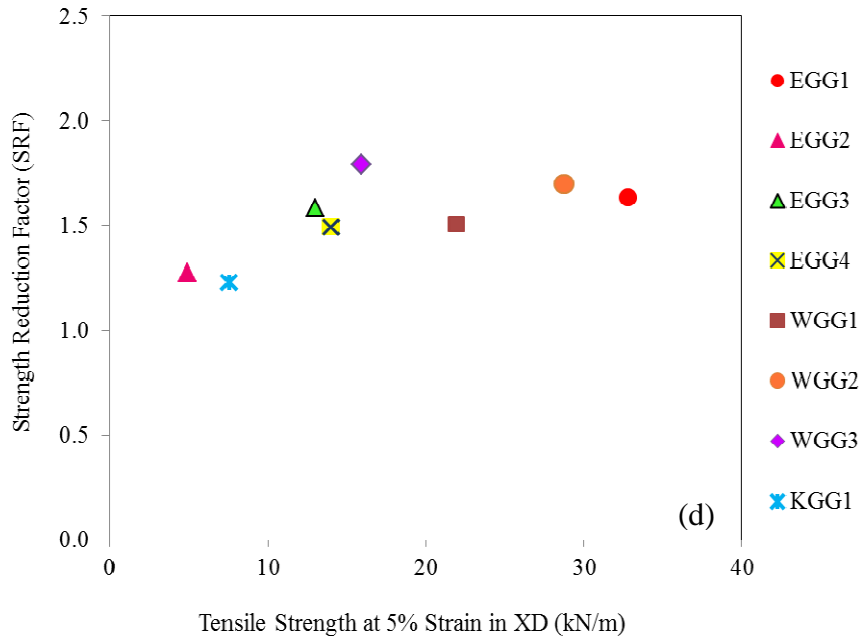
Figure 9.75. Strain distributions in the KGG1 geogrid

Figure 9.76 shows the correlations between the SRF values of the test models and the rib strength properties of all the geogrids tested in this study. **Figure 9.76** indicates that the SRF value of a reinforced model increases with the rib strength properties of the geogrid used. However, it is observed that the trend of increasing SRF value is more closely related to the rib strength at 2% strain in both MD and XD and rib strength at 5% strain in MD than the ultimate strength.

Figure 9.77 shows the correlations between the SRFs and ultimate junction strength properties of the all geogrids tested. These results indicate that the junction strength does not seem to be a governing factor in the performance of the reinforced model with respect to its SFR value for the base-subgrade models tested.







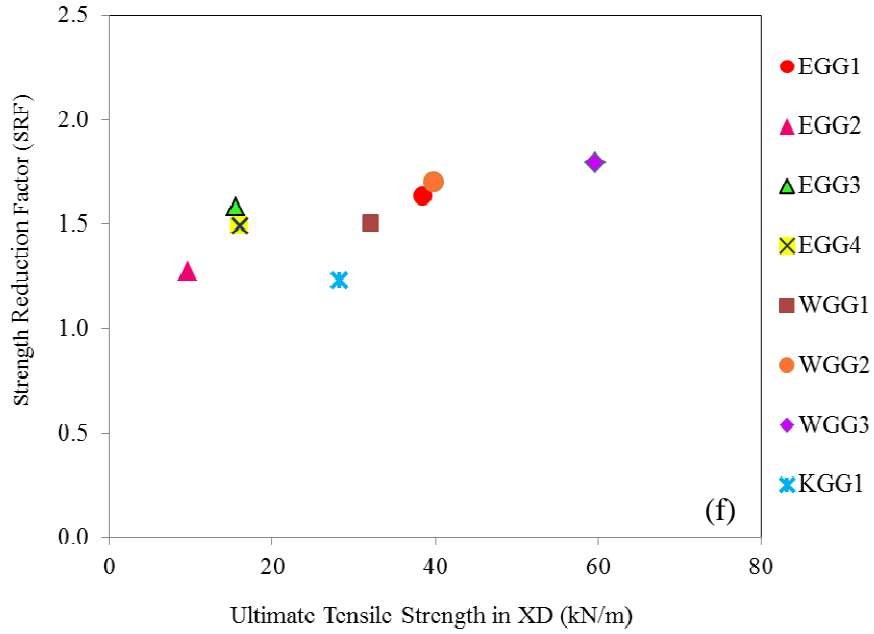
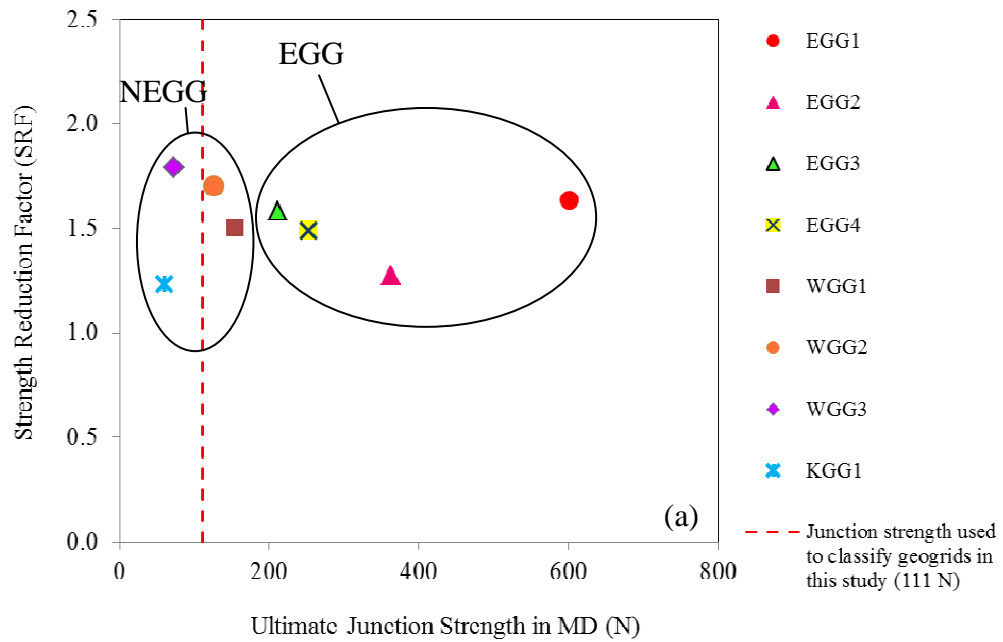


Figure 9.76. Correlation between SRF from cyclic plate load tests and rib strength values (a) at 2% strain in MD, (b) in XD, (c) at 5% strain in MD, (d) in XD, (e) ultimate rib strength in MD, (f) in XD



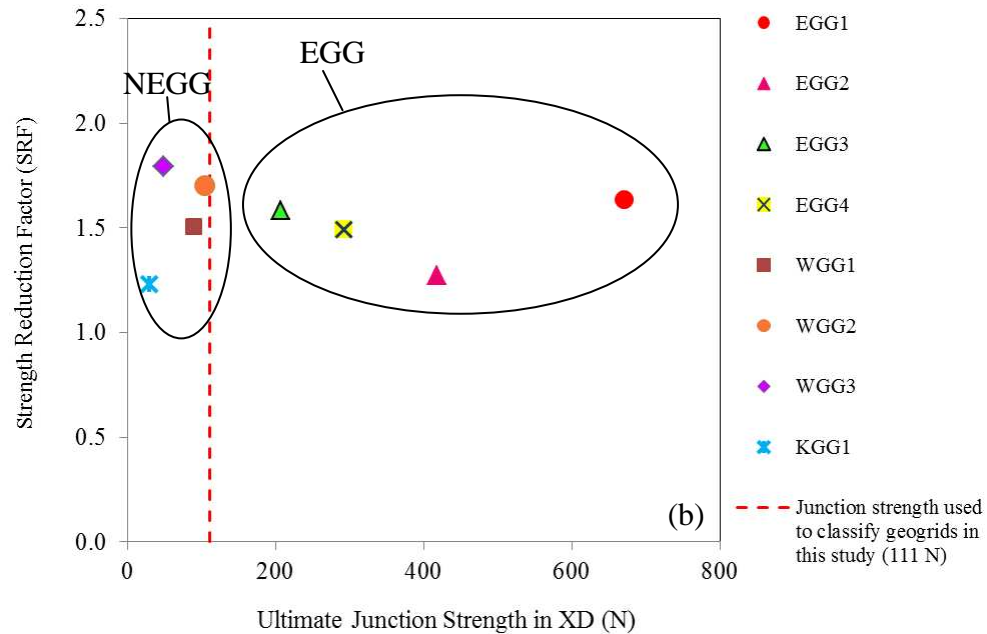
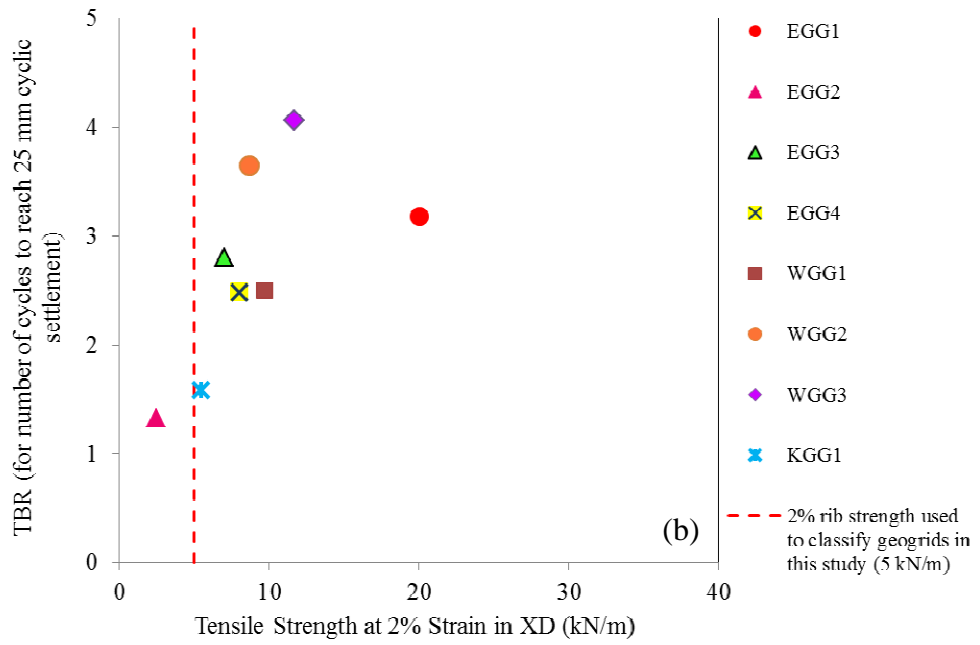
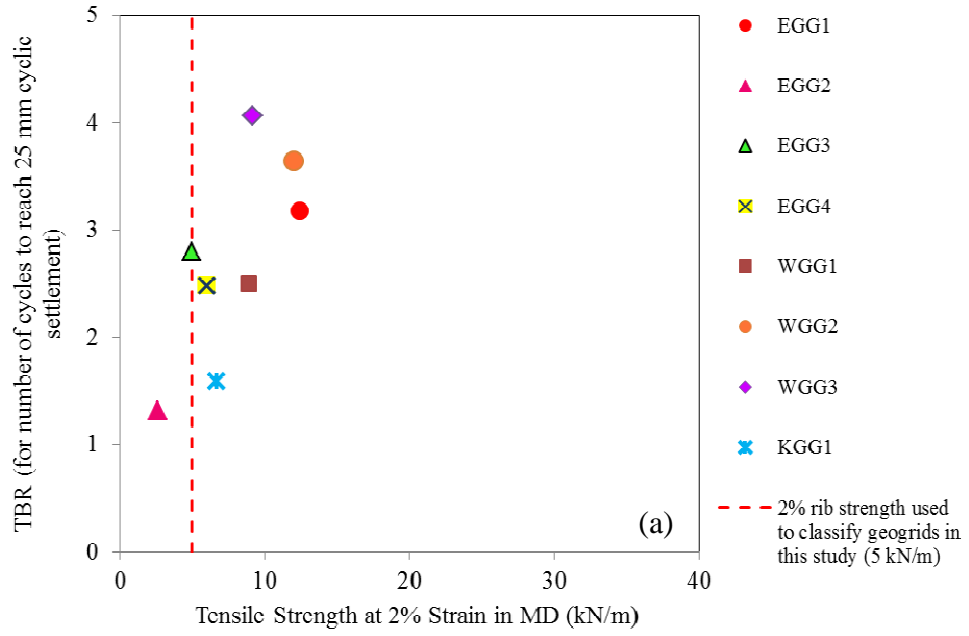
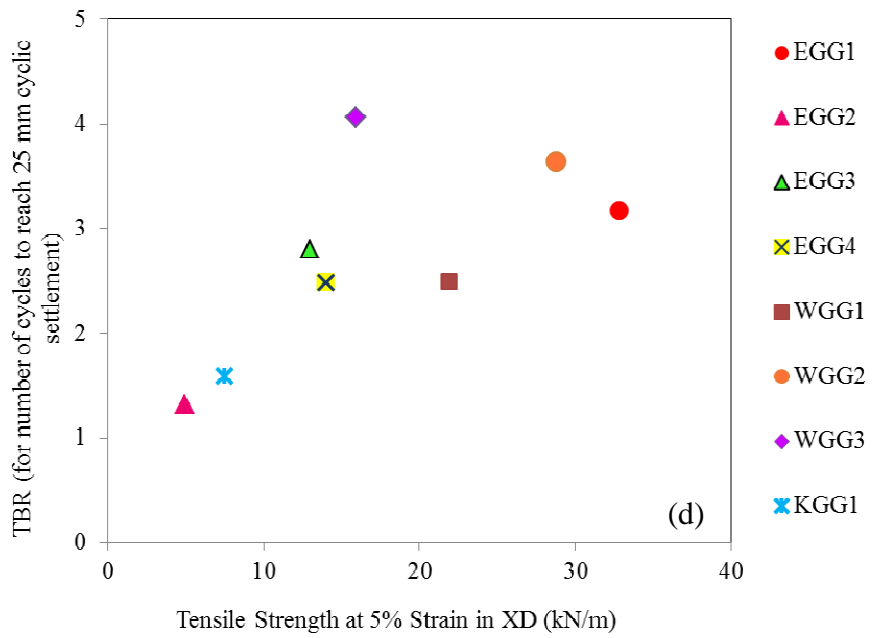
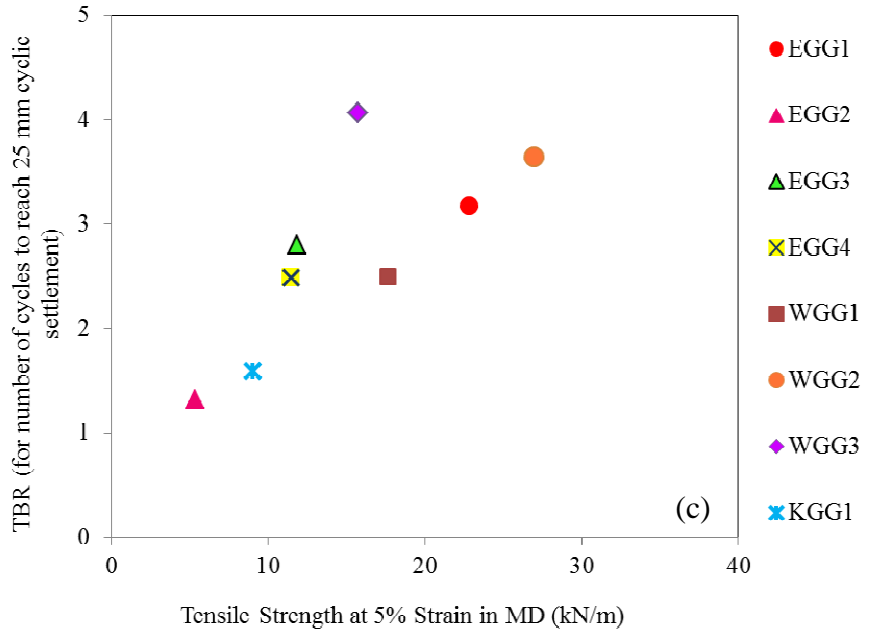


Figure 9.77. Correlation between SRF and ultimate junction strength in (a) MD, (b) XD

Figure 9.78 and **Figure 9.79** show the correlations between the TBR values of the test models and the rib and junction strength properties of the geogrids used in this study, respectively. The results in **Figure 9.78** show that the TBR value of a reinforced model increases with the rib strength properties of the geogrid used in the model. However, similar to the SRF value, the results do not show a conclusive dependence of the TRB value on the geogrid ultimate junction strength (**Figure 9.79**).

Taken together, the cyclic plate load test results indicated that the improvement in the performance of the base-subgrade models tested was, by and large, proportional to the rib index properties of the geogrid used.





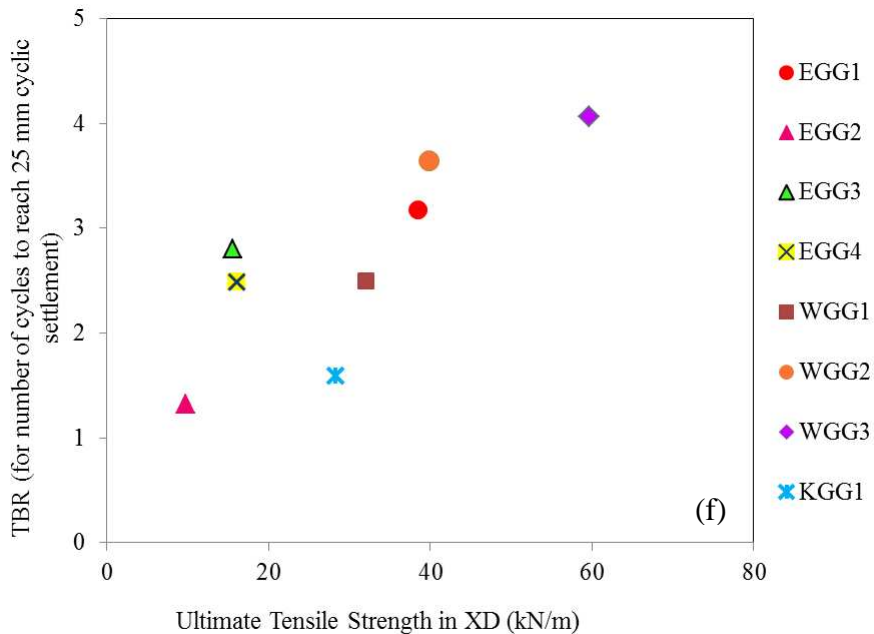
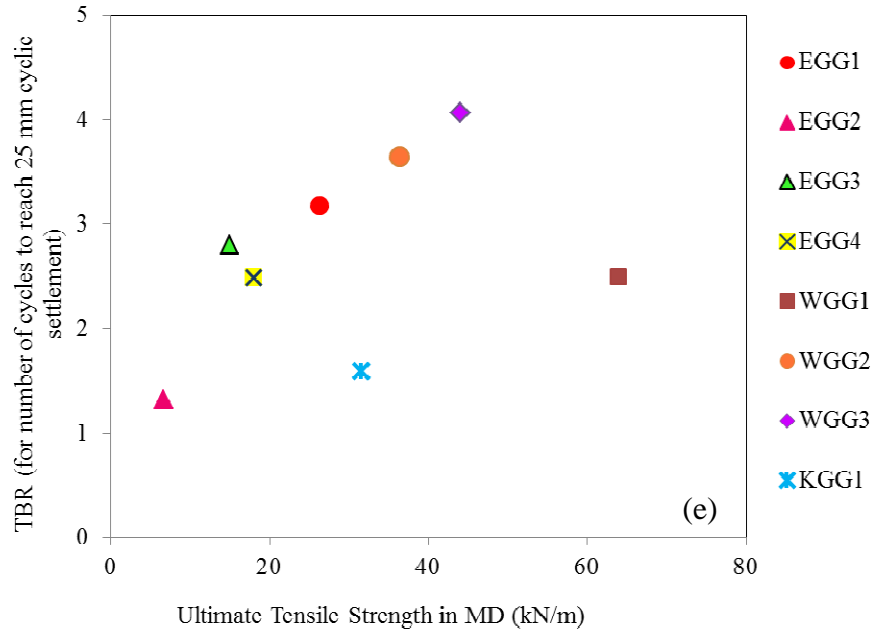


Figure 9.78. Correlation between (a) TBR and rib strengths at 2% strain in MD, (b) in XD, (c) TBR and rib strengths at 5% strain in MD, (d) in XD, (e) TBR and ultimate rib strengths in MD, (f) in XD

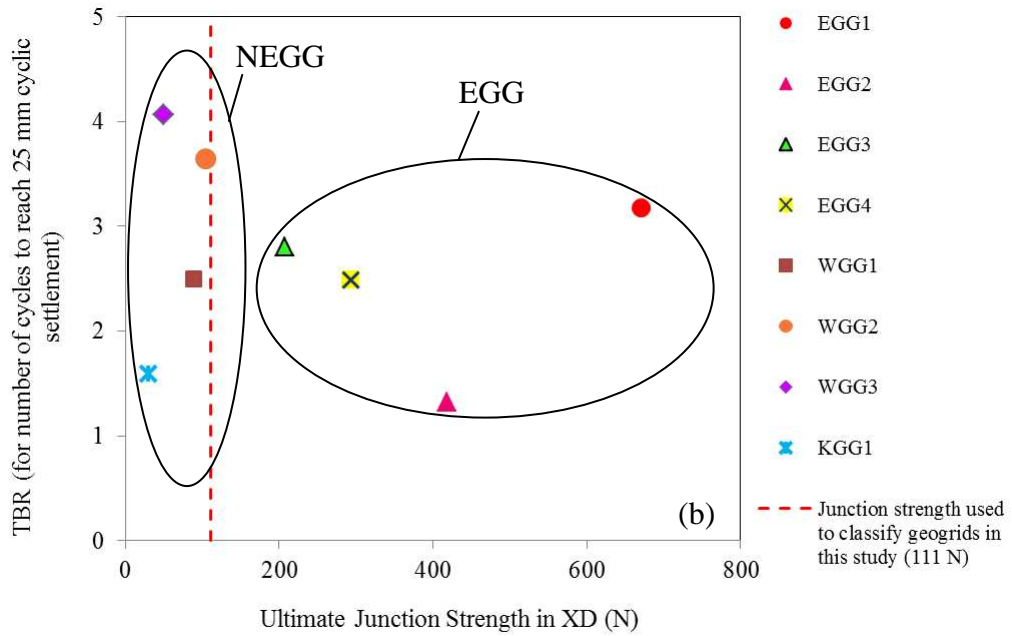
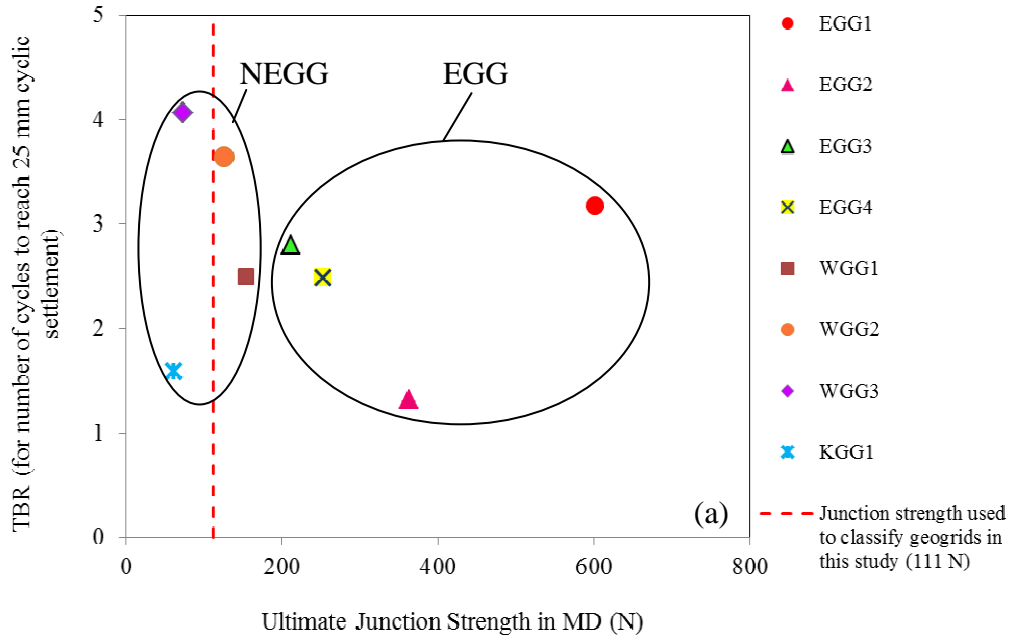


Figure 9.79. Correlation between TBR and ultimate junction strength (a) in MD, (b) in XD

9.3. TBR Correlation Equations for the Plate Load Test Models

In this study, it was observed that the TBR value of the plate load test models was, by and large, proportional to the rib strength properties of the geogrids tested (**Section 9.2.5**). Therefore, correlation equations were developed for the TBR values of the reinforced plate load models tested as described in the following sections.

9.3.1. Development of TBR Equations

EGG Products:

Model #1: TBR as a function of the geogrid rib strength at 2% strain, rib strength at 5% strain and ultimate rib strength properties

$$\text{TBR} = \beta_0 + \beta_1 X_1 + \beta_2 X_2 + \beta_3 X_3 \quad (9.3.1)$$

β_0 , β_1 , β_2 and β_3 = Regression coefficients as determined through multiple regression analysis using Microsoft Excel and the SPSS (2012) statistics software program

X_1 = Rib strength at 2% strain

X_2 = Rib strength at 5% strain

X_3 = Ultimate rib strength

Table 9.2. Regression coefficients for EGG products using Model #1

Regression Coefficient	β_0	β_1	β_2	β_3
MD	0.44308	-0.55431	0.29354	0.11039
XD	0.7051774	-1.1957	0.92678	-0.10216
ln (MD)	-2.8806	-2.0926	2.7945	0.791156
ln (XD)	-5.938	-8.15677	10.83937	-1.16447

Model #2: TBR as a function of the geogrid rib strength at 2% strain, rib strength at 5% strain and their cross-correlation

$$\text{TBR} = \beta_0 + \beta_1 X_1 + \beta_2 X_2 + \beta_3 X_1 X_2 \quad (9.3.2)$$

where $\beta_0 - \beta_3$ and, X_1 and X_2 were defined in Equation 9.3.1.

Table 9.3. Regression coefficients for EGG products using Model #2

Regression Coefficient	β_0	β_1	β_2	β_3
MD	-0.16	-0.08	0.348	-0.013
XD	0.006	-1.066	0.810	-0.003
ln (MD)	-1.089	417.2	421.0	-418.6
ln (XD)	-7.422	-- $1.31 \times 10^{15}*$	-1.31×10^{15}	1.31×10^{15}

* Unrealistically high values, hence this model was discarded.

NEGG products:

Model #1: TBR based on rib strength at 2% strain, rib strength at 5% strain and ultimate rib strength properties

$$\text{TBR} = \beta_0 + \beta_1 X_1 + \beta_2 X_2 + \beta_3 X_3 \quad (9.3.3)$$

where $\beta_0 - \beta_3$ and $X_1 - X_3$ were defined in Equation 9.3.1.

Table 9.4. Regression coefficients for NEGG products using Model #1

Regression Coefficient	β_0	β_1	β_2	β_3
MD	-11.22	2.75	-0.71	0.03
XD	-0.645	-0.085	0.068	0.078
ln (MD)	-34.203	30.93	-15.115	3.006
ln (XD)	-9.984	-1.124	1.053	3.398

Model #2: TBR based on rib strength at 2% strain, rib strength at 5% strain and the interaction between them

$$\text{TBR} = \beta_0 + \beta_1 X_1 + \beta_2 X_2 + \beta_3 X_1 X_2 \quad (9.3.4)$$

where $\beta_0 - \beta_3$ and, X_1 and X_2 were defined in Equation 9.3.1.

Table 9.5. Regression Coefficients for NEGG products using Model #2

Regression Coefficient	β_0	β_1	β_2	β_3
MD	-11.664	2.587	-0.269	-0.026
XD	-25.433	3.915	2.285	-0.283
ln (MD)	-6.084	1327.22	1321.51	-1322.28
ln (XD)	-190.51	54568.73	54542.63	-54517.66

9.3.2. Verification of TBR Correlation Equations

Table 9.6 and **Table 9.7** show a summary of R^2 values for the regression models developed for the EGG and NEGG geogrids. These results indicate that the R^2 values for all final regression models are greater than 0.999 which indicate that these models fit the data nearly perfectly (except for cases of \ln (MD) and \ln (XD) in **Table 9.7**). In comparison, the R^2 value for a linear equation developed by Gu (2011) for base layer thickness, geogrid tensile modulus and subgrade strength was 0.96. However, the R^2 values for the \ln (MD) equation using Model #2 for the EGG and NEGG products are 0.91 and 0.53, respectively. Hence these models were labeled as ‘not satisfactory’ in the list of final regression models examined in this study (**Section 9.3.3**).

Table 9.6. R^2 -values for EGG regression equations using Model #1

Regression Model Equation	R^2 -value
MD	0.999985
XD	0.999962
\ln (MD)	0.999992
\ln (XD)	0.999966

Table 9.7. R^2 -values for EGG regression equations using Model #2

Regression Model Equation	R^2 -value
MD	0.99991389
XD	0.99932166
\ln (MD)	0.91216934
\ln (XD)	-608.24

Table 9.8 and **Table 9.9** show that the final models have R^2 of 0.99 [except for the case of \ln (MD) in **Table 9.9**], which suggested that the models well fit the data used.

Table 9.8. R^2 -values for NEGG regression equations using Model #1

Regression Model Equation	R^2 -value
MD	0.999890
XD	0.999954
\ln (MD)	0.999924
\ln (XD)	0.999989

Table 9.9. R^2 -values for NEGG regression equations using Model #2

Regression Model Equation	R^2 -value
MD	0.999945
XD	0.999883
\ln (MD)	0.534975
\ln (XD)	Unrealistic

A summary of test types, geogrid properties and TRB values reported in selected previous studies is given in **Table 9.10** which was used for comparison purposes in this study. The geogrid properties reported in **Table 9.10** were used in Equations 9.3.5 through 9.3.20 (**Section 9.3.3**) and the corresponding predicted TRB values were compared against those reported in previous studies as plotted in **Figure 9.80** through **Figure 9.89**. Regression equations using the data from this study that did not result in $R^2 \approx 1$ were discarded.

Table 9.10. Summary of test types, geogrid properties and TRB values reported in selected previous studies

Previous Studies	Type of Tests	Geogrid	Type	Rib strength at 2% strain	Rib strength at 2% strain	Rib strength at 5% strain	Rib strength at 5% strain	Ultimate Rib Strength (MD)	Ultimate Rib Strength (XD)	Mesured TBR
Abu-Farsakh and Chen (2011)	Cyclic plate load tests	GG1	EGG	4.1	6.6	-	-	-	-	5.5
		GG2	EGG	6	9	-	-	-	-	6.1
		GG3	EGG	8.6	8.6	-	-	-	-	6.4
		GG4	EGG	9.5	9.5	-	-	-	-	7.4
Cuelho and Perkins (2009)	Field tests	Integrally Formed Grid (IFG-3)	EGG	7.5	12.8	15.2	24.8	22.6	32.4	5.9
		IFG-5	EGG	5.7	8.3	11.3	14.5	16	21.6	4.7
		Woven Grid (WoG-7)	NEGG	6.9	9.9	16.3	16.4	33.9	48.9	5.2
		WoG-8	NEGG	7	8.6	13.1	12.2	31.3	53.7	3.8
Chehab et al. (2007)	Accelerated Pavement Tests in laboratory, APT-I	Tensar BX1200	EGG	9.8	15.6	16.8	29.3	23.9	32.9	76.0
		Mirafi BXG11	NEGG	10.3	11.0	18.1	17.4	39.5	52.8	120.0
	APT-II	Tensar BX1200	EGG	9.8	15.6	16.8	29.3	23.9	32.9	1.8
		Huesker Fornit 30	NEGG	11.4	17.2	22.7	32.8	N/A	N/A	1.9
		Mirafi BXG11	NEGG	10.3	11.0	18.1	17.4	39.5	52.8	62.5
Tingle and Jersey (2005)	Cyclic plate load tests	Geogrid	EGG	-	-	13.2	17.9	-	-	1.5

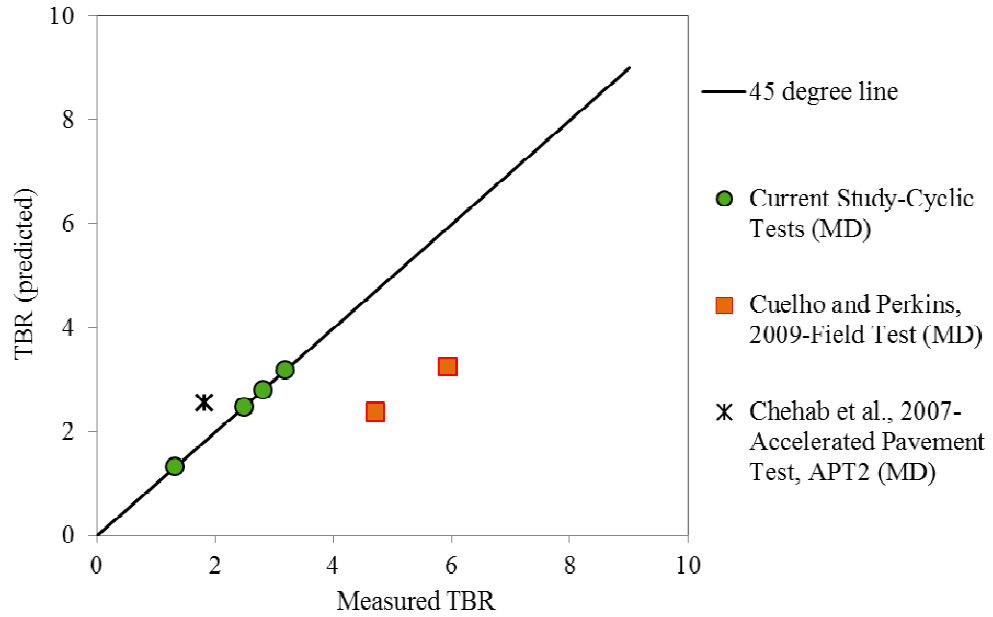


Figure 9.80. Predicted (Equation 9.3.5) vs. measured TBR values in the current and previous studies

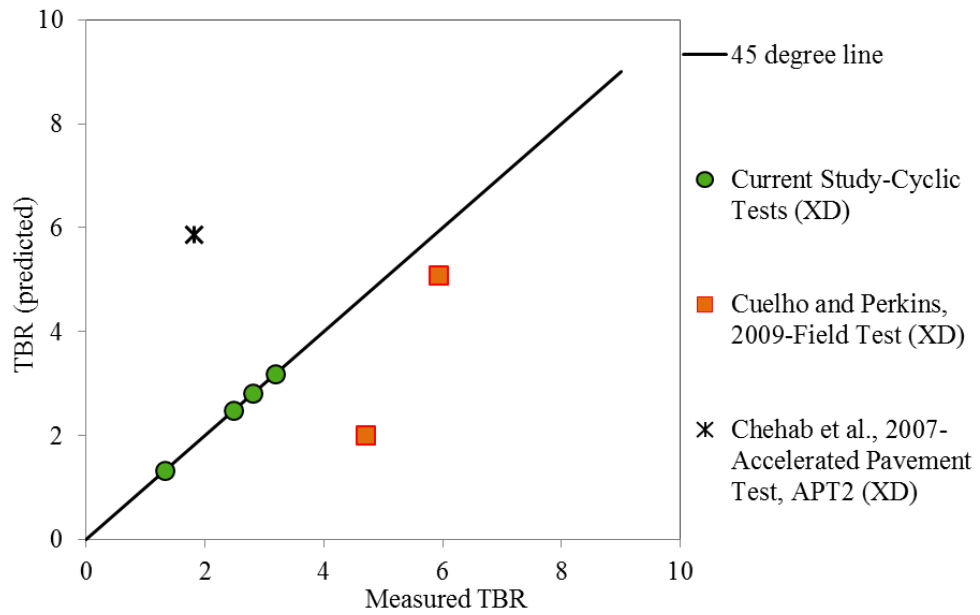


Figure 9.81. Predicted (Equation 9.3.6) vs. measured TBR values in the current and previous studies

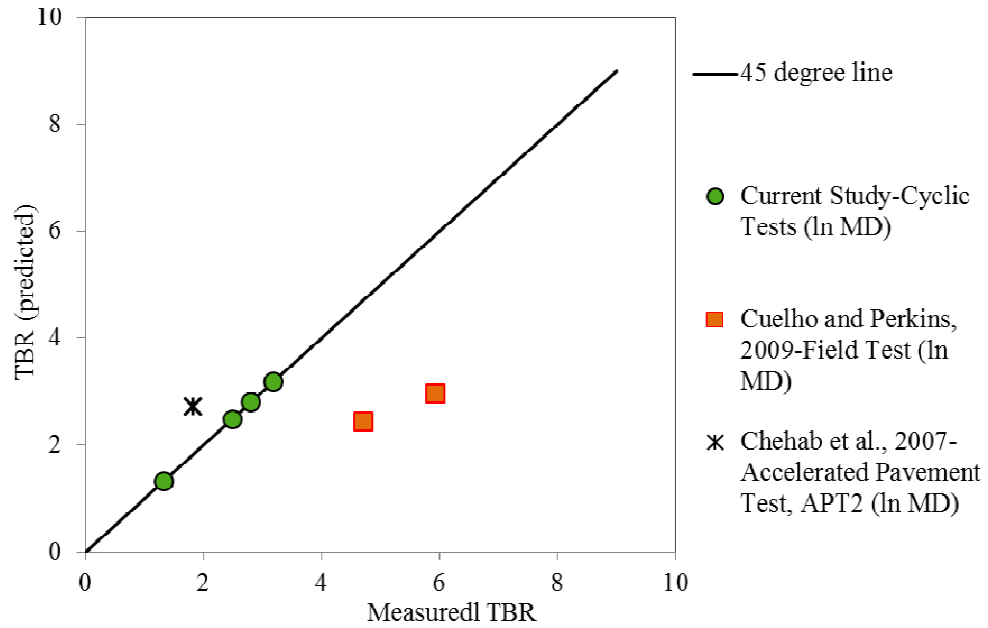


Figure 9.82. Predicted (Equation 9.3.7) vs. measured TBR values in the current and previous studies

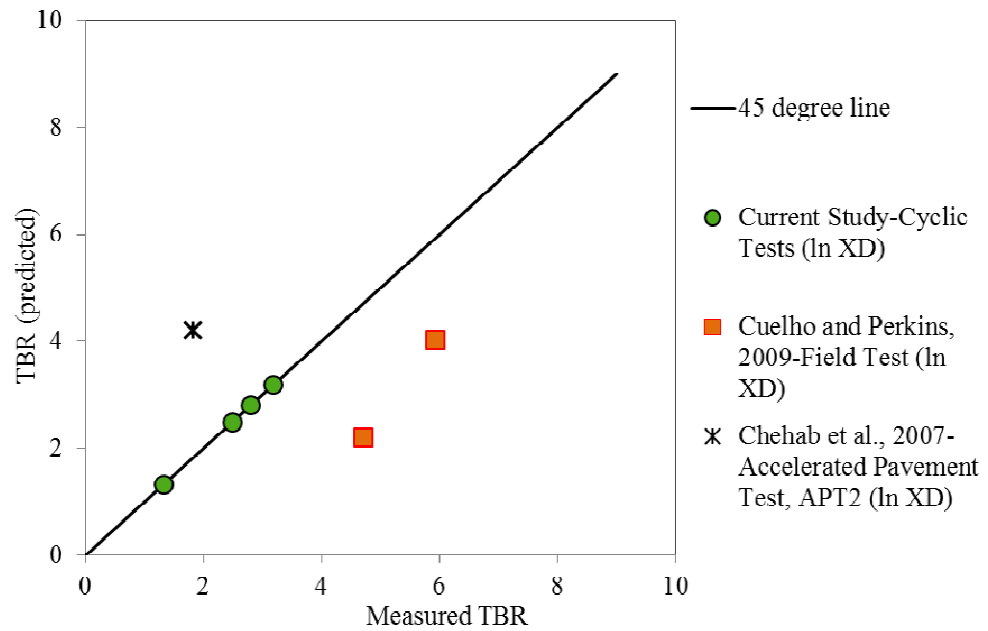


Figure 9.83. Predicted (Equation 9.3.8) vs. measured TBR values in the current and previous studies

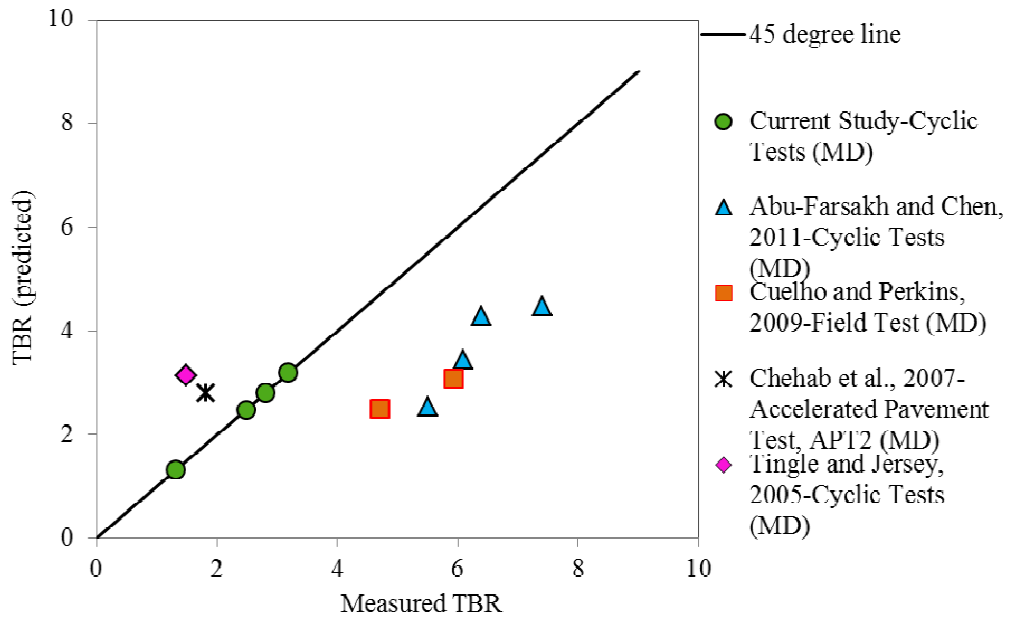


Figure 9.84. Predicted (Equation 9.3.9) vs. measured TBR values in the current and previous studies

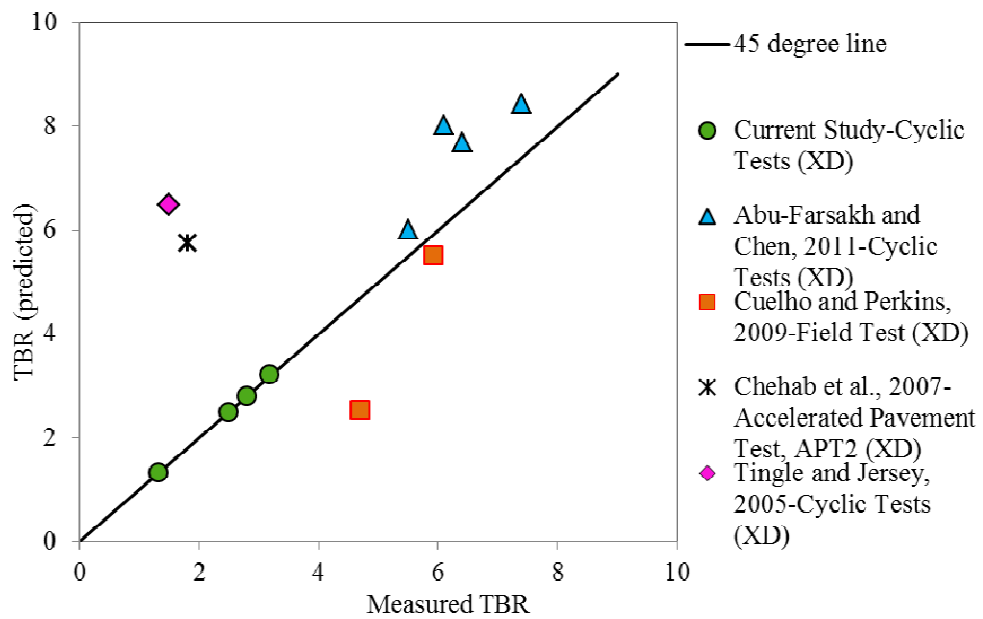


Figure 9.85. Predicted (Equation 9.3.10) vs. measured TBR values in the current and previous studies

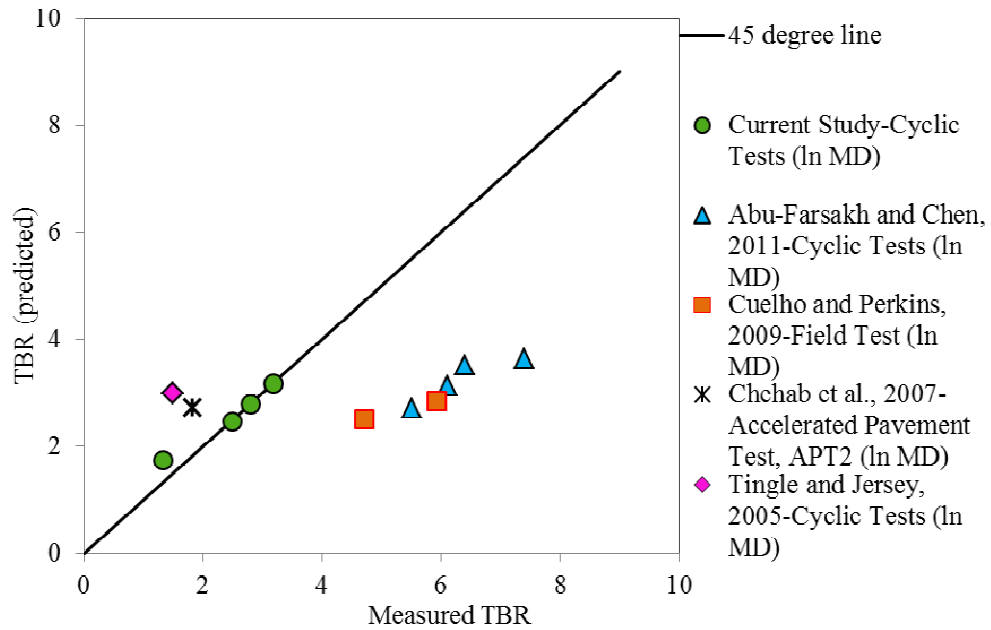


Figure 9.86. Predicted (Equation 9.3.11) vs. measured TBR values in the current and previous studies

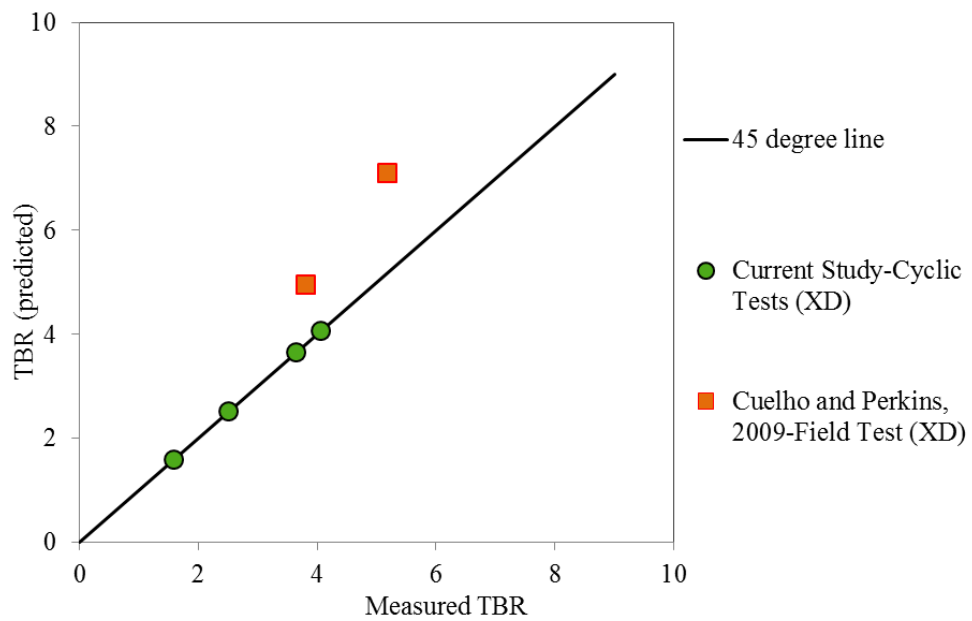


Figure 9.87. Predicted (Equation 9.3.14) vs. measured TBR values in the current and previous studies

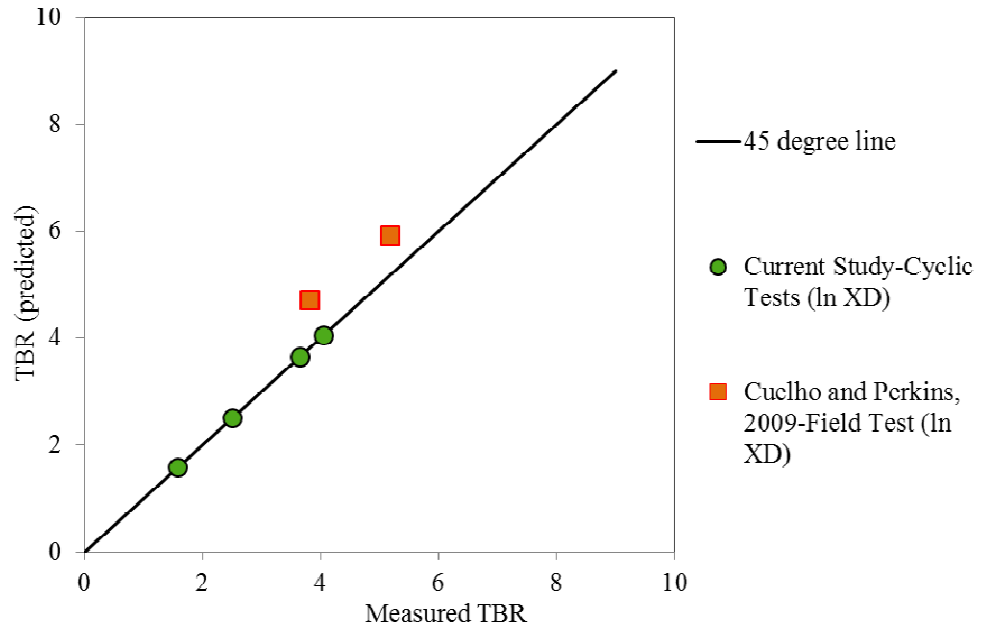


Figure 9.88. Predicted (Equation 9.3.16) vs. measured TBR values in the current and previous studies

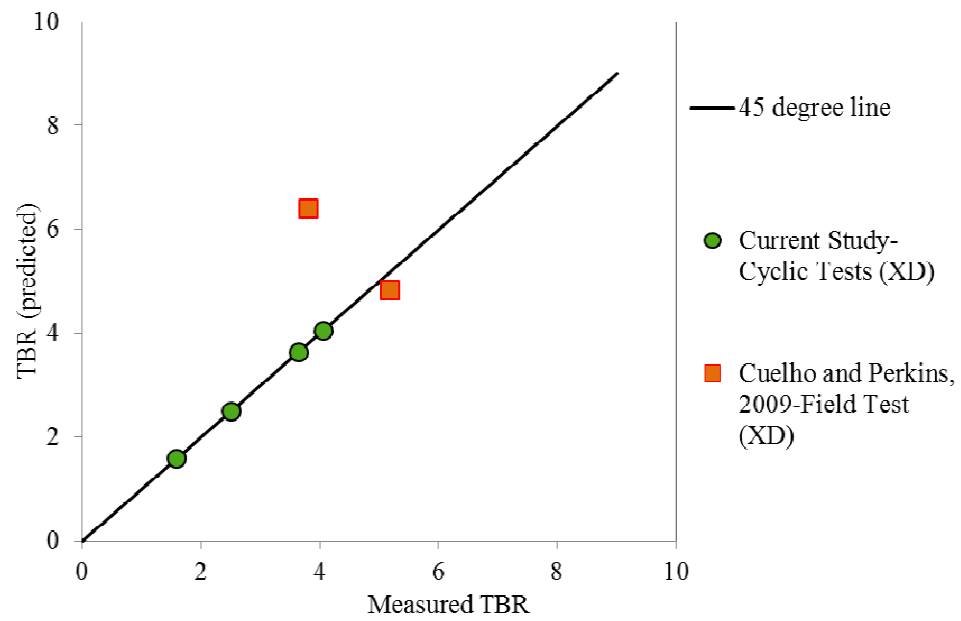


Figure 9.89. Predicted (Equation 9.3.18) vs. measured TBR values in the current and previous studies

Results shown in **Figure 9.80** through **Figure 9.89** indicate that the TBR values calculated using the regression equations in this study for different previous studies were somewhat comparable but not perfectly consistent with the corresponding measured values. Therefore, the following literature survey was carried out to determine possible reasons for the differences observed between the results of previous studies and those of the current study:

Abu-Farsakh and Chen (2011)



A steel test box with inside dimensions of 2 m (length) \times 2 m (width) \times 1.7 m (height) was constructed to house model pavement sections (**Figure 9.90**). The subgrade consisted of silty clay, having a liquid limit of 31 and a plasticity index (PI) of 15. Kentucky crushed limestone material was used in the base course layer for all test sections. Base thickness was about 320 mm. The crushed limestone had a 100% passing 37.5-mm opening sieve, 92% passing 19-mm opening sieve, 61% passing No. 4 opening sieve and 0.35% passing No. 200 opening sieve with an effective particle size (D_{10}) of 0.382 mm, a mean particle size (D_{50}) of 3.126 mm, a uniformity coefficient (C_u) of 11.80 and a coefficient of curvature (C_c) of 1.07. A 60 mm-thick layer of hot mix asphalt (HMA) was used over the base course.



Figure 9.90. Laboratory test box, hydraulic actuator and reaction system in the study by Abu-Farsakh and Chen (2011)

Four different extruded polypropylene geogrids, GG1, GG2, GG3 and GG4 were used to reinforce the base layer in the pavement test sections (**Table 9.11**). Abu-Farsakh and Chen (2011) determined TBR values for different base reinforced sections at the rut depth of 19 mm. However, in the current study TBR was calculated at a rut depth of 25 mm.

Table 9.11. Properties of geogrids used in the study by Abu-Farsakh and Chen (2011)

Reinforcement	Aperture shape	T^a (kN/m)		J^b (kN/m)		Aperture stability (kg-cm/deg)	Aperture size (mm)
		MD ^c	CD ^d	MD ^c	CD ^d		
GG1 biaxial geogrid		4.1	6.6	205	330	3.2	25 x 33
GG2 biaxial geogrid		6.0	9.0	300	450	6.5	25 x 33
GG3 triaxial geogrid		8.6 ^e		430 ^e		3.6	40 x 40 x 40
GG4 triaxial geogrid		9.5 ^e		475 ^e		7.8	40 x 40 x 40

^aTensile strength (at 2% strain) (in accordance with ASTM D6637 for GG1 and ISO 10319:1996 for GG2).

^bTensile modulus (at 2% strain).

^cMachine direction.

^dCross machine direction.

^eRadial direction.

Cuelho and Perkins (2009)

Cuelho and Perkins (2009) constructed field test sections to evaluate the performance of several geosynthetics for subgrade stabilization applications. A sandy clay soil was prepared as a weak roadbed material at a CBR value of approximately 1.8, and a 200 mm thick aggregate layer (crushed gravel) was compacted over the geosynthetic reinforcement. They examined the effects of the tensile strength at 2% strain, 5% strain and the ultimate tensile strength on the rutting performance of geogrid-reinforced roadway test sections.

A single-drum vibratory roller was used to compact the base aggregate. Traffic load was applied to the test sections using a fully loaded three-axle dump truck in a single direction until an average of 100 mm of rut was developed in each of the individual test sections. The properties of geogrids used in Cuelho and Perkins' study are given in **Table 9.12**. A summary of test section properties with their comparative rutting performance is presented in **Table 9.13**.

Table 9.12. Properties of geosynthetics used in the study by Cuelho and Perkins (2009)

Geosynthetic Test Section*	Tested by WTI						Published by Manufacturers ^a					
	Strength ^b @ 2% (kN/m)		Strength ^b @ 5% (kN/m)		Ultimate ^b Strength (kN/m)		Strength ^b @ 2% (kN/m)		Strength ^b @ 5% (kN/m)		Ultimate ^b Strength (kN/m)	
	MD	XMD	MD	XMD	MD	XMD	MD	XMD	MD	XMD	MD	XMD
WeG-1	9.5	9.7	19.6	20.4	29.9	35.3	10.7	10.7	21.3	21.3	32.0	32.0
WeG-2	13.2	13.0	25.7	26.1	38.4	39.6	8	8	16	16	20	20
IFG-3	7.5	12.8	15.2	24.8	22.6	32.4	6.0	9.0	11.8	19.6	19.2	28.8
CoG-4	13.6	14.4	27.3	28.0	41.8	43.8	12	12	24	24	30 ^d	30 ^d
IFG-5	5.7	8.3	11.3	14.5	16.0	21.6	4.1	6.6	8.5	13.4	12.4	19.0
WeG-6	13.9	13.7	27.1	27.2	40.7	41.2	12	12	24	24	30	30
WoG-7	6.9	9.9	16.3	16.4	33.9	48.9	7.3	7.3	13.4	13.4	29.2	29.2
WoG-8	7.0	8.6	13.1	12.2	31.3	53.7	7.7	8.4	11.5	15.2	34.9	56.5
WoT-9	7.5	12.5	20.8	27.2	59.8	71.1	8.8	8.8	21.9	21.9	52.5	47.3
NWoT-10	0.1	0.2	0.6	0.7	17.5	12.7	NP		NP		912 ^e	

*Acronym meanings: WeG = Welded grid, IFG = integrally-formed grid, CoG = composite grid, WoG = woven grid, WoT = woven textile, NWoT = non-woven textiles; numbers represent position along length of test site

^aManufacturers' minimum average roll values (MARV)

^bASTM D4595 and ASTM D6637

^cTested by WTI as a composite, i.e., not separately

^dNon-woven portion of this material increases the ultimate strength by 6kN/m in the MD and by 10kN/m in the XMD

^eGrab tensile strength (ASTM D-4632) in Newtons at 50% elongation

NP - information was not provided by the manufacturer

Table 9.13. Summary of test section properties and comparative rutting performance in the study by Cuelho and Perkins (2009)

Geosynthetic Test Section	Average Base Thickness (mm)	Composite Subgrade CBR after Construction	Composite Subgrade CBR after Trafficking	N_{field}
Control 1	211	1.80	1.31	12.5
WeG-1	216	1.96	1.20	78.3
WeG-2	215	1.72	1.25	87.4
IFG-3	211	1.69	1.32	80.0
CoG-4	206	1.69	1.30	87.4
IFG-5	199	1.82	1.25	36.3
WeG-6	192	1.79	1.16	67.6
WoG-7	184	1.99	1.46	96.4
WoG-8	178	1.88	1.31	70.9
WoT-9	173	1.72	1.30	52.1
NWoT-10	171	1.66	1.29	34.0
Control 2	172	2.11	1.40	18.6

Note: N_{field} = Number of standard axle passes to reach 100 mm of rut for each section

Chehab et al. (2007)

Chehab et al. (2007) studied the effects of aperture size, tensile strength at 2% strain, ultimate tensile strength, junction strength and flexural rigidity of geogrids on rutting performance of small-scale roadway models. They performed two accelerated pavement tests (APT) in a 2.2 m-wide by 3.7 m-long test pit. The pit was originally 4.3 m deep but was backfilled with a Type-2A aggregate base conforming to the PennDOT specifications. The densely-compacted aggregate layer served as a bedrock-like support. The top 400 mm was considered as the pavement section. A silty-sandy soil typical of

central Pennsylvania was used as the subgrade, and Type-2A aggregate according to PennDOT specifications was used as the base layer in their model. An asphalt slab was constructed on the top of the base layer.

APT Test I

Four geogrid products, SF11, Fornit 30, BX1100 and BXG11 were used for the reinforced test sections R1, R2, R3 and R4, respectively. C1 was the control section. 19 mm rut deformation, with cracks along the edge of the wheel path occurred at 1,000 wheel cycles in the control section C1. From **Figure 9.91**, it was observed that same amount of rut deformation (about 19 mm) occurred at 76,000 and 120,000 wheel cycles in Sections R3 and R4, respectively. This information was used to calculate TBR values for APT Test I.

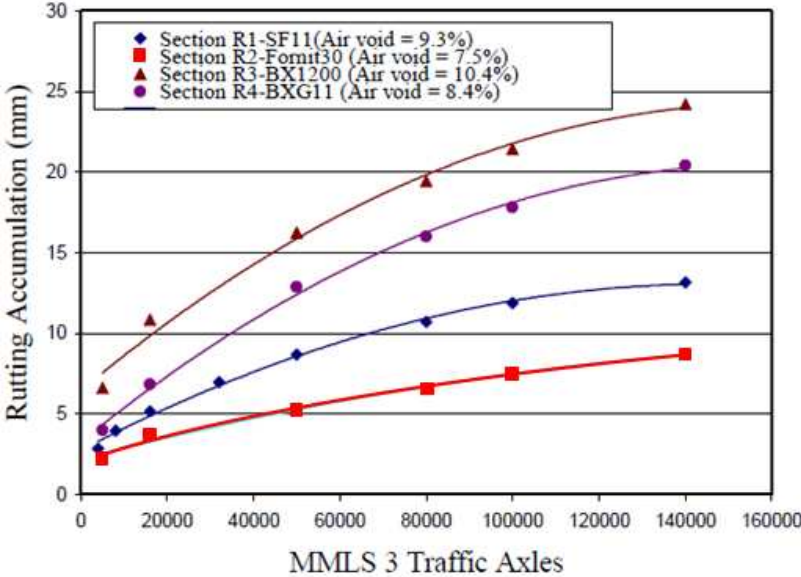


Figure 9.91. Rutting accumulation for locations where maximum rut occurred in case of APT I (Chehab et al. 2007)

APT Test II

In order to investigate the effectiveness of geogrid reinforcement in a different thickness of subgrade, four other sections were constructed. The four sections were denoted as P1, P2, P3 and P4. Section P1 was the control section without geogrid reinforcement. Sections P2, P3 and P4 were reinforced with Fornit30, BX1200 and BXG11 geogrids, respectively. The geogrid arrangement and dimensions of the above sections are given in **Table 9.14**.

Table 9.14. Structure parameters of test slabs (Chehab et al. 2007)

Section	Subgrade Thickness (in)	Base Course Thickness (in)	AC Thickness (in)	Geogrid Type
T1	11	3.9	N/A	Tensar BX1200
C1	10.5	2	1.5	N/A
R1	9.3	2.6	1.5	Synten SF11
R2	9.3	2.6	1.5	Huesker Fornit30
R3	9.3	2.6	1.5	Tensar BX1200
R4	9.3	2.6	1.5	Mirafi BXG11
P1	6	2	1.5	N/A
P2	6	2	1.5	Huesker Fornit30
P3	6	2	1.5	Tensar BX1200
P4	6	2	1.5	Mirafi BXG11

Results shown in **Figure 9.92** indicate that the maximum rut deformation in all test sections was 15 mm. Therefore, in APT Test II series the number of traffic axles to reach 15 mm rut deformation for each test section was used to calculate the corresponding TBR value. It was found that 1600, 3100, 2900 and 100,000 traffic axles were needed to produce nearly 15 mm rut deformation in Sections P1, P2, P3 and P4, respectively.

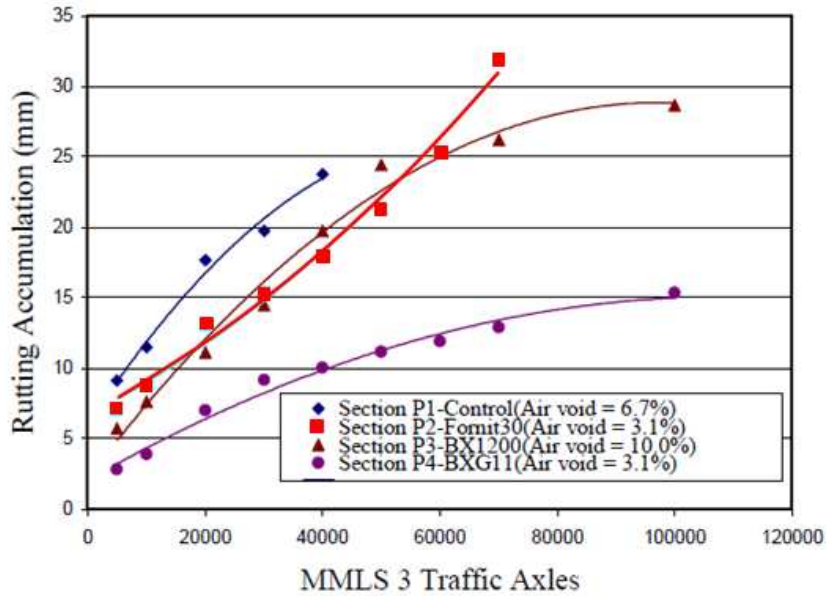


Figure 9.92. Rutting accumulation for locations where maximum rut occurred in APT II test series (Chehab et al. 2007)

Tingle and Jersey (2005)

Tingle and Jersey (2005) carried out cyclic plate load tests on an unbound aggregate. A 1.83 m × 1.83 m × 1.37 m deep reinforced steel box was fabricated to construct the model pavement sections. The subgrade was composed of high-plasticity clay (CH) with a liquid limit of 79, a plastic limit of 23, and a plasticity index of 56. The CH material had 100% passing the No. 10 sieve and 96% passing the No. 200 sieve. The moisture content and CBR value of the subgrade was 47% and 1, respectively. A crushed limestone aggregate (SW-SM) with non-plastic fines was used for the base aggregate material. The maximum aggregate size of the crushed limestone was 38 mm with 57% passing the No. 4 sieve, 30% passing No. 10 sieve, 12% passing the No. 40 sieve, and 6% passing the No. 200 sieve. All geosynthetics were placed on

the top of the subgrade at the base-subgrade interface. The properties of geosynthetics used are given in **Table 9.15**.

Table 9.15. Properties of geosynthetics used in the study by Tingle and Jersey (2005)

Property	Reported Value ^a	Measured Value ^b	Corresponding ASTM Standard
Geotextile			
Color	Grey	-	-
Material	Polypropylene	-	-
Manufacturing process	Needle-punched	-	-
Mass per unit area (g/m ²)	Not reported	193.1	ASTM D5261
Apparent opening size (mm)	0.212	0.074	ASTM D4751
Permittivity (s ⁻²)	1.3	1.192	ASTM D4491
Puncture (kN)	0.375	0.463	ASTM D4833
Trapezoid tear strength (kN)	0.265	0.303	ASTM D4533
Grab tensile strength (kN)	0.71	0.79	ASTM D4632
Geogrid			
Color	Black	-	-
Material	Polypropylene	-	-
Manufacturing process	Biaxial punched and drawn	-	-
Mass per unit area (g/m ²)	305	-	ASTM D5261
Aperture size ^a MD by XD (mm)	25.4 by 33.0	-	Direct measure
Machine wide width tensile strength at 5% strain (kN/m)	11.8	13.2	ASTM D6637
Cross-machine wide width tensile strength at 5% strain (kN/m)	19.8	17.9	ASTM D6637

^a Reported by manufacturer in *Geotechnical Fabrics Report* (8).

^b Mean value from three replicates.

^c Machine direction by cross-machine direction (MD x XD).

From **Figure 9.93** it can be seen that Section 6 (i.e. Item 6, circled by red boxes) is the only section that could be compared with the current study. The thicknesses of the base and subgrade layers in Item 6 were 360 mm and 810 mm, respectively. The TBR value reported for 25 mm rutting deformation was 1.5.

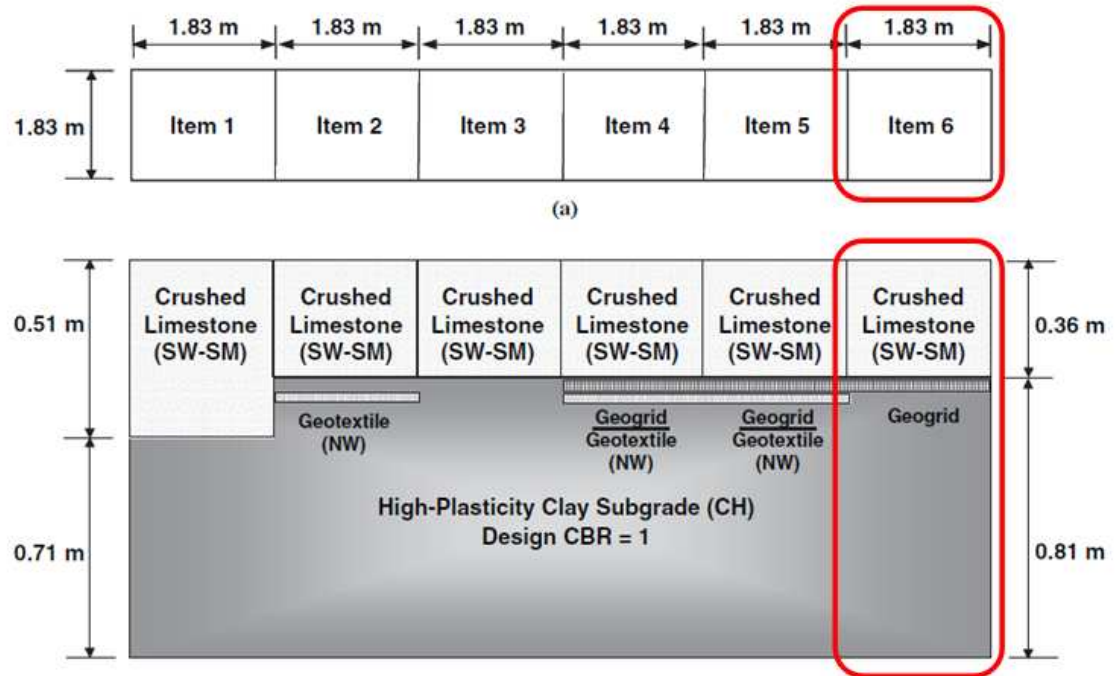


Figure 9.93. Laboratory pavement test items: (a) plan and (b) profile layout (Tingle and Jersey 2005)

9.3.3. The Final TBR Model Based on Rib Strength Properties

EGG: Model #1

$$\text{MD: TBR} = 0.443 - 0.554 X_1 + 0.294 X_2 - 0.11 X_3 \quad (9.3.5)$$

$$\text{XD: TBR} = 0.705 - 1.196 X_1 + 0.927 X_2 - 0.102 X_3 \quad (9.3.6)$$

$$\ln \text{MD: TBR} = -2.881 - 2.093 X_1 + 2.795 X_2 + 0.791 X_3 \quad (9.3.7)$$

$$\ln \text{XD: TBR} = -5.938 - 80157 X_1 + 10.839 X_2 - 1.165 X_3 \quad (9.3.8)$$

EGG: Model #2

$$\text{MD: TBR} = -0.16 - 0.08 X_1 + 0.3478 X_2 - 0.0127 X_1 X_2 \quad (9.3.9)$$

$$\text{XD: TBR} = 0.006 - 1.0664 X_1 + 0.8105 X_2 - 0.003 X_1 X_2 \quad (9.3.10)$$

$$\ln \text{MD: TBR} = -1.0887 + 417.197 X_1 + 421.014 X_2 - 418.558 X_1 X_2 \quad (9.3.11)$$

$$\ln \text{XD: TBR} = -7.42 - 1.3e^{15} X_1 - 1.3e^{15} X_2 + 1.3e^{15} X_1 X_2 \quad (\text{not satisfactory})$$

(9.3.12)

NEGG: Model #1

$$\text{MD: TBR} = -11.22 - 2.75 X_1 - 0.71 X_2 - 0.03 X_1 X_2 \quad (\text{not satisfactory})$$

(9.3.13)

$$\text{XD: TBR} = -0.645 - 0.085 X_1 + 0.068 X_2 + 0.078 X_3 \quad (9.3.14)$$

$$\ln \text{MD: TBR} = -34.203 + 30.93 X_1 - 15.115 X_2 + 3 X_1 X_2 \quad (\text{not satisfactory})$$

(9.3.15)

$$\ln \text{XD: TBR} = -9.984 - 1.124 X_1 + 1.053 X_2 + 3.398 X_3 \quad (9.3.16)$$

NEGG: Model #2

$$\text{MD: TBR} = -11.664 + 2.59 X_1 - 0.27 X_2 - 0.026 X_1 X_2 \quad (\text{not satisfactory})$$

(9.3.17)

$$\text{XD: TBR} = -25.433 + 3.915 X_1 + 2.285 X_2 - 0.283 X_3 \quad (9.3.18)$$

$$\ln \text{MD: TBR} = -6.084 + 1327.2 X_1 + 1321.5 X_2 - 1322.28 X_1 X_2 \quad (\text{not satisfactory})$$

(9.3.19)

$$\ln XD: TBR = -190.5 + 54568.73 X_1 + 54542.63 X_2 - 54517.66 X_1X_2 \text{ (not satisfactory)}$$

(9.3.20)

For any given geogrid in the EGG or NEGG category, Equations 9.3.5 through 9.3.20 could be used as applicable and discard the values that appear to be unreasonable (e.g. TRB < 1).. The smallest TRB value from the remaining set could be considered as the recommended (conservative) value for that specific geogrid based on the results of this study.

Finally, it should be highlighted that the above regression equations were developed based on a series of cyclic plate load tests on ODOT Type-A Aggregate underlain by a CBR = 4 sand substrate in a 1.83 m (L) x 1.83 m (W) x 1.07 m (H) steel test box. Further testing using a wider range of aggregates, substrate materials and reinforcement products would be needed to improve the accuracy and reliability of the proposed equations.

CHAPTER TEN

CONCLUSIONS AND RECOMMENDATIONS

10.1. Conclusions

The primary objective of this study was to investigate the influence of selected in-isolation properties of geogrids on their in-aggregate performance. The focus of the study was on the geogrids rib and junction strength properties. More specifically, the ultimate junction strength, rib strength at 2% strain and 5% strain and ultimate rib strength were investigated in machine and cross-machine directions. The geogrids investigated in the study were classified in two basic categories of extruded (EGG) and non-extruded (NEGG) geogrids. The latter category primarily included the woven and knitted geogrid products. Pullout tests, installation damage tests and cyclic plate load tests were carried out to understand the in-aggregate performance of selected geogrids.

A comprehensive survey was carried out on geogrids available on the market and those (or equivalent properties) recommended by the departments of transportation across the U.S. The analysis of geogrid properties from this survey resulted in a total of eight geogrid products which were selected for a more detailed study. A geogrid classification table was prepared using the information gathered from the survey, which could be useful for the selection of appropriate geogrid products in flexible pavement

design. The geogrid products examined in this study were accordingly classified based on their rib and junction strength properties.

A series of in-isolation and pullout tests were carried out on four extruded (EGG) and four non-extruded (NEGG) geogrids to investigate the significance of junction strength and rib strength properties on their pullout performance in aggregate base layers. The relationship between the index and in-aggregate properties of geogrids depends on several factors including the geogrid and aggregate properties, their frictional and interlocking characteristics and the overburden pressure. The aggregate used in the study was ODOT Type-A which is a dense-graded aggregate commonly used in Oklahoma.

It was observed that a greater overburden pressure resulted in a greater pullout resistance. It was also observed that extruded geogrids with greater junction strength as compared to non-extruded geogrids overall resulted in greater pullout capacity in the ODOT Type-A aggregate. The rib strength values at 2% strain and 5% strain and ultimate junction strength values both in MD and XD were found to be influential in the pullout performance of geogrids in both extruded and non-extruded categories. The rib strength at 2% strain in both MD and XD showed a stronger correlation than the strength at 5% strain with the pullout resistance of all geogrids tested. It was found that, there is no convincing correlation between the geogrid ultimate rib strength and its maximum pullout resistance if the manufacturing technique is not taken into account. However, when examined separately, the MD and XD ultimate rib strength values were found to be reasonably correlated with the pullout performance for the EGG products

tested. However, only the MD ultimate rib strength values were found to show a convincing correlation with the pullout performance of the NEGG products examined. Overall, it was observed that the rib strength properties in MD were slightly more influential than those in XD in the pullout performance of EGG products.

In summary, the low-strain rib strength (i.e. strength at 2% strain and 5% strain) and the ultimate junction strength were found to be important properties of geogrids that influence their pullout performance. The rib strength at 2% strain was found to play a more important role than rib strength at 5% strain, in both MD and XD. The ultimate rib strength also shows a reasonable correlation, when EGG and NEGG products were studied separately. Taken together, results of the study indicated that as a general rule, greater in-isolation strength properties of geogrids in the pullout direction result in greater in-aggregate pullout resistance.

Installation damage reduction factors (RF_{ID}) were determined for rib and junction strength properties of both extruded and non-extruded geogrids using outdoor installation damage tests. The range of installation damage factors for geogrids was found to vary between 1 and 2. The EGG3 and EGG4 products overall showed greater RF_{ID} values compared to other products tested. As a whole, partial reduction factors for the extruded geogrid (EGG) products were found to be larger than those of the non-extruded (NEGG) products. The RF_{ID} values for the rib tensile strength at 2% strain were found to be larger than those for the ultimate strength. This finding indicates that, the as-placed 2%-strain rib strength of the geogrid reinforcement in the field could be overestimated if the commonly-used, smaller reduction factors for ultimate strength are

used for serviceability design. This could result in additional deformations (rutting) and distress in the pavement before adequate strength of the reinforcement could be mobilized.

Static plate load test results indicated that adequate interlocking with aggregates is key to achieving effective reinforcement. Placement of a thin aggregate layer between the geogrid and geotextile layers could be an effective way in the laboratory to simulate the rugged interface that invariably exists between the aggregate base course and the underlying subgrade in the field, which allows the geogrid reinforcement to properly interlock with the aggregate.

Cyclic plate load test results on reinforced aggregate base-loose sand substrate models indicated that the SRF and TBR values of the models were, by and large, proportional to the rib strength of the geogrid reinforcement. However, the SRF and TBR values in either of the EGG or NEGG geogrid categories did not show a convincing dependence on their ultimate junction strength. Overall, the improvement in the performance of the aggregate base-subgrade models tested was found to be primarily proportional to the rib index properties of the geogrid used. A set of equations were developed to calculate a predicted TBR value for the reinforced aggregate-subgrade models with EGG and NEGG products as separate categories.

Based on the results of this study, it was concluded that low-strain rib strength and ultimate junction strength of the geogrids are among their most relevant index properties for base reinforcement applications regardless of the geogrid fabrication

technique (i.e. extruded, woven or knitted). The findings of this study are beneficial in identifying and quantifying the influence of selected index properties of geogrids on the mechanical performance of reinforced aggregate base layers. The large-scale pullout and cyclic plate load tests carried out in this study provides DOT agencies comparative performance data on a wider range of base reinforcement geogrids as compared to fairly limited selection of products that are typically included in their design guidelines and specifications (e.g. ODOT 2009). The laboratory data and analysis in this study are also beneficial in calibrating numerical and analytical models for mechanistic-empirical (M-E) design of reinforced base flexible pavements.

10.2. Recommendations

Based on the findings and observations made in this study, the following recommendations are made for future studies:

1. Additional in-isolation properties of geogrids need to be investigated in the continuation of this study including their aperture stability and the flexural rigidity of the ribs.

2. Other reinforcement products such as newer geotextile reinforcement and reinforcement/filter/drainage composite products need to be tested for base reinforcement and subgrade stabilization applications. Clearly, different index properties of such products from those of the geogrids would be relevant to the reinforcement application, which need to be evaluated.

3. Field-scale tests need to be conducted on roadway sections subjected to actual traffic load, subgrade types and conditions (e.g. soil type, ground water table, etc.), construction techniques and equipment, and climatic conditions that are representative of roadway projects in different states.

4. The results of this study can be further analyzed and used to develop and validate analytical and computational models for the mechanistic-empirical design of roadways that involve reinforced aggregate bases.

5. Cost-benefit analysis and case studies considering the market prices of different geosynthetic reinforcement products (including both geogrids and geotextiles) in relation to the quality of their reinforcement performance could also be useful to promote the application of such products among interested parties such as DOT agencies and roadway contractors.

REFERENCES

- AASHTO (1993). "Guide for Design of Pavement Structures", American Association of State Highway and Transportation Officials, Washington, DC.
- AASHTO (2001). "Recommended practice for geosynthetic reinforcement of the aggregate base course of flexible pavement structures", American Association of State Highway and Transportation Officials, Designation: PP 46-01, Washington, D.C.
- AASHTO (2002). "Standard specifications for transportation material and methods of sampling and testing", American Association of State Highways and Transportation Officials, Washington, D.C.
- AASHTO (2007). "LRFD bridge design specifications", 4th ed., AASHTO, Washington, D.C.
- AASHTO (2008). "Mechanistic-Empirical Pavement Design Guide: A Manual of Practice, Interim Edition", American Association of State Highway and Transportation Officials, Washington, DC.
- Abu-Farsakh, M. Y. and Chen, Q. (2011). "Evaluation of geogrid base reinforcement in flexible pavement using cyclic plate load testing", *International Journal of Pavement Engineering*, (12)3: 275-288
- Alzamora, D.E. and Anderson, S.A. (2012). "Geogrid specifications for base reinforcement", *Presentation at the Geosynthetics Committee Meeting at Geo-Congress*, Oakland, CA, March 2012.
- Aran, S. (2006). "Base reinforcement with biaxial geogrid: long-term performance", *Transportation Research Record*, 1975: 115-123.
- ASTM (1999). "Annual book of standards, road and paving materials", Vehicle Pavement Systems, American Society of Testing Materials, 04.03, West Conshohsken, PA.

- ASTM D6706-01 (2001). "Standard test method for measuring geosynthetic pullout resistance in soil", Annual Book of ASTM Standards, ASTM International, West Conshohocken, PA.
- ASTM (2009). "Book of standards, Volume 4.13: Construction: Geosynthetics", American Society for Testing and Materials, ASTM International.
- ASTM (2009). " Standard test method for: Tensile properties of geotextiles by the wide-width strip method", ASTM International, 100 Barr Harbor Drive, PO Box C700, West Conshohocken, PA 19428-2959, United States, 2009.
- Berg, R.R., Christopher, B.R. and Samtani, N.C. (2009). "Design and construction of Mechanically Stabilized Earth Walls and Reinforced Soil Slopes – Volume I", NHI Courses No. 132042 and 132043, *Report No. FHWA-NHI-10-024 FHWA GEC 011-Vol I*, FHWA, U.S. Department of Transportation, Washington, D.C.
- BS8006 (1995). "Code of practice for strengthened/reinforced soil and other fills", British Standards Institution, Milton Keynes, UK.
- Burgess, G.P. (1999). "Performance of two full-Scale model Geosynthetic-Reinforced Segmental Retaining Walls", *M.Sc. Thesis*, Royal Military College of Canada, Kingston, Ontario.
- Cuelho, E. and Perkins, S. (2009). "Field investigation of geosynthetics used for subgrade stabilization", *Report No. FHWA/MT-09-0003/8193*, Montana Department of Transportation, July 2009.
- Chehab, G.R., Palomino, A.M., Tang, X. (2007). "Lab evaluation and specification development for geogrids for highway engineering applications", *Report No. FHWA-PA-2007-009-050110*, Pennsylvania Transportation Institute, University Park, PA.
- Christopher, B.R., Cuelho, E.V., and Perknis, S.W. (2008). "Development of geogrid junction strength requirements for reinforced roadway base design", *Proceedings of GeoAmericas 2008 Conference*, Cancun, Mexico, 1003-1012.
- Christopher, B.R., Schwartz, C., and Boudreau, R. (2010). "Geotechnical aspects of pavements", National Highway Institute, *Report No. FHWA NHI-10-092*, Washington, DC.

- Douglas, S.C., Schaefer, V.R. and Berg, R.R. (2012). “Geotechnical solutions for soil improvement, rapid embankment construction, and stabilization of the pavement working platform: Web-Based Information and Guidance System Development Report (Draft)”, *SHRP 2 Renewal Project R02*, National Academy of Sciences, February, 2012.
- Federal Highway Administration (FHWA) (2009). “Design of Mechanically Stabilized Earth Walls and Reinforced Soil Slopes – Volume I”, *Report No. FHWA-NHI-10-024 FHWA GEC 011-Vol I*, Berg, R. R., Christopher, B. R. and Samtani, N. C., Federal Highway Administration, Washington, D.C.
- Gabr, M.A., Robinson B., Colin, J.G. and Berg R.R. (2006). “Promoting geosynthetics use on federal lands highway projects”, FHWA-CFL/TD-06-009.
- Giroud, J.P. and Han J. (2004). “Design method for geogrid-reinforced unpaved roads I. Development of design method”, *Journal of Geotechnical and Geoenvironmental Engineering*, 130: 775-786.
- GRI (2005). GRI-GG2: “Standard test method for individual geogrid junction strength”, Rev. 3, Geosynthetic Research Institute, Folsom, PA.
- Hatami, K., Ghabchi, R., Mahmood, T. and Zaman, M. (2011a). “In-aggregate performance of extruded and woven geogrids in open-graded and dense-graded aggregates”, *90th annual conference of Transportation Research Board*, Washington, D.C., 2011.
- Hatami, K., Wang Z., Mahmood, T., Ghabchi, R. and Zaman, M. M. (2011b). “In-aggregate testing of unitized and woven Geogrids for base reinforcement applications”, *Geo-Frontiers Conference*, Dallas, Texas, March, 2011.
- Holtz, R.D., Christopher, B.R. and Berg, R.R. (2008). “Geosynthetic design and construction guidelines”, U.S. Department of Transportation, Federal Highway Administration, Washington DC, *Report No. FHWA-NHI-07-092*, 2008, 592 p.
- Huang, B. and Bathurst, R. J. (2009). “Evaluation of soil-geogrid pullout models using a statistical approach”, *ASTM Geotechnical Testing Journal*, 32 (6): 489-504
- IFAI (2009). “Geosynthetics Specifier’s Guide”, *Industrial Fabrics Association International*, Roseville, MN.

- Jeon, Han-Yong and Bouazza, Abdelmalek (2008). “Analytical consideration of damage tests for geogrids”, *12th international conference of International Association for Computer Methods and Advances in Geomechanics (IACMAG)*.
- Kazmee, H.A. (2010). “Effect of gradation on stiffness and flow behavior of aggregate bases : a laboratory and field study”, *M.Sc. Thesis*, The University of Oklahoma, Norman, OK.
- Koerner, R.M. (2005). “Designing with Geosynthetics”, 5th ed. Pearson, Prentice-Hall, NJ, USA.
- Kwon, J. and Tutumluer, E. (2009). “Geogrid base reinforcement with aggregate interlock and modeling of the associated stiffness enhancement in mechanistic pavement analysis”, *88th annual conference of Transportation Research Board*, 85-95, Washington, D.C., 2012.
- Leng, J., and Gabr, M. A. (2002). “Characteristics of geogrid-reinforced aggregate under cyclic load”, *Transportation Research Record*, 1786: 29-35.
- Luo, R. and Prozzi , J. A. (2009). “Combining geogrid reinforcement and lime treatment to control dry land longitudinal cracking”, *Transportation Research Record*, 2104: 88-96, D.C. 2009.
- Mahmood, T., Hatami, K., Ghabchi, R. and Zaman. M. (2012). “Laboratory investigation of pullout behavior of non-extruded geogrids in a base aggregate”, *91st annual conference of Transportation Research Board*, Washington, D.C., 2012.
- Mahmood, T., Hatami, K., Ghabchi, R. and Zaman. M. (2012). “Pullout response of geogrids with different junction strength”, *Geo-Congress Conference, California*, March, 2012.
- Miura, N., Sakai, A., Taesiri, Y., Yamanouchi, T. and Yasuhara, K. (1990). “Polymer grid reinforced pavement on soft clay grounds”, *Geotextiles and Geomembranes*, 9,(1),:99-123.
- National Concrete Masonry Association (NCMA) (1997). “Design manual for Segmental Retaining Walls”, 2nd ed., J. Collin, Ed.; National Concrete Masonry Association, Herndon, VA.
- NCHRP (2004). National Cooperative Highway Research Program (NCHRP), Applied Research Associates, Inc. “Development of the 2002 Guide for the Design of New

- and Rehabilitated Pavement Structures”, *Final Report and Software (version 0.70) NCHRP Project 1-37A*, Transportation Research Board, Washington, DC, April 2004.
- ODOT (2009). “2009 Standard Specification for Highway Construction”, Oklahoma Department of Transportation, Section 700: Materials, 2009.
- Perkins, S.S. (1999). “Geosynthetic reinforcement of flexible pavements: laboratory based pavement test sections”, *Report No. FHWA/MT-99-001/8138*. US Department of Transportation, Federal Highway Administration, Washington, DC.
- Perkins, S.W., Christopher, B.R., Cuelho, E.L., Eiksund, G.R., Hoff, I., Schwartz, C.W., Svano, G. and Want, A. (2004). “Development of design methods for geosynthetic reinforced flexible pavements”, *Report No. FHWA Rep. DTFH61-01-X-00068*.
- Perkins, S. W., Christopher , B.R., Cuelho, E.L., Eiksund, G.R., Schwartz , C.S. and Svano, G. (2009). “A mechanistic-empirical model for base reinforced flexible pavements”, *International Journal of Pavement Engineering*, 10 (2):101-114, April 2009.
- SPSS (2012). “IBM (International Business Machines) SPSS (Statistical Package for the Social Sciences) Statistics”, Software, IBM Corporation, Software Group, <http://www-03.ibm.com/software/products/us/en/spss-stats-standard/>
- Tang, X., Chehab, G. R. and Palomino. A. (2008). “Evaluation of geogrids for stabilising weak pavement subgrade”, *International Journal of Pavement Engineering*, 9 (6): 413-429, December 2008.
- Tensar International Corporation. “Product specification - TriAx TX140 geogrid”, http://www.tensarcorp.com/uploadedFiles/TriAx_140_TX160_Specs.pdf
- Tingle, J. S. and Jersy, S. R. (2009). “Full-scale evaluation of geosynthetic reinforced aggregate roads”, *Transportation research record, Journal of the Transportation Research Board*, D.C., DOI: 10.3141/2116-13, 2116:96-107, 2009.
- TRI/Environmental, Inc. (TRI) (1998). “Installation Damage Testing of Coated PET Geogrids”, TRI/Environmental, Inc. (TRI), July, 1998.
- TRI/Environmental, Inc. (TRI) (2006). “Carthage Geogrids – Installation Damage Testing”, TRI/Environmental, Inc. (TRI), August 10, 2006.

- Tutumluer, E., Huang, H., and Bian, X. (2012). "Geogrid-aggregate interlock mechanism investigated through aggregate Imaging-Based Discrete Element Modeling Approach", *International Journal of Geomechanics*, 12 (4): 391-398, August, 2012.
- Vlachopoulos, N. (2000). "Performance of two full-scale model geosynthetic-reinforced Segmental Retaining Walls: Segmental and Wrapped-Faced", *M.Sc. Thesis*, Royal Military College of Canada, Kingston, Ontario.
- Wang, Z. (2009). "Influence of geogrids junction strength on the performance of reinforced aggregate base", *M.Sc. Thesis*, The University of Oklahoma, Norman, OK.
- Webster, S. L. (1993). "Geogrid reinforced base courses for flexible pavements for light aircraft: Test section construction, behavior under traffic, laboratory tests and design criteria", USAE Waterways Experiment Station, Vicksburg, MS, *Technical Report DOT/FAA/RD-92/225*, 100 p.

APPENDIX

**DATABASE OF GEOGRID PROPERTIES SURVEYED IN THIS
STUDY**

Table A.1. Properties of geogrids surveyed in the current study as available in the Geosynthetics Specifier's Guide (IFAI 2009)

Manufacturer	Geogrid Name	Dimensional Properties		Mechanical Properties					
		Aperture Size (mm)		Strength @ 5% Strain (kN/m)		Ultimate Strength (kN/m) / (%)			
		MD	XD	MD	XD	MD		XD	
Tensar Intl. Corp.	BX1100	25	33	8.5	13.4
	BX1200	25	33	11.8	19.6
	BX1300	46	64	10.5	17.5
	BX1500	25	31	17.5	20
	TX150
	TX160
	TX170
	CompoGnd CG50	50	3%	50	3%
	CompoGnd CG100	100	3%	100	3%
	GlassGrid 8501	12.5	12.5	.	.	100	3%	100	3%
	GlassGrid 8502	12.5	12.5	.	.	100	3%	200	3%
	GlassGrid 8511	25	25	.	.	100	3%	100	3%
	GlassGrid 8512	19	25	.	.	100	3%	200	3%
	GlassGrid 8550	25	25	.	.	50	3%	50	3%
	LH800	.	.	.	14
	UX1100HS	.	.	27	.	58	.	.	.
	UX1400HS	.	.	31	.	70	.	.	.
	UX1500HS	.	.	52	.	114	.	.	.
UX1600HS	.	.	58	.	144	.	.	.	
UX1700HS	.	.	75	.	175	.	.	.	
UX1800HS	.	.	95	.	210	.	.	.	
ACE Geos. Inc.	ACE GG30-II	25	28	15	.	30	.	30	.
	ACE GG300-II	25	30	120	..	300	.	300	.
	ACE GG60-I	24	28	30	...	60	.	30	.
	ACE GG100-I	21	28	50	.	100	.	30	.
	ACE GG150-I	20	28	75	..	150	.	30	.
	ACE GG400-I	23	26	160	.	400	.	50	.
	ACE GG800-I	24	24	200	.	800	.	100	.
Cartage Mills	GX-300	22	25	15	.	54.3	.	.	.
	GX-500	22	25	16.6	..	62.4	.	.	.
	GX-800	23	23	29.5	.	106.6	.	.	.
	Enkagrid Max 20	41	41	15.1	15.1	24.2	8%	24.2	8%
	Enkagrid Max 30	41	40	21.3	21.3	32	8%	32	8%

Table A.1. Properties of geogrids surveyed in the current study as available in the Geosynthetics Specifier's Guide (IFAI 2009) (continued)

Manufacturer	Geogrid Name	Dimensional Properties		Mechanical Properties					
		Aperture Size (mm)		Strength @ 5% Strain (kN/m)		Ultimate Strength (kN/m) / (%)			
		MD	XD	MD	XD	MD		XD	
Checkmate Geo. Inc.	BX1515PP	49	40.4	12.3	12.4	17.7		15.2	.
	BX2020PP	43.7	41.9	20.7	16	24.8		19.4	.
	BX2525PP	37.9	37.6	19.5	20.1	28.7		26	.
	BX3030PP	41.4	38.9	22.7	26.7	33.2		31.1	.
	BX4040PP	38.7	40.5	28.1	28.8	39.5		38.9	.
	UX10PET	.	.	14.1	.	31.7		.	.
	UX20PET	.	.	21.47	.	49.54		.	.
	UX30PET	.	..	29.82	.	73.68		.	.
	UX50PET	.	..	40.58	.	102.52		.	.
	UX70PET	.	..	45.72	.	114.3		.	.
	UX90PET	.	..	52.54	.	132.4		.	.
	UX100PET	.	.	58.8	.	158.8		.	.
	UX150PET	.	.	70.17	.	203.5		.	.
RG5050	25.4	25.4	.	.	51.6		56.4	.	
RG1010	25.4	25.4	.	.	103.9		102.1	.	
Colbond Inc.	Enkagrid Max 20	44	41	16	16	24	9%	24	9%
	Enkagrid Max 30	44	40	23	23	34	9%	34	9%
	Enkagrid PRO 40	111	41	33	.	44	6%	.	.
	Enkagrid PRO 60	111	37	51	.	70	6%	.	.
	Enkagrid PRO 90	111	35	81	.	105	6%	.	.
	Enkagrid PRO 120	111	34	87	.	127	6%	.	.
Enkagrid PRO 180	111	34	140	.	199	6%	.	.	
Highland Industries	HI-Grid II	23.88	7.11		.	42.311	.	.	.
	HI-Grid III	21.34	5.59		.	56.901	.	.	.
	HI-Grid IV	21.34	6.35		.	83.163	.	.	.
	HI-Grid VIII	22.23	4.06		.	124.015	.	.	.
Tenax Corp.	LBO 202	28	38	9.5	13.5	13		20.5	.
	LBO 302	28	38	14	23	17.5		31.5	.
	MS 220	42	50	9	13.42	13.5		20.5	.
	MS 330	42	50	13.5	19.6	20		30.7	.
	MS 500	60	60	13.5	19.6	22		35	.
TenCate Geos.	Mirafi BXG 11	25.4	25.4	13.4	13.4	29.2		29.2	.
	Mirafi BXG 12	25.4	25.4	13.4	19.7	29.2		58.4	.
	Mirafi Miramesh	3	3	.	.	21		25.3	.
	Miragrid 2XT	22	25	.	.	29.2		29.2	.
	Miragrid 3XT	22	25	15.4	.	46		.	.
	Miragrid 5XT	22	25	25.4	.	62.7		.	.
	Miragrid 7XT	22	25	31.5	.	83.2		.	.
	Miragrid 8XT	22	25	36.8	.	102.1		.	.
	Miragrid 10XT	22	25	45.5	.	138.6		.	.
	Miragrid 20XT	81	7.6	77.9	.	181.2		.	.
Miragrid 22XT	81	7.6	97.8	.	259.1		.	.	
Miragrid 24XT	101	17.8	102.1	.	370.3		..	.	

Table A.1. Properties of geogrids surveyed in the current study as available in the Geosynthetics Specifier's Guide (IFAI 2009) (continued)

Manufacturer	Geogrid Name	Dimensional Properties		Mechanical Properties					
		Aperture Size (mm)		Strength @ 5% Strain (kN/m)		Ultimate Strength (kN/m) / (%)			
		MD	XD	MD	XD	MD		XD	
Synteen Tech. Fab.	SF 11	25	25	15.2	11.5	34.9		56.5	.
	SF 110	20	20	.	.	150.1		.	.
	SF 12	25	25	15.2	19.9	34.9		76.8	.
	SF 20	20	20	.	.	30		.	.
	SF 35	20	20	.	.	50.2		.	.
	SF 350	20	20	.	.	401.3		.	.
	SF ff	20	20	.	.	68.4		.	.
	SF 80	20	20	.	.	108.4		.	.
SF 90	20	20	.	.	124.5		.	.	
TechFab India	Techgrid U-40	30	25	.	.	40		20	.
	Techgrid U-60	30	25	.	.	60		20	.
	Techgrid U-80	30	25	.	.	80		30	.
	Techgrid U-100	30	24	.	.	100		30	.
	Techgrid U-120	30	23	.	.	120		30	.
	Techgrid U-150	30	23	.	.	150		30	.
	Techgrid U-200	30	22	.	.	200		30	.
Samyang	TRIGRID EX 040	34	34	24	.	40		.	.
	TRIGRID EX 060	33	34	36	.	60		.	.
	TRIGRID EX 080	32	34	48	.	80		.	.
	TRIGRID EX 100	31	34	60	.	100		.	.
	TRIGRID EX 150	30	34	90	.	150		.	.
	TRIGRID EX 20/20	35	35	14	14	20		20	.
	TRIGRID EX 30/30	34	34	21	21	30		30	.
	TRIGRID EX 40/40	34	34	28	28	40		40	.
TRIGRID EX 60/60	33	33	38	38	60		60	.	
Strata Systems Inc.	Strata MicroGrid	6.35	2.54	8	5.8	29.2		29.2	.
	StrataGrid SG150	25.4	24.1	9.1	6.2	27.4		27.4	.
	StrataGrid SG200	18.3	16.5	.	.	52.5		.	.
	StrataGrid SG350	21.6	14	.	.	72.9		.	.
	StrataGrid SG500	62.2	25.4	.	.	93.4		.	.
	StrataGrid SG550	21.6	24.1	.	.	118.9		.	.
	StrataGrid SG600	62.2	24.1	..	.	132.8		.	.
StrataGrid SG700	62.2	24.1	.	.	172.2		.	.	
NAUE GmbH & Co. KG	Secugrid 30/30 Q6	34	34	24	24	30		30	.
	Secugrid 40/40 Q6	34	33	32	32	40		40	.
	Secugrid 60/20 R6	73	31	36	.	60		.	.
	Secugrid 80/20 R6	73	30	48	.	80		.	.
	Secugrid 120/40 R6	71	28	72	.	120		.	.
	Secugrid 200/40 R6	71	25	120	.	200		.	.
	Secugrid 20/20 Q1	32	32	16	16	20		20	.
	Secugrid 30/30 Q1	32	32	24	24	30		30	.
	Secugrid 40/40 Q1	31	31	32	32	40		40	.
Combigrid 30/30 Q1 151 GRK 3	32	32	24	24	30		30	.	
St-Gobian Tech. Fab.	CompoGrid CG 100	100	3%	100	3%
	CompoGrid CG 50	50	3%	50	3%
	GlasGrid 8501	12.5	12.5	.	.	100	3%	100	3%
	GlasGrid 8502	12.5	12.5	.	.	100	3%	200	3%
	GlasGrid 8511	25	25	.	.	100	3%	100	3%
	GlasGrid 8512	19	25	.	.	100	3%	200	3%
	GlasGrid 8550	25	25	.	.	50	3%	50	3%

Table A.1. Properties of geogrids surveyed in the current study as available in the Geosynthetics Specifier's Guide (IFAI 2009) (continued)

Manufacturer	Geogrid Name	Dimensional Properties		Mechanical Properties					
		Aperture Size (mm)		Strength @ 5% Strain (kN/m)		Ultimate Strength (kN/m) / (%)			
		MD	XD	MD	XD	MD		XD	
Lukenhaus Tech. Tex. Inc.	RAUGRID 11X3N	20	20	29.3	.	110	.	.	.
	RAUGRID 13X3N	20	20	41	.	130	.	.	.
	RAUGRID 15X3N	20	20	43.5	.	150	.	.	.
	RAUGRID 2X2N	20	20	8	.	20	20	.	.
	RAUGRID 3X3N	20	20	9.7	.	30	30	.	.
	RAUGRID 4X2N	20	20	11.4	.	40	.	.	.
	RAUGRID 5X2N	20	20	16	.	50	.	.	.
	RAUGRID 6X3N	20	20	17.9	.	60	.	.	.
	RAUGRID 8X3N	20	20	23.5	.	80	.	.	.
	STARGrid G+PF	30	30	.	.	50	50	.	.
STARGrid G-PS 100	30	30	.	.	100	100	.	.	
Maccaferri Inc.	MacGrid EB2	42	50	9	13.4	13.5	20.5	.	.
	MacGrid EB3	42	50	13.5	19.6	20	30.7	.	.
	MacGrid WG5	24	28	28	.	55	.	.	.
	MacGrid WG8	24	28	40	.	80	.	.	.
	MacGridWG11	21	24	55	.	110	.	.	.
	MacGridWG15	21	28	75	.	150	.	.	.
	MacGridWG20	19	28	100	.	200	.	.	.
	MacGridWG40	24	26	160	.	400	.	.	.
	MacGridWG60	34	26	180	.	600	.	.	.
	ParaLink 600	931	90	.	.	672	.	.	.
ParaLink 800	931	59	.	.	896	.	.	.	
Linear Composites	ParaGrid 30	426	51	.	.	30	5	.	.
	ParaGrid 50	426	51	.	.	50	5	.	.
	ParaGrid 80	426	51	.	.	80	5	.	.
	ParaGrid 100	426	51	.	.	100	5	.	.
	ParaGrid 150	426	42	.	.	150	5	.	.
	ParaGrid 200	426	42	.	.	200	5	.	.
	ParaLink 200	932	95	.	.	200	.	.	.
	ParaLink 300	932	92	.	.	300	.	.	.
	ParaLink 400	932	90	.	.	400	.	.	.
	ParaLink 500	932	90	.	.	500	.	.	.
	ParaLink 600	932	90	.	.	600	.	.	.
	ParaLink 700	932	89	.	.	700	.	.	.
	ParaLink 800	932	59	.	.	800	.	.	.
	ParaLink 900	932	34	.	.	900	.	.	.
	ParaLink 1000	932	34	.	.	1000	.	.	.
ParaLink 1250	932	8	.	.	1250	.	.	.	
Huesker Inc.	Formit 20	15	15	11	16	17	6%	24	6%
	Formit 30	15	15	20	27	27	6%	35	6%
	Formit 30/30	35	35	24	24	30	6%	30	6%
	Formit 40/40	40	40	32	32	40	6%	40	6%
	HaTelit C 40/17	40	40	.	.	50	10%	50	10%
	Fortrac 35	20	20	13
	Fortrac 55	20	20	18
	Fortrac 80	20	20	26
	Fortrac 110	20	20	33
	Fortrac 150	30	30	52
	Fortrac 200	30	30	69
	Fortrac 35 MP	20	30	34
	Fortrac 55 MP	20	30	49
	Fortrac 80 MP	20	30	72
	Fortrac 110 MP	20	30	98